Inaugural - Dissertation

zur Erlangung der Doktorwürde der
Naturwissenschaftlich-Mathematischen Gesamtfakultät der
Ruprecht-Karls-Universität
Heidelberg

Development and Implementation of High-Level Propagator Methods for the Description of Electronically Stable and Unstable States

vorgelegt von

Adrian Ludwig Dempwolff, Diplom-Chemiker
aus Celle

im Februar 2020

Gutachter:

Prof. Dr. Andreas Dreuw
Priv.-Doz. Dr. Kirill Gokhberg

Datum der mündlichen Prüfung: 8. April 2020

Für Laura

Zusammenfassung

Die Wechselwirkung mit elektromagnetischer Strahlung oder freien Elektronen kann in Atomen und Molekülen zu mannigfaltigen Umformungsprozessen führen. Solche Streuprozesse können elastischer Natur sein oder aber inelastisch. In diesem Fall können verschiedene Produkte gebildet werden, die sich durch ihre jeweiligen Quantenzustände unterscheiden. Die Produktverteilung ist dabei abhängig von der Art der Wechselwirkung und der beteiligten Teilchen sowie von der dabei übertragenen Energie.

Zu den beobachtbaren Prozessen gehören elektronische Anregungen, Photoionisationsprozesse sowie die Bildung elektronischer Resonanzzustände. Letztere können aus unterschiedlichen Anregungsprozessen hervorgehen oder durch Absorption langsamer Elektronen gebildet werden und sind metastabil bezüglich elektronischer Zerfallsreaktionen. In dieser Dissertation wird die Weiterentwicklung und Implementierung quantenchemischer Propagator-Methoden und deren Anwendung in Studien einer Auswahl der oben genannten Prozesse beschrieben.

Insbesondere werden verschiedene störungstheoretische Ansätze auf Basis des algebraisch-diagrammatischen Konstruktionsverfahrens (ADC) für den Elektronen- und Polarisations-Propagator verwendet. Im Rahmen dieser Methoden sind elektronische Einteilchen-Eigenschaften über die sogenannte *intermediate state representation* (ISR) zugänglich, mithilfe derer sich ADC-Wellenfunktionen explizit darstellen lassen. Die ADC-Schemata dritter Ordnung [ADC(3)] können dabei dadurch verbessert werden, dass der in den zugehörigen Gleichungen auftretende energieunabhängige Teil der sogenannten Selbstenergie dritter Ordnung $\Sigma(3)$ durch eine entsprechende Größe vierter Ordnung ersetzt wird, die zusätzlich Terme höherer Ordnung berücksichtigt und durch das selbstkonsistente $\Sigma(4+)$-Iterationsverfahren berechnet werden kann. Im Rahmen dieser Arbeit wurde diese Methodik mit ADC für Ionisierungspotentiale (IP-ADC), ADC für Elektronenaffinitäten (EA-ADC), sowie zum ersten Mal auch mit ADC für elektronische Anregungen (PP-ADC) kombiniert.

Im ersten Teil dieser Dissertation werden Photoionisationsprozesse untersucht, deren theoretische Beschreibung durch IP-ADC möglich ist. Im Rahmen dieser Arbeit wurde die Implementierung der IP-ADC(3)-Methode im quantenchemischen Programm Q-Chem

durch die Möglichkeit erweitert, Photoelektronen-Intensitäten zu berechnen, wodurch die Simulation von Photoelektronen-Spektren mit IP-ADC(3) nun möglich ist. Andere neue Funktionalitäten unterstützen die Interpretation von Ionisierungsprozessen durch Visualisierung von Dyson-Orbitalen und weiterer Größen wie beispielsweise Detachment- und Attachment-Dichten, die sich von der Einteilchen-Dichtematrix ableiten und mithilfe der ISR berechnet werden können.

In einer Benchmark-Studie wurde die Genauigkeit der IP-ADC(3)/ISR(2)-Methode zur Berechnung von Ionisierungspotentialen und Einteilchen-Eigenschaften untersucht, indem die für 44 elektronische Zustände kleiner Moleküle berechneten Werte mit hochgenauen Ergebnissen der Konfigurations-Wechselwirkungs-Methode verglichen wurden. Dabei wurde für Ionisierungspotentiale ein mittlerer absoluter Fehler von $\overline{|\Delta|} \approx 0.2\,\mathrm{eV}$ gefunden. Der entsprechende relative Fehler für Dipolmomente beträgt $\overline{|\Delta|} = 19\,\%$. Der Nutzen der Dichtematrix-basierten Visualisierung von Photoionisationsprozessen wird in einer zweiten IP-ADC(3)-Studie anhand des Beispiels des freien Radikals Galvinoxyl aufgezeigt.

Der zweite Teil dieser Arbeit beschäftigt sich mit elektronischen Resonanzzuständen. Aufgrund der ungebundenen Natur solcher Zustände stellt deren theoretische Beschreibung eine große Herausforderung dar. Zwei der bisher zur Behandlung solcher Zustände im Rahmen der Standard-Methoden der Quantenchemie entwickelten Ansätze werden im Rahmen dieser Dissertation eingehender betrachtet.

Zunächst wird die effiziente Implementierung der Fano-Stieltjes-ADC-Methode im quantenchemischen Programmpaket Q-Chem beschrieben. Zum ersten Mal wurden dabei das dritte-Ordnungs-Schema PP-ADC(3) sowie die *unrestricted*-Varianten der PP-ADC-Schemata mit dem Fano-Stieltjes-Ansatz kombiniert. Die Anwendbarkeit der neuartigen Implementierung auf die Berechnung elektronischer Resonanzzustände in mittelgroßen organischem Molekülen wird anhand des Beispiels von Naphthalin aufgezeigt.

Als zweite Möglichkeit zur Beschreibung elektronischer Resonanzzustände wurde eine Kombination der komplexen Absorptions-Potential-Methode (CAP) mit PP-ADC(3) und EA-ADC(3) in Betracht gezogen und weiter untersucht. Die mit der Q-Chem-Implementierung der neuartigen CAP-EA-ADC- und CAP-PP-ADC-Methoden berechneten Ergebnisse zeigen eine hervorragende Übereinstimmung mit experimentellen Daten und hochgenauen theoretischen Berechnungen. Die untersuchten Resonanzzustände umfassen den $^2\Pi_g$-Zustand des Distickstoff-Anions und die niedrigsten π^*-Resonanzzustände der Anionen der nicht-konjugierten organischen Diene Norbornadien und 1,4-Cyclohexadien. Die neuen CAP-EA-ADC(3)-Ergebnisse bestätigen bisherige Studien, die einen starken *through-bond*-Wechselwirkungs-Mechanismus für die Umkehrung der natürlichen energetischen Reihenfolge der π^*-Molekülorbitale von 1,4-Cyclohexadien verantwortlich machen.

Abstract

Interactions of atoms or molecules with electromagnetic radiation or free electrons can induce a variety of transformations. Apart from elastic scattering processes, in which the quantum states of the involved particles are preserved, inelastic scattering may occur. The distribution of product states depends on the kind of the interacting particles and the energy transferred in the scattering process.

Among the possible transformations are electronic excitation, photoionization and the formation of electronic resonances, i.e., metastable electronic states which undergo subsequent decay by emission of an electron. The latter states can evolve in electronic excitation processes or as a result of electron attachment. In this dissertation, the implementation and application of quantum chemical propagator methods for the description of the above-mentioned processes are presented.

More specifically, a number of perturbation theoretical methods based on the algebraic diagrammatic construction (ADC) schemes for the electron propagator and the polarization propagator are considered. In the framework of these methods, one-electron properties are available via the intermediate state representation (ISR) approach, which enables the computation of the explicit form of the respective wave functions. The third-order static self-energy $\Sigma(3)$ appearing in the third-order ADC(3) equations can thereby be replaced by an improved fourth-order quantity resulting from the so-called $\Sigma(4+)$-procedure, and this option has been explored in the context of ADC for ionization potentials (IP-ADC), electron affinities (EA-ADC) and, for the first time, excitation energies (PP-ADC).

In the first part of this dissertation, photoionization processes are considered, whose theoretical treatment is possible using IP-ADC(3). In the course of this work, the existing implementation of IP-ADC(3) in the Q-Chem quantum chemical program package has been extended by the possibility to compute photoelectron intensities, and therefore, to simulate photoelectron spectra. Other newly implemented features enable the interpretation of ionization transitions by means of visualization of Dyson orbitals and one-particle density matrix-based quantities as, e.g., detachment and attachment densities, which are available via the second-order ISR(2) approach.

The accuracy of the IP-ADC(3)/ISR(2) methodology with respect to ionization po-

tentials and one-particle properties of electron-detached states has been evaluated in a subsequent benchmark study. Therein, the results obtained for 44 electronic states of small molecules are compared to high-level configuration interaction results. For this set of transitions, ionization potentials exhibit a mean absolute error of $\overline{|\Delta|} \approx 0.2\,\text{eV}$. For dipole moments, a relative error of $\overline{|\Delta|} = 19\,\%$ is found. In a second IP-ADC(3) study, the applicability of the newly implemented density matrix-based analyses for the interpretation of photoelectron spectra is demonstrated using the example of the galvinoxyl free radical.

In the second part of this dissertation, electronic resonances are addressed. Due to the unbound nature of the involved electronic states, their theoretical treatment is challenging. Different theoretical approaches for their description within the framework of standard quantum chemical methods have been devised, two of which are considered in this work.

First, the efficient implementation of the Fano-Stieltjes-ADC method in the Q-Chem program is presented. For the first time, the third-order PP-ADC(3) scheme as well as various unrestricted PP-ADC schemes have been combined with the Fano-Stieltjes formalism. The applicability of the implementation for the description of resonances in medium-sized organic molecules is demonstrated in a study of a Feshbach resonance in the naphthalene molecule.

As a second option for the theoretical treatment of electronic resonances, the combination of the subspace-projected complex absorbing potential (CAP) method with PP-ADC(3) and EA-ADC(3) is considered. Results obtained using the novel CAP-EA-ADC and CAP-PP-ADC methods as implemented in the Q-Chem quantum chemical program package show an excellent agreement with theoretical best estimates and experimental data in studies of π^* shape resonances in unsaturated molecules. Among the studied resonance states are the $^2\Pi_g$ resonance of the dinitrogen anion as well as the lowest π^* resonances of the anions of the non-conjugated organic dienes norbornadiene and 1,4-cyclohexadiene. CAP-EA-ADC(3) calculations are in line with previous findings and show that a strong through-bond interaction mechanism reverses the natural ordering of the π^* molecular orbitals in 1,4-cyclohexadiene.

Contents

Abbreviations

3+	renormalized 3rd-order method
ADC	Algebraic Diagrammatic Construction
CAP	Complex Absorbing Potential
CC	Coupled-Cluster
CCSD	Coupled-Cluster Singles and Doubles
CI	Configuration Interaction
CISDTQ	Configuration Interaction accounting for Singly-, Doubly-, Triply- and Quadruply-excited states
COM	Center of Mass
CNC	Center of Nuclear Charges
CVS	Core-Valence Separation
DEM	Dyson Expansion Method
DFT	Density Functional Theory
DIIS	Direct Inversion of the Iterated Subspace
EA	Electron Affinity
EA-ADC	Algebraic Diagrammatic Construction for Electron Affinities
EEL	Electron Energy Loss
EOM	Equation-Of-Motion
ERI	Electronic Repulsion Integral
ES	Electron Scattering
ETI	Excitation Transfer Ionization
ETMD	Electron-Transfer Mediated Decay
ETS	Electron Transmission Spectroscopy
FCI	Full Configuration Interaction
FWHM	Full Width at Half Maximum
GFR	Galvinoxyl Free Radical
GS	Gram-Schmidt
HF	Hartree-Fock

ICD	Interatomic/Intermolecular Coulombic Decay
IP	Ionization Potential
IP-ADC	Algebraic Diagrammatic Construction for Ionization Potentials
ISR	Intermediate State Representation
KS	Kohn-Sham
MGS	Modified Gram-Schmidt
MO	Molecular Orbital
MP	Møller-Plesset
NR2	Non-diagonal Renormalized 2nd-order method
OVGF	Outer Valence Green's Function
P3	Partial 3rd-order method
P3+	renormalized Partial 3rd-order method
PES	Photoelectron Spectrum
PP-ADC	Algebraic Diagrammatic Construction for the Polarization Propagator
PT	Perturbation Theory
RHF	Restricted Hartree-Fock
SCF	Self-Consistent Field
SOMO	Singly Occupied Molecular Orbital
TBE	Theoretical Best Estimate
TRPES	Time-Resolved Photoelectron Spectroscopy
UHF	Unrestricted Hartree-Fock
UV	Ultra-Violet
VAE	Vertical Attachment Energy
VDE	Vertical Detachment Energy
XMCQDPT2	eXtended Multi-Configurational Quasi-Degenerate Perturbation Theory of 2nd order

Chapter I

Introduction

Atoms and molecules can undergo a large variety of transformations. Among the possible processes are interactions with electromagnetic radiation as well as with free electrons. Many of these transformations have been studied experimentally, and considerable knowledge about the electronic structure of matter has been gathered. The interpretation of experimental results can thereby be facilitated by accompanying theoretical investigations. In fact, physical modelling of the respective processes often makes an understanding possible at all.

In the course of this work, a number of theoretical methods have been developed and implemented, each of them designated for a specific electronic structure problem. This chapter provides a brief introduction to these methods and the processes which can be studied by their means.

One class of processes, which is considered in this thesis, is constituted by different ionization processes of atoms and molecules. These can proceed via different pathways, each of which starts with the interaction of the respective particle with a second particle or with electromagnetic radiation. During the interaction process, energy is transferred onto the atom or molecule to be ionized. In the case of interaction with electromagnetic radiation or, adopting the picture of a projectile hitting a target, with a photon, the energy transferred corresponds to the energy of this absorbed photon, and the description of the

Parts of this chapter have already been published in

- A. L. Dempwolff, M. Schneider, M. Hodecker, A. Dreuw, "Efficient Implementation of the Non-Dyson Third-Order Algebraic Diagrammatic Construction Approximation for the Electron Propagator for Closed- and Open-Shell Molecules", *J. Chem. Phys.* **2019**, *150*, 064108.
- A. L. Dempwolff, A. C. Paul, A. M. Belogolova, A. B. Trofimov, A. Dreuw, "Intermediate State Representation Approach to Physical Properties of Molecular Electron-Detached States: I. Theory and Implementation", *J. Chem. Phys.* **2020**, *152*, 024113.

underlying mechanism falls into the regime of photochemistry.

Besides the case of elastic scattering, the system may experience inelastic scattering, yielding a manifold of different reaction products. The product distribution is determined by the nature of the absorption process and the transferred energy. Among the observable processes are resonant electronic excitations as well as non-resonant photoionization processes leading to cationic species, the latter being one of the objectives of this dissertation. A more detailed discussion of the theoretical methods implemented in this work and subsequently used for the description of photoionization transitions is given in Section I.1.

In the case of resonant electronic excitation, a special case may occur if the generated ionized or excited species ends up in an electronic state characterized by an energy higher than the particle's ionization potential. Such systems are usually not stable and relax by subsequent emission of a free electron into the continuum. The respective processes are commonly summarized under the term *autoionization*. Closely related by means of their unbound nature are metastable anions with or without bound ground states, which can be formed under certain circumstances when a free electron is absorbed by a neutral particle. A common feature of all mentioned states in the energetic continuum region is their finite lifetime. They are examples for *electronic resonances*, which are the second objective of this dissertation. A more detailed introduction to this topic is given in Section I.2.

I.1. Direct Photoionization

The ionization potential (IP) is a fundamental molecular property defined as the energy required to remove one electron from the system, thus corresponding to the energy difference between the final ionized state and the initial neutral state. From this perspective, IPs are one-electron properties and can often be interpreted with reasonable accuracy in the single-particle picture of molecular orbitals (MOs) and their corresponding orbital energies. However, the single-particle picture breaks down for higher ionization potentials as well as in strongly correlated systems.[1]

Ionization potentials are physical observables which can be measured in the gas phase for example via photoelectron or photoemission spectroscopy (PES).[2] In these experiments, the molecules are ionized by X-ray or UV radiation of photon energy E_{ph}, and the kinetic energy E_{kin} of the emitted electron is recorded, yielding the photoelectron spectrum. The spectrum is directly related to ionization potentials via the equation $\mathrm{IP} = E_{\mathrm{ph}} - E_{\mathrm{kin}}$, reflecting Einstein's explanation of the photoelectric effect.[2] More recently, time-resolved PES was successfully used to investigate reaction intermediates.[3, 4] Furthermore, the IP is also of general interest to chemical and material science since it is directly related to

oxidation potentials and can thus serve as a molecular "ruler" for hole transport materials in organic semi-conductors.[5, 6]

The simplest and most straightforward way for a theoretical estimation of IPs is to rely on Koopmans' or Janak's theorems in Hartree–Fock (HF) or density functional theory (DFT), respectively, which are valid in the single-particle picture and state that the negative energy of an occupied orbital is equal to the ionization potential.[7, 8] Koopmans' theorem (KT) is usually a fairly accurate first approximation, since two effects are neglected, i.e., orbital relaxation upon ionization, and electron correlation (in the HF case), which counteract one another. The typical error, however, is still of the order of 1–2 eV.

A possible way to improve upon Koopmans' theorem is to perform two separate self-consistent field (SCF) HF calculations for the neutral N-electron and the ionized $(N-1)$-electron species and to take the difference of the two absolute energies. This approach is referred to as ΔSCF method which, however, usually underestimates IPs since the cationic species is stabilized due to the inclusion of orbital relaxation while electron correlation is still neglected. The latter can be accounted for by using, e.g., second-order Møller-Plesset (MP) perturbation theory or coupled-cluster methods,[9, 10] yielding so-called ΔMP2 or ΔCC values. Furthermore, all of these "Δ-methods" suffer from the disadvantages that two separate calculations have to be carried out, which do not necessarily converge to the desired state, and that the intrinsic errors of the two calculations accumulate.

Thus, it is generally desirable to obtain IPs directly in one calculation. To this end, several quantum chemical methods have been devised. In particular, various Green's function or propagator[11, 12] based computational schemes have been developed, which nowadays belong to standard tools of quantum chemistry.[13–17] They allow for a direct evaluation of vertical transition energies and amplitudes of single-electron detachment and attachment processes and are widely used in studies of molecules, clusters and ions.[1, 18–29] Viable electron propagator methods were obtained using the algebraic-diagrammatic construction (ADC) approach.[30, 31] The latter represents a general procedure for deriving higher-order approximation schemes,[13, 32–36] referred to as ADC(n) schemes.

All ADC schemes share a number of useful properties which make them highly competitive in practical applications.[13] ADC computational schemes are Hermitian eigenvalue problems with ADC matrix elements given by *regular* perturbation-theoretical (PT) expansions of Møller-Plesset type. The explicit ADC configuration spaces are distinctly smaller than those required within configuration interaction (CI) at similar PT accuracy, which is known as the *compactness* of ADC approximations.[37, 38] As a result, ADC schemes feature the best ratio of PT accuracy and computational effort among comparable quantum-chemical methods.[39, 40] Another property of ADC schemes is *size consistency*,

which guarantees *size-intensive* results for transition energies and amplitudes.[41]

In the case of the electron propagator $\mathbf{G}(\omega)$, the ADC procedure can be applied either to the self-energy $\mathbf{\Sigma}(\omega)$ of the Dyson equation[11, 12] or to the propagator itself. This yields two families of approximations, referred to as Dyson ADC[30] and non-Dyson ADC (nD-ADC)[31] schemes, respectively.

Dyson ADC schemes were derived up to the ADC(4) level of theory.[30] These methods were frequently used, usually in combination with a fourth-order treatment of the static self-energy $\Sigma(\infty)$ within the framework of the Dyson-expansion method (DEM),[21, 42] improving the overall accuracy of ADC results. In particular, various implementations of the ADC(3) scheme[21, 43, 44] were successfully employed in studies of valence-shell ionization processes (see, e.g., Refs. [1, 21, 45–58]).

Examples of Dyson propagator methods not related to the ADC approximation include earlier superoperator,[59–61] equation-of-motion (EOM)[62, 63] and two-particle-one-hole Tamm-Dancoff (2ph-TDA)[21] approaches, as well as the more recent renormalized third-order method (3+)[22] and nondiagonal renormalized second-order method (NR2)[64]. Simpler schemes are the outer-valence Green's function (OVGF),[21, 22, 65–67] partial third-order (P3)[68, 69] and renormalized partial third-order (P3+)[70] diagonal self-energy methods. The performance of many contemporary Dyson electron propagator methods was investigated in a series of recent comprehensive benchmark studies.[71–73]

A notable disadvantage of the Dyson approaches is that the $\mathbf{G}^-$ and $\mathbf{G}^+$ parts of the propagator are coupled by means of the Dyson equation, and the ensuing computational schemes are formulated with respect to both $(N-1)$- and $(N+1)$-electron configurations. This leads to difficult numerical procedures and increased computational costs, since only one type of solution (for the electron detachment or electron attachment problem) is typically sought at a time. This is achieved in the nD-ADC approach in which decoupling of the $(N-1)$- and $(N+1)$-electron spaces leads to IP-ADC (ADC for ionization potentials) and EA-ADC (ADC for electron affinities), depending on whether the ADC procedure is applied to the $\mathbf{G}^-$ or $\mathbf{G}^+$ propagators.[31] Using these methods, valence-shell electronic processes become easily tractable since the desired eigenvalues, i.e., electron detachment and electron attachment energies, are located at the low energy edge of the spectrum, rather than in the middle as in the Dyson approaches.

A first pilot implementation of IP-ADC(3)[74] was used to perform calculations for a series of prototype molecules, and various IP-ADC schemes were compared. IP-ADC(3) and Dyson-ADC(3) were found to have virtually the same accuracy when similar approximations to the static self-energy are employed.

The first efficient implementation of IP-ADC(3) for closed- and open-shell molecules

was recently realized within the Q-Chem software.[75–77] In the course of this dissertation, this implementation was extended by a number of features, including the possibility to compute spectral intensities of ionization transitions, making the simulation of photoelectron spectra possible and allowing for the visualization of ionization processes by means of Dyson orbitals. In addition, the existing code was extended by an improved fourth-order treatment of the static self-energy using the $\Sigma(4+)$ scheme,[74] which was subsequently also integrated into the EA-ADC and PP-ADC (ADC for the polarization propagator) implementations in Q-Chem, enabling the treatment of electron attachment and electronic excitation processes on an improved third-order level.

The key advantage of nD-ADC approaches over Dyson methods is the existence of the basis of explicit correlated states, the so-called intermediate states (IS),[37, 38, 78, 79] in which the nD-ADC equations are formulated. IP-ADC schemes are thus similar to the equation-of-motion ionization potential coupled-cluster (CC) methods (EOM-IP-CC),[79–88] which are obtained by representing $\hat{H} - E_0$ in a basis of biorthogonal CC correlated excited states.[37, 79] The availability of explicit expressions for the intermediate state basis opens a new dimension for IP-ADC applications, since wavefunctions of electron-detached states become accessible, and various one-electron properties can thus be calculated.[74]

In the course of this dissertation, the scope of the Q-Chem implementation of the second-order intermediate state representation (ISR) expressions for the one-particle (transition) density[89] was extended to allow for the inclusion of one-electron potentials in the Hamiltonian as well as density-based analyses. These techniques have been used in a number of computational studies,[90–98] however, only closed-shell systems could be treated. The new implementation also enables the investigation of electron detachment processes in open-shell molecules, and a related study is presented in Chapter V. Moreover, the IP-ADC/ISR methodology was benchmarked with respect to full configuration interaction (FCI) data, covering an comprehensive range of closed- and open-shell systems. The results of this benchmark study are presented in Chapter IV.

I.2. Electronic Resonances

Electronic resonances can be described as discrete states embedded in a continuum.[23, 99] Due to their interaction with the continuum they possess a finite lifetime τ, which is connected to the decay width Γ by the inverse relation

$$\tau = \frac{\hbar}{\Gamma}. \tag{1.1}$$

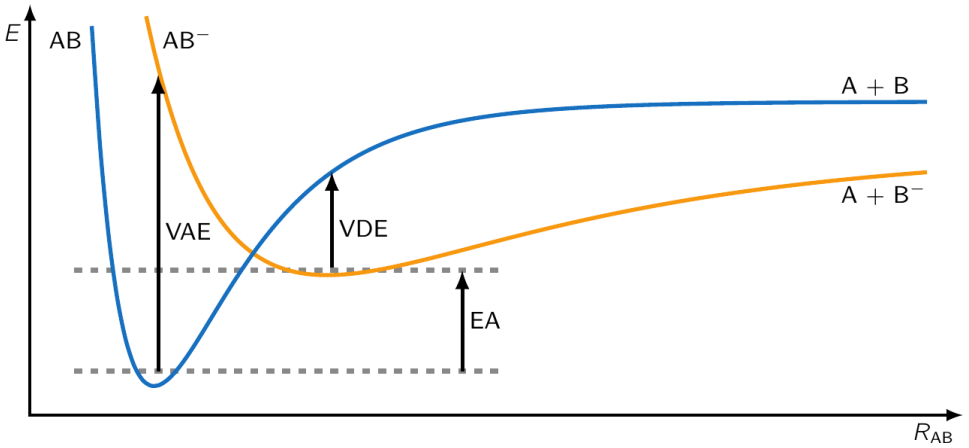

Figure I.1. Schematic illustration of an anion shape resonance. The anionic species (AB^-, orange potential curve) possesses a higher energy than its own continuum ($AB + e^-$, blue potential curve), but is trapped behind a potential barrier. Adapted from Ref. [101].

Consequently, the energy of an electronic resonance E_{res} is a discrete quantity, which, as a matter of fact, is complex. It is commonly referred to as *Siegert energy*,[100] and the characteristic parameters of the resonance, i.e., the resonance position E_r and width Γ are accessible as its real and imaginary part, i.e.,

$$E_{\text{res}} = E_r - i\frac{\Gamma}{2}. \tag{1.2}$$

Resonance states can be distinguished by different means, the most commonly used classification being the distinction between *shape* and *Feshbach resonances*. In general, the latter can only relax via two-electron processes, while the decay mechanism of shape resonances only involves one-particle transitions. In the following, an overview of the characteristics of different resonance types is given.

I.2.1. Shape Resonances

Electronic shape resonances are metastable states possessing electronic energies above their own continua.[101] This means that an electron may be ejected by means of a one-electron process, the released energy being transferred to this electron as kinetic energy. For this reason, shape resonances are often also referred to as *open-channel* resonances. Due to the one-particle nature of the decay mechanism, shape resonances are usually short-lived with typical lifetimes in the range of $\tau \sim 1\,\text{fs}$, corresponding to decay widths of $\Gamma \sim 0.1 \ldots 1\,\text{eV}$.

Figure I.1 schematically displays the situation encountered for a typical shape resonance at the example of a diatomic molecule AB. If an electron with a suitable kinetic energy

close to the vertical attachment energy (VAE) enters the system, it may be absorbed in a vertical electron attachment process. Depending on the energetics, the anionic system can relax to its minimum geometry by internal conversion. At this point, emission of the electron in a vertical detachment process is characterized by a positive vertical detachment energy (VDE), making the process unfeasible. However, the AB potential surface is accessible by tunneling through the potential barrier at a slightly distorted geometry.

Figure I.1 also demonstrates another common observation in the context of anion resonances, i.e., that the ground state of an anionic species can be a resonance state. In fact, such situations are very common, and shape resonances thus occur in a large variety of molecular systems. Experimentally, they have been detected in many unsaturated[102–104] as well as saturated[104, 105] organic compounds using, e.g., electron energy loss (EEL) or electron transmission spectroscopy (ETS). Besides temporary anions, shape resonances can also be encountered in highly excited or core-ionized electronic systems.[99, 101]

I.2.2. Feshbach Resonances

The second class of electronic resonances considered in this dissertation are Feshbach resonances, which are resonance states energetically lying below their own continua. In that sense, they are also called *closed-channel* resonances, meaning that a decay to the ground state of the electron-detached species is only possible via two-electron processes.[101] The lifetimes of electronic Feshbach resonances are consequently considerably higher than those of shape resonances, and are typically found to be in the range of $\tau \sim 10\,\mathrm{fs} \ldots 1\,\mathrm{ps}$.

Because of the two-electron nature of the decay mechanism of this type of resonances, a large variety of possible relaxation pathways exists, some of which include energy and even electron transfer from or to neighboring atoms or molecules. Feshbach resonances are electronically exited states which can be prepared by means of various kinds of transitions, including electronic excitation, ionization as well as electron attachment.

In order to classify different Feshbach-type autoionization processes with respect to the number of particles involved in the overall process, the type of the initial excitation or ionization (the *initial*, *bound* or *decaying state*) as well as the nature of the state the system relaxes to (the *final* or *continuum state*), a variety of naming conventions has been introduced. A non-exhaustive collection of named processes is shown in Figure I.2.

In the following, some of the processes indicated in Figure I.2 will be discussed in more detail. A first classification of Feshbach resonances can be accomplished by considering the kind of transition leading to the initial state, which can be a resonant or non-resonant process.

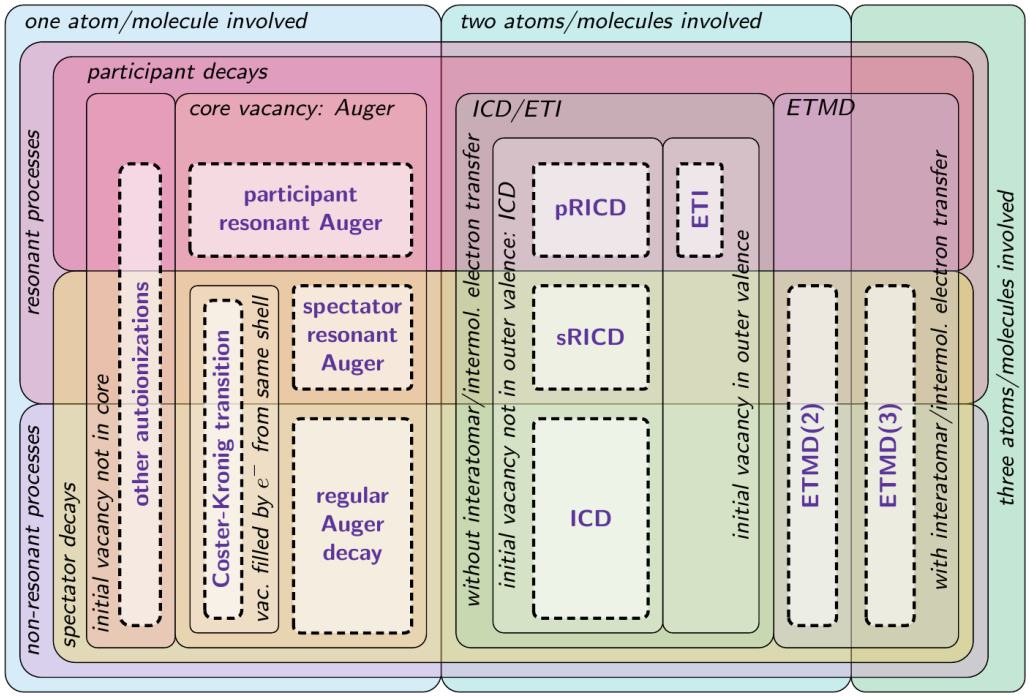

Figure I.2. Logical diagram illustrating naming conventions for different flavors of Feshbach autoionization. Each dashed box represents a named process, classified by means of the properties apparent from the intersection of the colored property boxes it covers.

Non-Resonant Processes

In non-resonant autoionization processes, the decaying state is usually formed by photoionization of a neutral particle, leading to a cationic species. If the vacancy created in this ionization process is located in the inner valence shell or the electronic core, the system ends up in an electronically excited state. Subsequent relaxation to the ground state can lead to autoionization if the released energy is transferred onto a valence electron which then leaves the system. Its kinetic energy is thereby determined by the energy of the decaying state and its ionization potential as well as the type of the electronic relaxation.

The most prominent example for non-resonant autoionization processes is the *Auger decay*[106, 107] which is sketched in Figure I.3. It occurs when core-ionizing an atom or molecule and the core-vacancy (indicated in the center of Figure I.3) is subsequently filled by an electron from a higher shell. The system can then relax by emission of a second (usually outer shell) electron. The special case in which the initial vacancy is filled by an electron from a higher subshell of the same shell is also called *Coster-Kronig transition*.

When going from isolated atoms or molecules to clusters consisting of two or more weakly bound particles, another mechanism of electronic decay becomes available, which

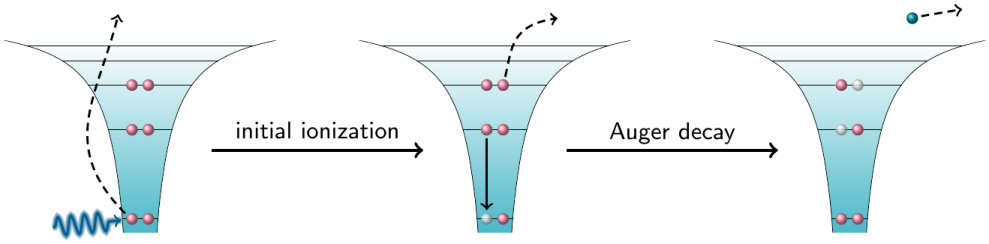

Figure I.3. Schematic illustration of the Auger decay as a special case of autoionization of a core-ionized state.

has been named *interatomic* or *intermolecular coulombic decay* (ICD). The effect has first been predicted theoretically[108] and was later confirmed experimentally.[109] The respective process can be pictured as follows: A particle can undergo photoionization by emitting an electron originating from the inner valence or an inner shell to the continuum. The resulting ionized species subsequently relaxes by filling the vacancy with an electron from the outer valence shell. If now an Auger-like process is not possible because the particle's second IP is too high to be overcome by the amount of energy released during the relaxation, an electronic decay can still happen if a second particle in the vicinity has a sufficiently low IP. In this case a doubly ionized system with one positive charge residing at each particle can be formed by energy transfer to the second particle by Coulomb interaction and subsequent electronic decay.

Closely related to ICD are processes in which the initial vacancy is filled by an electron originating from a neighboring particle. The corresponding processes thus involve charge redistribution or electron transfer between different particles and have been termed *electron-transfer mediated decay* (ETMD).[110, 111] If the second ionization takes place on the particle from which the electron was transferred, two particles are involved and the process is called ETMD(2). As another option, ionization may occur at a third particle, in which case one speaks of ETMD(3).

Resonant Processes

In contrast to non-resonant decay mechanisms, autoionizing states can also evolve from resonant electronic excitation. Compared to non-resonant processes, the probability of generating an autoionizing species is highly increased. In addition, decaying states produced by resonant photon absorption can generally relax via different pathways, which can be distinguished by means of the electronic configuration of the final ionized species. If the initial vacancy is filled by the initially excited electron, the final state is characterized by a singly-excited configuration and the process is termed *participant*. By contrast, processes

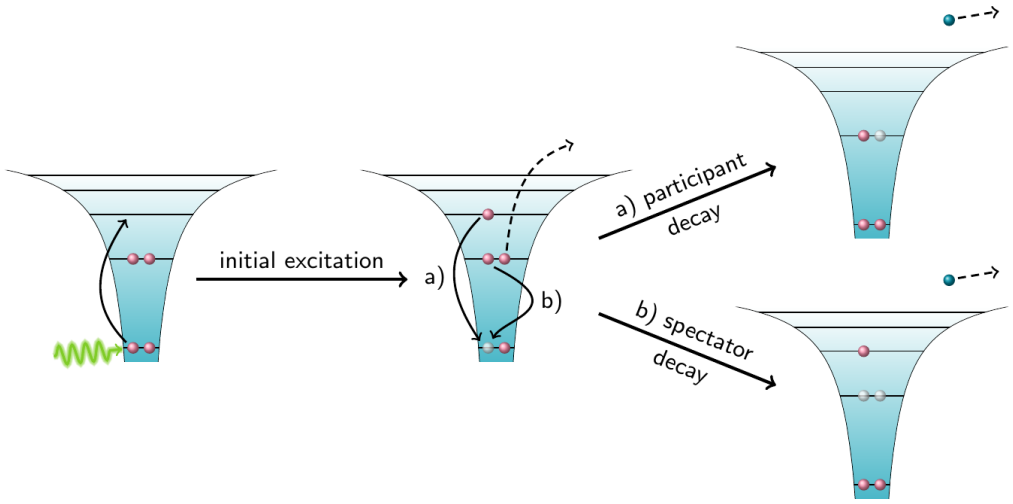

Figure I.4. Schematic illustration of possible autoionization processes of electronically excited systems. An excited state (middle) may relax by emission of an electron into the continuum a) via the *participant* pathway, leading to a single hole-particle ($1h1p$) final state, or b) via the *spectator* pathway, leading to a double hole-particle ($2h2p$) final state.

where the vacancy is filled by a second electron are called *spectator* decays, in which case the final state is overall doubly-excited with respect to the electronic ground state. The different decay pathways are illustrated at the example of resonant Auger decay in Figure I.4.

As a matter of fact, many non-resonant decay processes also have a resonant counterpart, as for example resonant Auger decay[112] and resonant ICD (RICD).[113] An additional flavor of ICD-like processes, which exists only in the context of resonant decay mechanisms, is the so-called *excitation transfer ionization* (ETI).[114] In this case, the initial species is an outer valence-excited state which cannot decay by means of a resonant Auger decay. The excitation energy may, however, be sufficient to ionize a neighboring particle, in which case an ICD-like process becomes possible. In this context, the enhancement of the autoionization efficiency has been compared with a radio setup consisting of an antenna coupling the system to a radiation field, a receiver consuming the harvested energy and a route to transfer the energy between them.[115] In this picture, the particle in which the initial excitation occurs would be the antenna and the finally ionized particle the receiver. The energy transfer route would be constituted by Coulombic interaction.

I.2.3. Electronic Resonances in Biological Systems

During the past few years it has been recognized that electronic resonances play a fundamental role in biological systems. This is especially true for ICD processes, since these

have been identified as a source of slow electrons[116] which are known to be active in radiation damage.[117, 118] Recently, it has been shown that slow electrons can evolve in a complicated chain of ultrafast ICD and ETMD processes following Auger decay in a solvated metal ion, as found in the active site of many biomolecules.[119]

Another process in which low-energy electrons created in an ICD process have been found to play a vital role is the light-driven DNA repair by (6-4) photolyases.[120–122] In the respective process, an initial excitation by UV radiation occurs in an antenna pigment. Electronic relaxation triggers an ICD in a neighboring reduced flavin adenine dinucleotide ($FADH^-$) molecule. The ICD electron originating from this process is subsequently transferred to the DNA lesion, triggering its repair.

I.2.4. Theoretical Approaches to the Problem of Electronic Resonances

The need for a theoretical description of autoionization processes, in particular the calculation of lifetimes and decay widths Γ, was recognized very early. A first treatment of the problem was reported as early as 1927 by Wentzel.[123]

One of the main difficulties encountered in this context arises from the fact that the involved scattering wavefunctions are not square-integrable and consequently cannot be treated directly within the framework of standard quantum chemical methods relying on $\mathcal{L}^2$ basis set representations. To overcome this issue, different theoretical approaches have been devised, two of which are considered in this work. In this section, a short overview of these methods is given.

Complex Absorbing Potentials

One possibility to deal with electronic resonances in the framework of $\mathcal{L}^2$-integrable quantum chemical methods is the *complex absorbing potential* (CAP) method. It is motivated by the fact that resonance states are characterized by discrete complex Siegert energies. It is thus straightforward to analytically continue the Hamiltonian into the complex energy plane,[124] which can in principle be done using different approaches.

In the CAP method, the Hamiltonian is augmented by a complex one-particle potential, thereby making all its eigenfunctions $\mathcal{L}^2$.[99, 125] It has been combined with a number of electronic structure methods, among them Dyson-ADC,[23, 126, 127] different EOM-CC schemes,[99, 128, 129] extended multi-configurational quasi-degenerate perturbation theory of second order (XMCQDPT2),[130] symmetry-adapted cluster-configuration interaction (SAC-CI),[131] and IP-ADC.[90] It has been noted that, due to the one-particle nature of the added potential, CAP methods have mostly been applied in the context of shape

resonances.[128] However, there have been also studies of Feshbach resonances which yielded satisfactory results.[130]

The CAP can be added to the Hamiltonian at different stages. For the use in wave function-based methods, it can already be considered during the Hartree-Fock calculation, and this approach has been followed in the context of EOM-CC methods.[99, 128]. Another possibility is to include it at the post-Hartree-Fock stage. In ADC or CC methods, for example, a suitable basis set representation of the CAP may be added to the respective Hamiltonian before diagonalization.[99]

In a computationally more feasible approach, the CAP is applied *a posteriori*, i.e., expanded into a subspace of electronic states computed using a standard electronic structure method. This formalism has first been used in the context of SAC-CI[131] and later also in conjunction with XMCQDPT2.[130]

In the course of this dissertation, the subspace projection approach has been used for the realization of the CAP-PP-ADC and CAP-EA-ADC methods. For this purpose, the intermediate state representation for EA-ADC[74] had to be implemented. In addition, the EA-ADC implementation in Q-Chem was extended to allow for the computation and visualization of Dyson orbitals. In Chapter VIII, conceptual and computational aspects of the new method are addressed, and a study of anionic shape resonances in unsaturated organic molecules is presented.

Fano-Stieltjes-ADC

Another methodology devised to deal with electronic resonances in the framework of standard quantum chemical methods is the *Fano formalism*. It relies on the projection method introduced by Feshbach.[132, 133] Within configuration interaction-like schemes, the Hamiltonian is projected onto different subspaces built up from a selection of configurations suitable to describe the resonance state and the decay channels, respectively. This formalism was first proposed by Fano[134] and later further developed by Hazi[135] and, in the context of atomic Auger decay, by Howat and coworkers.[136–138]

More recently, the method was successfully applied in conjunction with IP- and PP-ADC for the description of various autoionization processes as, e.g., atomic Auger decay,[139] resonant Auger decay of atoms and molecules,[140, 141] ICD, ETI or ETMD[124, 139] as well as for the calculation of total photoionization cross-sections.[142]

The resonance state as well as the final states are obtained by diagonalization of suitably projected Hamiltonian matrix representations. The decay width can then be determined by evaluating the coupling matrix elements between a resonance state and all accessible final states. In order to correct for wrongly discretized final state wavefunctions, postpro-

cessing using the so-called *Stieltjes imaging* technique is usually required.[143]

In this dissertation, an efficient implementation of the Fano-Stieltjes-ADC method for resonantly excited resonance states as introduced in, e.g., Refs. [140] and [141] is presented. For the first time, the third-order PP-ADC as well as unrestricted PP-ADC schemes were combined with the Fano-Stieltjes approach. In Chapter VII, results obtained using the novel implementation in the Q-Chem quantum chemical program package are presented, including the investigation of some conceptual aspects as well as the application to electronic resonances in medium-sized organic molecules.

Chapter II

Theoretical Methodology

The aim of this chapter is to give an overview of the theoretical methods which have been implemented in the course of this dissertation and were subsequently employed for the description of various ionization processes and properties of the resulting electron-detached states.

The basic concepts of the ADC approximation are introduced in Section II.1 using the example of IP-ADC, which can be employed to describe, e.g., direct photoionization from bound molecular ground states. The presented ADC derivation via the intermediate state representation formalism is, however, completely general and can in principle be applied to other propagators as well, reflected in a different set of excitation operators acting on the N-electron ground state.

In particular, electron-number preserving electronic excitation may be addressed by ADC for the polarization propagator. This option has been used in this work in conjunction with the Fano-Stieltjes method for the description of autoionization processes starting from metastable electronic states, which is covered in Section II.2.

Another method which can be employed to compute resonance energies and lifetimes of metastable electronic states is the complex absorbing potential method, in which the molecular Hamiltonian is augmented by a complex potential, thereby making all its eigenfunctions purely $\mathcal{L}^2$. The methodology introduced in Section II.3 is particularly suited for the description of low-lying shape resonances as usually found in temporary anions. It is therefore a natural choice to combine it with EA-ADC, which offers the possibility to com-

Parts of this chapter have already been published in

- A. L. Dempwolff, A. C. Paul, A. M. Belogolova, A. B. Trofimov, A. Dreuw, "Intermediate State Representation Approach to Physical Properties of Molecular Electron-Detached States: I. Theory and Implementation", *J. Chem. Phys.* **2020**, *152*, 024113.

pute electron-attached states based on an N-electron reference state. It can, however, also be combined successfully with PP-ADC, when a (possibly metastable) $(N-1)$-electron reference state is employed.

II.1. Algebraic Diagrammatic Construction for Ionization Potentials

II.1.1. Electron Propagator

The physical content of the electron propagator, also known as one-particle Green's function, is most explicit in its so-called spectral representation[13]

$$G_{pq}(\omega) = \sum_{n \in \{N+1\}} \frac{\langle \Psi_0^N | c_p | \Psi_n^{N+1} \rangle \langle \Psi_n^{N+1} | c_q^\dagger | \Psi_0^N \rangle}{\omega + E_0^N - E_n^{N+1} + i\eta} + \sum_{n \in \{N-1\}} \frac{\langle \Psi_0^N | c_q^\dagger | \Psi_n^{N-1} \rangle \langle \Psi_n^{N-1} | c_p | \Psi_0^N \rangle}{\omega + E_n^{N-1} - E_0^N - i\eta} . \tag{2.1}$$

Here $|\Psi_0^N\rangle$ denotes the exact (nondegenerate) N-electron ground state of energy E_0^N, and $c_p^\dagger$ and c_p denote creation and destruction operators of second quantization, respectively, associated with the HF orbital $|\varphi_p\rangle$. The summations are performed over exact $(N \pm 1)$-electron states $|\Psi_n^{N\pm1}\rangle$ with energies $E_n^{N\pm1}$, and $i\eta$ is a positive infinitesimal.

As follows from Eq. (2.1), the negative poles of $\mathbf{G}(\omega)$ can be identified as electron detachment energies $I_n = E_n^{N-1} - E_0^N$ (ionization potentials, IP) and electron attachment energies $A_n = E_0^N - E_n^{N+1}$ (electron affinities, EA). The corresponding residues correspond to the spectroscopic factors

$$x_p^{(n)} = \langle \Psi_n^{N-1} | c_p | \Psi_0^N \rangle, \quad n \in \{N-1\} \tag{2.2}$$

$$x_p^{(n)} = \langle \Psi_0^N | c_p | \Psi_n^{N+1} \rangle, \quad n \in \{N+1\} \tag{2.3}$$

which define the probabilities of the ionization and electron attachment events. More specifically, the partial photoelectron cross-section σ_n is, to a good approximation, proportional to the pole strength P_n which is defined with respect to $x_p^{(n)}$ according to

$$\sigma_n \propto P_n = \Big| \sum_p x_p^{(n)} \Big|^2 . \tag{2.4}$$

Simplified definitions of the pole strength can also be found in the literature, such as $P_n \approx \sum_p |x_p^{(n)}|^2$[74] and $P_n \approx |x_p^{(n)}|^2$.[21] In the latter case only the dominant term related to orbital p is taken into account.

The structure of Eq. (2.1) shows the electron propagator to consist of the $(N+1)$- and $(N-1)$-electron parts $\mathbf{G}^+(\omega)$ and $\mathbf{G}^-(\omega)$,

$$\mathbf{G}(\omega) = \mathbf{G}^+(\omega) + \mathbf{G}^-(\omega), \tag{2.5}$$

which can in principle be treated independently. This strategy is pursued in the non-Dyson approach to the electron propagator,[31] contrasting methods based on the Dyson equation.

II.1.2. Non-Dyson Approach to the Electron Propagator

In an independent treatment of the $(N+1)$- and $(N-1)$-parts of the electron propagator, distinct computational schemes for IPs and EAs are obtained.[31]

Using matrix notation, the spectral representation of $\mathbf{G}^-(\omega)$ (given by the second term of the right-hand side of Eq. (2.1)) can be rewritten as

$$\tilde{\mathbf{G}}(\omega) = \mathbf{x}^\dagger(\omega - \mathbf{\Omega})^{-1}\mathbf{x} \tag{2.6}$$

where $\tilde{\mathbf{G}}(\omega) = \mathbf{G}^-(\omega)^t$ with the infinitesimal $i\eta$ being dropped, and $\mathbf{\Omega}$ and $\mathbf{x}$ are matrices with elements $\Omega_{nm} = -(E_n^{N-1} - E_0^N)\delta_{mn}$ and $x_p^{(n)}$, respectively, the latter defined according to Eq. (2.2). In the IP-ADC approach, the spectral representation (2.6) is substituted by a more general ADC representation,

$$\tilde{\mathbf{G}}(\omega) = \mathbf{f}^\dagger(\omega - \mathbf{M})^{-1}\mathbf{f}, \tag{2.7}$$

where the matrix of "effective interaction" $\mathbf{M}$ is a nondiagonal analogue of the diagonal matrix $\mathbf{\Omega}$, and the matrix of "effective transition amplitudes" $\mathbf{f}$ is the corresponding generalization of the matrix of the spectroscopic amplitudes $\mathbf{x}$.

The Equations (2.6) and (2.7) are related by unitary transformation $\mathbf{Y}$,

$$\mathbf{f}^\dagger\mathbf{Y}\mathbf{Y}^\dagger(\omega - \mathbf{M})^{-1}\mathbf{Y}\mathbf{Y}^\dagger\mathbf{f} = \mathbf{x}^\dagger(\omega - \mathbf{\Omega})^{-1}\mathbf{x}, \tag{2.8}$$

which connects the basis of exact $(N-1)$-electron states $\left|\Psi_n^{N-1}\right\rangle$ with the basis of the so-called *intermediate states* (IS) $\left|\tilde{\Psi}_J^{N-1}\right\rangle$, in which the ADC equations are formulated:[37, 78]

$$\left|\Psi_n^{N-1}\right\rangle = \sum_J Y_{Jn}\left|\tilde{\Psi}_J^{N-1}\right\rangle, \quad Y_{Jn} = \left\langle\tilde{\Psi}_J^{N-1}\middle|\Psi_n^{N-1}\right\rangle. \tag{2.9}$$

As can be seen from Eq. (2.8), the ionization potentials can be extracted from the ADC

representation (2.7) of $\mathbf{G}^-(\omega)$ by solving the Hermitian eigenvalue problem

$$\mathbf{MY} = \mathbf{Y\Omega}, \quad \mathbf{Y}^\dagger\mathbf{Y} = \mathbf{1}. \tag{2.10}$$

This computational step yields the ionization energies given by the eigenvalues $\Omega_n \equiv \Omega_{nn}$ and information on the electronic structure of the final states $\left|\Psi_n^{N-1}\right\rangle$ contained in the corresponding eigenvectors $\mathbf{Y}_n$. The spectroscopic amplitudes can then be found according to Eq. (2.8) as

$$\mathbf{x} = \mathbf{Y}^\dagger\mathbf{f}. \tag{2.11}$$

The matrix of effective interaction $\mathbf{M}$ can be viewed as $(N-1)$-electron representation of the shifted Hamiltonian $\hat{H} - E_0^N$ in the IS basis:

$$M_{IJ} = \left\langle \tilde{\Psi}_I^{N-1}\middle|\hat{H} - E_0^N\middle|\tilde{\Psi}_J^{N-1}\right\rangle. \tag{2.12}$$

Accordingly, the effective transition amplitudes $\mathbf{f}$ are given by matrix elements

$$f_{Ip} = \left\langle \tilde{\Psi}_I^{N-1}\middle|c_p\middle|\Psi_0^N\right\rangle. \tag{2.13}$$

II.1.3. Intermediate State Representation

Once the intermediate states are known at some level of approximation, $\mathbf{M}$ and $\mathbf{f}$ can be evaluated. The construction of the $(N-1)$-electron IS proceeds in two steps.[37, 38, 78, 79]

In the first step, the so-called $(N-1)$-electron "correlated excited states" $\left|\Psi_J^{\#N-1}\right\rangle$ are obtained by acting with $(N-1)$-excitation operators $\hat{C}_J$ on the N-electron ground state $\left|\Psi_0^N\right\rangle$:

$$\left|\Psi_J^{\#N-1}\right\rangle = \hat{C}_J\left|\Psi_0^N\right\rangle . \tag{2.14}$$

Here J is a compound index enumerating classes of $(N-1)$-electron configurations such as one-hole ($1h$), two-hole-one-particle ($2h$-$1p$), ..., and $\hat{C}_J$ denotes operators which generate the respective classes of configurations when acting on the HF ground state,

$$\{\hat{C}_J\} \equiv \{c_i, c_a^\dagger c_i c_j, c_a^\dagger \hat{c}_b^\dagger c_i c_j c_k, \dots\}, \quad a < b < \dots, i < j < k < \dots. \tag{2.15}$$

Here and in the following, the subscripts $a, b, \dots$ and $i, j, \dots$ refer to unoccupied (virtual) and occupied orbitals relative to the HF ground state, respectively, and $p, q, r, \dots$ label general orbitals.

In the second step, the intermediate states $\left|\tilde{\Psi}_J^{N-1}\right\rangle$ are generated by Gram-Schmidt (GS) orthogonalization of the $(N-1)$-electron correlated excited states $\left|\Psi_J^{\#N-1}\right\rangle$ belonging to

different ionization classes,

$$\{|\Psi_J^{\#N-1}\rangle\} \xrightarrow{\text{GS}} \{|\tilde{\Psi}_J^{N-1}\rangle\}, \tag{2.16}$$

accompanied by symmetric orthogonalization of the states within each class.

In the ADC approach, the $\mathbf{M}$ and $\mathbf{f}$ matrices are assumed to have their own perturbative expansions in the residual electronic interaction,[74]

$$\mathbf{M} = \mathbf{M}^{(0)} + \mathbf{M}^{(1)} + \mathbf{M}^{(2)} + \ldots \tag{2.17}$$

$$\mathbf{f} = \mathbf{f}^{(0)} + \mathbf{f}^{(1)} + \mathbf{f}^{(2)} + \ldots . \tag{2.18}$$

The explicit expressions for $\mathbf{M}$ and $\mathbf{f}$ can be derived using Eqs. (2.12) and (2.13) by constructing intermediate states $|\tilde{\Psi}_J^{N-1}\rangle$ and employing perturbative representations of the N-electron ground state $|\Psi_0^N\rangle$ and the ground state energy E_0^N,[31, 78] assuming Møller-Plesset partitioning of the Hamiltonian.[9]

Identical equations are derived using a diagrammatic perturbation expansion of $\mathbf{G}^-(\omega)$.[31] However, for computing one-electron properties of electron-detached states one has to resort to the ISR, since the explicit form of the respective $(N-1)$-electron wave functions needs to be known for this purpose.

II.1.4. One-Particle Properties of Ionized Species

The intermediate states can be constructed explicitly and used for the representation of a general one-particle operator $\hat{D}$ according to

$$\widetilde{D}_{IJ} = \langle \tilde{\Psi}_I^{N-1} | \hat{D} | \tilde{\Psi}_J^{N-1} \rangle. \tag{2.19}$$

In second-quantization, $\hat{D}$ is given as

$$\hat{D} = \sum_{pq} d_{pq} c_p^\dagger c_q, \tag{2.20}$$

where $d_{pq} = \langle \varphi_p | \hat{d} | \varphi_q \rangle$ denote the one-particle matrix elements associated with $\hat{D}$, and the matrix element (2.19) can be rewritten as

$$\widetilde{D}_{IJ} = \sum_{pq} d_{pq} \langle \tilde{\Psi}_I^{N-1} | c_p^\dagger c_q | \tilde{\Psi}_J^{N-1} \rangle. \tag{2.21}$$

Once $\widetilde{\mathbf{D}}$ is known, the transition matrix elements T_{nm} between the electron-detached

states $\left|\Psi_n^{N-1}\right\rangle$ and $\left|\Psi_m^{N-1}\right\rangle$ can be found,

$$T_{nm}(\hat{D}) \equiv \left\langle \Psi_n^{N-1}\middle|\hat{D}\middle|\Psi_m^{N-1}\right\rangle = \mathbf{Y}_n^{\dagger}\widetilde{\mathbf{D}}\mathbf{Y}_m, \tag{2.22}$$

where $\mathbf{Y}_n$ and $\mathbf{Y}_m$ are eigenvectors of the ADC secular equation (2.10) for the states $\left|\Psi_n^{N-1}\right\rangle$ and $\left|\Psi_m^{N-1}\right\rangle$, respectively.

A computationally slightly different route to the desired one-particle properties is implied by Eq. (2.21). With its help, the transition matrix element (2.22) can be recast as

$$T_{nm}(\hat{D}) = \sum_{pq} d_{pq} \sum_{IJ} Y_{In}^{\dagger} \left\langle \tilde{\Psi}_I^{N-1}\middle|c_p^{\dagger}c_q\middle|\tilde{\Psi}_J^{N-1}\right\rangle Y_{Jm}, \tag{2.23}$$

or, using matrix notation, as

$$T_{nm}(\hat{D}) = \sum_{pq} d_{pq}\mathbf{Y}_n^{\dagger}\tilde{\boldsymbol{\rho}}_{pq}\mathbf{Y}_m = \mathrm{Tr}(\mathbf{d}\boldsymbol{\rho}_{nm}). \tag{2.24}$$

Therein, $\mathbf{d}$ is the matrix representation of the operator $\hat{D}$ with elements d_{pq}, and $\tilde{\boldsymbol{\rho}}$ and $\boldsymbol{\rho}$ are the one-particle transition density matrices defined with respect to the intermediate states and the final electron-detached states, respectively, with the matrix elements being $\tilde{\rho}_{IJ,pq} = \left\langle \tilde{\Psi}_I^{N-1}\middle|c_p^{\dagger}\hat{c}_q\middle|\tilde{\Psi}_J^{N-1}\right\rangle$ and $\rho_{nm,pq} = \left\langle \Psi_n^{N-1}\middle|c_p^{\dagger}\hat{c}_q\middle|\Psi_m^{N-1}\right\rangle$.

The one-particle density matrix $\boldsymbol{\rho}_n \equiv \boldsymbol{\rho}_{nn}$ for a particular electron-detached state $\left|\Psi_n^{N-1}\right\rangle$ can obviously be represented as a sum of the N-electron ground state density matrix $\boldsymbol{\rho}_0$ and the difference density matrix $\boldsymbol{\Delta}_n$,

$$\boldsymbol{\rho}_n = \boldsymbol{\rho}_0 + \boldsymbol{\Delta}_n, \tag{2.25}$$

where the difference density matrix $\boldsymbol{\Delta}_n$ is defined as

$$\boldsymbol{\Delta}_n = \boldsymbol{\rho}_n - \boldsymbol{\rho}_0. \tag{2.26}$$

Accordingly, the expectation value of $\hat{D}$ for the state $\left|\Psi_n^{N-1}\right\rangle$ can be written as

$$T_{nn} = \mathrm{Tr}(\mathbf{d}\boldsymbol{\rho}_n) = D_0 + \mathrm{Tr}(\mathbf{d}\boldsymbol{\Delta}_n)\,, \tag{2.27}$$

where D_0 denotes the N-electron ground state expectation value of $\hat{D}$, defined as $D_0 = \mathrm{Tr}(\mathbf{d}\boldsymbol{\rho}_0)$.

In a similar way, the whole one-particle transition density matrix $\boldsymbol{\rho}$ defined with respect

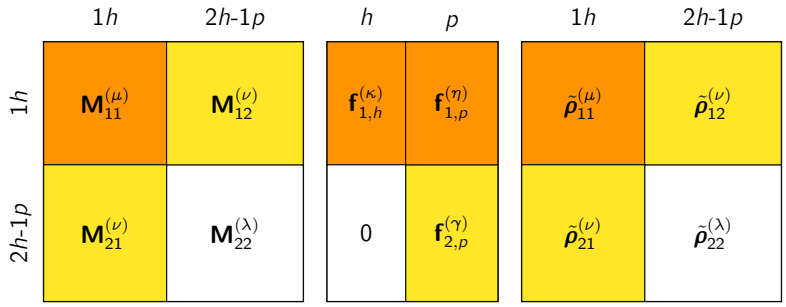

Scheme	$\mathbf{M}/\tilde{\boldsymbol{\rho}}$			$\mathbf{f}$		
	μ	ν	λ	κ	η	γ
IP-ADC(3)	0,2,3	1,2	0,1	0,2,3	2,3	1,2
IP-ADC(2)	0,2	1	0	0,2	2	1
ISR(2)	0,1,2	0,1	0			
ISR(0)	0	0	0			

Figure II.1. Block structure of the $\mathbf{M}$ and $\mathbf{f}$ matrices in the IP-ADC schemes and the $\tilde{\boldsymbol{\rho}}$ matrix in the ISR schemes along with the order of the perturbative expansions for matrix elements from different blocks. The subscripts 1 and 2 are used to label $1h$ and $2h$-$1p$ entries, respectively, and h and p label hole (occupied) and particle (virtual) HF orbital indices, respectively.

to the final electron-detached states can be partitioned. It can be constructed as a matrix comprising the electron-detached state density matrices $\boldsymbol{\rho}_n$ and transition density matrices $\boldsymbol{\rho}_{nm}$ as diagonal and off-diagonal blocks, respectively,

$$\boldsymbol{\rho} = \mathbf{1} \otimes \boldsymbol{\rho}_0 + \boldsymbol{\rho}', \tag{2.28}$$

where the quantity $\boldsymbol{\rho}'$ can be considered as generalized difference density matrix, with blocks equal to $\boldsymbol{\Delta}_n$ in the case of the diagonal elements and identical with $\boldsymbol{\rho}_{nm}$ otherwise,

$$\boldsymbol{\rho}'_{nm} = \begin{cases} \boldsymbol{\Delta}_n, & n = m \\ \boldsymbol{\rho}_{nm}, & n \neq m\,. \end{cases} \tag{2.29}$$

The knowledge of $\boldsymbol{\rho}'$ together with $\boldsymbol{\rho}_0$ allows any expectation value and transition property with respect to the final electron-detached states to be evaluated using Eqs. (2.24) and (2.27).

In the intermediate state basis, the one-particle operator $\widetilde{\mathbf{D}}$ and the transition density matrix $\tilde{\boldsymbol{\rho}}$ are, similar to the ADC quantities $\mathbf{M}$ and $\mathbf{f}$, subject to perturbative expansion,

$$\widetilde{\mathbf{D}} = \widetilde{\mathbf{D}}^{(0)} + \widetilde{\mathbf{D}}^{(1)} + \widetilde{\mathbf{D}}^{(2)} + \ldots \tag{2.30}$$

$$\tilde{\boldsymbol{\rho}} = \tilde{\boldsymbol{\rho}}^{(0)} + \tilde{\boldsymbol{\rho}}^{(1)} + \tilde{\boldsymbol{\rho}}^{(2)} + \ldots\,, \tag{2.31}$$

reflected in their block structure as depicted in Figure II.1. Throughout this work, the approximation level employed for $\widetilde{\mathbf{D}}$ or $\tilde{\boldsymbol{\rho}}$ is denoted as ISR(n). The ISR(n) approximation scheme allows for a consistent n-th order description of the transition matrix elements T_{nm} for the final electron-detached states $\left|\Psi_n^{N-1}\right\rangle$ and $\left|\Psi_m^{N-1}\right\rangle$ derived from the lowest ionization class, i.e., dominated by one-hole configurations.

The ISR(n) treatment can be combined with eigenvectors $\mathbf{Y}$ from various IP-ADC(m) schemes. This leads to a family of IP-ADC(m)/ISR(n) approximations consistent through order $l = \min(n, m)$.

II.1.5. Ground State One-Particle Density Matrix and Static Self-Energy

In the present formulation of the IP-ADC/ISR equations, the ground state density matrix $\boldsymbol{\rho}_0$ contribution represents a separate term, suggesting suitable treatments of $\boldsymbol{\rho}_0$ to be employed. In the ISR(2) scheme, the ground state density should be treated at least through second order of PT for consistent second-order results. In the IP-ADC(3) scheme a third-order $\boldsymbol{\rho}_0$ is available through the equation[31]

$$\boldsymbol{\rho}_0 = \mathbf{f}^\dagger \mathbf{f}\,, \tag{2.32}$$

where a consistent third-order treatment of the effective transition amplitudes $\mathbf{f}$ is assumed. However, contributions up to 6th order are generated because of the PT expansion of $\mathbf{f}$ as given by Eq. (2.18).

For reasons of consistency, supported also by computational tests, a "perturbative" evaluation of Eq. (2.32), in which higher-order terms are dropped, is preferable. Considering the block structure of the effective transition moments matrix $\mathbf{f}$ as depicted in Figure II.1, the third-order perturbation expansions of the diagonal blocks of $\boldsymbol{\rho}_0$ are given by

$$\boldsymbol{\rho}_{0,hh} = \mathbf{f}_{1,h}^{(0)} + 2\,\mathbf{f}_{1,h}^{(2)} + \left(\mathbf{f}_{1,h}^{(3)} + \mathbf{f}_{1,h}^{(3)\dagger}\right) + O(4) \tag{2.33}$$

$$\boldsymbol{\rho}_{0,pp} = \mathbf{f}_{2,p}^{(1)\dagger}\mathbf{f}_{2,p}^{(1)} + \mathbf{f}_{2,p}^{(1)\dagger}\mathbf{f}_{2,p}^{(2)} + \mathbf{f}_{2,p}^{(2)\dagger}\mathbf{f}_{2,p}^{(1)} + O(4), \tag{2.34}$$

where it has been used that $\mathbf{f}_{1,h}^{(2)}$ is Hermitian and that $\mathbf{f}_{1,h}^{(0)} = \boldsymbol{\rho}_{0,hh}^{(0)} = \delta_{ij}$.

For the off-diagonal blocks of the one-particle ground state density matrix $\boldsymbol{\rho}_{0,hp}$ (and $\boldsymbol{\rho}_{0,ph}$) the reverse relation to Eq. (2.32),

$$\mathbf{f}_{1,p} = \boldsymbol{\rho}_{0,hh}^{-\frac{1}{2}}\,\boldsymbol{\rho}_{0,hp}, \tag{2.35}$$

can be evaluated. Considering that $\boldsymbol{\rho}_{0,hp} = O(2)$ and $\boldsymbol{\rho}_{0,hh} = \delta_{ij} + O(2)$, one obtains an expression consistent through third order of perturbation theory,

$$\boldsymbol{\rho}_{0,hp} = \mathbf{f}^{(2)}_{1,p} + \mathbf{f}^{(3)}_{1,p} + O(4). \tag{2.36}$$

Higher-order contributions to $\boldsymbol{\rho}_0$ can be introduced in the form of infinite partial summations, when an improved fourth-order treatment of the static self-energy $\Sigma(\infty)$ is employed in the evaluation of $\mathbf{f}$. The static self-energy $\Sigma(\infty)$ contributes to the matrix elements $f^{(3)}_{i,a}$,[31, 74]

$$f^{(3)}_{i,a} = \frac{1}{\varepsilon_i - \varepsilon_a}\big(\Sigma^{(3)}_{ai}(\infty) + M^{(3)+}_{ai}(\varepsilon_i) + M^{(3)-}_{ai}(\varepsilon_a)\big), \tag{2.37}$$

where $M^{(3)\pm}_{ak}$ are the third-order dynamic self-energy contributions given in Section III.3.1,[21] and ε_p denote HF orbital energies. A strict third-order treatment of $\Sigma(\infty)$ is not sufficient for systematically accurate results.[42, 74, 144] A general procedure referred to as Dyson-expansion method or Σ(DEM) was developed and used as a part of the Dyson ADC(3) scheme.[42] In a procedure more appropriate for the non-Dyson IP-ADC approach, referred to as $\Sigma(4+)$ method,[31] one sets out from the expression for the matrix elements of the static self-energy,[13]

$$\Sigma_{pq}(\infty) = \sum_{r,s} \langle pr||qs\rangle \, \rho^{\mathrm{c}}_{sr} \,, \tag{2.38}$$

where

$$\rho^{\mathrm{c}}_{sr} = \big\langle \Psi_0 \big| c^\dagger_r \hat{c}_s \big| \Psi_0 \big\rangle - \big\langle \Phi_0 \big| c^\dagger_r c_s \big| \Phi_0 \big\rangle \tag{2.39}$$

is the matrix element of the difference density $\boldsymbol{\rho}^{\mathrm{c}} = \boldsymbol{\rho}_0 - \boldsymbol{\rho}^{(0)}_0$, with $\boldsymbol{\rho}^{(0)}_0$ being the HF density matrix and $\langle pr||qs\rangle$ anti-symmetrized two-electron Coulomb integrals in Physicist's notation. A fourth-order approximation to $\Sigma(\infty)$ can then be obtained by substituting a third-order $\boldsymbol{\rho}_0$ in Eq. (2.38). Since according to Eq. (2.37), the $\mathbf{f}^{(3)}$ again depends on $\Sigma(\infty)$, Eqs. (2.36) through (2.38) can be considered as a set of equations for finding $\Sigma(\infty)$, which can be solved iteratively.

It should, however, be noted that the $\Sigma(4+)$ procedure is not equivalent to the Σ(DEM) scheme, where a more complete partial summation of terms beyond fourth order is achieved. In the present IP-ADC(3) implementation the $\Sigma(4+)$ treatment is adopted as standard, and the corresponding improved third-order $\boldsymbol{\rho}_0$ is used in the ISR(2) implementation.

II.1.6. Density Analysis of Electron-Detached States

For the interpretation and understanding of detachment and attachment processes, analysis of the changes in the electronic structure is highly desirable. Therefore, approaches based on difference density functions and Dyson orbitals are useful. Both approaches are easily implemented in the context of the density-based formulation of the IP-ADC/ISR method.

The difference density function $\Delta_n(\mathbf{r})$ for state $\left|\Psi_n^{N-1}\right\rangle$ is defined as

$$\Delta_n(\mathbf{r}) = \rho_n(\mathbf{r}) - \rho_0(\mathbf{r}) \tag{2.40}$$

where $\rho_n(\mathbf{r})$ and $\rho_0(\mathbf{r})$ are the density functions associated with the electron-detached state $\left|\Psi_n^{N-1}\right\rangle$ and the ground state $\left|\Psi_0^{N}\right\rangle$, respectively.[145] The difference density function and matrix of Eq. (2.26) are related via the typical equation

$$\Delta_n(\mathbf{r}) = \sum_{pq} (\mathbf{\Delta}_n)_{pq} \varphi_p^*(\mathbf{r}) \varphi_q(\mathbf{r}) \,, \tag{2.41}$$

where $\varphi_p(\mathbf{r})$ and $\varphi_q(\mathbf{r})$ are HF orbitals.

The difference density can be decomposed into attachment and detachment parts corresponding to the addition and removal of electron density, respectively.[146] In the context of ionization, the α- and β-spin parts of the considered quantities are treated separately.

The Dyson orbitals ϕ_n are defined as overlaps of the ground state wavefunction $\left|\Psi_0^{N}\right\rangle$ with the electron-detached wavefunctions $\left|\Psi_n^{N-1}\right\rangle$.[13] The straightforward evaluation of this quantity yields the following expression:

$$|\phi_n\rangle = \sum_p |\varphi_p\rangle \left\langle \Psi_n^{N-1} \middle| \hat{c}_p \middle| \Psi_0^N \right\rangle = \sum_p x_p^{(n)} |\varphi_p\rangle \,, \tag{2.42}$$

where $|\varphi_p\rangle$ again denote HF orbitals, and $x_p^{(n)}$ are the spectroscopic amplitudes which are obtained in the IP-ADC calculations according to Eq. (2.2).

Dyson orbitals are linear combinations of the HF orbitals and allow the domain which has been occupied by the detached electron to be visualized. Since low-energy electron-detached states rarely demonstrate strong mixing of one-hole configurations, only one dominant term is present in Eq. (2.42), and Dyson orbitals are usually largely equivalent to HF orbitals. A limitation of Dyson orbitals is that they can be employed only for studies of single-electron processes because the expansion coefficients decrease as the $2h$-$1p$-character of $\left|\Psi_n^{N-1}\right\rangle$ increases and may even nearly vanish when the one-electron picture

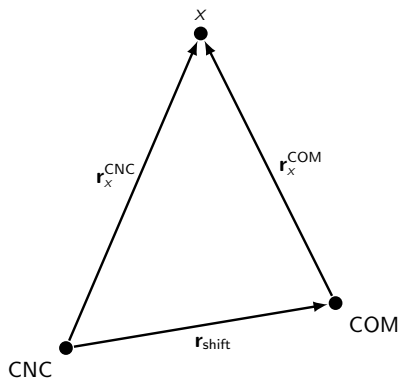

Figure II.2. Coordinates of a particle x relative to center of nuclear charges (CNC) and center of mass (COM).

of ionization breaks down.[1] In contrast to Dyson orbitals, the difference density approach is not affected by these limitations, and correlated wave functions of arbitrary complexity can be analyzed.

II.1.7. Dipole Moments of Charged States

Treating all particles in a molecular system as point charges, the dipole moment relative to the center of nuclear charges (CNC) is given as

$$\boldsymbol{\mu}^{\mathrm{CNC}} = \sum_i (-1)\, \mathbf{r}_i^{\mathrm{CNC}} + \sum_k Z_k \mathbf{R}_k^{\mathrm{CNC}} \tag{2.43}$$

$$= \sum_i (-1)\, \mathbf{r}_i^{\mathrm{CNC}} \tag{2.44}$$

where the nuclear contribution has been dropped since, by definition of the center of nuclear charges,

$$\sum_k Z_k \mathbf{R}_k^{\mathrm{CNC}} = 0. \tag{2.45}$$

In the expressions above, $\mathbf{R}_k^{\mathrm{CNC}}$ and $\mathbf{r}_i^{\mathrm{CNC}}$ are nuclear and electronic coordinates with respect to the center of nuclear charges.

Using the corresponding coordinates relative to the center of mass (COM) $\mathbf{r}_i^{\mathrm{COM}}$ and $\mathbf{R}_k^{\mathrm{COM}}$ (Figure II.2),

$$\mathbf{r}_i^{\mathrm{COM}} = \mathbf{r}_i^{\mathrm{CNC}} - \mathbf{r}_{\mathrm{shift}} \tag{2.46}$$

$$\mathbf{R}_k^{\mathrm{COM}} = \mathbf{R}_k^{\mathrm{CNC}} - \mathbf{r}_{\mathrm{shift}} \tag{2.47}$$

the dipole moment as seen from the center of mass is given as

$$\boldsymbol{\mu}^{\mathrm{COM}} = \sum_i (-1)\, \mathbf{r}_i^{\mathrm{COM}} + \sum_k Z_k \mathbf{R}_k^{\mathrm{COM}} \tag{2.48}$$

$$= \sum_i (-1)\, \left(\mathbf{r}_i^{\mathrm{CNC}} - \mathbf{r}_{\mathrm{shift}}\right) + \sum_k Z_k \left(\mathbf{R}_k^{\mathrm{CNC}} - \mathbf{r}_{\mathrm{shift}}\right) \tag{2.49}$$

$$= \boldsymbol{\mu}^{\mathrm{CNC}} - Q \cdot \mathbf{r}_{\mathrm{shift}}. \tag{2.50}$$

In the latter expression, Q denotes the net charge of the molecular system,

$$Q = \sum_i (-1) + \sum_k Z_k\,. \tag{2.51}$$

For neutral systems, $Q = 0$, meaning that in this case the dipole moment does not depend on the gauge origin. In contrast, the dipole moment of charged molecular systems is gauge dependent. For final states resulting from ionization from a neutral system ($Q = 1$) or electron attachment to a neutral system ($Q = -1$), Eq. (2.50) yields

$$\boldsymbol{\mu}^{\mathrm{COM}} = \begin{cases} \boldsymbol{\mu}^{\mathrm{CNC}} - \mathbf{r}_{\mathrm{shift}} & \text{ionization} \\ \boldsymbol{\mu}^{\mathrm{CNC}} + \mathbf{r}_{\mathrm{shift}} & \text{electron attachment.} \end{cases} \tag{2.52}$$

II.2. Fano-Stieltjes-ADC

For the description of metastable autoionizing wave functions using $\mathcal{L}^2$-integrable methods, different approaches have been developed, one of which is the Fano formalism. A brief outline of this method and its combination with ADC for the polarization propagator and the Stieltjes imaging technique is given in this section.

II.2.1. The Fano Formalism

The basic postulate within the Fano formalism is that the exact wavefunction of a system in the vicinity of an autoionizing state, i.e., at an energy E close to the resonance energy E_r, can be partitioned into a discrete bound-like component ϕ and a part of continuum-like states $\chi_{\beta,\epsilon_\beta}$ [136, 140]

$$\Psi_{\alpha,E} = a_\alpha(E)\phi + \sum_\beta^{N_c} \int b_{\beta,\alpha}(E,\epsilon_\beta)\chi^+_{\beta,\epsilon_\beta}\, \mathrm{d}\epsilon_\beta. \tag{2.53}$$

Therein, ϕ is chosen to correspond to the decaying N-electron state of the system having

the energy

$$E_\phi = \langle\phi|\hat{H}|\phi\rangle. \tag{2.54}$$

As continuum-like states $\chi^+_{\beta,\epsilon_\beta}$ all N_c energetically accessible decay channels are selected, i.e., the final continuum states representing the ionized system together with an ejected electron possessing the asymptotic kinetic energy

$$\epsilon_\beta = E - E_\beta > 0, \qquad \beta = 1, \ldots, N_c. \tag{2.55}$$

There are two important features of the method in this context. First, the $\chi^+_{\beta,\epsilon_\beta}$ are assumed to diagonalize the Hamiltonian of the system to a good approximation

$$\left\langle \chi^+_{\beta',\epsilon'_\beta} \middle| \hat{H} - E \middle| \chi^+_{\beta,\epsilon_\beta} \right\rangle \approx \delta_{\beta',\beta}\, \delta(E_{\beta'} + \epsilon'_\beta - E_\beta - \epsilon_\beta)\, (E_\beta + \epsilon_\beta - E). \tag{2.56}$$

Second, no orthogonality between the bound-like and continuum-like components is required.[133, 136] As will be discussed in Section II.2.2, the latter fact reasonably facilitates the construction of the involved electronic states.

In order to obtain an expression for the decay width Γ, one proceeds as follows. The wavefunction ansatz (2.53) is substituted into the time-independent Schrödinger equation

$$(\hat{H} - E)\, \Psi_E = 0. \tag{2.57}$$

Doing so and using relation (2.56), one obtains a system of equations coupling the amplitudes of the bound-like and continuum-like components

$$\begin{aligned} (E_\phi - E)\, a_\alpha(E) + \sum_\beta^{N_c} \int M_\beta(E, \epsilon_\beta)\, b_{\beta,\alpha}(E, \epsilon_\beta)\, \mathrm{d}\epsilon_\beta = 0 \\ a_\alpha(E)\, M^*_\beta(E, \epsilon_\beta) + (E_\beta + \epsilon_\beta - E)\, b_{\beta,\alpha}(E, \epsilon_\beta) = 0, \end{aligned} \tag{2.58}$$

where the bound-continuum coupling matrix elements

$$M_\beta(E, \epsilon_\beta) = \left\langle \phi \middle| \hat{H} - E \middle| \chi^+_{\beta,\epsilon_\beta} \right\rangle \tag{2.59}$$

have been introduced.

The solution of equations (2.58) is discussed in detail in Refs. [136] and [138]. As a result, the amplitude of the bound-like component $a_\alpha(E)$ can be stated as

$$a_\alpha(E) = \frac{M_\alpha(E, \epsilon_\alpha)}{E - E_r - i\pi \sum_\beta^{N_c} |M_\beta(E, \epsilon_\beta)|^2}\,. \tag{2.60}$$

Defining the quantities Γ and γ_β, respectively, by

$$\Gamma(E) = \sum_\beta^{N_c} \gamma_\beta(E) = 2\pi \sum_\beta^{N_c} |M_\beta(E, \epsilon_\beta)|^2 \tag{2.61}$$

and substituting them into Eq. (2.60) finally yields a Lorentzian expression for the squared amplitude of the bound-like component:

$$|a_\alpha(E)|^2 = \frac{\frac{1}{2}\gamma_\alpha/\pi}{(E - E_r)^2 + \Gamma^2/4}. \tag{2.62}$$

It is visible from Eq. (2.62) that Γ has the meaning of a width of the bound amplitude. The decay width of a given resonant state can thus be calculated by evaluating Eq. (2.61) at the resonance energy $E = E_r$, which is given as[135, 136, 138]

$$E_r = E_\phi + \sum_\beta^{N_c} \mathcal{P} \int \frac{|M_\beta(E, \epsilon_\beta)|^2}{E - E_\beta - \epsilon_\beta} \, \mathrm{d}\epsilon_\beta, \tag{2.63}$$

where $\mathcal{P}$ denotes that the Cauchy principal value of the integral is to be taken. The second term in Eq. (2.63) constitutes an energy shift due to the bound-continuum interaction. Since its contribution to E_r can be assumed to be smaller than the error in an *ab initio* computation, it may be discarded, thereby approximating the resonance energy by the expectation value of the Hamiltonian in the state ϕ, $E_r \approx E_\phi$.[138–140]

Given that the continuum-like components $\{\chi^+_{\beta,\epsilon_\beta}\}$ of the wavefunction of the autoionizing system are good approximations to the real final continuum states, the quantity γ_β can be identified as a partial decay width belonging to a specific open decay channel β.[137] It is noteworthy that any other choice of the continuum wave functions $\{\chi_{\beta,\epsilon_\beta}\}$ related to the real continuum wave functions $\{\chi^+_{\beta,\epsilon_\beta}\}$ by a unitary transformation leads to the same value for the total decay width Γ.[138, 139] This is easily seen if one substitutes Eq. (2.59) into Eq. (2.61). Doing so, one obtains

$$\Gamma(E) = 2\pi \sum_\beta^{N_c} \big\langle \phi \big| \hat{H} - E \big| \chi^+_{\beta,\epsilon_\beta} \big\rangle \big\langle \chi^+_{\beta,\epsilon_\beta} \big| \hat{H} - E \big| \phi \big\rangle, \tag{2.64}$$

wherein the resolution of the identity can be replaced according to

$$\sum_\beta^{N_c} \big| \chi^+_{\beta,\epsilon_\beta} \big\rangle \big\langle \chi^+_{\beta,\epsilon_\beta} \big| = \sum_\beta^{N_c} \big| \chi_{\beta,\epsilon_\beta} \big\rangle \big\langle \chi_{\beta,\epsilon_\beta} \big|. \tag{2.65}$$

Hence, Eq. (2.64) can be rewritten as

$$\Gamma(E) = 2\pi \sum_{\beta}^{N_c} \langle \phi | \hat{H} - E | \chi_{\beta,\epsilon_\beta} \rangle \langle \chi_{\beta,\epsilon_\beta} | \hat{H} - E | \phi \rangle. \tag{2.66}$$

II.2.2. Construction of Bound and Continuum States Within Fano-ADC

So far, the bound and continuum state wave functions ϕ and $\chi_{\beta,\epsilon_\beta}$ have not been defined. This can in general be done using the projection method by Feshbach.[132, 133] Within CI-like formalisms, two projection operators $\hat{P}$ and $\hat{Q}$ are chosen such that they project on configuration subspaces belonging to the final continuum states and the bound resonance state, respectively.[134, 138]

The bound state projector $\hat{Q}$ is constructed in such a way that it does not include any components contributing to the open decay channels β, i.e., according to Eq. (2.55), states lower in energy than the resonance state in question. More specifically, within the PP-ADC scheme, intermediate states which constitute reasonable contributions to the states representing open decay channels have to be excluded from $\hat{Q}$. This leads to difficulties, since knowledge of the $\hat{P}\hat{H}\hat{P}$ and $\hat{Q}\hat{H}\hat{Q}$ spectra is required for the construction of $\hat{P}$ and $\hat{Q}$, respectively.[140]

The problem can, however, be circumvented when treating the problem in zeroth order of perturbation theory, viz taking orbital energy differences as a selection criterion. The corresponding procedure can best be demonstrated by the application to a specific problem as for example the $2s^{-1}3p$ transition in the neon atom.[140, 141]

Because of energy conservation, no singly-excited configurations having a hole in the $2s$ orbital or in a deeper shell can contribute to the continuum states. Thus, all intermediate states constructed from the corresponding configurations are added to $\hat{Q}$. Similarly, no doubly-excited configurations with one hole at the $2s$ orbital or a deeper shell can contribute to the continuum states, allowing the corresponding intermediate states to be added to $\hat{Q}$ as well. Mathematically, this selection scheme can be formulated by introducing additional constraints for the excitation operator employed in the ISR derivation of the PP-ADC equations,

$$\{\hat{C}_J\} = \{c_a^\dagger c_i, \varepsilon_i \leq \varepsilon_{2s}; c_b^\dagger c_c^\dagger c_j c_k, b < c, j < k, \varepsilon_j + \varepsilon_k \leq \varepsilon_{2s}\}. \tag{2.67}$$

For the selection of configurations for the construction of the $\hat{P}$ projector, a similar strategy can be applied. First, it is noticed that any singly-excited configuration with a hole in one of the $2p$ orbitals represents an open decay channel and can thus be added

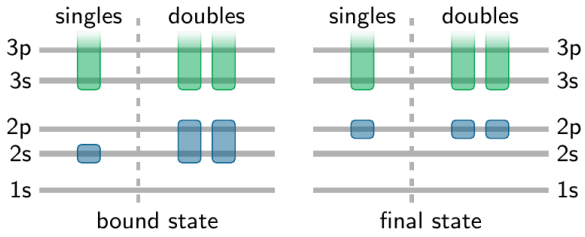

Figure II.3. Schematic view of the selection scheme for Ne autoionization as used in Ref. [140]. Occupied orbitals considered for the construction of the bound and continuum state projection operators $\hat{Q}$ and $\hat{P}$ are depicted in blue, virtual orbitals in green.

to $\hat{P}$. In order to account for electronic correlation, doubly-excited configurations having two holes in the $2p$ shell are added to $\hat{P}$ as well.

A schematic depiction of the selection scheme for the Ne autoionization process as applied in Ref. [141] can be found in Figure II.3. In addition to the selection discussed above, the energetically low-lying $1s$ orbital has been excluded from the occupied orbital space from which the configurations are generated, accounting for the fact that terms emerging from its inclusion would not constitute a substantial contribution to the description of the regarded process. Note, that in the specific case of Ne $2s^{-1}np$ autoionization, doubly-excited configurations having two holes in the $2p$ shell may also be used for the construction of $\hat{Q}$ because they are not among the accessible final states due to symmetry related reasons.[140]

Computation of Bound-Continuum Matrix Elements

Once the projection operators $\hat{Q}$ and $\hat{P}$ have been set up, the corresponding states are obtained by diagonalization of $\hat{Q}\hat{H}\hat{Q}$ and $\hat{P}\hat{H}\hat{P}$, respectively.

When applying an appropriate selection scheme, the resonance state in question will usually be one of the lowest eigenstates of the Hamiltonian projected onto the Q subspace. Hence, it is sufficient to compute only a few states at the lower bound of the $\hat{Q}\hat{H}\hat{Q}$ spectrum, which can be done using an iterative solver like, e.g., the Davidson algorithm,[147] and then to select the appropriate PP-ADC vector $\mathbf{Y}$.

As will be discussed in Section II.2.3, the full $\hat{P}\hat{H}\hat{P}$ spectrum is generally needed in order to find the desired decay width, making the method prohibitively computationally demanding even for moderate-sized systems. It has, however, been demonstrated that the demand for a full diagonalization of the Hamiltonian projected onto the P subspace can be lifted by applying the iterative block-Lanczos diagonalization algorithm,[124, 141, 142, 148] yielding continuum-state PP-ADC eigenvectors $\mathbf{X}_\beta$.

Using the PP-ADC vectors $\mathbf{Y}$ and $\mathbf{X}_\beta$, the bound-continuum coupling matrix elements

$M_\beta(E, \epsilon_\beta)$ can be computed according to Eq. (2.59). The explicit expression is given by

$$M_\beta(E_r, \epsilon_\beta) = \mathbf{X}_\beta^\dagger \mathbf{M} \mathbf{Y} - E_r \big(\mathbf{X}_\beta^\dagger \mathbf{Y}\big). \tag{2.68}$$

wherein $\mathbf{M}$ is the PP-ADC secular matrix. The second term in Eq. (2.68) is thereby the resonance energy multiplied by the overlap between the two states $\chi_{\beta,\epsilon_\beta}$ and ϕ and may be regarded as a correction term accounting for the fact that no orthogonality has been enforced between the bound and continuum states.

II.2.3. Stieltjes Imaging

Having an explicit expression for the bound-continuum matrix elements at hand, the decay width could in principle be calculated following Eq. (2.61). Since the continuum wave functions have been constructed using the wrong boundary conditions, i.e., $\mathcal{L}^2$ boundary conditions, the resulting states are unit normalized, whereas the real continuum states are energy normalized. In addition, the $\mathcal{L}^2$ boundary conditions cause the continuum states to form a discrete spectrum rather than a continuous one.[149] Hence, no physical meaning can in general be ascribed to the continuum states.

Using the *Stieltjes imaging* technique, these shortcomings can be overcome and a meaningful value for the decay width Γ can be extracted using the bound-continuum coupling matrix elements calculated using the wrongly normalized discrete quasi-continuum states. The idea is the following: The artificially discretized quasi-continuum states only fail to approximate the real continuum state wave functions in the region where the bound state wave function is effectively zero, i.e., in a region far from the nuclei. Hence, no contribution from this region is included in the bound-continuum matrix elements according to Eq. (2.59), meaning that the description of the bound-continuum interaction does, apart from the wrong normalization, not suffer from the approximation introduced by imposing the wrong boundary conditions.

The method was originally developed for the application to the calculation of total photoionization cross-sections[143, 150] and was first applied to the problem of decay widths by Hazi and coworkers.[135, 151] A brief outline of the basic concepts following Refs. [135] and [141] is given in this section.

Consider the so-called cumulative function $F(E)$ defined according to

$$F(E) = \int^E \mathrm{d}E' \, \Gamma(E') \tag{2.69}$$

or

$$\Gamma(E) = \frac{\mathrm{d}F}{\mathrm{d}E}. \tag{2.70}$$

This function can be approximated by a histogram function

$$\tilde{F}(E) = 0 \qquad 0 \leq E \leq \epsilon_1 \tag{2.71}$$

$$\tilde{F}(E) = \sum_{\beta=1}^{k} \gamma_\beta \qquad \epsilon_k < E < \epsilon_{k+1}, \tag{2.72}$$

where the pairs $\{\gamma_\beta, \epsilon_\beta\}$ correspond to the width matrix elements calculated according to Eq. (2.61) using the quasi-continuum states $\chi_{\beta,\epsilon_\beta}$ and the respective energies ϵ_β.

At the rise points, $E = \epsilon_k$, the cumulative function $F(E)$ is approximated by the mean of the two neighboring levels

$$\tilde{F}(\epsilon_k) = \frac{1}{2}\big(\tilde{F}(\epsilon_k - 0) + \tilde{F}(\epsilon_k + 0)\big) = \sum_{\beta=1}^{k-1} \gamma_\beta + \frac{1}{2}\,\gamma_k. \tag{2.73}$$

The Stieltjes derivative calculated according to Eq. (2.70) at the half-way points $E_\beta = \frac{1}{2}(\epsilon_\beta + \epsilon_{\beta+1})$ is then given as

$$\tilde{\Gamma}(E_\beta) = \frac{1}{2}\,\frac{\gamma_\beta + \gamma_{\beta+1}}{\epsilon_{\beta+1} - \epsilon_\beta}. \tag{2.74}$$

Inspecting the resulting expression reveals that the normalization constants associated with the discrete states $\chi_{\beta,\epsilon_\beta}$ are determined by the density of eigenvalues of the quasi-continuum spectrum.

Eq. (2.74) could in principle be used as a histogram approximation to the decay width $\Gamma(E)$. The numerical values obtained from a corresponding calculation are, however, not satisfying and tend to converge badly with improvement of the basis set used for the calculation of the required states.[141] Therefore, the $\{\gamma_\beta, \epsilon_\beta; \beta = 1, \ldots, N_c\}$ pairs are not employed directly but first 'smoothed' using a moment theoretical approach. The concept behind this is discussed in the remaining part of this section.

If the exact discrete and continuum functions φ and $\chi^+_{\beta,\epsilon_\beta}$ of the final states were known, the spectral moments associated with the decay width $\Gamma(E)$ could be stated as

$$M_n = \sum_i E_i^n \left|\langle\phi|\hat{H} - E|\varphi_i\rangle\right|^2 + \int_{E_t}^{\infty} E^n \left|\langle\phi\big|\hat{H} - E\big|\chi^+_{\beta,\epsilon_\beta}\rangle\right|^2 \mathrm{d}E. \tag{2.75}$$

Therein, E_t is the ionization threshold. E_i and E are the energies of the discrete and continuum functions of the final states.

One can now replace the exact resolution of the identity in Eq. (2.75) with the one constructed using the quasi-continuum functions $\chi_{\beta,\epsilon_\beta}$. Doing so, one obtains

$$M_n = \frac{1}{2\pi} \sum_\beta \epsilon_\beta^n \, \gamma_\beta. \tag{2.76}$$

The summation over all quasi-continuum states β in this expression is the reason for the general requirement for a full $\hat{P}\hat{H}\hat{P}$ diagonalization, as was already mentioned in Section II.2.2.

Using a numerically efficient technique discussed in detail in Ref. [149], the first $2M$ approximate inverse-power moments are used to obtain the 'smoothed' spectrum of value pairs

$$\left\{\bar{\gamma}_\beta^{(M)}, \bar{\epsilon}_\beta^{(M)}, \beta = 1, \ldots, M \leq N\right\}. \tag{2.77}$$

Repeating this procedure for increasing orders M, and substituting the resulting value pairs (2.77) into Eq. (2.74), a series of histogram approximations for the decay width $\Gamma(E)$ can be created. The desired value for $E = E_r$ can finally be computed for increasing orders M using an interpolation technique until the obtained $\Gamma(E_r)$ converges to a mutually consistent value.

II.3. Complex Absorbing Potential ADC

Another method devised for the description of electronic resonances beyond the ionization threshold is constituted by the complex absorbing potential method. In this section, a basic overview of the methodology and its combination with EA-ADC is given.

II.3.1. The Complex Absorbing Potential Method

Augmenting the molecular Hamiltonian with a complex one-particle potential $-i\eta\hat{W} = -i\eta W$ leads to a complex symmetric effective Hamiltonian

$$\hat{H}(\eta) = \hat{H} - i\eta\hat{W} \tag{2.78}$$

with a purely discrete spectrum and $\mathcal{L}^2$-integrable eigenfunctions.[125] Therein, the parameter η is used to control the strength of the CAP. The potential function $\hat{W}$ is required to

have a non-negative real part,

$$\mathrm{Re}\{W(\mathbf{r})\} \geq 0 \quad \text{and} \quad \mathrm{Re}\{W(\mathbf{r})\} \to \infty \text{ for } \mathbf{r} \to \infty. \tag{2.79}$$

In addition, the potential can be complex, in which case it has to hold that there exist positive real numbers c_0 and c_1 such that[125]

$$|\mathrm{Im}\{W(\mathbf{r})\}| \leq c_0 + c_1 \cdot \mathrm{Re}\{W(\mathbf{r})\}. \tag{2.80}$$

In order to rationalize how a CAP works, one may consider its effect in the time-dependent picture, where the real part of the $\hat{W}$ potential acts in a way that the outgoing electron is absorbed.[23] If the imaginary part of $\hat{W}$ is non-zero, it can be interpreted as an additional potential accelerating or slowing down the outgoing electron.

In the complete basis set limit, the exact Siegert energy E_r of a resonance is recovered as $E(\eta)$ in the limit $\eta \to 0^+$. In practical applications with finite basis sets, one has to resort to a larger potential strength in order to allow for a non-zero interaction of the CAP with the resonance wave function in question. Using larger η values, however, leads to a perturbation of the resonance wave function in the bound region of the electronic system because a part of the outgoing electron is reflected by the potential. Therefore one has to estimate the resonance energy from the spectrum of $\hat{H}(\eta)$ for large η values such that the perturbation caused by the potential is minimized.

This can be accomplished when considering an expansion of the trajectory $E(\eta)$ about $\tilde{\eta}$, a CAP strength for which the error introduced by the spatial basis set deficit is irrelevant,[23, 125]

$$E(\eta) = E(\tilde{\eta}) + \sum_{n=1}^{\infty} \frac{1}{n!} \left.\frac{\mathrm{d}^n E(\eta)}{\mathrm{d}\eta^n}\right|_{\eta=\tilde{\eta}} (\eta - \tilde{\eta})^n. \tag{2.81}$$

Evaluation of this expansion at $\eta = 0$,

$$E(0) = E(\tilde{\eta}) - \tilde{\eta} \left.\frac{\mathrm{d}E(\eta)}{\mathrm{d}\eta}\right|_{\eta=\tilde{\eta}} + \frac{1}{2}\tilde{\eta}^2 \left.\frac{\mathrm{d}^2 E(\eta)}{\mathrm{d}\eta^2}\right|_{\eta=\tilde{\eta}} + \cdots, \tag{2.82}$$

leads to a measure for the error caused by the perturbation of the resonance wave function by the CAP. Considering the *uncorrected* trajectory $E(\eta)$, this error is given by

$$|E(\eta) - E(0)| = \left|\eta \frac{\mathrm{d}E(\eta)}{\mathrm{d}\eta}\right| + O(\eta^2) \tag{2.83}$$

$$= \left|\frac{\mathrm{d}E(\eta)}{\mathrm{d}\ln\eta}\right| + O(\eta^2), \tag{2.84}$$

meaning that the best possible approximation to the exact Siegert energy is found for the value of η which minimizes the linear term in the expansion (2.82) or, in other words, at the minimum of the logarithmic velocity of $E(\eta)$ in the complex energy plane.

Consequently, an even better approximation to the exact Siegert energy may be obtained by considering the *corrected* trajectory

$$U(\eta) = E(\eta) - \eta \frac{\mathrm{d}E(\eta)}{\mathrm{d}\eta}, \tag{2.85}$$

in which case the error to be minimized can be stated as

$$|U(\eta) - E(0)| = \frac{1}{2} \left| \eta^2 \frac{\mathrm{d}^2 E(\eta)}{\mathrm{d}\eta^2} \right| + O(\eta)^3 \tag{2.86}$$

$$= \frac{1}{2} \left| \eta \frac{\mathrm{d}U(\eta)}{\mathrm{d}\eta} \right| + O(\eta^3) \tag{2.87}$$

$$= \frac{1}{2} \left| \frac{\mathrm{d}U(\eta)}{\mathrm{d}\ln\eta} \right| + O(\eta^3), \tag{2.88}$$

meaning that in this case the best approximation to the exact Siegert energy $E(0)$ is found at the minimum of the logarithmic velocity of $U(\eta)$.

The minima of the logarithmic velocity of the corrected trajectory $E(\eta)$ and the uncorrected trajectory $U(\eta)$ (Eqs. (2.84) and (2.88)) can be located by means of finite differences between eigenvalues of the effective Hamiltonian $\hat{H}(\eta)$ computed for different CAP strengths η.

One may be tempted to proceed in the same manner and consider even higher-order terms for the trajectory. It has, however, been pointed out that such a strategy does not guarantee more accurate results, since the basis set error gets more pronounced with increasing order in the expansion (2.82).[125] In practical applications, the first-order corrected trajectory (2.85) has proven to yield satisfactory results. It should be noted that results from this formalism are in principle only trustworthy in cases where the uncorrected and corrected treatments yield rather similar results.

II.3.2. Shape of the Potential

Apart from the conditions (2.79) and (2.80), the mathematical form of the absorbing potential has not yet been defined, and indeed a large class of potentials satisfies these conditions. In practical applications, quadratic potentials have been successfully employed, and this class of potentials was also used throughout this work.

In this section the most popular choices of quadratic potentials shall be briefly outlined.

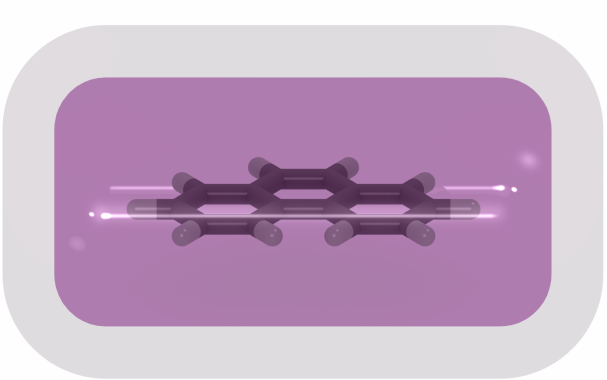

Figure II.4. Isosurface plot of a box CAP wrapped around a phenanthrene molecule drawn at values of 2.0 (purple) and 8.0 (light gray).

In general, the potential is designed such that it is zero in the inner region of the molecular potential, i.e., in the bound region. The simplest potential is a shifted quadratic spherical potential according to

$$W(r) = (r - c)^2 \tag{2.89}$$

with $r = \sqrt{x^2 + y^2 + z^2}$ being the radial distance from the molecular center. The parameter c defines the onset of the potential.

Obviously, the angular shape of this potential type is a good choice to deal with atoms and spherical molecular electronic systems. In addition, the point group symmetry of the molecular Hamiltonian is always preserved upon addition of the CAP. For molecules with a less isotropic spatial extent, however, different angular potential shapes are desirable.

One of the most widely used potentials is the so-called box CAP,[152] which has been successfully employed for a variety of metastable states.[130, 153, 154] The angular shape is determined by three cutoff parameters $\mathbf{c} = (c_x, c_y, c_z)^{\mathrm{T}}$ defining a rectangular box around the molecule inside which the CAP is zero. The box CAP then takes the form

$$W(\mathbf{r}; \mathbf{c}) = \sum_i W_i(r_i; c_i), \qquad i = x, y, z \tag{2.90}$$

$$W_i(r_i; c_i) = \begin{cases} (r_i + c_i)^2 & r_i < -c_i \\ 0 & -c_i \leq r_i \leq c_i \\ (r_i - c_i)^2 & c_i < r_i. \end{cases} \tag{2.91}$$

As is visible from Figure II.4, such a choice fits the shape of a planar organic molecule considerably better than a simple spherical CAP.

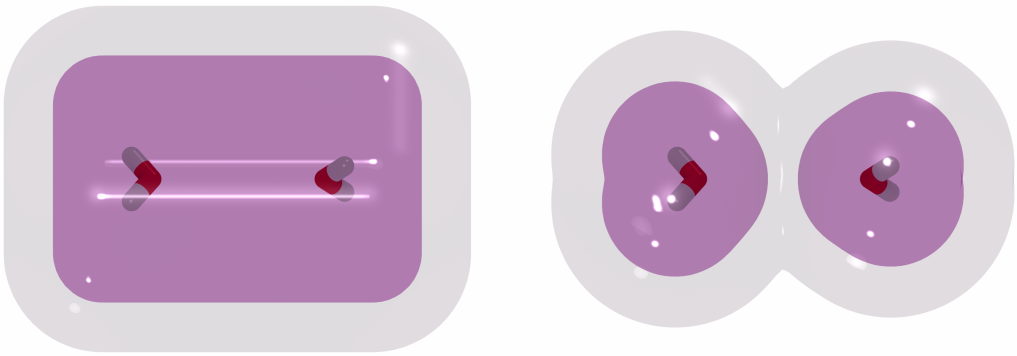

Figure II.5. Shape of different complex absorbing potentials. Left: box CAP; right: "smoothed Voronoi" CAP. Isosurfaces are drawn at potential values of 2.0 (purple) and 8.0 (light gray).

The downside of rectangular box CAPs is that the molecular point group may not be preserved. In addition, molecular clusters with relatively large distances between individual fragments cannot be treated in a satisfactory way, when a non-zero CAP is needed between the fragments. A depiction of such a situation is given in Figure II.5 with an artificial example of a cluster of two water molecules, where the box CAP shown on the left panel ignores the internal structure.

A more suitable way of defining the CAP is given by the so-called "smoothed Voronoi" CAP (right panel of Figure II.5).[155] In this approach, the angular shape of the CAP is determined by a single cutoff parameter r_{cut} which defines the minimum distance from an atom within the molecule at which the CAP can take non-zero values. At a point $\mathbf{r}$ in space, the potential is then simply given as

$$W(\mathbf{r}) = \begin{cases} 0 & r_{\mathrm{WA}} \leq r_{\mathrm{cut}} \\ (r_{\mathrm{WA}} - r_{\mathrm{cut}})^2 & r_{\mathrm{WA}} > r_{\mathrm{cut}}, \end{cases} \tag{2.92}$$

with r_{WA} being a weighted-average distance according to

$$r_{\mathrm{WA}}(\mathbf{r}) = \sqrt{\frac{\sum_\alpha w_\alpha r_\alpha^2}{\sum_\alpha w_\alpha}}\,. \tag{2.93}$$

Therein, $r_\alpha = \|\mathbf{r}_\alpha\| = \|\mathbf{r} - \mathbf{R}_\alpha\|$ is the distance between $\mathbf{r}$ and the coordinates $\mathbf{R}_\alpha$ of atom α, and the summations are carried out over all atoms α. The weight parameter w_α is given as

$$w_\alpha = \frac{1}{\left(r_\alpha^2 - r_{\mathrm{nearest}}^2 + (1\,\mathrm{a.u.})^2\right)^2}\,, \tag{2.94}$$

with $r_{\mathrm{nearest}} = \|\mathbf{r}_{\mathrm{nearest}}\| = \|\mathbf{r} - \mathbf{R}_{\mathrm{nearest}}\|$ being the distance between $\mathbf{r}$ and the atom

closest to this point in space. Weights are large for atoms α which are close to $\mathbf{r}$, i.e., which have similar distances as the nearest one, and small for atoms far away. As a result, only a few atoms gain considerable weight in the summations performed in Eq. (2.94). Using the weighted-average distance rather than employing r_{nearest} directly in Eq. (2.92) guarantees a smooth behavior of the potential at Voronoi cell edges.

II.3.3. Combining Complex Absorbing Potentials with ADC

In principle, the complex absorbing potential approach is applicable to any electronic structure method allowing for the description of the considered electronic resonance. Depending on the method, there are, however, different routes to the CAP inclusion. More specifically, within ADC schemes the effective CAP-augmented Hamiltonian can be formed at different stages.

In a first implementation, the CAP was introduced during the diagrammatic derivation of the Dyson-ADC equations.[23] Closely related is an approach followed in the context of EOM-CC[153] where the CAP is introduced already at the stage of the Hartree-Fock calculation, which is possible because the CAP is a one-particle potential. The resulting orbital energies and electron repulsion integrals are complex and can directly be employed in the ADC working equations. However, equations which have been optimized for computational efficiency under the assumption that real basis functions are used would have to be reformulated.

CAP Introduction via Intermediate State Representation

A more convenient way in conjunction with ADC schemes for which the intermediate state representation is available is to form a CAP-augmented effective ADC Hamiltonian by addition of the complex absorbing potential $\widetilde{\mathbf{W}}$, expanded into the IS basis according to Eq. (2.21), to the ADC effective interaction matrix (2.12). The Hermitian diagonalization problem (2.10) is such transferred into a complex symmetric diagonalization problem

$$\big(\mathbf{M} - i\eta\widetilde{\mathbf{W}}\big)\mathbf{Y}^c = \mathbf{Y}^c\mathbf{\Omega}^c \tag{2.95}$$

with $\mathbf{Y}^c$ now being the matrix of complex (column) eigenvectors $\mathbf{Y}_n^c$ of the CAP-augmented ADC secular matrix and $\mathbf{\Omega}^c$ the diagonal matrix of complex ADC eigenvalues Ω_n^c.

The beauty of this approach lies in its easy implementation, since no complex algebra is needed for its computational evaluation when matrix-free diagonalization procedures such as, e.g., the Davidson algorithm[147] are employed. This is easily established when treating the real and imaginary parts $\mathbf{Y}_n^{(R)}$ and $\mathbf{Y}_n^{(I)}$ of a complex ADC eigenvector $\mathbf{Y}_n^c =$

$\mathbf{Y}_n^{(R)} + i\mathbf{Y}_n^{(I)}$ separately. In case of purely imaginary CAPs, i.e., real CAP strengths η, the matrix vector product

$$\mathbf{R}_n^c = \big(\mathbf{M} - i\eta\widetilde{\mathbf{W}}\big)\mathbf{Y}_n^c \tag{2.96}$$

is cast into a sum of four matrix vector products according to

$$\begin{aligned}\mathbf{R}_n^c &= \big(\mathbf{M}\mathbf{Y}_n^{(R)} + \eta\widetilde{\mathbf{W}}\mathbf{Y}_n^{(I)}\big) + i\left(\mathbf{M}\mathbf{Y}_n^{(I)} - \eta\widetilde{\mathbf{W}}\mathbf{Y}_n^{(R)}\right) &(2.97)\\ &= \mathbf{R}_n^{(R)} + i\mathbf{R}_n^{(I)}. &(2.98)\end{aligned}$$

For complex potential strengths $\eta = |\eta|\,(\cos\vartheta + i\sin\vartheta)$, still only four matrix vector products have to be computed. Eq. (2.96) then evaluates to

$$\begin{aligned}\mathbf{R}_n^c = &\big((\mathbf{M} + |\eta|\sin\vartheta\,\widetilde{\mathbf{W}})\mathbf{Y}_n^{(R)} + |\eta|\cos\vartheta\,\widetilde{\mathbf{W}}\mathbf{Y}_n^{(I)}\big)\\ &+ i\big((\mathbf{M} + |\eta|\sin\vartheta\,\widetilde{\mathbf{W}})\mathbf{Y}_n^{(I)} - |\eta|\cos\vartheta\,\widetilde{\mathbf{W}}\mathbf{Y}_n^{(R)}\big).\end{aligned} \tag{2.99}$$

All CAP-ADC approaches discussed so far require the diagonalization procedure of the full ADC matrix to be carried out multiple times with different CAP strengths η, since a trajectory $\Omega_n^c(\eta)$ is required in order to determine the stabilization point by means of minimizing the expressions (2.84) or (2.88).

Subspace Projection Approach

Rather than expanding the absorbing potential into the IS basis and augmenting the ADC Hamiltonian (2.12), one can also add the CAP at the stage of converged ADC states using Eq. (2.24). One then has to solve the eigenvalue problem

$$\big(\mathbf{\Omega} - i\eta\mathbf{T}(\hat{W})\big)\mathbf{C} = \mathbf{C}\mathbf{\Omega}^c \tag{2.100}$$

where $\mathbf{\Omega}$ is the diagonal matrix of (real) eigenvalues of the non-CAP-augmented ADC secular matrix, $\mathbf{T}(\hat{W})$ is the transition moment matrix of the absorbing potential $\hat{W}$ according to Eq. (2.24), and $\mathbf{C}$ is the matrix of complex (column) vectors $\mathbf{C}_n = \mathbf{C}_n^{(R)} + i\mathbf{C}_n^{(I)}$ which can be viewed as expansion coefficients of the CAP-ADC eigenvectors $\mathbf{Y}_n^c$ into the eigenvector basis $\mathbf{Y}$ of the non-CAP-augmented ADC secular matrix. That is, the ISR of a CAP-ADC state can be computed according to

$$\mathbf{Y}_n^c = \mathbf{Y}\mathbf{C}_n = \sum_m C_{mn}\mathbf{Y}_m. \tag{2.101}$$

The motivation for this reformulation is that in the limit $\eta \to 0^+$, eigenvectors of

the non-CAP-augmented ADC Hamiltonian $\mathbf{M}$ give a description of resonance states or wrongly discretized continuum states possibly serving as decay channels. In particular, in the limit $\eta \to 0^+$, the non-CAP-augmented ADC eigenvalues are recovered,

$$\lim_{\eta \to 0^+} \Omega_n^c(\eta) = \Omega_n. \tag{2.102}$$

Thus, it can be sufficient to project the diagonalization problem (2.100) onto an ADC eigenstate subspace P spanned by i) the resonance state in question and ii) all relevant decay channels, i.e., those accessible starting from the resonance state. Given the corresponding projection matrix $\mathbf{P}$, the full diagonalization problem (2.100) reduces to

$$\mathbf{P}\big(\mathbf{\Omega} - i\eta\mathbf{T}(\hat{W})\big)\mathbf{P}\bar{\mathbf{C}} = \bar{\mathbf{C}}\bar{\mathbf{\Omega}}^c. \tag{2.103}$$

where the overbar indicates subspace projection, i.e., $\bar{\mathbf{C}}$ and $\bar{\mathbf{\Omega}}^c$ are the subspace-projected counterparts of the full-space quantities $\mathbf{C}$ and $\mathbf{\Omega}^c$, respectively.

This means that an η-trajectory can be computed basically at the expense of a single (full-IS space) ADC calculation if the dimensionality of the subspace P is sufficiently small. In practice, the projector is chosen by means of an energy criterion, owing to the fact that continuum states which are too high in energy are unlikely to serve as decay channels.

II.3.4. Dyson Orbitals Within CAP-EA-ADC

In the context of CAP-based description of resonance states using electronic structure methods giving access to electron-attached states, Dyson orbitals have proven to be a valuable tool for the visualization and interpretation of autoionization processes.[156] It has been shown[156] that the real part of a Dyson orbital of a resonance state is linked to its bound part, whereas the imaginary part gives a description of the decay channels involved, i.e., represents the wave function of the ejected electron.

Within the projected CAP-EA-ADC approach, Dyson orbitals can be computed by means of Eq. (2.42). The needed spectroscopic amplitudes are computed via Eq. (2.11) by inserting the ISR of CAP-EA-ADC states (2.101). Thereby, the imaginary (decay) and real (resonance) parts of the CAP-EA-ADC vector directly yield the desired spectroscopic amplitudes $\mathbf{x}_{\text{dec}}$ describing the decay channels and $\mathbf{x}_{\text{res}}$ describing the bound part of the

resonance state,

$$\mathbf{x}_{\mathrm{res}}^{(n)} = \mathbf{Y}_n^{(R)\dagger}\mathbf{f} = \bar{\mathbf{C}}_n^{(R)\dagger}\mathbf{Y}^\dagger\mathbf{f} = \sum_m \bar{C}_{mn}^{(R)}\mathbf{Y}_m\mathbf{f} \tag{2.104}$$

$$\mathbf{x}_{\mathrm{dec}}^{(n)} = \mathbf{Y}_n^{(I)\dagger}\mathbf{f} = \bar{\mathbf{C}}_n^{(I)\dagger}\mathbf{Y}^\dagger\mathbf{f} = \sum_m \bar{C}_{mn}^{(I)}\mathbf{Y}_m\mathbf{f}. \tag{2.105}$$

The right-hand side of Eqs. (2.104) and (2.105) thereby implies that the desired quantities are indeed just linear combinations of the spectroscopic amplitude vectors resulting from the underlying (non-CAP) EA-ADC calculation. Consequently, also Dyson orbitals of CAP-EA-ADC states can be computed as linear combinations of Dyson orbitals computed for the underlying EA-ADC states, using the real and imaginary parts of the subspace expansion vectors $\bar{\mathbf{C}}_n$ as coefficients.

Chapter III

Implementation

This chapter provides an overview of the implementation of theoretical methods considered in this dissertation. All of them are directly related to ADC and were implemented within the `adcman` suite of ADC methods for electronically excited states,[157] which is available as part of the Q-Chem quantum chemical program package.[75] A general overview of the code structure of `adcman` is given in Section III.1, followed by some general remarks (Section III.2).

Section III.3 covers the implementation aspects directly related to ADC methods. In particular, the implementation of the ISR as well as effective transition moments and Dyson orbitals for IP-ADC and EA-ADC is presented. In addition, the extension of the existing third-order PP-ADC, IP-ADC and EA-ADC codes by the improved fourth-order static self-energy scheme according to the $\Sigma(4+)$ procedure is described.

Selected aspects of the Fano-Stieltjes-ADC and CAP-ADC implementations are considered in the subsequent Sections III.4 and III.5, respectively. A summary of the implemented features is provided in Section III.6.

III.1. Code Structure

Figure III.1 displays the general structure of the ADC stack within the Q-Chem quantum chemical program package. The role of the individual modules and libraries is explained in this section.

After the initial RHF or UHF calculation, the host program hands over control to the respective submodule, which acts as a driver for the post-HF calculation. In case of Fano-Stieltjes-ADC calculations, the `fanoman` module is invoked, which is described in Section III.4.

For all other ADC calculations, the `adcman` module is directly invoked and controls all

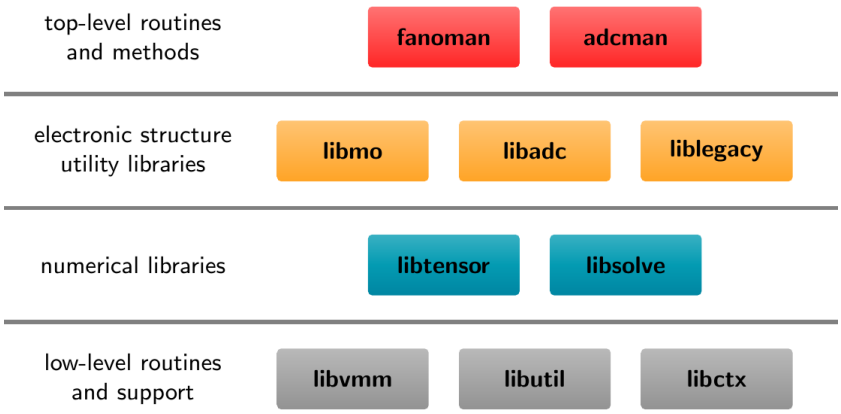

Figure III.1. Code structure related to ADC methods within the framework of the Q-Chem quantum chemical program package.

further tasks. In particular, it imports the SCF results of the initial HF calculation and triggers the computation and transformation of electron repulsion integrals (ERIs) through the `liblegacy` library, which provides the interface to all Q-Chem routines not directly related to ADC methods. A second library on which `adcman` depends is `libmo`, which handles the setup of symmetry-adapted orbital space definitions as well as transformations between different orbital representations. The `libadc` library provides the implementation of all explicit ADC equations.

Through the `libadc` library, the `adcman` module uses the numerical libraries, in particular the `libtensor` block tensor library,[158] which performs most of the numerical operations. As suggested by its name, `libsolve` implements numerical solver procedures as for example the Davidson[147] and DIIS[159] algorithms.

At the lowest level there are supporting libraries, among them `libvmm`, which accounts for virtual memory management, and `libctx`, which provides the infrastructure for storing and accessing data through context objects in a key-value-like fashion.

Since the block structure of tensors as provided by the `libtensor` library is important for parts of this dissertation, it is discussed in some detail in the following section.

III.1.1. Some Remarks on `libtensor`

`libtensor` is an open source numerical library which provides an efficient infrastructure for general block tensor operations.[158] In particular, it was designed to exploit various kinds of symmetry as illustrated in Figure III.2.

In this way it is possible to reduce the storage requirements of tensor objects and the computational costs of algebraic operations performed on it. The idea is that for each

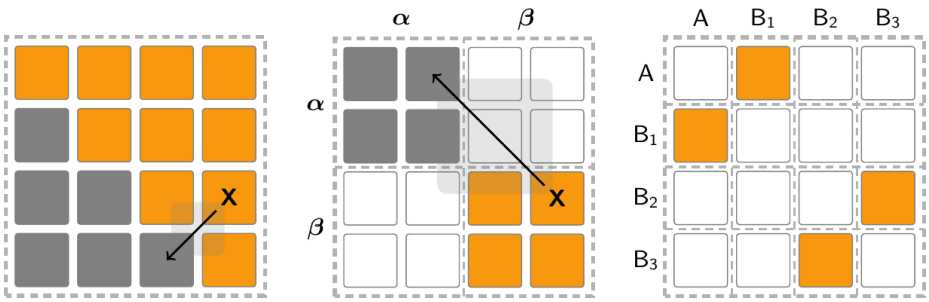

(a) Permutational symmetry. **(b)** Spin symmetry. **(c)** Point group symmetry.

Figure III.2. Different symmetry element types which can be handled by the `libtensor` library. Symmetry-related blocks are stored only once. These so-called *canonical* blocks are indicated in orange, whereas all other blocks are depicted using gray color. Blocks shown in white are not explicitly stored since they contain only zeros.

pair of blocks which are related by symmetry, only one needs to be stored. The other one can be deduced from this canonical block using a transformation, which consists of an index permutation and a scaling factor. Blocks which only contain zeros are not stored explicitly.

Three kinds of symmetry can be exploited. The first one is permutational symmetry as schematically depicted in Figure III.2a. It is used whenever two blocks can be mapped onto each other by permutation of two indices, which is, e.g., the case for anti-symmetrized ERIs. Another use case exploited in `adcman` is the antisymmetric behavior of the doubles part of a PP-ADC vector with respect to the permutation of two occupied or virtual indices according to

$$Y_{ij}^{ab} = -Y_{ji}^{ab} = -Y_{ij}^{ba} = Y_{ji}^{ba}. \tag{3.1}$$

In the original formulation, these permutations do not occur because double excitations are restricted to $i < j$ and $a < b$. Lifting these index restrictions, however, makes an efficient evaluation by means of block tensor operations possible at all. The antisymmetry thereby guarantees that the unphysical $i = j$ and $a = b$ vector elements remain zero.

A second type of symmetry is constituted by spin symmetry, which can be employed in restricted calculations. In this case, superblocks are introduced as a second level of block structure by equally partitioning the block tensor along each coordinate. The two-dimensional block tensor depicted in Figure III.2b, for example, may represent the singles part of a state vector in a restricted ADC calculation. In this case, all amplitudes of singly-excited configurations connecting an occupied α and a virtual β spin orbital and vice versa can be forced to be zero, avoiding the threefold computation of triplet states.

As another consequence, singlet and triplet states can easily be treated separately from each other by requesting appropriate mappings between the $\alpha\alpha$ and $\beta\beta$ parts of the singles vector.

The third type of symmetry implemented in the `libtensor` library is point group symmetry, enabling the separate treatment of excitations belonging to different irreducible representations of the molecular point symmetry group. A resulting tensor may have a structure as shown in Figure III.2c.

Apart from reduced storage requirements, the block structure implied by the means of symmetry can be used to efficiently distribute the computational costs associated with particular algebraic operations among multiple computational processes. A contraction of two two-dimensional block tensors $\mathbf{A}$ and $\mathbf{B}$, for example, can be split up into pairwise contractions of blocks according to

$$C_{ij} = \sum_k A_{ik}\, B_{kj}, \tag{3.2}$$

where the index k denotes all inner tensor indices. In addition, only contractions between non-zero canonical blocks need to be considered. All other contractions will again yield zero blocks and do not need to be performed explicitly. Similarly, blocks resulting from contractions of at least one non-canonical block can be deduced from the result of the contraction of the two associated canonical blocks by applying an appropriate transformation.

III.2. General Remarks

In this section, a brief overview of the conventions, intermediates and formula symbols used in the remaining part of this chapter are given.

For notational brevity, the amplitudes

$$t_{ijab} = \frac{\langle ij||ab\rangle}{(\varepsilon_a + \varepsilon_b - \varepsilon_i - \varepsilon_j)} \tag{3.3}$$

and

$$t_i^a = -\frac{\sum_{jkb} t_{jkab}\langle jk||ib\rangle + \sum_{jbc} t_{ijba}\langle ja||bc\rangle}{2(\varepsilon_a - \varepsilon_i)} \tag{3.4}$$

are defined, where ε_p is the HF orbital energy associated with the HF orbital $|\varphi_p\rangle$. As in Chapter II, the subscripts $a, b, \ldots$ refer to unoccupied (virtual) orbitals, whereas $i, j, \ldots$

denote occupied orbital indices, and the subscripts $p, q, \ldots$ may denote either of them. For an efficient evaluation, parts of the implemented equations have been optimized assuming real-valued anti-symmetrized ERIs, given in Physicist's notation as

$$\langle pq||rs\rangle = \langle rs||pq\rangle^* = \langle rs||pq\rangle. \tag{3.5}$$

A number of contractions between ERIs and t_{ijab} amplitudes formally scaling with n^6 have been replaced by the intermediate quantities

$$Z^{(1)}_{ijka} = \sum_{bc} t_{ijbc} \langle ka||bc\rangle \tag{3.6}$$

$$Z^{(2)}_{ijka} = \sum_{lb} t_{ilab} \langle lk||jb\rangle \tag{3.7}$$

$$Z^{(3)}_{ijab} = \sum_{kl} t_{klab} \langle ij||kl\rangle \tag{3.8}$$

$$Z^{(4)}_{ijab} = \sum_{kc} t_{jkac} \langle kb||ic\rangle \tag{3.9}$$

$$Z^{(5)}_{ijab} = \sum_{cd} t_{ijcd} \langle ab||cd\rangle \tag{3.10}$$

$$Z^{(6)}_{iabc} = \sum_{jk} t_{jkbc} \langle jk||ia\rangle \tag{3.11}$$

$$Z^{(7)}_{iabc} = \sum_{jd} t_{ijbd} \langle jc||ad\rangle. \tag{3.12}$$

In addition, the compound intermediates $Z^{(A)}_{ijka}$ and $Z^{(B)}_{iabc}$ have been defined according to

$$Z^{(A)}_{ijka} = \big(1 - \hat{P}_{ij}\big) Z^{(2)}_{ijka} + \frac{1}{2} Z^{(1)}_{ijka} \tag{3.13}$$

$$Z^{(B)}_{iabc} = \big(1 - \hat{P}_{bc}\big) Z^{(7)}_{iabc} - \frac{1}{2} Z^{(6)}_{iabc}, \tag{3.14}$$

where the permutation operator $\hat{P}_{pq}$ has been used which, when applied to some expression, permutes the indices p and q therein.

III.3. Implemented ADC Features

As already indicated in Chapter I, a number of new features which considerably extend the scope of the existing ADC implementation have been added to `adcman` and `libadc`.

III.3.1. IP-ADC Effective Transition Amplitudes

In order to enable the computation of pole strengths, needed for the simulation of photoelectron spectra, the IP-ADC implementation was extended by the effective transition amplitudes as given in Ref. [31]. The same quantity was further used for the computation of Dyson orbitals according to Eq. (2.42).

For an efficient evaluation, the equations have been optimized to exploit permutational symmetry, thereby assuming real basis functions. The matrix of effective transition moments $\mathbf{f}$ has the shape as indicated in Figure II.1.

The explicit equations for the $\mathbf{f}_{1,h}$ block up to second order are given as

$$f_{i,j}^{(0)} = \delta_{ij} \tag{3.15}$$

$$f_{i,j}^{(1)} = 0 \tag{3.16}$$

$$f_{i,j}^{(2)} = -\frac{1}{4} \sum_{abk} t_{ikab}\, t_{jkab}. \tag{3.17}$$

The third-order contribution to this block contains four different terms,

$$\begin{aligned} f_{i,j}^{(3)} = \frac{1}{4} \sum_{abk} t_{jkab} \frac{\sum_{cd} t_{ikcd} \langle ab||cd\rangle}{(\varepsilon_a + \varepsilon_b - \varepsilon_i - \varepsilon_k)} - \sum_{abk} t_{jkab} \frac{\sum_{lc} t_{ilac} \langle lb||kc\rangle}{(\varepsilon_a + \varepsilon_b - \varepsilon_i - \varepsilon_k)} \\ - \frac{1}{4} \sum_{abk} t_{jkab} \frac{\sum_{lm} t_{mlab} \langle ml||ki\rangle}{(\varepsilon_a + \varepsilon_b - \varepsilon_i - \varepsilon_k)} + \sum_{abk} t_{jkab} \frac{\sum_{lc} t_{klac} \langle lb||ic\rangle}{(\varepsilon_a + \varepsilon_b - \varepsilon_i - \varepsilon_k)}\,. \end{aligned} \tag{3.18}$$

Using Eqs. (3.8) through (3.10), Eq. (3.18) can be written in a more concise form, i.e.,

$$f_{i,j}^{(3)} = \sum_{abk} t_{jkab} \frac{\frac{1}{4}\big(Z_{ikab}^{(5)} + Z_{ikab}^{(3)}\big) + \big(1 - \hat{P}_{ik}\big) Z_{ikab}^{(4)}}{(\varepsilon_a + \varepsilon_b - \varepsilon_i - \varepsilon_k)}\,. \tag{3.19}$$

The contributions to the $1h$-p block of the effective transition moments matrix $\mathbf{f}_{1,p}$ up to second order are given by

$$f_{i,a}^{(0)} = 0 \tag{3.20}$$

$$f_{i,a}^{(1)} = 0 \tag{3.21}$$

$$f_{i,a}^{(2)} = \frac{1}{\varepsilon_i - \varepsilon_a} \left(\frac{1}{2} \sum_{bcj} \langle ja||bc\rangle\, t_{ijbc} + \frac{1}{2} \sum_{bjk} \langle jk||ib\rangle\, t_{jkab} \right) \tag{3.22}$$

The third-order contribution to this block as given in Eq. (2.37),

$$f_{i,a}^{(3)} = \frac{1}{\varepsilon_i - \varepsilon_a}\big(\Sigma_{ai}^{(3)}(\infty) + M_{ai}^{(3)+}(\varepsilon_i) + M_{ai}^{(3)-}(\varepsilon_a)\big), \tag{3.23}$$

consists of three terms of which the first one is the static self-energy as given in Eq. (2.38). The second and third term are the $(N \pm 1)$-parts of the dynamic self-energy $M^{(3)\pm}$, which have been given in matrix notation in, e.g., Ref. [21]. Evaluation of the matrix elements yields

$$M_{ai}^{(3)+}(\varepsilon_i) = \frac{1}{2}\sum_{jbc} t_{ijbc}\, Z_{jabc}^{(B)} - \sum_{jbc}\langle ja||bc\rangle\, \frac{\frac{1}{4}\big(Z_{ijbc}^{(3)} + Z_{ijbc}^{(5)}\big) + \big(1 - \hat{P}_{ij}\big)\, Z_{ijbc}^{(4)}}{(\varepsilon_b + \varepsilon_c - \varepsilon_i - \varepsilon_j)} \tag{3.24}$$

and

$$M_{ai}^{(3)-}(\varepsilon_a) = -\frac{1}{2}\sum_{jkb} t_{jkab}\, Z_{jkib}^{(A)} - \sum_{jkb}\langle jk||ib\rangle\, \frac{\frac{1}{4}\big(Z_{jkab}^{(3)} + Z_{jkab}^{(5)}\big) + \big(1 - \hat{P}_{ab}\big)\, Z_{jkab}^{(4)}}{(\varepsilon_a + \varepsilon_b - \varepsilon_j - \varepsilon_k)}\,, \tag{3.25}$$

where the intermediate quantities specified in Eqs. (3.6) through (3.12) have been used.

Finally, the contributions to the $2h1p$-p block of the matrix of effective transition amplitudes $\mathbf{f}_{2,p}$ are given as

$$f_{ija,b}^{(0)} = 0 \tag{3.26}$$

$$f_{ija,b}^{(1)} = -\frac{1}{\sqrt{2}}\, t_{ijab} \tag{3.27}$$

$$\begin{aligned} f_{ija,b}^{(2)} = \frac{1}{\sqrt{2}}\Bigg(&\frac{1}{2}\sum_{kl} t_{klab}\,\langle kl||ij\rangle + \frac{1}{2}\sum_{cd} t_{ijcd}\,\langle ab||cd\rangle \\ &+ \big(1 - \hat{P}_{ij}\big)\sum_{lc} t_{ljbc}\,\langle la||ic\rangle + \big(1 - \hat{P}_{ij}\big)\sum_{lc} t_{liac}\,\langle lb||jc\rangle\Bigg) \end{aligned} \tag{3.28}$$

$$= \frac{\frac{1}{2}\big(Z_{ijab}^{(3)} + Z_{ijab}^{(5)}\big) + \big(1 - \hat{P}_{ij}\big)\Big(\big(1 - \hat{P}_{ab}\big)\, Z_{ijab}^{(4)}\Big)}{\sqrt{2}\,(\varepsilon_a + \varepsilon_b - \varepsilon_i - \varepsilon_j)}\,, \tag{3.29}$$

where in the last expression the intermediate quantities from Eqs. (3.8) through (3.10) have again been used. Note that a prefactor of $1/\sqrt{2}$ has been used in the latter equations in order to account for the lifting of the $i < j$ index restriction in the IP-ADC matrix equations.

III.3.2. Iterative Scheme for an Improved Fourth-Order Static Self-Energy

As outlined in Section II.1.5, using the effective transition amplitudes of IP-ADC(3), a third-order ground state density can be computed by means of Eqs. (2.33) through (2.36).

This ground state density can further be used for the computation of an improved third-order ground state density and the connected improved fourth-order static self-energy $\Sigma(\infty)$ according to the so-called $\Sigma(4+)$ procedure as sketched in Section II.1.5.

This static self-energy scheme was implemented in `adcman`. The self-consistent iterative procedure was realized by means of the DIIS algorithm[159] as implemented in the `libsolve` library. It was combined with all available third-order ADC methods, i.e., PP-ADC(3), IP-ADC(3) and EA-ADC(3), using the scheme termed "full" in Ref. [39]. In this scheme, the second-order ground state density is replaced by the respective improved third-order quantity in all $\mathbf{M}$ matrix terms where it appears rather than only in terms related to the static self-energy. In addition, if the (improved) third-order treatment of the ground state density is used the same replacement procedure is also applied to the ISR one-particle (transition) density equations which are discussed in the following section.

III.3.3. IP-ADC ISR for the One-Particle (Transition) Density

The implementation of the ISR of the one-particle (transition) density for IP-ADC[74, 89] was further optimized for computational efficiency. The explicit expressions as implemented in Q-Chem 5.2 are given in this section.

As is visible from Figure II.1, IP-ADC(2) and IP-ADC(3) state vectors are specified in terms of a $1h$-part consisting of elements Y_i and a $2h$-$1p$-part consisting of elements Y_{ij}^a. For a concise notation of the following equations, IP-ADC state vectors $\mathbf{X} \equiv \mathbf{Y}_n$ and $\mathbf{Y} \equiv \mathbf{Y}_m$ referring to the $(N-1)$-electron states $\left|\Psi_n^{N-1}\right\rangle$ and $\left|\Psi_m^{N-1}\right\rangle$, respectively, are used.

The zeroth-order contributions to the generalized difference density matrix as defined by Eq. (2.29) are given as follows:

$$\rho'^{(0),1}_{nm,ij} = -X_j Y_i \tag{3.30}$$

$$\rho'^{(0),2}_{nm,ij} = 2\sum_{ka} X_{kj}^a Y_{ik}^a \tag{3.31}$$

$$\rho'^{(0),2}_{nm,ab} = \sum_{ij} X_{ij}^a Y_{ij}^b \tag{3.32}$$

$$\rho'^{(0)}_{nm,ia} = \sqrt{2} \sum_j X_j Y^a_{ij} \tag{3.33}$$

$$\rho'^{(0)}_{nm,ai} = \sqrt{2} \sum_j X^a_{ij} Y_j. \tag{3.34}$$

Using these expressions, the elements of the IP-ADC ISR of the generalized difference density matrix consistent through second order can be specified as

$$\rho'^{(2)}_{nm,ij} = \rho'^{(0),1}_{nm,ij} + \rho'^{(0),2}_{nm,ij} + \frac{1}{2} \sum_{ab} \left(\sum_k X_k \, t_{kiab} \right) \left(\sum_l Y_l \, t_{ljab} \right) - \frac{1}{2} Y_i \sum_k X_k \, \rho^{(2)}_{0,jk} - \frac{1}{2} X_j \sum_k Y_k \, \rho^{(2)}_{0,ki} \tag{3.35}$$

$$\rho'^{(2)}_{nm,ab} = \rho'^{(0),2}_{nm,ab} - \sum_{kc} \left(\sum_i X_i \, t_{kicb} \right) \left(\sum_j Y_j \, t_{kjca} \right) \tag{3.36}$$

$$\rho'^{(2)}_{nm,ia} = \rho'^{(0)}_{nm,ia} + \frac{1}{\sqrt{2}} Y_i \sum_{klb} X^b_{kl} \, t_{klba} + \sqrt{2} \sum_{kb} \left(\sum_l X^b_{kl} \, Y_l \right) t_{ikba} - Y_i \sum_k X_k \, \rho^{(2)}_{0,ka} \tag{3.37}$$

$$\rho'^{(2)}_{nm,ai} = \rho'^{(0)}_{nm,ai} + \frac{1}{\sqrt{2}} X_i \sum_{klb} Y^b_{kl} \, t_{klba} + \sqrt{2} \sum_{lb} \left(\sum_k X_k \, Y^b_{kl} \right) t_{liba} - X_i \sum_k Y_k \, \rho^{(2)}_{0,ka}. \tag{3.38}$$

Therein, $\rho^{(2)}_{0,pq}$ are elements of the second-order correction to the N-electron ground state one-particle density matrix given by the expressions

$$\rho^{(2)}_{0,ij} = -\frac{1}{2} \sum_{abk} t_{ikab} \, t_{jkab} \tag{3.39}$$

$$\rho^{(2)}_{0,ia} = t^a_i. \tag{3.40}$$

In the context of the computation of state densities, two different approaches are in principle possible: i) a combination of the difference density matrix with the second- or higher-order ground state density matrix as suggested by Eq. (2.25) and ii) the inclusion of the ground state density matrix according to the strict derivation of the IP-ADC ISR equations as given in Ref. [74], where the second- and possibly higher-order contributions to the ground state density are weighted according to the $1h$-character of the respective state, i.e., scaled with the norm of the $1h$-part of the corresponding state vector.

III.3.4. EA-ADC Effective Transition Amplitudes

In order to enable the computation of spectral amplitudes, the connected pole strengths and Dyson orbitals for the electron attachment case as well, the EA-ADC implementation was extended by the effective transition amplitudes as given in Ref. [31]. The explicit equations as implemented in `libadc` are given in the following.

The matrix of effective transition moments of EA-ADC is closely related to that of IP-ADC. In particular, the respective blocks have the same perturbation theoretical expansion as indicated in Figure II.1.

The explicit equations for the $\mathbf{f}_{p,1}$ block up to second order are given as

$$f_{a,b}^{(0)} = \delta_{ab} \tag{3.41}$$

$$f_{a,b}^{(1)} = 0 \tag{3.42}$$

$$f_{a,b}^{(2)} = -\frac{1}{4} \sum_{ijc} t_{ijbc}\, t_{ijac}. \tag{3.43}$$

As in the case of IP-ADC, the four terms appearing in the third-order contribution to this block can be combined for a more concise notation:

$$f_{a,b}^{(3)} = \sum_{ijc} t_{ijac} \frac{\frac{1}{4}\big(Z_{ijbc}^{(5)} + Z_{ijbc}^{(3)}\big) + \big(1 - \hat{P}_{ij}\big) Z_{ijbc}^{(4)}}{(\varepsilon_b + \varepsilon_c - \varepsilon_i - \varepsilon_j)}\,. \tag{3.44}$$

The contributions to the h-1p block of the effective transition moments matrix $\mathbf{f}_{h,1}$ up to second order are given by

$$f_{i,a}^{(0)} = 0 \tag{3.45}$$

$$f_{i,a}^{(1)} = 0 \tag{3.46}$$

$$f_{i,a}^{(2)} = \frac{1}{\varepsilon_a - \varepsilon_i} \left(\frac{1}{2} \sum_{bcj} \langle ja||bc\rangle\, t_{ijbc} + \frac{1}{2} \sum_{bjk} \langle jk||ib\rangle\, t_{jkab} \right) \tag{3.47}$$

The third-order contribution to this block can be computed according to

$$f_{i,a}^{(3)} = \frac{1}{\varepsilon_a - \varepsilon_i} \big(\Sigma_{ai}^{(3)}(\infty) + M_{ai}^{(3)+}(\varepsilon_i) + M_{ai}^{(3)-}(\varepsilon_a) \big), \tag{3.48}$$

and consists of three terms of which the first one is the static self-energy as given in Eq. (2.38). The second and third term are the $(N \pm 1)$-parts of the dynamic self-energy $M^{(3)\pm}$,

which are explicitly stated in Eqs. (3.24) and (3.25).

Finally, the contributions to the h-1h2p block of the matrix of effective transition moments $\mathbf{f}_{h,2}$ are given as

$$f^{(0)}_{j,iab} = 0 \tag{3.49}$$

$$f^{(1)}_{j,iab} = \frac{1}{\sqrt{2}}\, t_{ijab} \tag{3.50}$$

$$f^{(2)}_{j,iab} = \frac{\frac{1}{2}\big(Z^{(3)}_{ijab} + Z^{(5)}_{ijab}\big) + \big(1 - \hat{P}_{ij}\big)\Big(\big(1 - \hat{P}_{ab}\big)\, Z^{(4)}_{ijab}\Big)}{\sqrt{2}\,(\varepsilon_a + \varepsilon_b - \varepsilon_i - \varepsilon_j)}\,, \tag{3.51}$$

where in the last expression the intermediate quantities from Eqs. (3.8) through (3.10) have again been used. Note that the prefactor of $1/\sqrt{2}$ has been used in the latter equations in order to account for the lifting of the $a < b$ index restriction in the EA-ADC matrix equations.

III.3.5. EA-ADC ISR for the One-Particle (Transition) Density

The ISR of the one-particle (transition) density for EA-ADC has been implemented in development version of Q-Chem based on version 5.2.

EA-ADC(2) and EA-ADC(3) state vectors are specified in terms of a 1p-part consisting of elements Y^a and a 1h-2p-part consisting of elements Y^{ab}_i. For a concise notation of the following equations, EA-ADC state vectors $\mathbf{X} \equiv \mathbf{Y}_n$ and $\mathbf{Y} \equiv \mathbf{Y}_m$ referring to the $(N+1)$-electron states $\big|\Psi^{N+1}_n\big\rangle$ and $\big|\Psi^{N+1}_m\big\rangle$, respectively, are used.

First, the zeroth-order contributions to the generalized difference density matrix corresponding to that of IP-ADC (cf. Eq. (2.29)) are given:

$$\rho'^{(0),2}_{nm,ij} = -\sum_{ab} X^{ab}_j Y^{ab}_i \tag{3.52}$$

$$\rho'^{(0),1}_{nm,ab} = X^a Y^b \tag{3.53}$$

$$\rho'^{(0),2}_{nm,ab} = 2\sum_{ic} X^{ac}_i Y^{bc}_i \tag{3.54}$$

$$\rho'^{(0)}_{nm,ia} = \sqrt{2}\sum_{b} X^b Y^{ba}_i \tag{3.55}$$

$$\rho'^{(0)}_{nm,ai} = \sqrt{2}\sum_{b} X^{ba}_i Y^b. \tag{3.56}$$

Using these expressions, the elements of the EA-ADC ISR of the generalized difference

density matrix consistent through second order can be specified as

$$\rho'^{(2)}_{nm,ij} = \rho'^{(0),2}_{nm,ij} + \sum_{kc}\left(\sum_{a} X^a t_{ikac}\right)\left(\sum_{b} Y^b t_{jkbc}\right) \tag{3.57}$$

$$\rho'^{(2)}_{nm,ab} = \rho'^{(0),1}_{nm,ab} + \rho'^{(0),2}_{nm,ab} + \frac{1}{2}\sum_{ij}\left(\sum_{c} X^c\, t_{ijcb}\right)\left(\sum_{d} Y^d t_{ijad}\right) - \frac{1}{2}Y^b\sum_{c} X^c \rho^{(2)}_{0,ac} - \frac{1}{2}X^a\sum_{c} Y^c \rho^{(2)}_{0,bc} \tag{3.58}$$

$$\rho'^{(2)}_{nm,ia} = \rho'^{(0)}_{nm,ia} + \frac{1}{\sqrt{2}}Y^a\sum_{jbc} X^{bc}_j t_{ijbc} + \sqrt{2}\sum_{jc}\left(\sum_{b} X^{cb}_j Y^b\right) t_{ijac} - Y^a\sum_{b} X^b \rho^{(2)}_{0,ib} \tag{3.59}$$

$$\rho'^{(2)}_{nm,ai} = \rho'^{(0)}_{nm,ai} + \frac{1}{\sqrt{2}}X^a\sum_{jbc} Y^{bc}_j t_{ijbc} + \sqrt{2}\sum_{jc}\left(\sum_{b} X^b Y^{cb}_j\right) t_{ijac} - X^a\sum_{b} Y^b \rho^{(2)}_{0,ib}. \tag{3.60}$$

Therein, $\rho^{(2)}_{0,pq}$ are elements of the second-order correction to the N-electron ground state one-particle density matrix. The matrix elements of the occupied-virtual block have been stated in Eq. (3.40). The virtual-virtual block matrix elements are given as

$$\rho^{(2)}_{0,ab} = \frac{1}{2}\sum_{ijc} t_{ijac}\, t_{ijbc}. \tag{3.61}$$

As for IP-ADC, two different approaches for the computation of electron-attached state densities were implemented: i) a scheme in which the complete N-electron ground state density matrix is added to the state difference density matrix and ii) the evaluation according to the strict derivation of the ISR equations, in which all contributions of second and possibly higher order to the ground state density matrix are scaled with the $1p$-character of the respective state, i.e., with the Euclidean norm of the $1p$-part of the corresponding state vector.

III.4. Implementation of Fano-Stieltjes-ADC

The Fano-Stieltjes-ADC method has been integrated into a development version of Q-Chem based on version 5.0.[75] The respective code was mainly implemented by means of a new module called `fanoman`. For the ADC calculations, `fanoman` was interfaced to the `adcman` module[157] which had to be extended in order to allow for IS subspace-projected ADC matrix diagonalizations, block-Lanczos matrix diagonalization, and to share the ADC results with the `fanoman` module.

In principle, three tasks have to be processed by an implementation of the Fano-Stieltjes-

ADC method. These can be stated as

1. performing ADC calculations of the bound and continuum states,
2. computation of the coupling matrix elements between these, and
3. calculation of the decay width using the Stieltjes imaging procedure.

In this section, the implementation of these tasks in the new `fanoman` module is presented.

III.4.1. General Structure of the `fanoman` Module

The objective for the implementation of the Fano-Stieltjes-ADC method was to keep the code modularized, since an efficient implementation of ADC is already available through the `adcman` module.[157] For this reason, the method was implemented as a new module rather than adding the code to the `adcman` module. For the implementation, the `C++` programming language was used.

Reference Data Import

The first operation to be performed is the import of reference data, i.e., HF and MO data as well as anti-symmetrized ERIs within the full configuration space. This data is needed later by different parts of the module. For the import process, the existing infrastructure in `adcman/liblegacy` is used.

Program Control and Input Parsing

Within a Q-Chem instance, the `fanoman` module is invoked by setting the *METHOD* keyword in the `$rem` section of the Q-Chem input file to *FANO*. The desired ADC methods for the bound and continuum state ADC calculations as well as further parameters required to control the two different `adcman` invocations thus need to be set separately for each calculation.

For this reason, the input file syntax was extended by the two new input sections `$fano_bound` and `$fano_continuum`, and an input parser was implemented in `fanoman` in order to handle these new input sections. Using this input parser, parameters are read from the respective input section and set up before an `adcman` instance is started. After the ADC calculation, the parameters affected by the parser instance are restored to their initial values. Global input parameters other than the *METHOD* keyword can still be specified in the `$rem` input section, but are overridden during the respective ADC calculation when encountering the same parameter in one of the `fanoman`-specific input sections.

```
$molecule
  0 1
  Ne
$end

$rem
  JOBTYPE              SP
  METHOD               FANO
  FANO_PRINT           3
  BASIS                aug-cc-pCVTZ
$end

$fano_bound
  METHOD               ADC(2)-x
  FANO_MODE            1
  FANO_CONFIGS_SINGLE  2
  FANO_CONFIGS_DOUBLE  2-5;2-5
  EE_SINGLETS          [0,0,0,0,0,3,0,0]
  ! Largest Abelian subgroup is D2h
$end

$fano_continuum
  METHOD               ADC(2)-x
  FANO_MODE            1
  FANO_CONFIGS_SINGLE  3-5
  FANO_CONFIGS_DOUBLE  3-5;3-5
  ADC_NGUESS_SINGLES   100
  ADC_DO_BLOCK_LANCZOS TRUE
  EE_SINGLETS          [0,0,0,0,0,600,0,0]
$end
```

Listing III.1. Typical Q-Chem input file for a `fanoman` job showing the main input needed to calculate decay widths for the $2s^{-1}np$ series of Feshbach resonances in the neon atom.

The structure of a typical `fanoman` input file is given in Listing III.1. Therein, some additional parameters appear, i.e., the *FANO_CONFIGS_SINGLE*, *FANO_CONFIGS_DOUBLE* and *FANO_MODE* keywords. These parameters are used to control the bound and continuum IS subspace projection schemes and the ADC variants to be used, and will be described further in Sections III.4.2 and III.4.3.

Handling of ADC Calculations

Once the parameters needed for an ADC calculation have been set up, the `adcman` module is invoked.

At the beginning of a normal ADC calculation, `adcman` sets up a virtual memory manager, which releases all allocated memory after termination of the ADC calculation. Because in the present context `adcman` and `fanoman` need to share data before and after the invocation of the `adcman` module, two changes had to be made in `adcman`.

First, memory and a persistent `libctx::context` object are set up right after the invocation of the `fanoman` module, and an appropriately named subtree of the context object is passed to each of the two subsequently created `adcman` instances. Using this mechanism, it is also possible to supply additional data needed by the IS subspace-projected ADC method, which was implemented in order to enable appropriate configuration selection schemes (cf. Section III.4.3). Second, the `adcman` module was modified in a way that it does not release memory at its shutdown if invocation by `fanoman` is detected. Instead, the memory consumed by the data accessible via the context object is released when shutting down the `fanoman` module.

Further Data Processing

After termination of the second `adcman` instance, the ADC results stored in the context object are further processed. In particular, coupling and overlap matrix elements as well as partial decay widths and energy differences between all possible pairs of bound and continuum states within a specific irreducible representation of the molecular point symmetry group are computed and stored in the context.

Finally, the Stieltjes imaging procedure is applied for the calculation of the desired decay width. The implementation concerning these steps is discussed in more detail in Sections III.4.4 and III.4.6.

III.4.2. ADC Methods

Inspecting the IS subspace projection scheme displayed in Figure II.3, the need for a specialized ADC method becomes obvious. Some cases, however, may still be treated using ADC methods already implemented within the `adcman` module. The available options can be requested by setting the *FANO_MODE* keyword in the respective input sections and are briefly outlined below.

Setting *FANO_MODE=0* triggers a generic ADC calculation. In this case, occupied orbitals may be restricted using the *CC_REST_OCC* keyword in order to achieve configuration selection schemes as for example used for the bound state calculation in the context of the neon $2s^{-1}np$ series of resonances. Core-valence separated (CVS) ADC calculations[160] can be requested by setting *FANO_MODE=2*. In addition, *FANO_MODE=1* may be specified. This will cause `adcman` to perform an ADC calculation using a newly implemented ADC variant, the implementation of which is discussed in some detail in the following section.

III.4.3. Implementation of an ADC Variant Allowing for Arbitrary IS Subspace Projection Schemes

In order to overcome the restrictions imposed by the available methods, a new ADC variant allowing for arbitrary IS subspace projections of the ADC matrix was implemented in the `adcman` module.

The projection formalism was implemented in a straightforward way. Since `adcman` exclusively uses matrix-free diagonalization algorithms, the projection matrix is not applied to the ADC matrix itself but instead to ADC state vectors. In this respect, only element-wise multiplications with the diagonal of the projection matrix have to be performed.

For the specification of the desired configuration selection, two new input parameters were implemented, i.e., the *FANO_CONFIGS_SINGLE* and *FANO_CONFIGS_DOUBLE* keywords. By their means, specification of the occupied molecular orbitals allowed in the subspace configurations is possible. A list of orbitals may be given in terms of a comma-separated list of orbital numbers as yielded from the Q-Chem SCF calculation. In addition, ranges may be specified using a dash. Doubly-excited configurations are given by connecting two orbital index lists using a semicolon.

The diagonal of the projection matrix is set up by `fanoman` for each irreducible representation of the molecular point symmetry group and supplied to `adcman` via the passed `libctx::context` object. To this end, it is of utmost importance to correctly handle all kinds of symmetry supported by `libtensor`, since otherwise the state vector symmetry may be destroyed, leading to a considerably worse convergence behavior during the diagonalization procedure and increased computational cost.

III.4.4. Computation of the Coupling Matrix Elements

Using the ADC vectors of the bound and continuum states computed by the respective `adcman` instances and stored in the corresponding context subtrees, computation of the coupling matrix elements is straightforward. The numerical value for each state pair is readily obtained by substituting the ADC vectors and corresponding energies into Eq. (2.68).

Special care has to be taken if the bound and continuum ADC calculations have been performed using different vector sizes, i.e., when using the CVS approximation or when restricting the IS subspace using the *CC_REST_OCC* keyword. In this case, the corresponding ADC vectors have to be transformed to the full IS space.

To this end, a transformation mechanism with several tasks was implemented. First, a mapping between input (reduced space) and output (full space) indices is created using

the information accessible via the context object associated to the bound or continuum calculation and that created by the reference data import, respectively. Second, the single and double parts of the ADC vector are rewritten using this orbital index map. If permutational symmetry in the doubles part of the ADC vector with respect to the occupied orbital space was turned off during the ADC calculation, i.e., in the case of a CVS calculation, it is created in this step. In this case, the resulting ADC vector has to be renormalized.

For the task of rewriting the ADC vector, element-wise read and write access on `libtensor::btensor` block tensor objects is required. For write access dealing with the tensor's inherent symmetry, the `libtensor::btod_set_elem` class as provided by the `libtensor` library was employed.

Element-Wise Read Access to `libtensor` Block Tensor Objects

For read access, a separate mechanism was implemented as a `C++` class template. The constructor of this class takes a `libtensor` block tensor object as an argument. For access to a specific value stored in this tensor, the access `operator[]` method was overloaded, taking a `libtensor::index` object holding the absolute index of the requested value as argument. The procedure to fetch a value stored at a specific absolute index within a block tensor can be summarized as follows:

1. Translate the absolute index to the corresponding block index and index within this block (in-block index).
2. Translate the block index to the block index of the corresponding canonical block and look up the transformation between these two blocks, consisting of an index permutation and a scalar.
3. Permute the in-block index according to the permutation.
4. Fetch the value stored in the canonical block at the permuted in-block index.
5. Scale this value by the scalar and return it.

III.4.5. Block-Lanczos Diagonalization

As outlined above, the computation of continuum states usually requires an approximated spectrum yielded from the block-Lanczos iterative diagonalization procedure.[141, 142, 148] In the course of this dissertation, this solver algorithm was implemented in the `libsolve` library following Ref. [161].

Orthogonalization within the Krylov subspace turned out to be an indispensable prerequisite, and the modified Gram-Schmidt (MGS) procedure[162] was found to yield particularly satisfactory results. Here, it has to be noted that not all orthogonalization procedures can easily be implemented in the `libtensor/libsolve` setup due to a relatively restricted set of possible algebraic operations.

For the purpose of continuum state subspace-projected ADC calculations, i.e., to compute a satisfactory spectral envelope, no additional features are needed. It shall, however, be noted that an extension of the new block-Lanczos implementation by means of, e.g., implicit restarting and convergence checks is straightforward.

All PP-ADC methods available through `adcman` were subsequently interfaced to the block-Lanczos implementation, and its invocation can be requested by setting the keyword *ADC_DO_BLOCK_LANCZOS=TRUE* in the respective input section of the Q-Chem input file. In addition, the maximum number of iterations to be performed can be indicated by setting *ADC_BLOCK_LANCZOS_MAXITER* to the desired value.

III.4.6. Stieltjes Imaging Program

The Stieltjes imaging procedure was implemented according to the detailed tutorial given in Ref. [149] and following a previous implementation used in Ref. [139], which is available on the internet as a modified version through Ref. [163]. In addition to the implementation as part of the `fanoman` module, a standalone version of the program was developed.

As input, the partial decay widths

$$\gamma_\beta = 2\pi \left| M_\beta(E_\phi, \epsilon_\beta) \right|^2 \tag{3.62}$$

calculated using the previously determined bound-continuum coupling matrix elements along with the corresponding energies

$$\epsilon_\beta = E_\beta - E_r \approx E_\beta - E_\phi \tag{3.63}$$

are directly employed. Note that the approximation $E_r \approx E_\phi$ (cf. Section II.2.3) is used at this point.

As introduced in Section II.2.3, the technique relies on the calculation of negative spectral moments. According to Eq. (2.76), high negative powers of the energy differences between the continuum and the bound state have to be evaluated. As has been pointed out in Ref. [149], this is a source of round-off errors which can accumulate to a considerable overall error. The issue can, however, be circumvented when using more precise floating

point types for the calculation.

To this end, quadruple precision has been used previously.[149] In `C++`, floating point types with arbitrary precision are available through the `Boost` library.[164] In order to take benefit from this, the procedure was implemented in a templated manner, taking the desired floating point type as a template parameter.

The use of arbitrary precision floating point types within the Stieltjes procedure requires a suitable implementation of the QR algorithm for the diagonalization of tridiagonal matrices. As has been pointed out at the end of Section II.2.3, there is also a need for an interpolation algorithm working with arbitrary floating point types. Hence, both algorithms were implemented using `C++` class templates taking the floating point type as template parameter. The QR algorithm was implemented following Ref. [165]. As interpolation algorithm, a monotonicity-preserving cubic Hermite spline[166, 167] using the Fritsch-Carlson method[168] for the determination of approximate derivatives was chosen.

III.5. Implementation of CAP-ADC Methods

In contrast to Fano-Stieltjes-ADC, the implementation of CAP-based methods requires considerably less effort. This is especially the case for the subspace-projected CAP approach, since standard quantum chemical methods can be directly employed for this purpose. The only requirement which has to be fulfilled by the employed method is the possibility to compute the CAP, or more generally, a one-particle operator representation within a subspace of eigenstates of the respective Hamiltonian.

For ADC methods, this infrastructure is provided by the ISR, which gives access to the explicit form of the respective wave functions, and the CAP representation can be computed, e.g., via a one-particle density matrix-driven approach as implied by Eq. (2.24).

III.5.1. Basis Set Representation of the Complex Absorbing Potential

In order to evaluate the transition matrix elements of the potential operator, the one-particle basis representation of the potential has to be computed first. For this task, the infrastructure already available in the Q-Chem program was used.[128, 129, 156] Therein, the basis set representation of a shifted quadratic potential as discussed in Section II.3.2 is computed by numerical quadrature on a standard grid as used in DFT calculations. The grid size can thereby be controlled using the *XC_GRID* input parameter.

A number of different angular CAP shapes is available. In particular, all potentials discussed in Section II.3.2 can be used. By setting *CAP_TYPE=0* a spherical CAP is computed, whereas *CAP_TYPE=2* requests the calculation of a smoothed Voronoi CAP. In

both cases, the onset of the CAP is controlled by the *CAP_X* keyword, in the spherical case being interpreted as distance from the molecular center. In the context of the smoothed Voronoi CAP, *CAP_X* is directly interpreted as onset parameter r_{cut} as defined in Section II.3.2. Finally, *CAP_TYPE=1* triggers the computation of a box CAP, in which case the three needed onset parameters are specified using the *CAP_X*, *CAP_Y* and *CAP_Z* keywords.

III.5.2. Computation of CAP Onset Series

In the subspace-projected CAP approach, the evaluation of transition matrix elements of the CAP is associated with negligible computational costs once the one-particle (transition) density matrices within the considered eigenstate subspace have been computed. For this reason, a series of CAPs with different onset parameters may be evaluated in a single electronic structure calculation, which is particularly simple in the case of the smoothed Voronoi CAP which is fully determined by a single onset parameter. The idea has been followed in this work, allowing for more flexibility in the subsequent analysis of CAP trajectories. The lowest desired onset value can thus be specified using the usual *CAP_X* keyword. In order to enable the definition of a series of onsets, the new keywords *CAP_X_END* and *CAP_X_STEP*, defining the maximum CAP onset and the step size in the range of onset values, respectively, have been introduced.

III.5.3. CAP-ADC Methods

Since the only prerequisite of a combination of the subspace-projected CAP approach with ADC methods is the availability of the ISR for a general one-particle operator, in principle all variants of CAP-PP-ADC, CAP-IP-ADC and CAP-EA-ADC are possible candidates. In the course of this dissertation, this option has been realized for PP-ADC and EA-ADC. The extension to IP-ADC, however, is also straightforward.

The evaluation of a CAP is triggered by setting the Q-Chem input keyword *CAP_ETA* to non-zero values. Since the objective is only a single CAP evaluation per onset, it is sensible to set this option to *CAP_ETA=10000*, which corresponds to a potential strength of $\eta = 1$. The computation and evaluation of η-trajectories has been implemented as a separate program which will be briefly presented in the following Section III.5.4.

A typical input file for a CAP-EA-ADC(3) calculation of the $^2\Pi_{\mathrm{g}}$ resonance in the dinitrogen anion is given in Listing III.2. Therein, D_{2h} point group symmetry is assumed, being the largest Abelian subgroup of $D_{\infty h}$. Consequently, the computation of 50 CAP-EA-ADC states of B_{2g} symmetry and the subsequent computation of the CAP representation within the subspace of converged EA-ADC(3) eigenstates are requested.

```
$molecule
  0 1
  N
  N 1 1.0975135
$end

$rem
  JOBTYPE              SP
  METHOD               EA-ADC(3)
  BASIS                aug-cc-pVQZ
  ! Setting CAP_ETA triggers the CAP calculation and should
  ! be set to 10000, corresponding to a CAP strength of 1
  CAP_ETA              10000
  CAP_TYPE             2
  XC_GRID              000250000974
  CAP_X                2000
  CAP_X_STEP           500
  CAP_X_END            4000
  ! Largest Abelian subgroup is D2h
  EA_STATES            [0,0,50,0,0,0,0,0]
$end
```

Listing III.2. Q-Chem input file for a typical CAP-EA-ADC(3) calculation aiming at the $^2\Pi_g$ shape resonance in the dinitrogen anion. A series of smoothed Voronoi CAPs with onsets of 2.0, 2.5, 3.0, 3.5 and 4.0 r_{Bohr} is computed.

The CAP representation is eventually written to the Q-Chem output file for each requested CAP onset and can be further processed by means of a standalone program for the evaluation of η-trajectories.

III.5.4. Evaluation of CAP Trajectories

For the task of the evaluation of η-trajectories, a standalone program was implemented in `Python`. The possibility of integrating postprocessing routines directly into Q-Chem was not pursued further, since a number of parameters have to be chosen, which partly depend on the electronic structure calculation and can thus not be determined beforehand.

The standalone program for the evaluation of η-trajectories was written in `Python`. Complex matrix diagonalization and evaluation of the η-trajectories were realized using `NumPy`,[169] further data processing makes use of `SciPy` signal processing routines.[170]

Among the implemented features are the evaluation of corrected and uncorrected trajectories as discussed in Section II.3.1. Real as well as complex potential strengths can be used, allowing for a very flexible determination of stabilization points, as it has been shown in Ref. [130] and will be demonstrated in Chapter VIII at the example of a CAP-EA-ADC application.

III.6. Overview of Implemented Features

The features implemented in the Q-Chem program in the course of this dissertation are summarized in this section.

ISR for IP-ADC and EA-ADC

- The implementation of the ISR(2) for IP-ADC has been optimized and extended. It is available in Q-Chem 5.2.
- The ISR(2) for EA-ADC has been implemented in a development version of Q-Chem based version 5.2.
- Electron-detached and electron-attached state dipole moments and $\langle \hat{r} \rangle^2$ expectation values are computed when setting *ADC_PROP_ES=TRUE*.
- Transition dipole moments among all computed electron-detached or electron-attached states are evaluated when setting *ADC_PROP_ES2ES=TRUE*.
- One-particle density matrix-based quantities for electron-detachment and electron-attachment processes as, for example, detachment and attachment densities can be plotted by specifying *STATE_ANALYSIS=TRUE* and providing a suitable `$plot` input section in the Q-Chem input file.
- The strict ground state density treatment, i.e., scaling of second- and higher-order contributions to the ground state density matrix with the norm of the $1h$-part (IP-ADC) or $1p$-part (EA-ADC) of the respective state vector, can be requested by setting *ADC_STRICT_ISR=TRUE*.

Effective Transition Amplitudes and Dyson Orbitals for IP-ADC and EA-ADC

- Pole strengths are automatically computed in IP-ADC and EA-ADC calculations. In the case of ADC(3) calculations, second-order effective transition amplitudes are computed by default since only small variations are seen with respect to the third-order ones.
- Setting *ADC_DO_DYSON=TRUE* in conjunction with *STATE_ANALYSIS=TRUE* triggers plotting of Dyson orbitals for IP-ADC and EA-ADC. In this case, also a suitable `$plot` input section has to be provided.
- Exploiting the intermediates needed for the computation of IP-ADC(3) effective transition amplitudes, the prefactor in the computational scaling of PP-ADC(3) matrix-vector product evaluations could be reduced by ∼70 %. The trade-off is an increase in memory usage by ∼10 %. The slower but more memory-efficient behavior can be restored by setting *ADC_DIRECT=TRUE*.

Improved Fourth-Order Static Self-Energy

- For all implemented ADC(3) methods, i.e., PP-ADC(3), IP-ADC(3) and EA-ADC(3), schemes in which the fourth-order or improved fourth-order static self-energy $\Sigma(4)$ and $\Sigma(4+)$ is used throughout have been implemented in Q-Chem 5.2 (PP-ADC(3) and IP-ADC(3)) or a development version of Q-Chem based on this version (EA-ADC(3)).

- The self-consistent iterative procedure for the computation of $\Sigma(4+)$ uses Pulay's DIIS algorithm as implemented in the `libsolve` library. Convergence is determined by means of the Euclidean norm of the difference density matrix computed between the ground state density matrices of two subsequent solver iterations. The maximum of solver iterations and the convergence criterion can be influenced via the *ADC_DENSITY_MAXITER* and *ADC_DENSITY_CONV* keywords.

- The $\Sigma(4)$ scheme is requested by setting *ADC_DENSITY_ORDER=3*. In this case, third-order pole strengths and Dyson orbitals are computed for IP-ADC and EA-ADC, and the third-order ground state density is also used in the respective ISR calculations.

- The self-consistent $\Sigma(4+)$ scheme is requested by setting *ADC_DENSITY_ORDER=4*. In this case, improved third-order pole strengths and Dyson orbitals are computed for IP-ADC and EA-ADC, and the improved third-order ground state density is also used in the respective ISR calculations.

Fano-Stieltjes-ADC

- A new module named `fanoman` was added to a development version of Q-Chem based on version 5.0, providing an implementation of the Fano-Stieltjes-ADC method. Therein, the restricted and unrestricted variants of all PP-ADC schemes up to third order can be used.

- The module is invoked by setting *METHOD=FANO* in the `$rem` section of the Q-Chem input file. Its verbosity level can be controlled via the *FANO_PRINT* option.

- In order to control two distinct invocations of the `adcman` module, two new input sections, `$fano_bound` and `$fano_continuum`, were added. Options related to the `adcman` module can thus be set for each of the two required ADC calculations.

- Different PP-ADC variants can be invoked for the state calculations, setting the *FANO_MODE* option to an appropriate value. The supported methods comprise generic ADC (*FANO_MODE=0*) as well as CVS-ADC (*FANO_MODE=2*).

- In addition, a new variant of PP-ADC up to third order was implemented in `adcman`, which allows for arbitrary IS subspace projection of the ADC matrix. This variant is invoked by setting *FANO_MODE=1*.
- The new keywords *FANO_CONFIGS_SINGLE* and *FANO_CONFIGS_DOUBLE* have been added to enable the definition of subspace projection schemes.
- For the computation of continuum state-projected ADC spectra, the block-Lanczos iterative matrix diagonalization algorithm was implemented in the `libsolve` library. It is invoked by setting *ADC_DO_BLOCK_LANCZOS=TRUE*. The maximum number of iterations to be carried out can be controlled via the *ADC_BLOCK_LANCZOS_MAXITER* keyword.
- The Stieltjes imaging procedure needed for the decay width evaluation was implemented as part of the new module and, in addition, as a standalone program. Taking benefit from `C++` templates and the `Boost` library, floating point types of arbitrary precision can be used.

CAP-ADC

- The new CAP-EA-ADC and CAP-PP-ADC methods have been implemented in a development version of Q-Chem based on version 5.2 using a subspace projection approach. The unrestricted and restricted versions of all ADC schemes up to third order can be employed.
- The new methods are invoked by setting *CAP_ETA=10000*, corresponding to a potential strength of $\eta = 1$.
- Smoothed Voronoi (*CAP_TYPE=2*) CAP series with different onsets can be specified. For this purpose, the already existing *CAP_X* keyword is used to define the lower bound of the range of onsets to consider. The upper bound and step size can then be specified using the new keywords *CAP_X_END* and *CAP_X_STEP*, respectively.
- The evaluation of η-trajectories was implemented in a separate `Python` program.

Chapter IV

Benchmarking the IP-ADC/ISR Method

In this chapter, the IP-ADC/ISR approach to one-electron properties of electron-detached states is studied. In Section IV.2 the basis set dependence of electron-detached state dipole moments is investigated. A systematic benchmark study comparing electron-detachment energies and dipole moments computed using various IP-ADC/ISR schemes with FCI data is presented in Section IV.3.

IV.1. Computational Details

All IP-(U)ADC/ISR calculations presented in this chapter were carried out using Q-Chem 5.2 or a development version based on this version.[75] In the computation of electron-detached state dipole moments, second- and higher-order contributions to the N-electron ground state dipole moment were included scaled with the $1h$-character of the respective states according to the original definition in Ref. [74]. Dipole moments of charged states are given with respect to the center of mass.

For the results of the FCI benchmark study presented in Section IV.3, two schemes differing in the treatment of constant diagrams were employed in the case of IP-(U)ADC(3): (i) a scheme with iterative fourth-order treatment of the static self-energy according to the so-called $\Sigma(4+)$ procedure,[74] also referred to as "standard" IP-ADC(3) scheme (in

Parts of this chapter have already been published in

- A. L. Dempwolff, A. C. Paul, A. M. Belogolova, A. B. Trofimov, A. Dreuw, "Intermediate State Representation Approach to Physical Properties of Molecular Electron-Detached States: I. Theory and Implementation", *J. Chem. Phys.* **2020**, *152*, 024113.
- A. L. Dempwolff, A. C. Paul, A. M. Belogolova, A. B. Trofimov, A. Dreuw, "Intermediate State Representation Approach to Physical Properties of Molecular Electron-Detached States: II. Benchmarking", *J. Chem. Phys.* **2020**, *152*, 024125.

subsequent tables denoted as "3(4+)"), and (ii) a scheme with strict third-order treatment of constant diagrams, also referred to as "strict" IP-ADC(3) scheme (in subsequent tables denoted as "3(3)"). In addition, also the results of the strict IP-ADC(2) scheme (in subsequent tables denoted as "2") are shown. The results shown in Section IV.2 were computed using the standard IP-(U)ADC(3)/ISR(2) scheme employing the improved fourth-order static self-energy.

The FCI and CISDTQ results were provided by Prof. Alexander Trofimov. The FCI calculations for the initial and electron-detached states were performed using the determinant configuration interaction (CI) method[171, 172] as implemented in the GAMESS-US program.[173, 174] For CO, HCN and NO_2^- as well as $HCN^{\bullet-}$ and $NO_2^{\bullet}$, FCI calculations were not computationally feasible, and the truncated CI method accounting for singly-, doubly-, triply- and quadruply-excited determinants (CISDTQ) was employed instead. The CISDTQ calculations were carried out using the occupation restricted multiple active space (ORMAS) CI[171, 172] code, also available in the GAMESS-US program. In all FCI and CISDTQ calculations $1s$ orbitals of second-row atoms were kept frozen.

IV.1.1. Geometrical Parameters

The geometrical parameters used for the open-shell molecules $NH_2^{\bullet}$, $OH^{\bullet}$, $CN^{\bullet}$ and $NO_2^{\bullet}$ and the corresponding closed-shell anions NH_2^-, OH^-, CN^- and NO_2^- were: R_{NH} = 1.0245 Å, $\angle_{HNH}$ = 103.34°;[175] R_{OH} = 0.96966 Å;[176] R_{CN} = 1.1718 Å;[176] R_{NO} = 1.1934 Å, $\angle_{NON}$ = 134.1°.[177]

For the closed-shell molecules CO, LiH, NH_3, H_2O, HF and HCN as well as the corresponding radical anions $LiH^{\bullet-}$, $NH_3^{\bullet-}$, $H_2O^{\bullet-}$, $HF^{\bullet-}$ and $HCN^{\bullet-}$ the following geometrical parameters were used: R_{CO} = 2.132 r_{Bohr};[176] R_{LiH} = 1.5957 Å;[176] R_{NH} = 1.0124 Å, $\angle_{HNH}$ = 106.67°;[177] R_{OH} = 0.957 Å, $\angle_{HOH}$ = 104.5°;[178] R_{HF} = 0.917 Å;[176] R_{HC} = 1.064 Å, R_{CN} = 1.156 Å.[177]

IV.1.2. Basis Sets

In all calculations presented in this chapter, the Cartesian representation of d-functions was used.

For the basis set dependence study presented in Section IV.2, basis sets of improving quality ranging from cc-pVDZ to cc-pVQZ[179] and aug-cc-pVDZ to aug-cc-pVQZ[180] were employed.

The basis sets used in the FCI and IP-(U)ADC/ISR calculations presented in Section IV.3 are listed in the following:

- For H_2O, NH_3 and HF and their corresponding radical anions $H_2O^{\bullet-}$, $NH_3^{\bullet-}$ and $HF^{\bullet-}$, the 6-31++G* basis set[181–184] was employed.
- For CN^- and NO_2^- as well as $NO_2^\bullet$, the smaller 6-31+G and 6-31G basis sets[181–184] were used, respectively.
- The correlation-consistent polarized-valence basis set cc-pVDZ[179] was used for CO, HCN and OH^- and the radical anion $HCN^{\bullet-}$.
- In the case of LiH and $LiH^{\bullet-}$, calculations were performed using the aug-cc-pVDZ basis set[179, 180, 185] where for Li an earlier parametrization of polarization and diffuse functions as available through the basis set exchange database[186, 187] was employed (i.e., 0.00864 (s), 0.00579 (p), 0.1239 (d), 0.0725 (d)).
- Finally, the calculations of NH_2^- and $NH_2^\bullet$ were performed using a modified aug-cc-pVDZ basis set[179, 180] without polarization diffuse functions on N and H atoms.

IV.2. Basis Set Dependence of Dipole Moments

As a first test of the IP-(U)ADC/ISR method, the ground state dipole moments of several neutral closed- and open-shell molecules have been computed. To this end, electron detachment from the corresponding anions was considered. In the same way, electron affinities (EA) of the neutral systems are accessible as electron-detachment energies of the anionic systems. The basis set dependence of the respective quantities is studied by considering a number of systematically improving basis sets.

IV.2.1. Closed-Shell Initial State

The IP-ADC/ISR approach can be useful in studies of neutral radicals ($N^\bullet$) in their ground and excited states. Such states can be accessed by applying the IP-ADC/ISR to the corresponding closed-shell negative ions (A^-) according to the scheme

$$A^- - e^- \rightarrow N^\bullet.$$

In this section this option is explored on the example of the $NH_2^\bullet$, $OH^\bullet$, $CN^\bullet$, and $NO_2^\bullet$ radicals, for which experimental electron affinities (EA) and dipole moments are available.[176, 188–193] In Table IV.1 the results of standard IP-ADC(3)/ISR(2) calculations for the corresponding anions are presented.

Table IV.1. Vertical electron affinities (EA, eV) and absolute ground state dipole moments (μ_0, D) of $NH_2^\bullet$, $OH^\bullet$, $CN^\bullet$, and $NO_2^\bullet$ computed using the closed-shell IP-ADC(3)/ISR(2) method setting out from the corresponding anions.[a] The results for systematically improving basis sets in the range cc-pVDZ to cc-pVQZ and aug-cc-pVDZ to aug-cc-pVQZ are shown in comparison with experimental data.

Basis set	$NH_2^\bullet$ ($^2B_1$)		$OH^\bullet$ ($^2\Pi$)		$CN^\bullet$ ($^2\Sigma^+$)		$NO_2^\bullet$ ($^2A_1$)	
	EA	μ_0	EA	μ_0	EA	μ_0	EA	μ_0
cc-pVDZ	−1.17	1.58	−0.42	1.48	2.90	1.40	−0.08	0.42
cc-pVTZ	−0.06	1.61	0.95	1.47	3.68	1.55	0.88	0.41
cc-pVQZ	0.40	1.61	1.56	1.46	3.93	1.62	1.27	0.43
aug-cc-pVDZ	0.71	1.62	2.05	1.43	3.87	1.65	1.38	0.48
aug-cc-pVTZ	0.84	1.59	2.16	1.41	4.02	1.64	1.54	0.48
aug-cc-pVQZ	0.88	1.60	2.21	1.42	4.07	1.66	1.61	0.48
Expt.[b]	0.77[d]	1.82[f]	1.83[d]	1.66[h]	3.86[d]	1.45[i]	2.27[d]	0.32[j]
Expt.[c]	0.78[e]		1.82[g]		3.82[g]			

[a] The theoretical EAs were obtained as the vertical ionization energies of the closed-shell anions at the equilibrium geometries of the neutral radicals.
[b] Experimental adiabatic EAs of the neutral radicals.
[c] Experimental EAs estimated as ionization energies of the corresponding negative ions.
[d] Ref. [188]
[e] Ref. [189]
[f] Ref. [190]
[g] Ref. [176]
[h] Ref. [191]
[i] Ref. [192]
[j] Ref. [193]

As can be seen, the computed ground state dipole moments (μ_0) show a good agreement with experimental data which does not depend very much on the basis set employed. Even at the cc-pVDZ level, the IP-ADC/ISR values are quite satisfactory, and nearly no improvement upon extension of the basis set or its augmentation by diffuse functions can be observed. The results obtained using the most extended aug-cc-pVQZ basis set are within 12–14% off the experimental values for $NH_2^\bullet$, $OH^\bullet$ and $CN^\bullet$. For $NO_2^\bullet$, however, the relative error of about 50% may not be an appropriate characteristic in view of the small experimental value of 0.32 D.[193] The absolute deviation of the computed value (0.48 D) in this case is only 0.16 D.

The weak basis set dependence of μ_0 can be explained by the fact that it refers to the ground state of the neutral radical which is reasonably well described already at cc-pVDZ level.

By contrast, EAs are strongly underestimated when non-augmented basis sets are used, while addition of diffuse basis functions dramatically improves the results. This observation can easily be attributed to the diffuse nature of the involved anionic ground states which can not be captured by standard basis sets. Hence, diffuse basis functions have

Table IV.2. Vertical electron affinities (EA, eV) and absolute ground state dipole moments (μ_0, D) of LiH, NH_3, H_2O, HF, and HCN computed using the open-shell IP-UADC(3)/ISR(2) method setting out from the corresponding radical anions.[a] The results for systematically improving basis sets in the range cc-pVDZ to cc-pVQZ and aug-cc-pVDZ to aug-cc-pVQZ are shown in comparison with experimental data.

Basis set	LiH ($^1\Sigma^+$)		NH_3 (^{1}A)		H_2O ($^1A_1$)		HF ($^1\Sigma^+$)		HCN ($^1\Sigma^+$)	
	EA	μ_0	EA	μ_0	EA	μ_0	EA	μ_0	EA	μ_0
cc-pVDZ	0.05	5.75	−4.45	1.60	−4.52	1.93	−4.67	1.83	−4.36	3.11
cc-pVTZ	0.14	5.85	−3.03	1.58	−3.10	1.93	−3.25	1.85	−3.20	3.23
cc-pVQZ	0.23	5.88	−2.36	1.56	−2.39	1.91	−2.52	1.85	−2.57	3.23
aug-cc-pVDZ	0.29	5.97	−0.79	1.55	−0.78	1.89	−0.84	1.83	−0.70	3.10
aug-cc-pVTZ	0.28	5.91	−0.64	1.56	−0.65	1.89	−0.69	1.84	−0.53	3.11
aug-cc-pVQZ	0.29	5.91	−0.57	1.57	−0.57	1.90	−0.60	1.85	−0.44	3.12
Expt.	0.34[b]	5.88[c]		1.47[d]		1.85[e]		1.82[f]		2.98[g]

[a] The theoretical EAs were obtained as the vertical ionization energies of the open-shell radical anions at the equilibrium geometries of the neutral molecules.
[b] Ref. [188].
[c] Ref. [194].
[d] Ref. [195].
[e] Ref. [176].
[f] Ref. [196].
[g] Ref. [197].

to be included for a reasonable description, leading to considerable stabilization of the anionic ground states and thus to larger electron detachment energies. The same trend, albeit less pronounced, has also been found for ionization energies of neutral molecules.[76]

The EA values computed at the IP-ADC(3)/aug-cc-pVQZ level are in good agreement with experimental data, demonstrating an error of about 0.1–0.4 eV for $NH_2^\bullet$, $OH^\bullet$, and $CN^\bullet$. In the case of $NO_2^\bullet$, a larger deviation from experimental data of 0.66 eV is obtained. Here it has however to be noted that the theoretical vertical EA value is compared with the experimental value from Ref. [188], which refers to adiabatic EA. The present deviation from experiment might therefore reflect the large difference between the adiabatic and vertical EA values for $NO_2^\bullet$.

IV.2.2. Open-Shell Initial State

In the case of radical anions $A^{\bullet-}$, the energetically lowest electron-detached states are the electronic ground states of the corresponding neutral closed-shell molecules (N) according to the scheme

$$A^{\bullet-} - e^- \rightarrow N.$$

Since the ground state dipole moments of neutral molecules are well known, these are convenient test systems for the capabilities of the new open-shell methodology. In this first

test, the LiH, NH_3, H_2O, HF, and HCN molecules are considered. Among these systems, however, experimental EA data is only available for LiH[188] since only for this system a stable anionic ground state exists. In Table IV.2, results obtained using the standard IP-UADC(3)/ISR(2) scheme are presented.

As for the neutral radicals the ground state dipole moments μ_0 demonstrate only a rather weak basis set dependence. A larger change in the calculated values can be seen when going from cc-pVDZ to cc-pVTZ and from non-augmented to augmented basis sets, which is especially pronounced in the case of LiH and HCN. Beyond the level of the aug-cc-pVTZ basis set the dipole moments seem to be consistently well converged for all molecules. The IP-UADC(3)/aug-cc-pVQZ results are in excellent agreement with experimental values, the mean error being only $\sim$3%.

The electron affinities, as for the neutral radicals, demonstrate a much stronger basis set dependence. A regular convergence pattern can be seen only within the augmented series of basis sets, providing a better description of the unoccupied orbitals crucial for binding of the excess electron. The EA of LiH calculated at the IP-UADC(3)/aug-cc-pVQZ level (0.29 eV) is in very good agreement with the experimental value of 0.34 eV.[188]

IV.3. Benchmarking Against Full Configuration Interaction

The accuracy of IP-(U)ADC(3) electron detachment energies has previously been investigated in various methodological and applied studies[74, 76, 77, 198] and by comparison to the even better studied Dyson-ADC(3) scheme.[21, 71–73] However, its accuracy has not been calibrated against full configuration interaction (FCI) results so far.

In this section, the performance of the IP-(U)ADC(3)/ISR(2) scheme for the computation of electron detachment energies and electron-detached state dipole moments with respect to FCI is evaluated. In this systematic test various electronic states of closed- and open-shell systems are considered. As closed-shell examples, LiH, NH_3, H_2O, HF, CO and HCN as well as NH_2^-, OH^-, CN^- and NO_2^- were chosen (Section IV.3.1). In Section IV.3.2, the open-shell methodology is applied to $NH_2^\bullet$ and $NO_2^\bullet$ as well as to $LiH^{\bullet-}$, $NH_3^{\bullet-}$, $H_2O^{\bullet-}$, $HF^{\bullet-}$ and $HCN^{\bullet-}$. In addition, the IP-UADC(3)/ISR(2) method is employed for the treatment of triplet-excited reference states of LiH, NH_3 and H_2O, demonstrating how a different set of electron-detached states than accessible by means of electron detachment from closed-shell references can be obtained.

Table IV.3. Comparison between FCI and IP-ADC/ISR results for vertical ionization energies of LiH, NH_3, H_2O, HF, CO, and HCN (IP, eV) and dipole moments of electron-detached states (μ_n^{N-1}, D).[a] The IP-ADC(n)/ISR(m) schemes are denoted by the short-hand notations n/m. For the IP-ADC(3) schemes the order of the constant diagrams treatment is shown in parentheses (see text for details). The last lines give the mean error ($\bar{\Delta}$) and its standard deviation ($\sigma(\Delta)$) as well as the mean absolute error ($\overline{|\Delta|}$) and maximum absolute error ($|\Delta|_{\max}$) relative to FCI (in eV for IPs and in percent for μ_n^{N-1}). The relative photoelectron intensity (or pole strength, P) is also shown.

Initial molecule and final state[e]		IP				μ_n^{N-1}				P
		FCI	3(4+)/2[b]	3(3)/2	2/2	FCI	3(4+)/2[b]	3(3)/2	2/2	3(4+)/2[b]
LiH	$^1\Sigma^+$									
$1\,^2\Sigma^+$	$2\sigma^{-1}$	7.94	7.77	7.81	7.93	−0.49	−0.50	−0.49	−0.38	0.891
$1\,^2\Pi$	$2\sigma^{-2}\pi$	19.71	18.81	18.81		3.27	3.28	3.28		0.003
$2\,^2\Sigma^+$	$2\sigma^{-2}\sigma$	19.88	19.02	19.02		7.40	7.40	7.40		0.049
NH_3[c]	$^1A_1$									
$1\,^2A$	$3a^{-1}$	10.46	10.61	10.57	9.80	1.41	1.34	1.34	1.42	0.924
$1\,^2E$	$1e^{-1}$	16.40	16.53	16.50	15.79	2.54	2.50	2.51	2.63	0.931
$2\,^2A$	$3a^{-2}a$	23.54	26.22	26.22		0.47	1.12	1.11		0.023
$2\,^2E$	$3a^{-2}e$	25.49	27.08	27.08		2.44	1.94	1.94		0.001
H_2O	$^1A_1$									
$1\,^2B_1$	$1b_1^{-1}$	12.30	12.56	12.72	11.07	−2.55	−2.44	−2.44	−2.57	0.928
$1\,^2A_1$	$3a_1^{-1}$	14.63	14.89	15.04	13.43	−2.12	−2.04	−2.03	−2.09	0.929
$1\,^2B_2$	$1b_2^{-1}$	18.97	19.15	19.30	17.99	−3.09	−3.05	−3.05	−3.15	0.937
$2\,^2B_1$	$3a_1^{-1}1b_1^{-1}a_1$	26.88	31.17	31.17		0.55	0.96	0.96		< 0.001
$2\,^2A_1$	$1b_1^{-2}a_1$	26.99	30.50	30.52		0.15	0.66	0.69		0.078
HF	$^1\Sigma^+$									
$1\,^2\Pi$	$1\pi^{-1}$	15.93	16.28	16.68	14.24	2.35	2.24	2.21	2.33	0.935
$1\,^2\Sigma^+$	$3\sigma^{-1}$	19.98	20.23	20.58	18.58	2.44	2.41	2.40	2.37	0.940
$1\,^2\Sigma^-$	$1\pi^{-2}\sigma$	32.25	37.72	37.72		−1.92	−2.42	−2.42		< 0.001
$1\,^2\Delta$	$1\pi^{-2}\sigma$	34.50	38.88	38.88		−1.77	−2.20	−2.20		< 0.001
CO	$^1\Sigma^+$									
$1\,^2\Sigma^+$	$5\sigma^{-1}$	13.56	13.67	13.38	13.72	2.60	2.88	2.67	2.21	0.903
$1\,^2\Pi$	$1\pi^{-1}$	16.68	16.68	16.88	16.20	0.27	0.08	−0.19	−0.07	0.911
$2\,^2\Sigma^+$	$4\sigma^{-1}$	19.39	19.90	20.23	18.21	−0.74	−1.22	−1.41	−1.14	0.800
$2\,^2\Pi$	$5\sigma^{-2}\pi$	22.96	22.88	22.88		2.27	2.60	2.60		0.004
$1\,^2\Sigma^-$	$1\pi^{-1}5\sigma^{-1}\pi$	23.16	21.70	21.70		2.08	2.01	2.01		< 0.001
HCN	$^1\Sigma^+$									
$1\,^2\Pi$	$1\pi^{-1}$	13.45	13.41	13.26	13.46	−3.38	−3.35	−3.31	−3.48	0.922
$1\,^2\Sigma^+$	$5\sigma^{-1}$	13.59	14.01	13.90	12.69	−1.67	−1.00	−0.97	−1.48	0.888
$2\,^2\Sigma^+$	$4\sigma^{-1}$	20.14	20.35	20.22	20.08	−5.87	−6.22	−6.20	−6.07	0.849
$2\,^2\Pi$	$1\pi^{-2}\pi$	21.35	19.97	19.97		−2.72	−2.17	−2.17		0.002
$\bar{\Delta}$[d]			0.19	0.26	−0.73		−4	−10	−8	
$\sigma(\Delta)$[d]			0.18	0.33	0.59		29	54	38	
$\overline{\lvert\Delta\rvert}$[d]			0.22	0.33	0.76		15	24	18	
$\lvert\Delta\rvert_{\max}$[d]			0.51	0.84	1.69		70	170	126	

[a] For CO and HCN results of CISDTQ calculations are shown.

[b] Iterative fourth-order treatment of constant diagrams according to the so-called $\Sigma(4+)$ procedure,[74] also referred to as "standard" IP-ADC(3) scheme.

[c] The modulus of the dipole moment is shown because of degenerate ^{2}E states.

[d] Only transitions with dominant $1h$-character are taken into account.

[e] Final-state $(N-1)$-electron configuration relative to the RHF reference.

Table IV.4. Comparison between FCI and IP-ADC/ISR results for vertical electron detachment energies of NH_2^-, OH^-, CN^-, and NO_2^- (IP, eV) and dipole moments of electron-detached states (μ_n^{N-1}, D).[a] The IP-ADC(n)/ISR(m) schemes are denoted by the short-hand notations n/m. For the IP-ADC(3) schemes the order of the constant diagrams treatment is shown in parentheses (see text for details). The last lines give the mean error ($\bar{\Delta}$) and its standard deviation ($\sigma(\Delta)$) as well as the mean absolute error ($\overline{|\Delta|}$) and maximum absolute error ($|\Delta|_{\max}$) relative to FCI (in eV for IPs and in percent for μ_n^{N-1}). The relative photoelectron intensity (or pole strength, P) is also shown.

Initial anion and final state[d]		IP				μ_n^{N-1}				P
		FCI	3(4+)/2[b]	3(3)/2	2/2	FCI	3(4+)/2[b]	3(3)/2	2/2	3(4+)/2[b]
NH_2^-	$^1A_1$									
$1\,^2B_1$	$1b_1^{-1}$	0.31	0.54	0.70	−0.70	2.00	1.90	1.88	2.06	0.897
$1\,^2A_1$	$3a_1^{-1}$	2.49	2.93	3.09	1.23	1.34	1.26	1.25	1.31	0.898
$1\,^2B_2$	$1b_2^{-1}$	7.02	7.43	7.63	5.87	2.76	2.76	2.74	2.96	0.900
$2\,^2A_1$	$1b_1^{-2}a_1$	7.84	10.25	10.26		−1.67	−2.44	−2.45		0.005
$2\,^2B_1$	$3a_1^{-1}1b_1^{-1}a_1$	7.84	11.63	11.63		−2.04	−0.40	−0.41		0.011
OH^-	$^1\Sigma^+$									
$1\,^2\Pi$	$1\pi^{-1}$	−0.62	−0.42	−0.47	−1.43	1.80	1.48	1.50	1.66	0.935
$1\,^2\Sigma^+$	$3\sigma^{-1}$	3.74	3.82	3.80	3.16	1.68	1.75	1.75	1.75	0.943
$1\,^2\Sigma^-$	$1\pi^{-2}\sigma$	8.00	11.96	11.96		−2.80	−3.55	−3.55		< 0.001
$1\,^2\Delta$	$1\pi^{-2}\sigma$	9.68	12.79	12.79		−2.73	−3.36	−3.36		< 0.001
CN^-	$^1\Sigma^+$									
$1\,^2\Sigma^+$	$5\sigma^{-1}$	3.26	3.52	3.22	2.84	−1.56	−1.89	−1.83	−0.55	0.890
$1\,^2\Pi$	$1\pi^{-1}$	5.11	5.21	5.02	4.78	0.10	0.17	0.36	0.33	0.902
$2\,^2\Sigma^+$	$4\sigma^{-1}$	6.46	7.02	7.01	5.57	1.31	2.02	2.33	0.99	0.828
$2\,^2\Pi$	$5\sigma^{-2}\pi$	11.11	11.82	11.82		−0.42	−0.76	−0.76		0.001
$1\,^2\Delta$	$1\pi^{-1}5\sigma^{-1}\pi$	12.44	11.90	11.90		−1.20	−2.61	−2.61		< 0.001
NO_2^-	$^1A_1$									
$1\,^2A_1$	$6a_1^{-1}$	−0.17	0.17	−0.08	−0.75	0.23	0.36	0.35	−0.04	0.929
$1\,^2B_1$	$6a_1^{-2}b_1$	2.66	2.87	2.87		0.35	0.65	0.65		0.001
$1\,^2B_2$	$4b_2^{-1}$	3.32	3.93	3.91	2.30	−0.64	−0.68	−0.76	−0.68	0.841
$1\,^2A_2$	$1a_2^{-1}$	3.58	3.61	3.61	3.16	−0.87	−0.88	−0.97	−1.02	0.911
$2\,^2B_2$	$1a_2^{-1}6a_1^{-1}b_1$	5.80	5.30	5.30		−0.25	0.04	0.04		0.066
$\bar{\Delta}$[c]			0.30	0.27	−0.77		17	37	5	
$\sigma(\Delta)$[c]			0.19	0.28	0.32		30	79	85	
$\overline{\lvert\Delta\rvert}$[c]			0.30	0.29	0.77		22	43	44	
$\lvert\Delta\rvert_{\max}$[c]			0.61	0.61	1.26		70	260	230	

[a] For NO_2^- results of CISDTQ calculations are shown.
[b] Iterative fourth-order treatment of constant diagrams according to the so-called $\Sigma(4+)$ procedure,[74] also referred to as "standard" IP-ADC(3) scheme.
[c] Only transitions with dominant $1h$-character are taken into account.
[d] Final-state $(N-1)$-electron configuration relative to the RHF reference.

IV.3.1. Closed-Shell Initial State

The FCI and IP-ADC/ISR results for ionization energies and dipole moments of the energetically lowest electron-detached states in the series of closed-shell neutrals (LiH, NH_3, H_2O, HF, CO, and HCN) and anions (NH_2^-, OH^-, CN^-, and NO_2^-) are listed in Tables IV.3 and IV.4, respectively. $1h$-type ionization transitions corresponding to ionization of

outer-valence orbitals are shown, followed by one or two lowest photoelectron satellites associated with doublet ($S = 1/2$) ionization transitions of $2h$-$1p$-type.

Ionization Energies

In agreement with previous findings, the mean error of the different IP-ADC(3) variants computed for the set of 25 $1h$-type ionization transitions in neutral molecules and anions is 0.2–0.3 eV, with a maximum error of 0.6–0.8 eV. The scheme with iterative fourth-order treatment of the static self-energy appears to be overall slightly more accurate than the strict third order scheme (the mean signed error and its standard deviation $\bar{\Delta} \pm \sigma(\Delta)$ is 0.24 ± 0.19 and 0.26 ± 0.30 eV, respectively) and more reliable (the maximum absolute error $|\Delta|_{\max}$ is 0.61 and 0.84 eV, respectively). In addition, IP-ADC(3) performs equally well for neutral and anionic closed-shell systems.

The second-order IP-ADC scheme exhibits much larger overall $\bar{\Delta}$ and $|\Delta|_{\max}$ values of -0.75 ± 0.48 and 1.69 eV, respectively. Hence it is not sufficient if quantitative results are desired. Moreover, since IP-ADC(2) treats $2h$-$1p$-states only through zeroth order, it cannot be expected to yield even a qualitatively correct representation of the ionization spectrum beyond the outer-valence energy domain.

In IP-ADC(3), $2h$-$1p$-states are treated through first order, providing a level of accuracy characterized by $\overline{|\Delta|}$ and $|\Delta|_{\max}$ values of 2.2 and 5.5 eV, respectively, as computed from the set of 19 transitions of $2h$-$1p$-type in the neutral molecules and anions presented in Tables IV.3 and IV.4. Although such a level of accuracy is insufficient for an accurate description of photoelectron satellites, it allows the principle features of the physical situation concerning main lines and satellites to be reproduced, which is crucial for studies of photoelectron spectra beyond the outer-valence energy regime in which the one-electron picture of ionization is known to break down.[1] Interestingly, the overall performance of IP-ADC(3) with respect to $2h$-$1p$-ionization energies is better for anions than for neutral molecules. The standard IP-ADC(3) scheme exhibits a mean absolute error for anions and neutrals of $\overline{|\Delta|} = 1.90$ eV and $\overline{|\Delta|} = 2.42$ eV and a maximum absolute error of $|\Delta|_{\max} = 3.96$ eV and $|\Delta|_{\max} = 5.47$ eV, respectively.

Dipole Moments

The dipole moments of $1h$-states in neutral molecules (Table IV.3) computed at the IP-ADC(3)/ISR(2) level of theory are in excellent agreement with FCI data. For this set of states, IP-ADC(2)/ISR(2) is only slightly less accurate. The situation however is different for CO and HCN with a more complex electronic structure. The agreement with FCI

becomes less uniform, and differences between various IP-ADC/ISR schemes get more pronounced.

From a theoretical perspective, both IP-ADC(3)/ISR(2) and IP-ADC(2)/ISR(2) formally provide the same second-order treatment of dipole moments of $1h$-states. However, in the context of electron number-preserving electronic excitations it has been observed that third-order contributions introduced by IP-ADC(3) eigenvectors generally improve the results.[199] This is also observed here, especially for anions as well as neutral CO and HCN (Tables IV.3 and IV.4). Whereas the mean absolute error in neutral molecules is 15–25 %, it increases up to 25–50 % in the case of anions. The overall accuracy decreases in the order of standard IP-ADC(3)/ISR(2) > IP-ADC(2)/ISR(2) > strict IP-ADC(3)/ISR(2), with mean absolute errors $\overline{|\Delta|}$ of 18, 29, and 32 % and maximum errors $|\Delta|_{\max}$ of 70, 230, and 260 %, respectively. This somewhat unexpected trend indicates that the ground state contribution to the evaluated property matters in a significant way. It should, however, also be noted that the large maximum absolute errors found for the strict IP-ADC(3)/ISR(2) and IP-ADC(2)/ISR(2) schemes arise in cases of ionized states with small absolute dipole moments, i.e., for the $1\,^2\Pi$ states of $CO^{\bullet+}$ and $CN^{\bullet}$.

The above trend in accuracy is in line with the observation from ionization energy calculations, i.e, the results improve when constant diagrams in the IP-ADC(3) scheme are treated beyond third order.

The accuracy of IP-ADC(3)/ISR(2) with respect to the dipole moments of primarily $2h$-$1p$-states is not very high, since these are treated only through first order. For such states, the mean absolute error $\overline{|\Delta|}$ is 60 and 72 % in the case of neutral molecules and anions, respectively. The overall $\overline{|\Delta|}$ and $|\Delta|_{\max}$ errors of the whole set of 19 $2h$-$1p$-states shown in Tables IV.3 and IV.4 is ∼65 and ∼340 %, respectively. The above estimates obviously refer only to the IP-ADC(3)-based schemes and are the virtually same for all variants of these schemes, since all such schemes treat the $2h$-$1p$-states only through first order.

IV.3.2. Open-Shell Initial State

In this section the performance of the IP-UADC/ISR schemes for open-shell systems is studied systematically. For a better coverage of situations met in practice, several types of open-shell initial states are considered: (i) neutral radicals with doublet ground state, (ii) triplet ground states of neutral molecules and (iii) radical anions with doublet ground state. All these types of open-shell states can be represented by a single-determinant UHF reference (if the ground state is not degenerate for point-group symmetry reasons), and

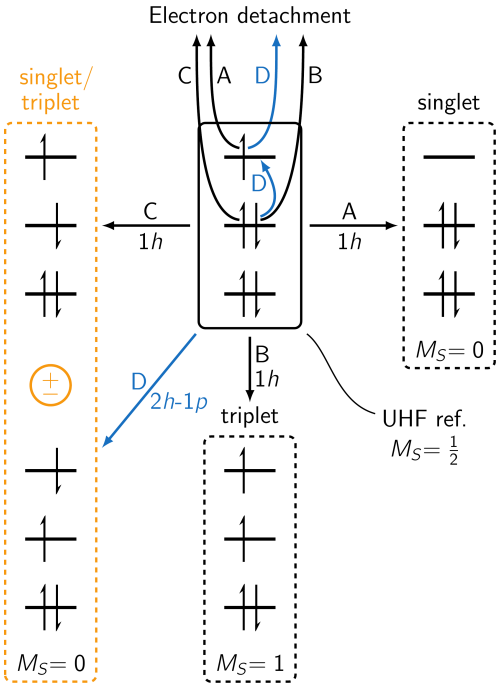

Figure IV.1. Schematic overview of different final electronic configurations accessible by $1h$-type electron detachment from an open-shell doublet UHF reference state. For the $M_S = 0$ open-shell singlet and triplet states, linear combination with $2h$-$1p$-configurations is required to form correct $\hat{S}^2$ eigenfunctions.

thus can be treated using the present implementation of the IP-UADC/ISR method.

State Assignment for Electron-Detachment from Open-Shell Reference States

In the case of doublet UHF references (Tables IV.5 and IV.8) with one "unpaired" electron in the singly occupied molecular orbital (SOMO), special care has to be taken when classifying the resulting IP-UADC states with respect to spin multiplicity. In principle, such an assignment is only possible if the reference state exhibits a correct $\hat{S}^2$ eigenvalue of 0.75 and if all occupied orbitals except the SOMO can be grouped in pairs with similar spatial part. For the following discussion, a $M_S = 1/2$ UHF reference with α-SOMO is assumed. An overview of the character of possible electron-detached states is given in Figure IV.1.

Final states resulting from β-detachment can easily be identified as $M_S = 1$ triplet components (case B in Figure IV.1). For α-detachment processes, leading to states characterized by $M_S = 0$, the situation is more involved. Apart from the trivial case of detachment from SOMO which yields a closed-shell singlet state (case A in Figure IV.1), $\hat{S}^2$ eigenfunctions cannot result from pure $1h$-processes since the opposite-spin configurations

required for the construction of such states are missing at first glance. However, they are in fact present in the configurational space, being generated by appropriate $2h$-$1p$-excitation operators (case C and D in Figure IV.1).

Consequently, the IP-UADC description of such states is formally unbalanced, since $1h$- and $2h$-$1p$-configurations are treated in different orders of perturbation theory (PT), and the corresponding state energies are correct only through the lowest PT order involved. Especially for IP-UADC(2), in which $2h$-$1p$-configurations are treated in zeroth order, reliable results can not be expected, and such states are thus not considered in this context.

In the case of IP-UADC(3) the respective energies are correct through first order, and one can usually identify singlet/triplet state pairs. In such cases, the state with lower energy is assigned as the $M_S = 0$ triplet component. The quality of this approximation may be judged by comparing the energy of the latter state to that of the respective $M_S = 1$ triplet component formed by β-detachment (case B in Figure IV.1). Since in this case only $1h$-transitions are involved, the energy is correct through third order. For this reason, the values stated in Tables IV.5 and IV.8 refer to computed $M_S = 1$ triplet components. As numerical example, the respective values computed for the lowest triplet ionized state of $NH_2^\bullet$ may be considered ($1\,^3B_1$, Table IV.5). Using the standard IP-UADC(3) scheme, state energies of 11.75 and 11.94 eV were computed for the $M_S = 1$ and $M_S = 0$ component, respectively. However, larger deviations can be observed for other states or systems.

For IP-UADC calculations based on $M_S = 1$ triplet UHF reference states (Tables IV.6 and IV.7), the possible final states resulting from α- and β-detachment are characterized by $M_S = 1/2$ and $M_S = 3/2$, respectively, the latter clearly being quartet states. For α-detachment, similar considerations as in the case of doublet UHF references have to be made, since here doublet or quartet final states may be formed. All $M_S = 1/2$ states considered in Table IV.6 can, however, be characterized by leading configurations with only one unpaired electron, and can thus be safely assigned as doublets.

Neutral Radicals with Doublet Ground States

Stable neutral radicals with spatially non-degenerate doublet ground states form a large class of chemically relevant molecules with well-established spectroscopy.[200] Among the systems considered in the present work, only $NH_2^\bullet$ ($^2B_1$) and $NO_2^\bullet$ ($^2A_1$) can be treated using the UHF approach, yielding reference states with S^2 values of 0.76 and 0.77, respectively (Table IV.5). The OH radical drops out for its spatially-degenerate $^2\Pi$ ground state, and in the case of $CN^\bullet$ ($^2\Sigma^+$) UHF calculations yield a strongly spin-contaminated ground-state solution (characterized by an S^2 value of 1.26), which leads at the IP-UADC(3) level

Table IV.5. Comparison between FCI and IP-UADC/ISR results for vertical ionization energies of $NH_2^\bullet$ and $NO_2^\bullet$ (IP, eV) and dipole moments of electron-detached states (μ_n^{N-1}, D).[a,b] The IP-UADC(n)/ISR(m) schemes are denoted by the short-hand notations n/m. For the IP-UADC(3) schemes the order of the constant diagrams treatment is shown in parentheses (see text for details). The last lines give the mean error ($\bar{\Delta}$) and its standard deviation ($\sigma(\Delta)$) as well as the mean absolute error ($\overline{|\Delta|}$) and maximum absolute error ($|\Delta|_{\max}$) relative to FCI (in eV for IPs and in percent for μ_n^{N-1}). The relative photoelectron intensity (or pole strength, P) is also shown.

Neutral radical and final state[d]		IP				μ_n^{N-1}				P
		FCI	3(4+)/2[c]	3(3)/2	2/2	FCI	3(4+)/2[c]	3(3)/2	2/2	3(4+)/2[c]
$NH_2^\bullet$	$^2B_1$									
$1\,^3B_1$	$3a_1^{-1}$	11.68	11.75	11.75	11.06	1.53	1.47	1.47	1.51	0.924
$1\,^1A_1$	$1b_1^{-1}$	12.20	12.27	12.34	11.83	2.22	2.12	2.14	2.32	0.893
$1\,^1B_1$	$3a_1^{-1}$	13.96	14.22	14.23		1.78	1.49	1.50		0.383
$NO_2^{\bullet}$[b]	$^2A_1$									
$1\,^1A_1$	$6a_1^{-1}$	10.84	11.28	10.78	9.81	0.34	0.50	0.37	−0.03	0.906
$1\,^3B_2$	$4b_2^{-1}$	13.19	12.64	12.56	11.96	0.10	0.10	−0.21	−0.06	0.918
$1\,^1B_2$	$4b_2^{-1}$	14.72	14.71	14.68		0.64	0.60	0.43		0.583
$\bar{\Delta}$[e]			0.01	−0.12	−0.81		10	−77	−66	
$\sigma(\Delta)$[e]			0.41	0.45	0.39		25	155	81	
$\overline{\lvert\Delta\rvert}$[e]			0.28	0.23	0.81		14	82	69	
$\lvert\Delta\rvert_{\max}$[e]			0.55	0.63	1.23		47	310	160	

[a] IP-UADC/ISR calculations based on UHF references.
[b] For $NO_2^\bullet$ results of CISDTQ calculations are shown.
[c] Iterative fourth-order treatment of constant diagrams, according to the so-called $\Sigma(4+)$ procedure,[74] also referred to as "standard" IP-UADC(3) scheme.
[d] Final-state $(N-1)$-electron configuration relative to the UHF reference.
[e] Only transitions which can be represented by a single $1h$-configuration are taken into account. See Section IV.3.2 for details.

of theory to a physically incorrect spectrum of electron-detached states.

The results obtained for ionization from the SOMO and the lowest doubly occupied orbital (cf. Figure IV.1) are presented in Table IV.5. Standard and strict IP-UADC(3) exhibit mean absolute errors for vertical ionization energies of 0.28 and 0.23 eV and maximum absolute errors of 0.55 and 0.63 eV, respectively. They are thus in the same range as in the case of closed-shell IP-ADC(3) (cf. Table IV.9). The same accuracy level as in the closed-shell IP-ADC(2) case is also found for IP-UADC(2), the respective error measures in this case being $\overline{|\Delta|} = 0.81$ eV and $|\Delta|_{\max} = 1.23$ eV.

As mentioned above, ionization from doublet ground states can result in singlet and triplet final states. Both types of transitions are allowed by the monopole selection rules for spin ($\Delta S = \pm 1/2$) and can appear in the photoelectron spectra. The corresponding relative photoelectron intensities P predicted by IP-UADC(3) calculations are shown in Table IV.5. As expected, all ionization transitions of $1h$-type are characterized by large P values close to unity, regardless of the spin multiplicity of the final states.

The dipole moments of the electron-detached states computed using the standard IP-

UADC(3)/ISR(2) approach with fourth-order treatment of the static self-energy agree well with FCI results. The observed $\bar{\Delta}$ and $\Delta_{\max}$ values are well below the corresponding error estimates found for the closed-shell systems (Table IV.4). By contrast, the results obtained for the dipole moments using the strict IP-UADC(3)/ISR(2) scheme do not reach this level of accuracy, which indicates that the initial-state electron correlation effects accounted for by the static self-energy terms play an important role in these systems. The results of the strict second-order treatment, IP-UADC(2)/ISR(2), are also less accurate than in the closed-shell case. In particular, for the $NO_2^{\bullet}$ radical, an incorrect orientation of the dipole moment is systematically predicted.

Triplet-Excited States of Neutral Molecules

The lowest triplet-excited state (T_1) of neutral molecules is an interesting case of initial-state open-shell systems which is important, e.g., as model for biradicals and in the context of time-resolved photoelectron spectroscopy (TRPES). Only spatially non-degenerate T_1 states can generally be treated by the single-determinant UHF approach. This is the case for the LiH molecule in the $^3\Sigma^+(2\sigma \rightarrow 3\sigma)$ state, the NH_3 molecule in the $^3A(3a \rightarrow 4a)$ state, and the H_2O molecule in the $^3B_1(1b_1 \rightarrow 4a_1)$ state (Table IV.5). The S^2 values computed for these UHF reference states are 2.00 for LiH and 2.01 for NH_3 and H_2O.

The present test is particularly insightful, since the electron-detached states are the same as in the corresponding closed-shell case (Section IV.3.1, Table IV.3). However, the use of the reference configuration (vacuum state) with two singly occupied MOs yields another set of cationic configurations compared to the case of the closed-shell vacuum. The differences are demonstrated in Table IV.7 where configurations obtained by applying $\hat{C}_{1h}$ and $\hat{C}_{2h\text{-}1p}$ ionization operators to the open-shell vacuum state $|T_1\rangle \equiv |o^2O^1V^1v^0\rangle$ are classified in terms of the familiar $1h$-, $2h$-$1p$- and $3h$-$2p$-nomenclature with respect to the closed-shell vacuum state $|S_0\rangle \equiv |o^2O^2V^0v^0\rangle$ (here O and V denote HOMO and LUMO, respectively, o denotes any occupied MO except HOMO and v denotes any unoccupied MO except LUMO).

As can be seen, $\hat{C}_{1h}$ operators produce $2h$-$1p$-states, unless the electron is detached from the singly-occupied HOMO. The other $1h$-states are produced by suitably chosen $\hat{C}_{2h\text{-}1p}$ operators. Depending on the $\hat{C}_{2p\text{-}1h}$ operator, also $2h$-$1p$- and $3h$-$2p$-states can be obtained. This implies that at the IP-UADC(3) level of theory, in contrast to the closed-shell case, all $1h$-states except HOMO^{-1} are treated only through first order. On the other hand, the $2h$-$1p$-states characterized by the orbital occupation pattern of the types: HOMO^{-1}-LUMO^1 and HOMO^{-2}-LUMO^1 are treated through third order. Remarkably,

also certain types of the $3h$-$2p$-states, for closed-shell singlet references first considered at the IP-(U)ADC(4) level of theory, become accessible and are treated through first order.

The agreement of ionization energies computed using the IP-UADC(3) and IP-UADC(2) schemes based on the triplet-excited UHF reference with FCI results is very convincing (Table IV.6). The errors for transitions with dominant $1h$-character with respect to the triplet vacuum state is smaller than that found in the closed-shell calculations. The good agreement with FCI results extends also to transitions of $2h$-$1p$-type. Interestingly, the error of the IP-UADC(3) schemes for these transitions exhibits nearly the same magnitude as for the transitions of $1h$-type.

Table IV.6. Comparison between FCI and IP-UADC/ISR results for vertical ionization energies of triplet-excited LiH^*, NH_3^*, and H_2O^* molecules (IP, eV) and dipole moments of electron-detached states (μ_n^{N-1}, D).[a,b] The IP-UADC(n)/ISR(m) schemes are denoted by the short-hand notations n/m. For the IP-UADC(3) schemes the order of the constant diagrams treatment is shown in parentheses (see text for details). The last lines give the mean error ($\bar{\Delta}$) and its standard deviation ($\sigma(\Delta)$) as well as the mean absolute error ($\overline{|\Delta|}$) and maximum absolute error ($|\Delta|_{\max}$) relative to FCI (in eV for IPs and in percent for μ_n^{N-1}). The relative photoelectron intensity (or pole strength, P) is also shown.

Initial triplet-excited		IP				μ_n^{N-1}				P
molecule and final state[c]		FCI	3(4+)/2[b]	3(3)/2	2/2	FCI	3(4+)/2[b]	3(3)/2	2/2	3(4+)/2[b]
LiH^*	$^3\Sigma^+$ ($2\sigma \to 3\sigma$)									
	$1\,^2\Sigma^+$ $3\sigma^{-1}$	4.76	4.75	4.75	4.76	−0.49	−0.48	−0.49	−0.56	0.997
	$1\,^2\Pi^f$ $2\sigma^{-1}3\sigma^{-1}\pi$	16.53	16.50	16.50		3.27	3.27	3.27		< 0.001
	$2\,^2\Sigma^{+f}$ $2\sigma^{-1}$	16.69	16.68	16.69	17.03	7.40	7.39	7.41	9.60	0.850
NH_3^*[d]	^{3}A (3a → 4a)									
	$1\,^2$A $4a^{-1}$	4.46	4.43	4.43	4.40	1.41	1.42	1.43	1.46	0.990
	$1\,^2$E $1e^{-1}4a^{-1}3a$	10.40	10.78	10.78		2.54	3.00	3.00		< 0.001
	$2\,^2A^f$ $3a^{-1}$	17.54	17.81	17.94	17.82	0.47	0.78	0.89	0.93	0.832
	$2\,^2E^f$ $3a^{-1}4a^{-1}e$	19.50	20.33	20.34		2.44	2.27	2.28		0.048
H_2O^*	$^3B_1$ ($1b_1 \to 4a_1$)									
	$1\,^2B_1$ $4a_1^{-1}$	5.30	5.27	5.28	5.22	−2.55	−2.55	−2.56	−2.59	0.989
	$1\,^2A_1$ $3a_1^{-1}4a_1^{-1}1b_1$	7.63	7.58	7.58		−2.12	−2.15	−2.15		< 0.001
	$1\,^2B_2$ $1b_2^{-1}4a_1^{-1}1b_1$	11.97	12.17	12.17		−3.09	−3.49	−3.49		< 0.001
	$1\,^4B_1{}^f$ $3a_1^{-1}$	18.68	18.85	19.02	18.49	0.56	0.67	0.78	1.00	0.790
	$2\,^2A_1{}^f$ $1b_1^{-1}$	19.99	20.40	20.61	20.04	0.15	0.40	0.51	0.61	0.810
$\bar{\Delta}$[e]			0.11	0.19	0.05		36	53	76	
$\sigma(\Delta)$[e]			0.18	0.26	0.19		63	89	108	
$\overline{\lvert\Delta\rvert}$[e]			0.13	0.20	0.14		36	53	76	
$\lvert\Delta\rvert_{\max}$[e]			0.41	0.62	0.34		167	240	307	

[a] IP-UADC/ISR calculations performed based on UHF references.

[b] Iterative fourth-order treatment of constant diagrams, according to the so-called Σ(4+) procedure,[74] also referred to as "standard" IP-UADC(3) scheme.

[c] Final-state $(N-1)$-electron configuration relative to the UHF reference.

[d] The modulus of the dipole moment is shown because of degenerate ^{2}E states.

[e] Only transitions with dominant $1h$-character (with respect to the triplet-excited vacuum state) are taken into account.

[f] Transitions having $2h$-$1p$-character with respect to the closed-shell reference state.

Table IV.7. Electron configurations obtained by applying $\hat{C}_{1h}$ and $\hat{C}_{2h\text{-}1p}$ excitation operators to the open-shell reference state $|\mathrm{T}_1\rangle \equiv |o^2O^1V^1v^0\rangle$ and their character with respect to the closed-shell configuration $|\mathrm{S}_0\rangle \equiv |o^2O^2V^0v^0\rangle$. O and V denote HOMO and LUMO, respectively, o denotes any occupied MO except HOMO and v denotes any unoccupied MO except LUMO.

$\hat{C}_{1h}\,\|\mathrm{T}_1\rangle$	Character w.r.t. $\|\mathrm{S}_0\rangle$	$\hat{C}_{2h\text{-}1p}\,\|\mathrm{T}_1\rangle$	Character w.r.t. $\|\mathrm{S}_0\rangle$
$\|o^2O^1V^0v^0\rangle$	$1h$	$\|o^1O^2V^0v^0\rangle$	$1h$
$\|o^2O^0V^1v^0\rangle$	$2h$-$1p$	$\|o^2O^0V^0v^1\rangle$	$2h$-$1p$
$\|o^1O^1V^1v^0\rangle$	$2h$-$1p$	$\|o^1O^1V^0v^1\rangle$	$2h$-$1p$
		$\|o^0O^2V^1v^0\rangle$	$2h$-$1p$
		$\|o^1O^0V^1v^1\rangle$	$3h$-$2p$
		$\|o^1O^0V^2v^0\rangle$	$3h$-$2p$
		$\|o^0O^1V^2v^0\rangle$	$3h$-$2p$
		$\|o^0O^1V^1v^1\rangle$	$3h$-$2p$

By comparison with the data provided in Table IV.3, it can readily be established that the $1\,^2\Pi$ and $2\,^2\Sigma$ states of LiH, the $2\,^2\mathrm{A}$ and $2\,^2\mathrm{E}$ states of NH_3 and the $2\,^2\mathrm{B}_1$ and $2\,^2\mathrm{A}_1$ states of H_2O are transitions of $2h$-$1p$-type with respect to the closed-shell reference. For these transitions a very good agreement with FCI is found when the triplet reference is employed, which contrasts the results obtained using the closed-shell reference where, especially for NH_3 and H_2O, larger errors are found (Table IV.3). This indicates that triplet references can be used in computations of neutral molecules to improve the IP-UADC(3) results specifically for $2h$-$1p$ satellite states.

Another important aspect in the context of electron detachment from triplet-excited molecules is that in this situation quartet electron-detached states can acquire photoelectron intensities, according to the monopole selection rules for spin ($\Delta S = \pm 1/2$). The $S = 3/2$ states can be obtained first for the spin coupling of three electrons in three different orbitals, that is in the case of $2h$-$1p$ satellites. In Table IV.6 this possibility is illustrated by the lowest $1\,^4\mathrm{B}_1$ ($3\mathrm{a}_1^{-1}$) state of H_2O with the "absolute" electron configuration $3\mathrm{a}_1^1\,1\mathrm{b}_1^1\,4\,a_1^1$. As can be seen from the pole strengths (P) computed at the IP-UADC(3) level of theory and shown in the last column of Table IV.6, the $3\mathrm{a}_1^{-1}$ ($1\,^4\mathrm{B}_1$) transition indeed, on par with the doublet $1h$-transitions, obtains a considerable photoelectron intensity of 0.79. This example in particular demonstrates that quartet cationic states can be studied both theoretically and spectroscopically when ionization from the lowest triplet (T_1) state of the neutral molecule is considered, e.g., in two-photon TRPES experiments.

The dipole moments of the cationic states computed using a triplet reference are in many cases very accurate, especially at the IP-UADC(3)/ISR(2) level of theory. As expected, lower errors are found for states accessible by $1h$-ionization with respect to the triplet vacuum state than for states resulting from $2h$-$1p$-type transitions. As seen in

the previous sections, the quality of computed dipole moments increases in the order IP-UADC(2)/ISR(2) < strict IP-UADC(3)/ISR(2) < standard IP-UADC(3)/ISR(2).

Radical Anions with Doublet Ground States

Radical anions with doublet ground states can be prepared for example by electron attachment to neutral closed-shell molecules. A number of such species is known, playing an important role in chemistry.[188] However, most radical anions are unstable with respect to electron loss and cannot be treated within the standard quantum chemical framework building upon square-integrable basis set representations. In this section, the results for electron detachment from the lowest spatially non-degenerate electronic states of $LiH^{\bullet-}$, $NH_3^{\bullet-}$, $H_2O^{\bullet-}$, $HF^{\bullet-}$ and $HCN^{\bullet-}$ are presented (Table IV.8). For these systems, the S^2 values computed for the respective UHF wavefunctions are 0.75, 0.76, 0.76, 0.75 and 0.78. With the exception of $LiH^{\bullet-}$, these systems are unstable anions and in the context of the present study only considered as model systems.

A problematic case is $HCN^{\bullet-}$, where large deviations from high-level CI results are observed for the $1\,^{1,3}\Pi$ states. This can be explained by the fact that the $^2\Sigma^+$ reference employed in the IP-UADC calculations is in UHF an excited state lying 0.12 eV above the $^2\Pi$ state. By contrast, CISDTQ predicts a $^2\Sigma^+$ ground state, $^2\Pi$ being the lowest excited state with a vertical excitation energy of 0.27 eV. Strictly speaking, the UHF reference wavefunction cannot be employed in this case, and the results computed for $HCN^{\bullet-}$ are excluded from the statistical error analysis.

For all other considered systems, IP-UADC(3) yields reliable electron detachment energies (Table IV.8). We find mean signed errors of $\bar{\Delta} = 0.13 \pm 0.26$ eV and $\bar{\Delta} = 0.21 \pm 0.37$ eV for the standard and strict IP-UADC(3) schemes, respectively. The corresponding mean and maximum absolute errors with respect to FCI results are $\overline{|\Delta|} = 0.19$ eV and $|\Delta|_{\max} = 0.53$ eV for the standard and $\overline{|\Delta|} = 0.25$ eV and $|\Delta|_{\max} = 0.91$ eV for the strict IP-UADC(3) scheme. For these systems, IP-UADC(2) is only slightly less accurate with $\bar{\Delta} = -0.17 \pm 0.45$ eV, $\overline{|\Delta|} = 0.32$ eV and $|\Delta|_{\max} = 0.87$ eV.

Again, as for the neutral radicals considered above, both singlet and triplet final states can be obtained as a result of electron detachment. The corresponding transitions acquire photoelectron intensities and should be seen in the spectrum. This also follows from the respective calculations predicting significant pole strengths for transitions to singlet and triplet states (Table IV.8).

The IP-UADC/ISR dipole moments for the electronic states obtained by electron detachment from radical anions are in very good agreement with FCI data. The errors for all

Table IV.8. Comparison between FCI and IP-UADC/ISR results for vertical electron detachment energies of $LiH^{\bullet -}$, $NH_3^{\bullet -}$, $H_2O^{\bullet -}$, $HF^{\bullet -}$, and $HCN^{\bullet -}$ (IP, eV) and dipole moments of electron-detached states (μ_n^{N-1}, D).[a,b] The IP-UADC(n)/ISR(m) schemes are denoted by the short-hand notations n/m. For the IP-UADC(3) schemes the order of the constant diagrams treatment is shown in parentheses (see text for details). The last lines give the mean error ($\bar{\Delta}$) and its standard deviation ($\sigma(\Delta)$) as well as the mean absolute error ($\overline{|\Delta|}$) and maximum absolute error ($\Delta_{\max}$) relative to FCI (in eV for IPs and in percent for μ_n^{N-1}). The relative photoelectron intensity (or pole strength, P) is also shown.

Initial radical anion		IP				μ_n^{N-1}				P
and final state[e]		FCI	3(4+)/2[c]	3(3)/2	2/2	FCI	3(4+)/2[c]	3(3)/2	2/2	3(4+)/2[c]
$LiH^{\bullet -}$	$^2\Sigma^+$									
$1\,^1\Sigma^+$	$3\sigma^{-1}$	0.30	0.29	0.29	0.29	−5.90	−5.97	−5.98	−6.22	0.991
$1\,^3\Sigma^+$	$2\sigma^{-1}$	3.49	3.34	3.41	4.10	4.40	3.94	4.04	8.40	0.590
$2\,^1\Sigma^+$	$2\sigma^{-1}$	3.85	3.93	3.96		5.13	5.95	6.10		0.335
$NH_3^{\bullet -}$[d]	^{2}A									
$1\,^1$A	$4a^{-1}$	−0.95	−0.99	−0.98	−1.01	1.90	1.93	1.93	1.96	0.993
$1\,^3$A	$3a^{-1}$	5.04	5.34	5.34	4.78	1.05	1.30	1.33	1.42	0.826
$2\,^1$A	$3a^{-1}$	5.33	6.13	6.13		0.91	1.18	1.19		0.061
$H_2O^{\bullet -}$	$^2A_2$									
$1\,^1A_1$	$4a_1^{-1}$	−0.94	−0.97	−0.96	−1.00	−2.28	−2.30	−2.29	−2.32	0.994
$1\,^3B_1$	$1b_1^{-1}$	6.06	6.50	6.70	5.42	0.99	1.31	1.35	1.49	0.791
$1\,^1B_1$	$1b_1^{-1}$	6.44	7.33	7.37		1.22	1.51	1.55		0.099
$HF^{\bullet -}$	$^2\Sigma^+$									
$1\,^1\Sigma^+$	$4\sigma^{-1}$	−0.99	−1.02	−1.00	−1.04	2.02	2.04	2.01	2.04	0.996
$1\,^3\Pi$	$1\pi^{-1}$	9.00	9.53	9.91	8.13	−2.50	−2.86	−2.89	−3.38	0.750
$1\,^1\Pi$	$1\pi^{-1}$	9.39	10.35	10.45		−2.72	−2.98	−3.08		0.113
$HCN^{\bullet -}$[f]	$^2\Sigma^+$									
$1\,^1\Sigma^+$	$6\sigma^{-1}$	−4.41	−4.36	−4.42	−4.25	−2.77	−3.11	−2.90	−2.83	0.967
$1\,^3\Pi$	$1\pi^{-1}$	4.05	6.01	6.29	6.59	−0.39	3.50	3.98	5.00	0.861
$1\,^1\Pi$	$1\pi^{-1}$	5.39	6.86	6.71		−0.93	4.71	4.56		0.567
$\bar{\Delta}$[h]			0.13	0.21	−0.17		8	9	28	
$\sigma(\Delta)$[h]			0.26	0.37	0.45		14	15	32	
$\overline{\lvert\Delta\rvert}$[h]			0.19	0.25	0.32		11	11	28	
$\lvert\Delta\rvert_{\max}$[h]			0.53	0.91	0.87		32	36	91	

[a] IP-UADC/ISR calculations based on UHF references.
[b] For $HCN^{\bullet -}$ results of CISDTQ calculations are shown.
[c] Iterative fourth-order treatment of constant diagrams, according to the so-called $\Sigma(4+)$ procedure,[74] also referred to as "standard" IP-UADC(3) scheme.
[d] The modulus of the dipole moment is shown because of degenerate ^{2}E states.
[e] Final-state $(N-1)$-electron configuration relative to the UHF reference.
[f] The $^2\Sigma^+$ reference employed in the IP-UADC calculations is not the UHF ground state. See text for details.
[g] Exempting results for $HCN^{\bullet -}$ (see footnote f).
[h] Only transitions which can be represented by a single $1h$-configuration are taken into account. See Section IV.3.2 for details.

three IP-UADC/ISR schemes compared in Table IV.8 are of the same order of magnitude as for the closed-shell systems (Table IV.3).

Table IV.9. The mean ($\bar{\Delta}$) absolute error and its standard deviation ($\sigma(\Delta)$) as well as the maximum absolute error ($\Delta_{\max}$) of the IP-(U)ADC/ISR schemes relative to FCI with respect to $1h$-type electron detachment processes in open- and closed-shell systems. The values are given in units of eV for vertical electron detachment energies (IP) and percent for dipole moments of electron-detached states (μ_n^{N-1}). The closed-shell systems comprise neutral molecules (N, Table IV.3) and anions (A, Table IV.4); the open-shell systems comprise neutral radicals (NR, Table IV.5), molecules in lowest triplet excited states (T_1, Table IV.7) and radical anions (RA, Table IV.8). The number of states considered in each case is denoted by k. The IP-(U)ADC(n)/ISR(m) schemes are denoted by the short-hand notations n/m. For the IP-(U)ADC(3) schemes the order of the static self-energy treatment is shown in parentheses (see text for details).

Initial system	Error	IP			μ_n^{N-1}			k
		3(4+)/2[a]	3(3)/2	2/2	3(4+)/2[a]	3(3)/2	2/2	
Closed-shell								
N	$\bar{\Delta} \pm \sigma(\Delta)$	0.19 ± 0.18	0.26 ± 0.33	-0.73 ± 0.59	-4 ± 29	-10 ± 54	-8 ± 38	
	$\overline{\lvert\Delta\rvert}$	0.22	0.33	0.76	15	24	18	14
	$\lvert\Delta\rvert_{\max}$	0.51	0.84	1.69	70	170	126	
A	$\bar{\Delta} \pm \sigma(\Delta)$	0.30 ± 0.19	0.27 ± 0.28	-0.77 ± 0.32	17 ± 30	37 ± 79	5 ± 85	
	$\overline{\lvert\Delta\rvert}$	0.30	0.29	0.77	22	43	44	11
	$\lvert\Delta\rvert_{\max}$	0.61	0.61	1.26	70	260	230	
Overall closed-shell	$\bar{\Delta} \pm \sigma(\Delta)$	0.24 ± 0.19	0.26 ± 0.30	-0.75 ± 0.48	5 ± 30	11 ± 69	-2 ± 62	
	$\overline{\lvert\Delta\rvert}$	0.25	0.31	0.76	18	32	29	25
	$\lvert\Delta\rvert_{\max}$	0.61	0.84	1.69	70	260	230	
Open-shell								
NR	$\bar{\Delta} \pm \sigma(\Delta)$	0.01 ± 0.41	-0.12 ± 0.35	-0.81 ± 0.39	10 ± 25	-77 ± 155	-66 ± 81	
	$\overline{\lvert\Delta\rvert}$	0.28	0.23	0.81	14	82	69	4
	$\lvert\Delta\rvert_{\max}$	0.55	0.63	1.23	47	310	160	
T_1	$\bar{\Delta} \pm \sigma(\Delta)$	0.11 ± 0.18	0.19 ± 0.26	0.05 ± 0.19	36 ± 63	53 ± 89	76 ± 108	
	$\overline{\lvert\Delta\rvert}$	0.13	0.20	0.14	36	53	76	7
	$\lvert\Delta\rvert_{\max}$	0.41	0.62	0.34	167	240	307	
RA	$\bar{\Delta} \pm \sigma(\Delta)$	0.13 ± 0.26	0.21 ± 0.37	-0.17 ± 0.45	8 ± 14	9 ± 15	28 ± 32	
	$\overline{\lvert\Delta\rvert}$	0.19	0.25	0.32	11	11	28	8
	$\lvert\Delta\rvert_{\max}$	0.53	0.91	0.87	32	36	91	
Overall open-shell	$\bar{\Delta} \pm \sigma(\Delta)$	0.10 ± 0.26	0.13 ± 0.34	-0.22 ± 0.47	19 ± 41	7 ± 96	26 ± 91	
	$\overline{\lvert\Delta\rvert}$	0.19	0.23	0.36	21	41	54	19
	$\lvert\Delta\rvert_{\max}$	0.55	0.91	1.23	167	310	307	
Overall	$\bar{\Delta} \pm \sigma(\Delta)$	0.17 ± 0.23	0.21 ± 0.32	-0.52 ± 0.54	11 ± 35	9 ± 80	10 ± 76	
	$\overline{\lvert\Delta\rvert}$	0.22	0.28	0.59	19	36	40	44
	$\lvert\Delta\rvert_{\max}$	0.61	0.91	1.69	167	310	307	

[a] Iterative fourth-order treatment of the static self-energy according to the so-called $\Sigma(4+)$ procedure,[74] also referred to as "standard" IP-(U)ADC(3) scheme.

IV.3.3. Overall Error Metrics

The combined error statistics computed for the total set of 44 $1h$-type transitions are summarized in Table IV.9, accompanied by the individual error statistics for each considered case.

The standard IP-(U)ADC(3)/ISR(2) methods with iterative fourth-order treatment of the static self-energy yield very convincing results for both electron-detachment energies and electron-detached state dipole moments, exhibiting an equally good performance for closed- and open-shell systems. The overall mean signed and mean absolute errors of electron detachment energies computed for the total set of 44 states are $\bar{\Delta} \pm \sigma(\Delta) = 0.17 \pm 0.23$ eV and $\overline{|\Delta|} = 0.22$ eV, the maximum absolute error being $|\Delta|_{\text{max}} = 0.61$ eV. For dipole moments, a similarly good accuracy is found, the respective error measures being $\bar{\Delta} \pm \sigma(\Delta) = 11 \pm 35\,\%$, $\overline{|\Delta|} = 19\,\%$ and $|\Delta|_{\text{max}} = 167\,\%$.

For the calculation of electron-detachment energies, the strict IP-(U)ADC(3)/ISR(2) methods employing the perturbative second-order ground state density perform similarly well. The overall error measures computed for this approximation scheme are $\bar{\Delta} \pm \sigma(\Delta) = 0.21 \pm 0.32$ eV, $\overline{|\Delta|} = 0.28$ eV and $|\Delta|_{\text{max}} = 0.91$ eV. The larger maximum error and standard deviation of the error encountered in this case, however, render the method less trustworthy than standard IP-(U)ADC(3)/ISR(2). For dipole moments, the same trend is observed in a considerably more pronounced manner.

As found previously, the pure second-order IP-(U)ADC(2)/ISR(2) schemes cannot be employed if quantitative results are desired. For electron-detachment energies, a mean error of $\bar{\Delta} \pm \sigma(\Delta) = -0.52 \pm 0.54$ eV is found, the mean and maximum absolute errors being $\overline{|\Delta|} = 0.59$ eV and $|\Delta|_{\text{max}} = 1.69$ eV. The same unreliable behavior is seen for dipole moments with mean and maximum absolute errors of 40 % and 307 %, respectively.

Chapter V

IP-UADC Case Study: The Galvinoxyl Free Radical

As an example how IP-UADC can be used in practical electronic structure studies of open-shell systems, the photoelectron spectrum (PES) of the galvinoxyl free radical (GFR) $C_{29}H_{41}O_2$ (Figure V.1) has been investigated. It is one of the most stable organic free radicals, and is widely employed in organic synthesis as radical scavenger to suppress undesired radical side reactions.[201, 202] GFR is also used as a mechanistic probe in the investigation of reaction pathways involving radical intermediates.[203]

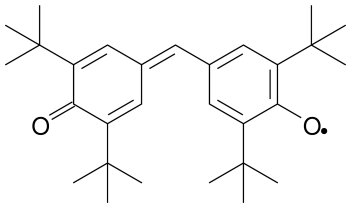

Figure V.1. Molecular structure of the galvinoxyl free radical.

Parts of this chapter have already been published in

- A. L. Dempwolff, M. Schneider, M. Hodecker, A. Dreuw, "Efficient Implementation of the Non-Dyson Third-Order Algebraic Diagrammatic Construction Approximation for the Electron Propagator for Closed- and Open-Shell Molecules", *J. Chem. Phys.* **2019**, *150*, 064108.

- A. L. Dempwolff, A. C. Paul, A. M. Belogolova, A. B. Trofimov, A. Dreuw, "Intermediate State Representation Approach to Physical Properties of Molecular Electron-Detached States: I. Theory and Implementation", *J. Chem. Phys.* **2020**, *152*, 024113.

V.1. Computational Details

The vertical ionization spectrum and one-electron properties of the final cationic states of GFR were computed at the strict IP-UADC(3)/cc-pVDZ[179] level. The ionized state dipole moments are given with respect to the center of mass (COM). The molecular geometry of C_2 point-group symmetry as computed in Ref. [204] at the DFT (M06-2X)/6-31+G(d,p) level of theory was used. The UHF reference state employed for the IP-UADC calculations was assumed to be of ^{2}A symmetry characterized by $M_S = 1/2$, i.e., with an excess α-electron.

The theoretical spectrum shown in Figure V.2 was simulated by convoluting the IP-UADC(3)/cc-pVDZ stick spectrum with Lorentzians of 0.5 eV FWHM (full width at half maximum). Orbital and density visualizations were computed using version 1.9.4a27 of the VMD software.[205] Dyson orbital isosurfaces were plotted at function values of ±0.03. For attachment and detachment density plots, isovalues of ±0.0025 were chosen.

V.2. Simulation of the Photoelectron Spectrum and State Assignment

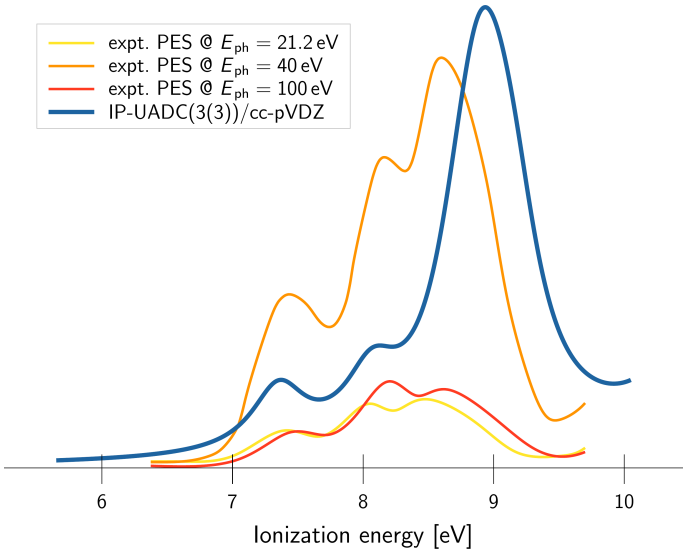

Figure V.2. The simulated and experimental photoelectron spectra of GFR. The simulated spectrum was obtained by convoluting the vertical IP-ADC(3)/cc-pVDZ spectrum with Lorentzians of 0.5 eV FWHM (full width at half maximum). Experimental data for different photon energies E_{ph} was digitized from Ref. [204].

Recently, the experimental gas phase photoelectron spectrum of GFR has been reported,

Table V.1. Lowest vertical IPs (eV), pole strength (P) and cationic-state dipole moments (μ_n^{N-1}, D) of GFR computed using the IP-UADC(3)/ISR(2) method employing the cc-pVDZ basis set, along with the available experimental data.

State	Transition	Type	IP	P	μ_n^{N-1}	Expt.[a]	Band
1	α-59a^{-1}	π	7.35	0.87	2.72	7.42	1
2	β-57b^{-1}	π	8.07	0.87	4.07	8.01	2
3	α-56b^{-1}	π	8.71	0.85	3.00	8.61	3
4	β-55b^{-1}	σ	8.83	0.85	1.65		
5	α-57b^{-1}	π	8.86	0.87	2.00		
6	α-58a^{-1}	π	8.90	0.87	2.40		
7	β-57a^{-1}	σ	8.91	0.84	1.31		
8	β-56b^{-1}	π	9.02	0.86	2.18		
9	β-58a^{-1}	π	9.03	0.86	2.74		
10	α-55b^{-1}	σ	9.15	0.82	1.35		
11	α-57a^{-1}	σ	9.18	0.81	1.36		
12	α-55b^{-1}	$2h$-$1p$	10.53	0.01	2.69		

[a] Experimental data from Ref. [204]. The stated values refer to band maxima.

and assignments of the first three bands in the low-energy range between 6.5 and 9.5 eV were made based on a Koopmans-like interpretation of Kohn-Sham (KS) density functional theory (DFT) orbitals.[204]

According to these results, the first band was assigned to an ionization from the π-type singly occupied molecular orbital (SOMO), which was found to be delocalized over the whole molecule. The second and third bands were assigned to ionizations from SOMO-1, mainly localized at the methine bridge, and SOMO-2 with large contributions from the in-plane lone pairs at the oxygen sites, respectively.

The experimental spectrum as digitized from Ref. [204] is shown in Figure V.2 along with the simulated IP-UADC spectrum. The spectral structure with three distinct bands is thereby correctly reproduced by the IP-UADC(3) calculation.

The calculated energies and pole strengths for the vertical ionization transitions of GFR along with the dipole moments of the corresponding final electron-detached states are listed in Table V.1.

According to IP-UADC(3), the lowest experimental band with a maximum at 7.42 eV mainly results from ionization from the π-type SOMO (α-59a). The calculated vertical ionization energy of this transition leading to the cationic ground state is 7.35 eV which is in excellent agreement with experiment. The corresponding Dyson orbital and α-part of the detachment density are shown in Figure V.3. As noted before, the shape of the Dyson orbital resembles the respective part of the detachment density, as the corresponding ionization process can be well described by a single $1h$-configuration.

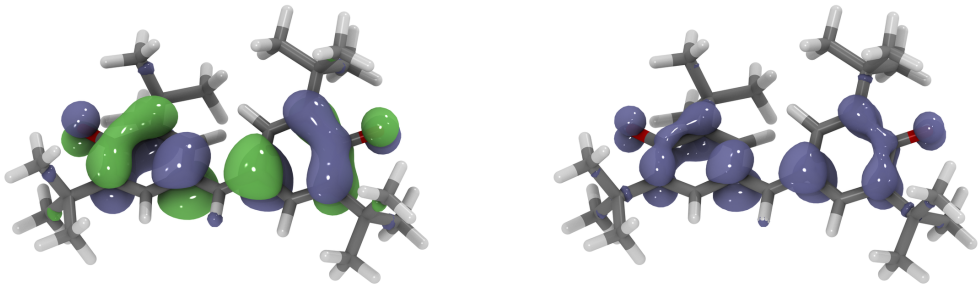

Figure V.3. Dyson orbital (left) and α-part of the detachment density (right) associated with the lowest IP in GFR (state 1 in Table V.1).

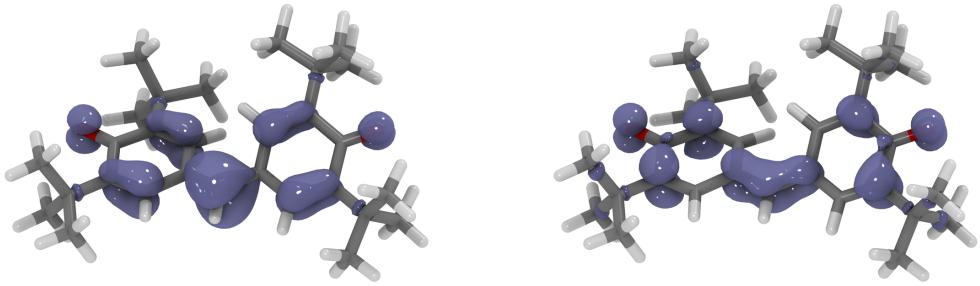

Figure V.4. Detachment densities for the SOMO−1 ionization transitions in GFR. Left panel: β-part of the detachment density associated with the first excited state of the GFR cation (state 2 in Table V.1), being responsible for the second PES band; Right panel: α-part of the detachment density associated with the second excited state of the GFR cation (state 3 in Table V.1), contributing to the third PES band.

The second photoelectron band is also due to a single transition, i.e, electron detachment from β-57b (SOMO−1). The computed vertical ionization energy of 8.07 eV again agrees very well with the observed band maximum at 8.01 eV. The β-part of the detachment density associated with this ionization process is depicted in the left panel of Figure V.4, reflecting the π-type of the associated spin-orbital with a large density contribution residing at the methine bridge.

The third PES band, however, turns out to have a more complex underlying structure, as one can identify nine transitions contributing to this spectral feature. The lowest of these corresponds to detachment from a π-type orbital (α-56b, state 3 in Table V.1, left panel of Figure V.5), having a similar spatial structure as that responsible for the second PES band.

The remaining eight transitions can further be categorized into two groups of four with respect to their σ- or π-character, each including α- and β-detachment of A and B

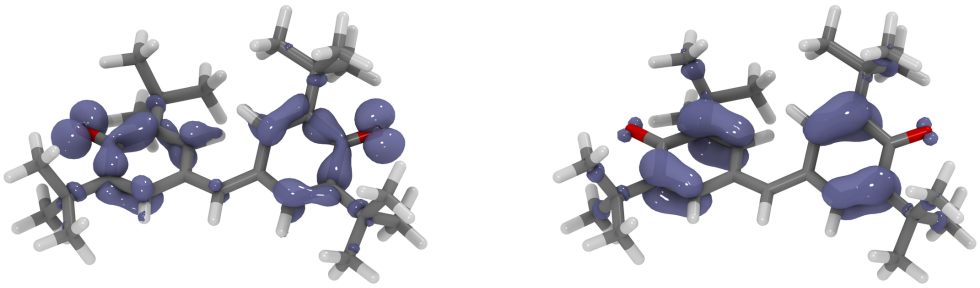

Figure V.5. Detachment densities for higher-lying ionization transitions in GFR contributing to the third PES band. Left panel: β-part of the detachment density associated with the third excited state of the GFR cation (state 4 in Table V.1); Right panel: α-part of the detachment density associated with the fourth excited state of the GFR cation (state 5 in Table V.1).

symmetry. The first group comprises states 4, 7, 10 and 11 of Table V.1, all describing σ-type detachment from the oxygen in-plane lone pairs. As representative example, the β-part of the detachment density of state 4 is shown in the left panel of Figure V.5.

The remaining four states 5, 6, 8 and 9 of Table V.1 result from higher-energy ionizations from the π-system, which can be visualized in terms of detachment densities as that of state 5 exemplarily depicted in the right panel of Figure V.5.

It is thus obvious that a simple Koopmans-like approach based on KS-DFT calculations provides only limited insight into electron detachment processes, and conclusions drawn based on such simple approaches need to be considered carefully. Moreover, the difficulties of the single-electron approximation related to the appearance of photoelectron satellites predicted above 10.5 eV have to be kept in mind.

In order to emphasize the different meanings of detachment densities and Dyson orbitals, the 12th transition (Table V.1) with a vertical ionization energy of 10.53 eV and a pole strength of $P = 0.01$ can be considered.

According to IP-UADC(3), this state results from a $2h$-$1p$-satellite transition which gains its photoelectron intensity from the α-55b^{-1} main state. The corresponding Dyson orbital shown in Figure V.6 indicates that the ejected electron wavefunction is predominantly described by a σ-type function.

The associated detachment and attachment densities are depicted in Figure V.7. Focusing first on the β-part shown in the right column, one can identify an $n \rightarrow \pi^*$ excitation accompanying the α-detachment. In contrast, the α-part (Figure V.7, left column) partially compensates the density loss in the σ-system by pulling density from the π-system, in which the largest part of the hole resides in the final state.

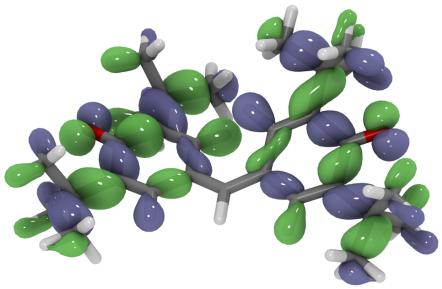

Figure V.6. Dyson orbital associated with the 11th excited state in the GFR cation.

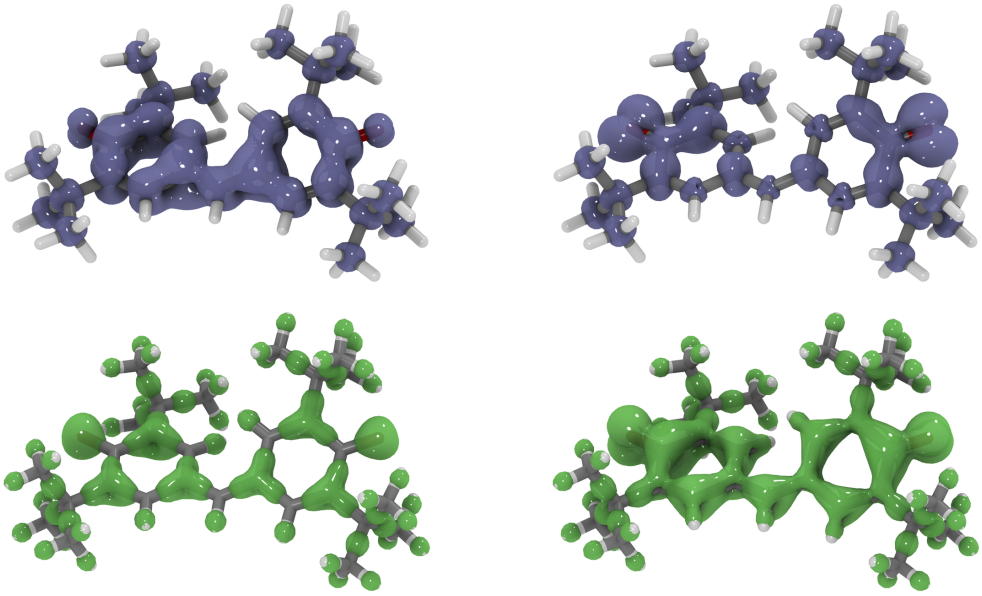

Figure V.7. Detachment (upper row) and attachment densities (lower row) associated with the 11th excited state in the GFR cation. The α-contributions are shown on the left side, the β-contributions on the right.

Chapter VI

Benchmarking Third-Order ADC Schemes for the Polarization Propagator

In this chapter, the accuracy of different third-order ADC schemes for the polarization propagator (PP-ADC) with respect to the treatment of the static self-energy $\Sigma(\infty)$ is evaluated using the implementation presented in Section III.3.2. Apart from the well-established strict third-order scheme employing the third-order static self-energy, ADC(3(3)), the corresponding schemes employing the fourth-order and improved fourth-order static self-energy, ADC(3(4)) and ADC(3(4+)), are considered.

VI.1. Computational Details

All calculations presented in this chapter were performed using Q-Chem 5.2.[75]

For the comparison with Σ(DEM) (Section VI.2, Table VI.1), all parameters were chosen as in the original literature, i.e., Ref. [39] and Refs. [206–208].

For the neon atom, slightly different parameters were used for the calculation of singlet and triplet excited states. For singlet states, the cc-pVDZ basis set[179] was employed, additionally augmented with diffuse functions with exponents 0.04 (s) and 0.03 (p), and no orbitals were frozen. In the corresponding triplet state calculations, the aug-cc-pVDZ basis set[180] was used. In this case the $1s$ orbital was kept frozen.

The geometry used for the computation of singlet and triplet excited states of the water molecule was O(0, 0, 0), H(0, $\pm$1.429 937 284 r_{Bohr}, $-$1.107 175 113 r_{Bohr}). In both cases, the cc-pVDZ basis set[179] was employed, additionally augmented with diffuse functions with the same exponents as in the aug-cc-pVDZ basis set,[180] i.e., 0.07896 (s), 0.06856 (p) on O and 0.02974 (s) on H. In the respective calculations, the $1s$ orbital on O was kept frozen.

In the case of the dinitrogen molecule, the internuclear distance was chosen as $R_{\mathrm{NN}} = 2.068\ r_{\mathrm{Bohr}}$, and the cc-pVDZ basis set[179] was used. The $1s$ orbitals on the nitrogen atoms were kept frozen.

For the hydrogen fluoride molecule, an internuclear distance of $R_{\mathrm{HF}} = 1.732\,879\,5\ r_{\mathrm{Bohr}}$ was used. For both triplet and singlet state calculations, the aug-cc-pVDZ basis set[180] was employed. In this case, the frozen-core approximation was also applied.

For the extended benchmark study presented in Section VI.3, all parameters were chosen as in the respective reference literature.

For the computation of excited states from the Thiel benchmark set[209] (Table VI.2) the def-TZVP basis set[210] was employed. The geometries used were the same as previously used in Ref. [211], being the same as in the original literature[209] or re-optimized at the MP2/6-31G* level in cases where the molecular point group symmetry was not correct. In a few cases a different state assignment as in Ref. [211] was done in order to achieve a better agreement of the single-excitation character of the respective states with the literature value. For the statistical error evaluation, only states for which theoretical best estimates (TBE) are available were considered, and the mean signed error ($\bar{\Delta}$) and its standard deviation ($\sigma(\Delta)$) as well as the mean absolute error ($\overline{|\Delta|}$) and maximum absolute error ($|\Delta|_{\mathrm{max}}$) were computed with respect to these values.

In the case of the Jacquemin benchmark set[212] (Table VI.3), the CC3/aug-cc-pVTZ geometries available through Ref. [212] were used, and the aug-cc-pVTZ basis set[180] was employed for excited state calculations. As for the Thiel benchmark set, all error measures were computed with respect to TBE values.

VI.2. Comparison with the Dyson Expansion Method

The improved fourth-order static self-energy obtained using the $\Sigma(4+)$ method as outlined in Section II.1.5 has previously been shown to be a good approximation to that one available through the Dyson expansion method, $\Sigma(\mathrm{DEM})$, by comparing the diagonal contributions $\Sigma_{kk}(\infty)$ among the different schemes.[74] In the same study, ionization potentials were computed using the corresponding IP-ADC(3) schemes and compared to experimental data. In this respect, only minor deviations between IP-ADC(3(4+)) and IP-ADC(3(DEM)) were observed, suggesting that the $\Sigma(4+)$ scheme can indeed be used as a replacement for the computationally more demanding Dyson expansion method. Considering the performance of different IP-ADC(3) schemes with respect to experimental data, IP-ADC(3(4+)) was observed to exhibit a higher accuracy than the strict third-order IP-ADC(3(3)) scheme, IP-ADC(3(4)) being only slightly less accurate.

In a second study focusing on PP-ADC, ADC(3(DEM)) was found to perform significantly better with respect to full configuration interaction than the strict third-order ADC(3(3)) scheme.[39] Neither the fourth-order $\Sigma(4)$ nor the improved fourth-order static self-energy according to the $\Sigma(4+)$ scheme have, however, been employed in this context so far.

In order to test the applicability of the $\Sigma(4)$ and $\Sigma(4+)$ schemes for PP-ADC, the excitation energies of the neon atom, hydrogen fluoride, water and dinitrogen have been computed and are compared to ADC(3(DEM)) and FCI results available through Ref. [39] and Refs. [206–208], respectively (Table VI.1).

Table VI.1. Comparison of different third-order ADC(3) schemes with ADC(3(DEM)) and FCI results from Ref. [39].

Compound	State	FCI	ADC(3(3))	ADC(3(4))	ADC(3(4+))	ADC(3(DEM))[a]
Neon atom[b]						
	$1\,^1\mathrm{P}$	16.40	16.78	16.46	16.56	16.57
	$1\,^1\mathrm{D}$	18.21	18.61	18.29	18.39	18.39
	$2\,^1\mathrm{P}$	18.26	18.65	18.33	18.43	18.44
	$2\,^1\mathrm{S}$	18.48	18.98	18.64	18.74	18.75
	$3\,^1\mathrm{S}$	44.05	44.63	44.30	44.40	44.40
	$1\,^3\mathrm{P}$	18.70	19.16	18.68	18.84	18.83
	$1\,^3\mathrm{S}$	19.96	20.35	19.90	20.05	20.06
	$1\,^3\mathrm{D}$	20.62	21.07	20.59	20.75	20.75
	$2\,^3\mathrm{P}$	20.97	21.43	20.95	21.11	21.10
	$2\,^3\mathrm{S}$	45.43	46.15	45.68	45.83	45.83
	$\bar{\Delta} \pm \sigma(\Delta)$		0.47 ± 0.11	0.07 ± 0.11	0.20 ± 0.10	0.20 ± 0.10
	$\overline{\lvert\Delta\rvert}$		0.47	0.10	0.20	0.20
	$\lvert\Delta\rvert_{\max}$		0.72	0.25	0.40	0.40
Hydrogen fluoride[c]						
	$1\,^1\Pi$	10.44	10.96	10.43	10.63	10.62
	$2\,^1\Pi$	14.21	14.74	14.21	14.41	14.40
	$2\,^1\Sigma^+$	14.58	15.00	14.53	14.70	14.68
	$1\,^1\Delta$	15.20	15.65	15.13	15.32	15.32
	$1\,^1\Sigma^-$	15.28	15.71	15.20	15.39	15.40
	$3\,^1\Pi$	15.77	16.35	15.79	16.00	16.00
	$3\,^1\Sigma^+$	16.43	17.12	16.54	16.75	16.80
	$1\,^3\Pi$	10.04	10.50	10.00	10.19	10.18
	$1\,^3\Sigma^+$	13.54	13.80	13.42	13.56	13.59
	$2\,^3\Pi$	14.01	14.53	14.01	14.20	14.20
	$2\,^3\Sigma^+$	14.46	14.83	14.34	14.52	14.53
	$1\,^3\Delta$	14.93	15.33	14.83	15.02	15.03
	$1\,^3\Sigma^-$	15.25	15.68	15.17	15.36	15.37
	$3\,^3\Pi$	15.57	16.13	15.59	15.79	15.79
	$\bar{\Delta} \pm \sigma(\Delta)$		0.47 ± 0.11	-0.04 ± 0.07	0.15 ± 0.08	0.16 ± 0.08
	$\overline{\lvert\Delta\rvert}$		0.47	0.06	0.15	0.16
	$\lvert\Delta\rvert_{\max}$		0.69	0.12	0.32	0.37

Table VI.1. (continued)

Compound	State	FCI	ADC(3(3))	ADC(3(4))	ADC(3(4+))	ADC(3(DEM))[a]
Water[d]						
	$2\,^1A_1$	9.87	10.15	9.98	10.04	10.01
	$1\,^1B_1$	7.45	7.72	7.55	7.61	7.58
	$1\,^1B_2$	11.61	11.91	11.74	11.80	11.79
	$1\,^1A_2$	9.21	9.50	9.33	9.39	9.38
	$1\,^3B_1$	7.06	7.27	7.11	7.17	7.15
	$1\,^3A_2$	9.04	9.30	9.14	9.20	9.18
	$1\,^3A_1$	9.44	9.64	9.49	9.55	9.54
	$2\,^3A_1$	10.83	10.95	10.79	10.85	10.84
	$2\,^3B_1$	11.05	11.27	11.10	11.17	11.16
	$1\,^3B_2$	11.32	11.54	11.39	11.44	11.45
	$\bar{\Delta} \pm \sigma(\Delta)$		0.24 ± 0.06	0.07 ± 0.05	0.13 ± 0.05	0.12 ± 0.05
	$\overline{\lvert\Delta\rvert}$		0.24	0.08	0.13	0.12
	$\lvert\Delta\rvert_{\max}$		0.30	0.13	0.19	0.18
Dinitrogen[d]						
	$1\,^1\Pi_g$	9.58	9.45	9.48	9.48	9.41
	$1\,^1\Sigma_u^-$	10.33	9.85	9.84	9.84	10.00
	$1\,^1\Delta_u$	10.72	10.24	10.24	10.24	10.35
	$1\,^1\Pi_u$	13.61	13.44	13.46	13.46	13.38
	$1\,^3\Sigma_u^+$	7.90	7.52	7.50	7.49	7.71
	$1\,^3\Pi_g$	8.16	7.94	7.97	7.96	7.87
	$1\,^3\Delta_u$	9.19	8.76	8.75	8.74	8.92
	$1\,^3\Sigma_u^-$	10.00	9.57	9.56	9.56	9.71
	$1\,^3\Pi_u$	11.44	11.29	11.31	11.31	11.25
	$\bar{\Delta} \pm \sigma(\Delta)$		-0.32 ± 0.15	-0.31 ± 0.16	-0.32 ± 0.17	-0.26 ± 0.07
	$\overline{\lvert\Delta\rvert}$		0.32	0.31	0.32	0.26
	$\lvert\Delta\rvert_{\max}$		0.48	0.49	0.49	0.37
Overall						
	$\bar{\Delta} \pm \sigma(\Delta)$		0.25 ± 0.33	-0.04 ± 0.18	0.06 ± 0.22	0.07 ± 0.19
	$\overline{\lvert\Delta\rvert}$		0.39	0.13	0.19	0.18
	$\lvert\Delta\rvert_{\max}$		0.72	0.49	0.49	0.40

[a] ADC(3(DEM)) values from Ref. [39].
[b] FCI values for singlet states from Ref. [206]; FCI values for triplet states from Ref. [208].
[c] FCI values for singlet and triplet states from Ref. [208].
[d] FCI values for singlet states from Ref. [207]; FCI values for triplet states from Ref. [208].

An inspection of Table VI.1 shows that the ADC(3(4+)) method indeed reproduces the ADC(3(DEM)) results for the first three systems considered, i.e., the neon atom, hydrogen fluoride and the water molecule. Compared to the strict ADC(3(3)) method, the mean and maximum absolute errors computed for the respective sets of states are found to be considerably smaller for these three systems. As an example the water molecule may be considered, where the mean absolute error computed for ADC(3(3)) and ADC(3(4+)) is 0.24 ± 0.06 eV and 0.13 ± 0.05 eV, respectively, the corresponding maximum absolute errors being 0.30 eV and 0.19 eV. For these systems, ADC(3(4)) interestingly yields even more accurate results, and this scheme is consequently also evaluated in the extended

benchmark study presented in the following section.

In the remaining case of the dinitrogen molecule with a more complicated electronic structure, however, a completely different behavior is observed. For this system, ADC(3(3)), ADC(3(4)) and ADC(3(4+)) yield virtually identical results, and no systematic improvement with respect to FCI data is found. By contrast, the ADC(3(DEM)) scheme employing the iterated ground state density available through the Dyson expansion method performs better, although the improvement upon ADC(3(3)) is not as pronounced as observed for the first three examples.

The above findings indicate that the general applicability of the improved third-order ground state density connected to the $\Sigma(4+)$ scheme as a replacement for that one related to the Σ(DEM) scheme is not as clear as observed in the context of IP-ADC.[74] Nevertheless, the overall error measures computed for the total set of 43 states considered in Table VI.1 imply that ADC(3(4+)) has the potential to improve the accuracy of ADC(3) results for excitation energies.

VI.3. Extended Benchmarking

The accuracy of the three ADC(3) schemes differing by the static self-energy treatment was further investigated in an extended benchmark study. Therein, two different sets of molecules were considered, the first of which is the well-established benchmark set by Thiel and co-workers,[209] which comprises 28 small and medium-sized organic molecules. The second benchmark set was published recently by Jacquemin and co-workers[212] and covers 18 small inorganic and organic molecules.

VI.3.1. Thiel Benchmark Set

In Table VI.2, the errors with respect to theoretical best estimates computed for each individual molecule are summarized, accompanied by the overall statistical error measures for 104 singlet and 63 triplet states as well as the total set of 167 states. The results for the individual excited singlet and triplet states are given in Appendix A.1 in Tables A.1 and A.2, respectively.

The performance of ADC(3(3)) has previously been evaluated using the same benchmark set in Ref. [211]. As noted above, in the present work states were assigned differing from the previous study in a few cases, which is reflected in slightly different overall error measures. For singlet and triplet excited states, a mean signed error of $\bar{\Delta} \pm \sigma(\Delta) = 0.11 \pm 0.31$ eV and $\bar{\Delta} \pm \sigma(\Delta) = -0.19 \pm 0.17$ eV is computed, respectively. The respective maximum absolute errors for singlet and triplet states are found to be 0.92 eV and 0.50 eV. For the

Table VI.2. Error measures for the individual molecules in the Thiel benchmark set in units of eV. Only states for which theoretical best estimates are available were included in the statistical error evaluation. The number of states considered in each case is denoted as k.

Compound	ADC(3(3))			ADC(3(4))			ADC(3(4+))			k
	$\bar{\Delta} \pm \sigma(\Delta)$	$\overline{\lvert\Delta\rvert}$	$\lvert\Delta\rvert_{\max}$	$\bar{\Delta} \pm \sigma(\Delta)$	$\overline{\lvert\Delta\rvert}$	$\lvert\Delta\rvert_{\max}$	$\bar{\Delta} \pm \sigma(\Delta)$	$\overline{\lvert\Delta\rvert}$	$\lvert\Delta\rvert_{\max}$	
Ethylene	0.04 ± 0.43	0.30	0.34	0.09 ± 0.42	0.30	0.39	0.07 ± 0.42	0.30	0.37	2
Butadiene	-0.24 ± 0.40	0.33	0.78	-0.22 ± 0.40	0.31	0.78	-0.22 ± 0.40	0.32	0.78	4
Hexatriene	-0.18 ± 0.37	0.31	0.56	-0.17 ± 0.36	0.29	0.57	-0.17 ± 0.36	0.30	0.57	4
Octatetraene	-0.28 ± 0.48	0.40	0.92	-0.28 ± 0.48	0.39	0.93	-0.28 ± 0.48	0.39	0.93	4
Cyclopropene	-0.15 ± 0.10	0.15	0.26	-0.12 ± 0.10	0.13	0.23	-0.13 ± 0.10	0.13	0.24	4
Cyclopentadiene	-0.27 ± 0.19	0.27	0.50	-0.24 ± 0.20	0.24	0.50	-0.25 ± 0.20	0.25	0.50	4
Norbornadiene	-0.00 ± 0.30	0.25	0.34	0.02 ± 0.30	0.25	0.36	0.01 ± 0.30	0.25	0.36	4
Benzene	-0.04 ± 0.19	0.17	0.27	-0.00 ± 0.22	0.19	0.30	-0.01 ± 0.21	0.18	0.27	8
Naphthalene	-0.16 ± 0.20	0.24	0.50	-0.15 ± 0.21	0.24	0.49	-0.16 ± 0.21	0.24	0.50	18
Furan	-0.10 ± 0.19	0.17	0.33	-0.07 ± 0.20	0.16	0.25	-0.08 ± 0.19	0.17	0.29	5
Pyrrole	-0.11 ± 0.14	0.12	0.27	-0.08 ± 0.14	0.11	0.23	-0.09 ± 0.14	0.10	0.25	5
Imidazole	-0.13 ± 0.23	0.23	0.35	-0.11 ± 0.23	0.23	0.34	-0.12 ± 0.23	0.23	0.33	7
Pyridine	0.21 ± 0.26	0.27	0.69	0.19 ± 0.24	0.25	0.60	0.20 ± 0.26	0.26	0.67	12
Pyrazine	0.13 ± 0.34	0.29	0.74	0.12 ± 0.33	0.27	0.75	0.12 ± 0.34	0.28	0.75	14
Pyrimidine	0.01 ± 0.21	0.16	0.44	-0.03 ± 0.18	0.14	0.36	-0.02 ± 0.21	0.16	0.42	10
Pyridazine	0.06 ± 0.21	0.16	0.44	0.04 ± 0.18	0.14	0.36	0.04 ± 0.20	0.15	0.42	10
Triazine	0.10 ± 0.22	0.18	0.44	0.05 ± 0.19	0.14	0.36	0.07 ± 0.22	0.17	0.45	10
Tetrazine	-0.09 ± 0.37	0.30	0.73	-0.10 ± 0.38	0.31	0.75	-0.10 ± 0.38	0.31	0.74	15
Formaldehyde	-0.15 ± 0.17	0.15	0.41	-0.43 ± 0.11	0.43	0.61	-0.31 ± 0.16	0.31	0.58	5
Acetone	0.04 ± 0.32	0.20	0.56	-0.31 ± 0.38	0.44	0.64	-0.15 ± 0.40	0.35	0.56	5
Benzoquinone	-0.04 ± 0.20	0.16	0.36	-0.25 ± 0.23	0.31	0.49	-0.14 ± 0.18	0.19	0.44	10
Formamide	-0.03 ± 0.13	0.08	0.23	-0.43 ± 0.14	0.43	0.52	-0.26 ± 0.15	0.26	0.45	4
Acetamide	0.04 ± 0.21	0.14	0.32	-0.39 ± 0.29	0.41	0.58	-0.21 ± 0.27	0.30	0.43	4
Propanamide	0.08 ± 0.23	0.17	0.38	-0.35 ± 0.30	0.40	0.53	-0.17 ± 0.28	0.29	0.43	4
Cytosine	0.27 ± 0.39	0.33	0.90	-0.10 ± 0.36	0.29	0.53	0.04 ± 0.36	0.27	0.52	6
Thymine	0.20 ± 0.21	0.25	0.42	-0.16 ± 0.28	0.23	0.53	0.01 ± 0.26	0.21	0.43	7
Uracil	0.20 ± 0.23	0.24	0.58	-0.13 ± 0.30	0.25	0.53	0.01 ± 0.24	0.18	0.43	8
Adenine	0.11 ± 0.24	0.19	0.44	-0.10 ± 0.36	0.29	0.53	-0.02 ± 0.31	0.25	0.43	6
Overall										
Singlets	0.11 ± 0.31	0.25	0.92	0.00 ± 0.32	0.25	0.93	0.05 ± 0.30	0.23	0.93	104
Triplets	-0.19 ± 0.17	0.22	0.50	-0.25 ± 0.19	0.28	0.64	-0.23 ± 0.17	0.26	0.58	63
Singl. and tripl.	0.00 ± 0.24	0.24	0.92	-0.09 ± 0.30	0.26	0.93	-0.05 ± 0.29	0.24	0.93	167

whole set of 167 singlet and triplet excited states, an error of $\bar{\Delta} \pm \sigma(\Delta) = 0.00 \pm 0.24$ eV is found.

When taking into account third-order ground state density contributions as used throughout the $\Sigma(4)$ scheme, only small changes can be observed with respect to the strict third-order treatment. The most pronounced effect is seen in the case of singlet excited states where the mean signed error reduces to $\bar{\Delta} \pm \sigma(\Delta) = 0.00 \pm 0.32$ eV. For triplet excited states, no significant change with respect to ADC(3(3)) is found. Considering the combined set of singlet and triplet excited states, however, a larger standard deviation of the error of $\sigma(\Delta) = 0.30$ eV is found, rendering the ADC(3(4)) scheme less trustworthy as the strict third-order scheme.

For singlet excited states, the ADC(3(4+)) scheme yields slightly more favorable results than ADC(3(3)), reflected in the smaller mean absolute error of $\overline{|\Delta|} = 0.23$ eV. By contrast,

Table VI.3. Error measures for the individual molecules in the Jacquemin benchmark set in units of eV. Only compounds with more than one computed transition are listed. The number of states considered in each case is denoted as k.

Compound	ADC(3(3))			ADC(3(4))			ADC(3(4+))			k
	$\bar{\Delta} \pm \sigma(\Delta)$	$\overline{\lvert\Delta\rvert}$	$\lvert\Delta\rvert_{\max}$	$\bar{\Delta} \pm \sigma(\Delta)$	$\overline{\lvert\Delta\rvert}$	$\lvert\Delta\rvert_{\max}$	$\bar{\Delta} \pm \sigma(\Delta)$	$\overline{\lvert\Delta\rvert}$	$\lvert\Delta\rvert_{\max}$	
Acetaldehyde	-0.05 ± 0.04	0.05	0.08	-0.41 ± 0.03	0.41	0.43	-0.25 ± 0.04	0.25	0.28	2
Acetylene	-0.35 ± 0.04	0.35	0.38	-0.30 ± 0.03	0.30	0.32	-0.32 ± 0.03	0.32	0.34	5
Ammonia	0.04 ± 0.02	0.04	0.05	0.15 ± 0.02	0.15	0.16	0.09 ± 0.02	0.09	0.10	5
CO	-0.22 ± 0.05	0.22	0.32	-0.26 ± 0.49	0.45	0.80	-0.23 ± 0.31	0.31	0.58	11
Cyclopropene	-0.22 ± 0.07	0.22	0.30	-0.19 ± 0.07	0.19	0.27	-0.20 ± 0.07	0.20	0.29	4
Diazomethane	-0.37 ± 0.07	0.37	0.47	-0.34 ± 0.17	0.34	0.49	-0.38 ± 0.15	0.38	0.54	7
Dinitrogen	-0.29 ± 0.23	0.29	0.56	-0.22 ± 0.32	0.33	0.55	-0.24 ± 0.30	0.32	0.56	11
Ethylene	-0.22 ± 0.04	0.22	0.26	-0.11 ± 0.07	0.11	0.21	-0.14 ± 0.06	0.14	0.23	6
Formaldehyde	0.11 ± 0.30	0.28	0.39	-0.15 ± 0.29	0.26	0.59	-0.01 ± 0.33	0.30	0.52	13
Formamide	0.21 ± 0.28	0.28	0.50	-0.15 ± 0.31	0.28	0.45	0.01 ± 0.31	0.28	0.38	6
H_2S	-0.10 ± 0.04	0.10	0.14	-0.11 ± 0.03	0.11	0.14	-0.11 ± 0.03	0.11	0.14	4
Ketene	-0.15 ± 0.06	0.15	0.23	-0.04 ± 0.19	0.16	0.26	-0.06 ± 0.14	0.12	0.24	7
Methanimine	-0.21 ± 0.02	0.21	0.22	-0.24 ± 0.02	0.24	0.26	-0.24 ± 0.02	0.24	0.25	2
Nitrosomethane	-0.26 ± 0.27	0.30	0.56	-0.38 ± 0.39	0.46	0.77	-0.31 ± 0.37	0.40	0.72	4
Streptocyan.-C1	-0.06 ± 0.13	0.09	0.15	-0.18 ± 0.13	0.18	0.27	-0.16 ± 0.16	0.16	0.27	2
H_2CS	-0.18 ± 0.18	0.19	0.40	-0.31 ± 0.16	0.31	0.45	-0.25 ± 0.18	0.25	0.42	6
Water	0.20 ± 0.03	0.20	0.23	0.12 ± 0.02	0.12	0.15	0.14 ± 0.02	0.14	0.16	6
Overall										
Singlets	-0.11 ± 0.28	0.23	0.79	-0.16 ± 0.30	0.27	0.79	-0.12 ± 0.28	0.25	0.81	61
Triplets	-0.18 ± 0.22	0.25	0.56	-0.25 ± 0.27	0.30	0.80	-0.22 ± 0.25	0.28	0.72	47
Singl. and tripl.	-0.14 ± 0.25	0.24	0.79	-0.20 ± 0.29	0.29	0.80	-0.17 ± 0.27	0.26	0.81	108

the results computed for triplet states are less accurate.

Overall, the accuracy decreases in the order ADC(3(3)) > ADC(3(4+)) > ADC(3(4)). However, no systematic improvement can be seen for the individual molecules in this benchmark set when comparing the results of two methods, and no clear recommendation may be given based on these results.

VI.3.2. Jacquemin Benchmark Set

In Table VI.3, the errors with respect to theoretical best estimates computed for each individual molecule in Jacquemin's benchmark set are summarized, accompanied by the overall statistical error measures for singlet and triplet states as well as the total set of 108 states. The results for the individual excited singlet and triplet states are given in Appendix A.2 in Tables A.3 and A.4, respectively.

For this set of electronically excited states, no clear trend in accuracy can be observed. The overall error estimates are similar to those obtained for Thiel's benchmark set. An exception are singlet excitation energies which are overall underestimated here and, by contrast, overestimated in the case of Thiel's benchmark set.

The same trend as seen in the case of the Thiel benchmark set is also found in this

Table VI.4. Statistical error analysis for the combined Thiel and Jacquemin benchmark sets. All error measures are given in units of eV. The number of states considered is denoted as k.

	ADC(3(3))			ADC(3(4))			ADC(3(4+))			k
	$\bar{\Delta} \pm \sigma(\Delta)$	$\overline{\lvert\Delta\rvert}$	$\lvert\Delta\rvert_{\max}$	$\bar{\Delta} \pm \sigma(\Delta)$	$\overline{\lvert\Delta\rvert}$	$\lvert\Delta\rvert_{\max}$	$\bar{\Delta} \pm \sigma(\Delta)$	$\overline{\lvert\Delta\rvert}$	$\lvert\Delta\rvert_{\max}$	
Singlets	0.03 ± 0.31	0.24	0.92	-0.06 ± 0.32	0.26	0.93	-0.01 ± 0.30	0.24	0.93	165
Triplets	-0.18 ± 0.19	0.23	0.56	-0.25 ± 0.23	0.29	0.80	-0.23 ± 0.20	0.27	0.72	110
Singl. and tripl.	-0.06 ± 0.29	0.24	0.92	-0.14 ± 0.30	0.27	0.93	-0.10 ± 0.29	0.25	0.93	275

case. For the whole set of 108 singlet and triplet excited states, the overall accuracy decreases in the order ADC(3(3)) > ADC(3(4+)) > ADC(3(4)), the mean signed error and its standard deviation $\bar{\Delta} \pm \sigma(\Delta)$ being -0.14 ± 0.25, -0.17 ± 0.27 and -0.20 ± 0.29, respectively. Considering the results computed for the individual molecules, again no systematic improvement can be seen when going from one method to another.

VI.3.3. Combined Benchmark Sets

Combining the two benchmark sets considered above, a statistical error analysis was conducted for 165 singlet and 110 triplet excited states and the total set of 275 electronically excited states. The results are summarized in Table VI.4.

Inspecting the computed error measures, it is readily seen that the three considered methods yield virtually identical results. Based on these values, a slight preference for ADC(3(3)) over ADC(3(4+)) may be seen, ADC(3(4)) being the least accurate of the three schemes.

In this respect, the findings of Section VI.2 can be reconsidered. Indeed, the accuracy behavior observed in the extended benchmark study presented in this section is comparable to that found for the dinitrogen molecule (last entry in Table VI.1). The other three systems considered in Section VI.2, i.e., the neon atom, hydrogen fluoride and the water molecule should therefore be regarded as special cases.

Chapter VII

Computational and Conceptual Aspects of Fano-Stieltjes-ADC

In order to evaluate the applicability of the different components of the Fano-Stieltjes-ADC implementation introduced in Section III.4 a number of computational tests have been carried out. The results are presented in this chapter.

In Section VII.2, the applicability of the implemented block-Lanczos diagonalization procedure is evaluated by consideration of the cumulative decay width function computed using increasing sizes of the block-Lanczos vector subspace describing the continuum-state pseudo-spectrum. Section VII.3 covers different aspects of the Stieltjes imaging procedure, especially the choice of different input parameters. Finally, in Section VII.4 numerical results obtained using the novel implementation are presented. In particular, the behavior of the Fano-Stieltjes-ADC method upon scaling to larger molecular systems is discussed at the example of Feshbach resonances in the benzene (C_6H_6) and naphthalene ($C_{10}H_8$) molecules.

VII.1. Computational Details

The subspace-projected ADC diagonalizations and computations of bound-continuum coupling matrix elements were carried out using the Fano-ADC implementation in a development version of the Q-Chem quantum chemical program package based on version 5.0 as outlined in Section III.4. For bound-state ADC diagonalizations, the Davidson algorithm[147] was used. Continuum-state ADC diagonalizations were performed using the block-Lanczos implementation as described in Section III.4.5.

Stieltjes imaging calculations were performed using the standalone Stieltjes imaging program presented in Section III.4.6, employing quadruple or higher-precision floating

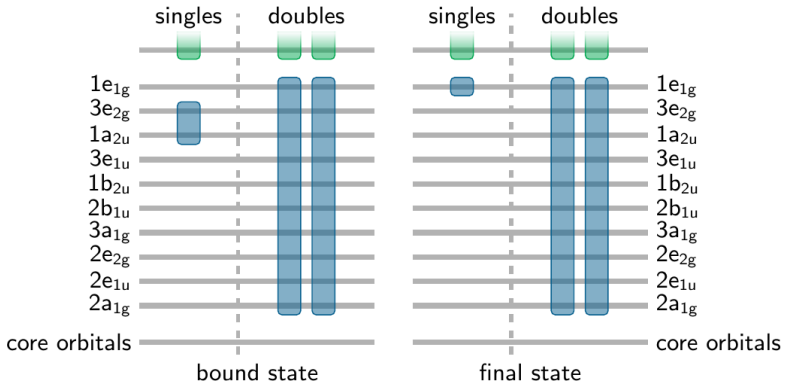

Figure VII.1. Schematic depiction of the subspace selection scheme used in the context of the $3e_{2g}{}^{-1}3pe_{1u}$ resonance in benzene. Occupied orbitals considered for the construction of the bound and continuum state projection operators $\hat{Q}$ and $\hat{P}$ are depicted in blue, virtual orbitals in green.

point arithmetic. All Fano-Stieltjes-ADC decay widths presented in this chapter were obtained by numerical derivation of the cumulative width function by means of Stieltjes derivatives according to Eq. (2.73) at the Stieltjes order indicated in each individual case.

For the computation of the decay width of the $2s^{-1}3p$ resonance in the neon atom, the subspace projection scheme as used in Ref. [140] was employed (cf. Figure II.3). That is, the $1s$ orbital was kept frozen, and all $1h1p$-configurations with a hole in the $2s$ orbital as well as all possible $2h2p$-configurations were included in the bound-state subspace. For the continuum-state subspace, all configurations with holes in the $2p$ orbitals were considered. As in Ref. [140], the cc-pCVTZ basis set,[179, 213] additionally augmented with $15s9d$ continuum- and $6p$ Rydberg-like Gaussian basis functions[214] was employed. The additional exponents were: 0.2456452, 0.0984957, 0.0527254, 0.0327748, 0.0223274, 0.0161822, 0.0122645, 0.0096146, 0.0077393, 0.0063635, 0.0053244, 0.0045206, 0.0038859, 0.0033761, 0.0029604 (s); 0.6225575, 0.2421608, 0.1278396, 0.0788350, 0.0534281, 0.0385827, 0.0291633, 0.0228152, 0.0183349 (d); 0.2242059, 0.1510640, 0.1054753, 0.0758656, 0.0559584, 0.0421752 (p). If not stated otherwise, the extended second-order ADC scheme (ADC(2)-x) was employed. During Stieltjes imaging calculations, energies $E - E_r$ were shifted such that the lowest energy was 0.2 Hartree in order to avoid numerical problems in the vicinity of $E - E_r = 0$.

In case of the benzene molecule, the geometrical parameters were optimized at the MP2/cc-pVDZ[179] level of theory using Q-Chem 4.4.[75] The Fano-Stieltjes-ADC(2) calculations of the $3e_{2g}{}^{-1}3pe_{1u}$ resonance were carried out using the aug-cc-pVDZ basis set[179, 180] and employing the subspace selection scheme as used in Ref. [141] (Figure VII.1). Here, the energetic shift applied in the Stieltjes imaging procedure was chosen such that the lowest input energy $E - E_r$ was 1.0 Hartree.

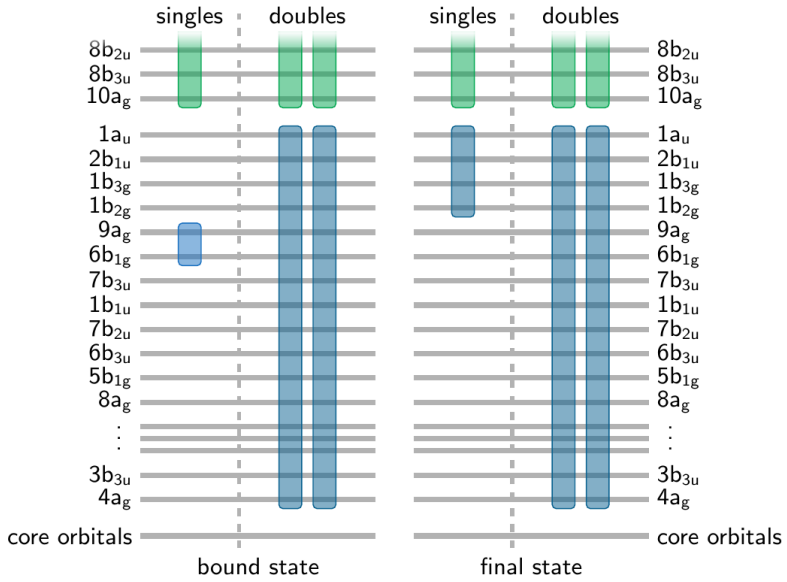

Figure VII.2. Schematic depiction of the subspace selection scheme used in the context of the $9a_g{}^{-1}8b_{2u}$ resonance in naphthalene. Virtual orbitals considered for the construction of the bound and continuum state projection operators $\hat{Q}$ and $\hat{P}$ are depicted in green, occupied orbitals in blue.

Finally, the geometrical parameters of the naphthalene molecule were optimized using Q-Chem 5.0[75] at the MP2/aug-cc-pVDZ[179, 180] level of theory. The same aug-cc-pVDZ basis set as used for the geometry optimization was also employed in the Fano-Stieltjes-ADC(2) calculations of the $9a_g{}^{-1}8b_{2u}$ resonance in naphthalene. If not stated otherwise, the bound- and continuum-state subspaces were constructed following a similar procedure as in the benzene case and are shown in Figure VII.2. As for benzene, the energetic shift applied to the energies entering the Stieltjes imaging procedure were chosen such that the lowest input energy $E - E_r$ was 1.0 Hartree.

VII.2. Convergence of Block-Lanczos Pseudo-Spectra

The convergence of block-Lanczos pseudo-spectra with respect to full diagonalization is a prerequisite for the application of the Fano-Stieltjes-ADC method to larger molecular systems, since full diagonalization of the connected continuum-state projected ADC eigenvalue problems is usually computationally not feasible in practical cases. The applicability of the block-Lanczos diagonalization procedure is justified by the fact that it preserves the spectral moments.[148] It has been applied in a number of Fano-Stieltjes-ADC studies,[124, 141, 142] which suggested a fast convergence of computed decay widths $\Gamma(E_r)$ with the number of block-Lanczos iterations or subspace vectors. However, apart from the

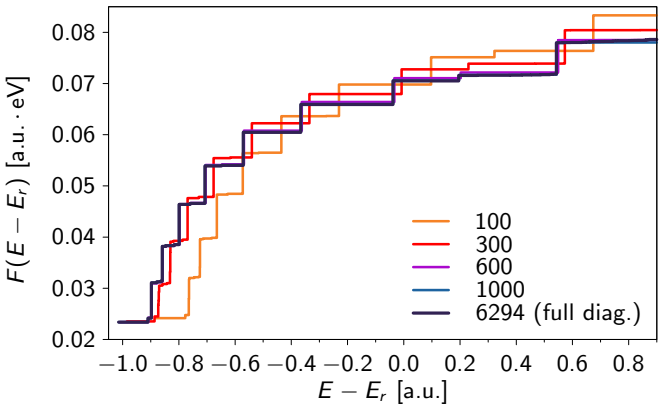

Figure VII.3. Convergence of the block-Lanczos pseudo-spectrum with respect to full diagonalization shown at the example of the cumulative decay width $F(E - E_r)$ computed for the Ne $2s^{-1}3p$ resonance and different numbers of block-Lanczos subspace vectors.

final computed decay widths, no data has been available to illustrate this behavior.

For this reason, the convergence of block-Lanczos pseudo-spectra with respect to full diagonalization has been investigated at the example of the cumulative decay width $F(E - E_r)$ computed for the $2s^{-1}3p$ resonance in the neon atom. Figure VII.3 shows the cumulative decay width $F(E - E_r)$ in the spectral region of interest, i.e., close to the resonance energy $E = E_r$, for different numbers of block-Lanczos subspace vectors, employing an initial block of 100 guess vectors covering all 62 single excitations of the same symmetry as the initial state as well as 38 double excitations corresponding to the lowest diagonal elements of the subspace-projected ADC(2)-x matrix.

It is easily seen that the spectrum is nearly converged to that obtained by full diagonalization after 6 block-Lanczos iterations (i.e., after computation of 600 subspace vectors), and can hardly be distinguished from the fully diagonalized one after 10 iterations have been carried out. In fact, even after as few as 3 iterations, the cumulative decay width seems to be quite satisfactorily described and might serve as a reasonable approximation. These findings are also supported by the convergence of the decay width, which will be discussed in more detail in Section VII.4.1.

Figure VII.3 also indicates that full diagonalization is not needed in order to judge the convergence behavior, which makes a related study also possible for larger molecular systems. Here, this option is explored on the example of the $9a_g{}^{-1}8b_{2u}$ resonance in naphthalene. In this case, the initial block entering the block-Lanczos procedure consisted of all 81 possible single excitation vectors of B_{2u} symmetry within the given subspace projection scheme as visualized in Figure VII.2. Figure VII.4 displays the cumulative decay width evaluated after 1, 2, 4, 8 and 11 block-Lanczos iterations corresponding to

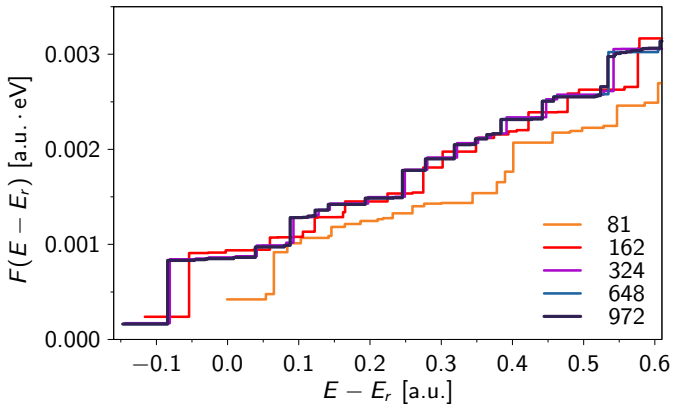

Figure VII.4. Convergence of the block-Lanczos pseudo-spectrum shown at the example of the cumulative decay width $F(E - E_r)$ computed for the $9a_g{}^{-1}8b_{2u}$ resonance in the naphthalene molecule using different numbers of block-Lanczos subspace vectors.

81, 162, 324, 648 and 972 subspace vectors, respectively.

In the spectral region of interest, i.e., in the vicinity of $E - E_r = 0$, the spectrum obtained after 4 iterations (324 subspace vectors) is already sufficiently well converged with respect to that computed with 972 subspace vectors. Compared to the case of the neon resonance discussed above, the convergence behavior is even faster, giving strong support for the application of this methodology.

VII.3. Stieltjes Imaging Technique

As discussed in Section II.2.3, the Stieltjes imaging technique allows for replacement of the real continuum spectrum employed in the Fano ansatz by a discretized spectrum obtained within the framework of $\mathcal{L}^2$-integrable quantum chemical methods. Thereby, it has been pointed out that only a small number of spectral moments, i.e., the first few negative moments, should be used in the Stieltjes imaging procedure, since only these supply reliable physical information.[149] By using only these low Stieltjes orders to compute the spectrum of bound-continuum coupling elements or partial decay widths the spectrum is effectively smoothed.

This can readily be understood when inspecting Figure VII.5. Increasing the Stieltjes order leads to a better approximation of the raw spectrum, i.e., that one yielded from the ADC calculation without application of further postprocessing. Consequently, also all spectral features resulting from wrongly discretized pseudo-continuum states are resolved, which is not desired. As a consequence, the spectral distribution of the desired quantity, the decay width $\Gamma(E)$, becomes less smooth, which is visualized in Figure VII.6.

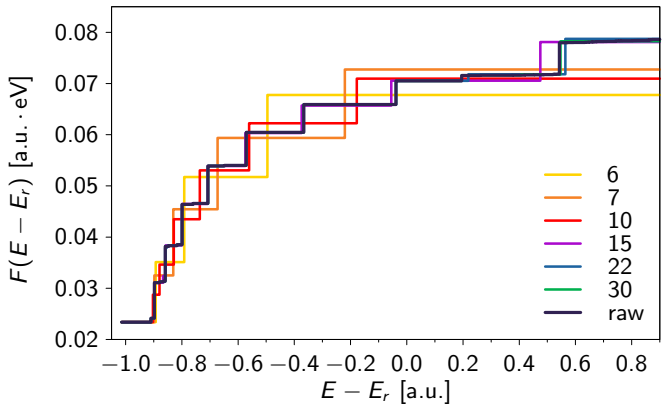

Figure VII.5. Cumulative width functions $F(E - E_r)$ connected to the $2s^{-1}3p$ resonance in the neon atom computed for different Stieltjes orders, compared to the "raw" spectrum as yielded from the respective ADC calculation. Plots were generated employing the fully diagonalized continuum-state spectrum.

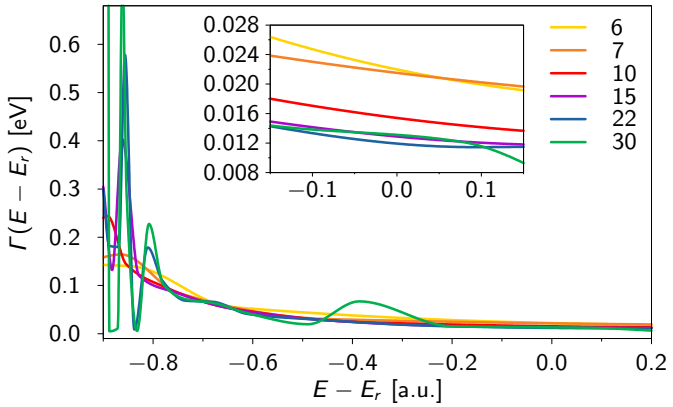

Figure VII.6. Decay width $\Gamma(E)$ connected to the neon $2s^{-1}3p$ resonance evaluated for different Stieltjes orders. A better approximation to the "raw" input spectrum is reflected in a less smooth distribution. Plots were generated employing the fully diagonalized continuum-state spectrum.

In the particular case of the neon $2s^{-1}3p$ resonance, Stieltjes orders as large as 30 still give satisfactory results, since the distribution $\Gamma(E)$ is sufficiently smooth in the region of the resonance energy. Another picture may be found for different systems, as is evident from Figure VII.7, which displays a similar plot for the naphthalene $9a_g{}^{-1}8b_{2u}$ resonance. Therein, convergence is observed between Stieltjes orders 8 and 12, and the width function becomes less smooth when going to higher orders as low as 15.

This effect can best be visualized by means of a graphical visualization of the decay width computed for increasing Stieltjes orders. Figure VII.8 shows the corresponding plot of the interpolated decay width $\Gamma(E_r)$ of the naphthalene $9a_g{}^{-1}8b_{2u}$ resonance for Stieltjes

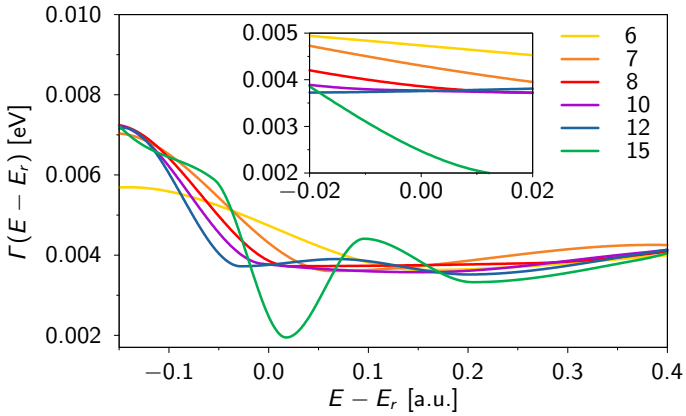

Figure VII.7. Decay width $\Gamma(E)$ connected to the naphthalene $8a_g{}^{-1}9b_{2u}$ resonance evaluated for different Stieltjes orders. Plots were generated using the continuum-state pseudo-spectrum obtained after 11 block-Lanczos iterations, employing an initial block of 81 vectors, i.e., 972 subspace vectors.

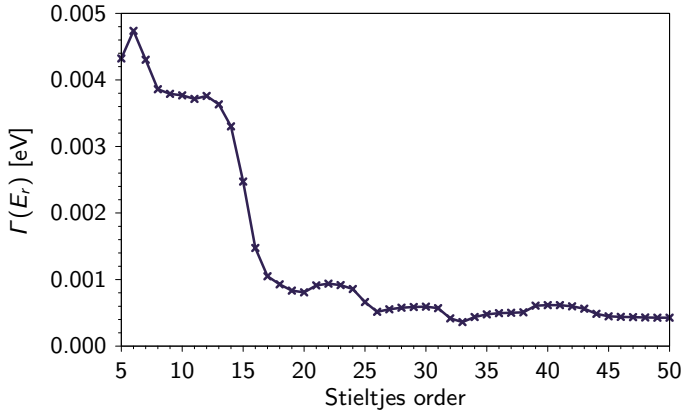

Figure VII.8. Interpolated values of the decay width $\Gamma(E_r)$ of the naphthalene $9a_g{}^{-1}8b_{2u}$ resonance for a series of Stieltjes orders between 5 and 50. As continuum-state spectrum, the pseudo-spectrum with 972 subspace vectors obtained after 11 block-Lanczos iterations was used.

orders 5 through 50.

At low Stieltjes orders, the decay width $\Gamma(E_r)$ quite quickly stabilizes at a plateau starting at Stieltjes order 8. For higher Stieltjes orders above 13, the imaging technique delivers less stable decay widths, and a massive decrease is seen, before the width stabilizes again at a value of $\Gamma(E_r) \approx 0.5\,\text{meV}$. The latter stabilization ows to the fact that the raw spectrum in the spectral region close to the resonance energy has already been restored completely for these "high" Stieltjes orders. Because only a smooth width function can be expected to yield physically meaningful information, proper autoionization widths should consequently rather be extracted from low Stieltjes orders, i.e., between orders 8 and 13.

VII.4. Applications of the Fano-Stieltjes-ADC Method

In order to verify the implementation and to evaluate the applicability of the methodology to larger molecular systems, a number of calculations have been conducted, whose results are presented in this section and, if possible, compared to experimental data or previous theoretical studies.

VII.4.1. Neon $2s^{-1}3p$ Resonance

The $2s^{-1}3p$ resonance in the neon atom is an autoionizing Feshbach resonance, the energy of which has been experimentally determined to be $E_r = 45.5\,\text{meV}$.[215, 216] The line width of this transition has been reported as $\Gamma(E_r) = 16 \pm 2\,\text{meV}$ and $\Gamma(E_r) = 13 \pm 2\,\text{meV}$ in Refs. [215] and [216], respectively.

A number of theoretical studies on this resonance state have been conducted.[140, 141, 216] Most notably, the same Fano-Stieltjes-ADC(2) and -ADC(2)-x methodology in conjunction with the same basis set as in this study has been used in Ref. [140]. The decay width computed using the new implementation can thus directly be compared to the previously determined theoretical values.

Table VII.1. Resonance parameters of the $2s^{-1}3p$ Feshbach resonance in the neon atom computed using the Fano-Stieltjes approach and employing bound and continuum state spectra obtained using different ADC(n) schemes. Decay widths Γ of the present study were obtained as the mean of the widths computed for Stieltjes orders 14 through 16.

ADC scheme	Ref. [140]		This study	
	E_r [eV]	Γ [meV]	E_r [eV]	Γ [meV]
ADC(1)	—	30.48	49.64	32.44
ADC(2)	—	8.93	44.77	10.67
ADC(2)-x	—	11.46	44.50	13.11
ADC(3)	—	—	46.23	20.38

The results obtained using fully diagonalized continuum state spectra are compiled in Table VII.1. It is notable that all ADC schemes except ADC(1) yield resonance energies differing by a maximum of $\pm 1\,\text{eV}$ from the experimentally determined value of $E_r = 45.5\,\text{eV}$. A similar situation is found for the decay width $\Gamma(E_r)$. The value computed at the ADC(2)-x level of 13.11 meV is in perfect agreement with the more recently determined experimental value of $13 \pm 2\,\text{meV}$.[216] Using ADC(2), a somewhat lower value of 10.67 meV is found. The ADC(3) value of $\Gamma(E_r) = 20.38\,\text{meV}$, however, is slightly too large, even if compared to the experimental value of $\Gamma(E_r) = 16 \pm 2\,\text{meV}$ given in Ref. [215]. Turning to the ADC(1) results, one notes that for this neon resonance state, qualitatively correct results can be obtained even at this rather low level of theory. For systems

with a more complex electronic structure, however, a similarly satisfactory performance of Fano-Stieltjes-ADC(1) cannot be expected.

It is noteworthy that the decay widths computed in this study are slightly higher than those given in Ref. [140]. The differences encountered may most likely result from differences in the Stieltjes procedure such as, e.g., energetic shift, Stieltjes order or the particular cubic Hermite spline used for interpolation of the numerical derivatives of the cumulative width function.

Table VII.2. Resonance width $\Gamma(E_r)$ of the $2s^{-1}3p$ Feshbach resonance in the neon atom computed using Fano-Stieltjes-ADC(2)-x with different numbers of block-Lanczos subspace vectors representing the continuum-state spectrum. The stated values were obtained as the mean of the widths computed for Stieltjes orders 14 through 16.

Block-Lanczos subspace size	ADC(2)-x	ADC(3)
	$\Gamma(E_r)$ [meV]	$\Gamma(E_r)$ [meV]
100	16.72	24.47
200	13.98	21.52
300	13.73	21.20
400	13.44	20.84
500	13.01	20.27
600	13.01	20.21
700	13.04	20.24
800	12.98	20.19
900	12.97	20.17
1000	12.99	20.20
6294 (full diag.)	13.11	20.38

In Table VII.2, the ADC(2)-x and ADC(3) decay widths computed using different numbers of block-Lanczos subspace vectors are summarized. A similar ADC(2)-x study of the same resonance, but employing a different basis set, has been presented in Ref. [141]. In the latter study, the dimension of the continuum-state diagonalization problem was 5500, and satisfactory widths were obtained with 500 to 600 block-Lanczos subspace vectors. Here, a similar convergence behavior is observed: The computed value drops with the number of block-Lanczos subspace vectors until it becomes nearly stationary. The width computed using 500 block-Lanczos vectors is already close to the value obtained by full diagonalization, and no large variations are found when increasing the continuum-state subspace size further.

VII.4.2. Benzene $3e_{2g}{}^{-1}3pe_{1u}$ Resonance

To further verify the presented Fano-Stieltjes-ADC implementation, the decay width of the $3e_{2g}{}^{-1}3pe_{1u}$ resonance in benzene was computed. In a previous study,[141] this resonance state had been targeted using the same methodology, i.e., Fano-Stieltjes-ADC(2)

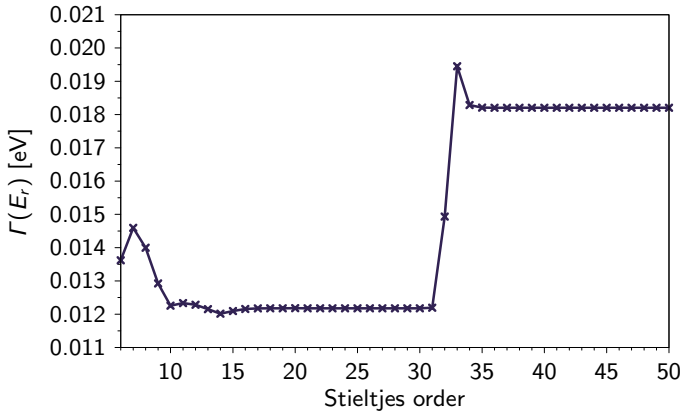

Figure VII.9. Decay width $\Gamma(E_r)$ of the $3e_{2g}{}^{-1}3p e_{1u}$ resonance in benzene computed for different Stieltjes orders. The continuum-state spectrum was computed by 50 block-Lanczos iterations, employing a starting block covering all 26 singly-excited configurations in the respective subspace.

in conjunction with block-Lanczos diagonalization of the continuum-state projected ADC matrix.

Unfortunately, no further information on the parameters used in the Stieltjes imaging procedure was provided, such that a reasonable choice of the Stieltjes order to use had to be determined first. For this purpose, it is helpful to inspect Figure VII.9, which displays the interpolated decay width $\Gamma(E_r)$ computed for different Stieltjes orders. As discussed above, the most trustworthy region is the first plateau, which in this case is encountered above Stieltjes order 10. Above order 16, a stabilization sets in and, although very similar to the values encountered between orders 10 and 16, this higher region is likely not usable. In the further investigation, the decay width is therefore taken as the mean of the values computed for Stieltjes orders 14 through 16.

Experimentally, the resonance position has been determined as $E_r \approx 9.3\,\text{eV}$,[217] but no experimental measurement of the decay width is available. The ADC(2) resonance energy computed employing the bound-state subspace projection scheme displayed in Figure VII.1 was given in Ref. [141] as $E_r = 9.52\,\text{eV}$. In the present study, the same ADC(2)/aug-cc-pVDZ method yielded a value of $E_r = 9.51\,\text{eV}$, but the source of this discrepancy could not be determined.

Table VII.3 shows a comparison of the decay widths available through Ref. [141] and computed in the present work. It is easily noticed that there are considerable differences between the two series of computed decay widths. In particular, the convergence is considerably faster in the present study, where the final result is recovered after only 10 block-Lanczos iterations, i.e., after 260 subspace vectors have been computed. The reason

Table VII.3. Resonance width $\Gamma(E_r)$ of the $3e_{2g}{}^{-1}3pe_{1u}$ Feshbach resonance of the benzene molecule using Fano-Stieltjes-ADC(2) with different numbers of block-Lanczos subspace vectors representing the continuum-state spectrum. The stated values were obtained as the mean of the widths computed for Stieltjes orders 14 through 16.

Block-Lanczos subspace size	Ref. [141]	This study
	$\Gamma(E_r)$ [meV]	$\Gamma(E_r)$ [meV]
26	6.1	0.00972
130	12.9	12.22
260	13.6	12.09
780	14.9	12.09
1300	15.0	12.09

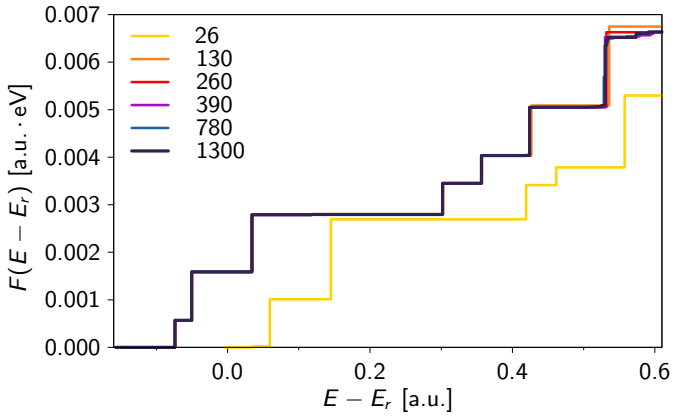

Figure VII.10. Cumulative width $F(E - E_r)$ of the $3e_{2g}{}^{-1}3pe_{1u}$ resonance of the benzene molecule computed for continuum-state pseudo-spectra generated from different numbers of block-Lanczos subspace vectors.

for this is that in this case the block-Lanczos procedure converges extremely fast, as is visible from Figure VII.10.

In the vicinity of $E - E_r = 0$, a reasonable approximation for the cumulative width computed from the continuum-state pseudo-spectrum constructed from 1300 block-Lanczos vectors is already achieved with 130 subspace vectors. Figure VII.10 also reveals the reason for the failure in case of only 26 subspace vectors: The cumulative width is neither with respect to structure nor to state energies (rise points) satisfactorily well described. The latter observation is, however, not unexpected since block-Lanczos diagonalization using a starting block of all single excitations is equivalent to diagonalization of the singles-singles block of the ADC matrix, treated separately from the doubles-doubles and coupling blocks. Contributions from doubly-excited configurations, usually needed to describe electronic correlation, are thus completely neglected.

Another observation is that the block-Lanczos spectrum obtained after 50 iterations, i.e.,

that computed from 1300 subspace vectors, is converged with respect to full diagonalization within the lowest 18 eV, the largest residual vector norm in this range being below 10^{-6}. It is therefore clear that further enlargement of the block-Lanczos subspace will not have any impact on the final result for the decay width.

Taking together these findings, it cannot be stated what the source of the differences with respect to Ref. [141] is. The convergence behavior of the block-Lanczos pseudo-spectra computed using the presented implementation is, however, fully consistent with the observed convergence of the decay widths. It was therefore concluded that the methodology can be safely applied to larger molecular systems.

VII.4.3. Application to Larger Molecules: Naphthalene

The Fano-Stieltjes-ADC methodology was subsequently applied for the study of a Feshbach resonance in naphthalene. In this case, no experimental data is available. However, by comparison of threshold and He I photoelectron spectra it has been concluded that a considerable share of the full photoelectron yield above the lowest ionization potential of 8.14 eV is in fact a result of autoionization processes.[218] Especially in the region just below the second ionization potential of 8.91 eV, i.e., between 8.6 eV and 8.9 eV an intense background photoelectron yield was recorded.[218]

In this region, an ADC(2)/aug-cc-pVDZ calculation in the full configuration space predicts a strong transition of B_{2u} symmetry at 8.81 eV with an oscillator strength of 0.114, the leading configuration with respect to the ground state being $9a_g{}^{-1}8b_{2u}$. This transition was further investigated using the Fano-Stieltjes-ADC methodology.

First, a suitable scheme for the bound-state subspace projection was determined. For this purpose, different ranges of occupied orbitals were allowed for forming singly-excited configurations. The occupied orbital ordering is schematically depicted in Figure VII.2, which also displays the continuum-state subspace projection scheme employed throughout this section. In the respective calculations, a continuum-state block-Lanczos pseudo-spectrum computed from 324 subspace vectors was employed.

The interpolated decay widths computed for different bound-state subspace projection schemes are displayed in Figure VII.11. As a first observation, there are no large differences between different projection schemes. In addition, a clustering can be seen at approximately 3.8 meV. Table VII.4 summarizes the computed resonance parameters.

The variation of the state energies computed using the different considered projection schemes lies within a range of ∼1 %. The variations in the computed decay widths are somewhat larger, but still well below the uncertainty caused by the Stieltjes imaging

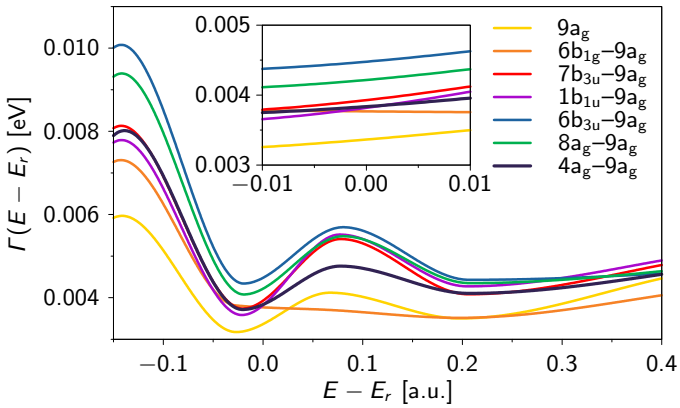

Figure VII.11. Interpolated width function obtained at Stieltjes order 12 using different bound-state subspace projection schemes. The full valence configuration space was used for doubly-excited configurations, while single excitations were restricted to those having a hole in the occupied orbital range stated for each individual case.

Table VII.4. Resonance parameters computed for various bound-state subspace projection schemes. Holes of singly-excited configurations were allowed only in the range of occupied orbitals specified in each case. The whole valence space was used for the doubles part. The given widths were taken as the mean of the widths computed for Stieltjes orders 10 through 12 using a continuum-state pseudo-spectrum obtained from 324 block-Lanczos vectors.

Singles hole conf. space	E_r [eV]	$\Gamma(E_r)$ [meV]	osc. strength
$9a_g$	8.81	3.39	0.112
$6b_{1g}$–$9a_g$	8.86	3.74	0.100
$7b_{3u}$–$9a_g$	8.87	4.04	0.095
$1b_{1u}$–$9a_g$	8.88	3.93	0.095
$6b_{3u}$–$9a_g$	8.88	4.54	0.072
$8a_g$–$9a_g$	8.90	4.30	0.080
$4a_g$–$9a_g$	8.91	3.88	0.095

procedure. It seems thus reasonable to follow a similar approach as in the case of benzene, i.e., to allow the hole of singly-excited configurations to be in the $6b_{1g}$ and $9a_g$ orbitals only, and this bound-state subspace projection scheme was used throughout the remaining part of this section.

As already discussed in Section VII.2, a fast convergence of the computed width with respect to the block-Lanczos subspace size can be expected. This assumption is confirmed by the results summarized in Table VII.5. Nearly perfect convergence to the final value of $\Gamma(E_r) = 3.75\,\text{meV}$ is already seen after four block-Lanczos iterations, resulting in a matrix size of 324. This observation is thus in line with the prediction based on the inspection of Figure VII.4, i.e., that the cumulative width is satisfactorily well described once it has converged to a mutually consistent global shape.

Table VII.5. Resonance width $\Gamma(E_r)$ of the $9a_g{}^{-1}8b_{2u}$ Feshbach resonance of the naphthalene molecule computed using Fano-Stieltjes-ADC(2) with different numbers of block-Lanczos subspace vectors representing the continuum-state spectrum. The stated values were obtained as the mean of the widths computed for Stieltjes orders 10 through 12.

Block-Lanczos subspace size	$\Gamma(E_r)$ [meV]
81	0.21
162	4.06
324	3.74
486	3.74
648	3.75
810	3.75
972	3.75

The results presented in this section show that the Fano-Stieltjes-ADC methodology can be applied to medium-sized organic molecules. One of the necessary properties is that the energy and character of the resonance state in question change only marginally when modifying the subspace projection scheme. In contrast to previous findings,[141] ADC schemes fulfill this prerequisite, as can be followed from the results presented in Table VII.4. A second prerequisite is the replacement of the fully diagonalized continuum-state spectrum by a computationally feasible alternative as provided by block-Lanczos pseudo-spectra. The very fast convergence found for benzene and naphthalene (Tables VII.3 and VII.5), suggests that the application of the Fano-Stieltjes-ADC methodology for the description of resonances in even larger molecular systems is possible.

Chapter VIII

Methodological Aspects and Pilot Applications of CAP-EA-ADC

The implementation of the novel CAP-EA-ADC approach as described in Section III.5 was subsequently applied for the computational description of a number of π^* resonance states. As a first test, different methodological aspects were investigated at the example of the well-studied $^2\Pi_g$ resonance state of the dinitrogen anion N_2^- (Section VIII.2). The applicability of the method was further evaluated in a study of π^* resonances in unsaturated organic hydrocarbons, namely ethylene (Section VIII.3.1) as well as norbornadiene and 1,4-cyclohexadiene (Section VIII.3.2). The diene molecules are of particular interest because the properties of π^* resonance states can directly be interpreted by means of the concept of through-bond and through-space interactions, which has been an active field of research for a long time.[219, 220]

VIII.1. Computational Details

All results presented in this chapter were computed using a development version of the Q-Chem software[75] based on version 5.2.

For the dinitrogen molecule, an internuclear distance of 2.074 r_{Bohr} was assumed. In the remaining cases, molecular geometries obtained for the neutral molecules at the MP2/cc-pVTZ[179] level of theory were employed throughout, being of D_{2h} symmetry in the case of ethylene and cyclohexadiene and C_{2v} symmetry in the case of norbornadiene.

In the case of dinitrogen, the aug-cc-pVQZ basis set[179, 180] was employed on the nitrogen atoms, and additional $3s3p3d$ diffuse functions were added on the molecular center. The exponents of the additional functions were: 0.0273200, 0.0136600, 0.0068300 (s); 0.0220100, 0.0110050, 0.0055025 (p); 0.0555000, 0.0277500, 0.0138750 (d). For ethylene,

cyclohexadiene and norbornadiene, two different basis set combinations were used: i) cc-pVDZ[179] on hydrogen atoms and aug-cc-pVDZ[179, 180] on carbon atoms, with additional $4p1d$ diffuse functions centered at the carbon atoms, the exponents being 0.0269400, 0.0179600, 0.0119733, 0.0079822 (p) and 0.0755000 (d), denoted "DZ" throughout the remaining part of this chapter; ii) cc-pVTZ[179] on hydrogen atoms and aug-cc-pVTZ[179, 180] on carbon atoms, with additional $4p1d$ diffuse functions centered at the carbon atoms, the exponents being 0.0237933, 0.0158622, 0.0105748, 0.0070499 (p) and 0.0400000 (d), denoted "TZ" throughout the remaining part of this chapter.

In the case of third-order EA-ADC calculations, two schemes differing by the static self-energy treatment were used: i) a scheme in which the third-order static self-energy and corresponding ground state density was used throughout (denoted as "strict" EA-ADC(3) scheme), and ii) a scheme employing the improved fourth-order static self-energy and corresponding ground state density computed according to the $\Sigma(4+)$ procedure (denoted as "standard" EA-ADC(3) scheme).

CAP-EA-ADC calculations were performed using the implementation presented in Section III.5 based on the subspace projection approach discussed in Section II.3.3. A smoothed Voronoi CAP with an onset of $r_{\text{cut}} = 3.5\, r_{\text{Bohr}}$ was employed throughout, whose basis set representation was computed by numerical quadrature on a grid consisting of 974 Lebedev angular and 250 Euler-MacLaurin radial points as implemented in Q-Chem 5.2 (i.e., by setting `XC_GRID=000250000974`).

The number of EA-ADC vectors with lowest eigenvalues included within the CAP calculations were: 30 (ethylene anion B_{2g} resonance), 30 (cyclohexadiene anion A_u and B_{2g} resonances), 50 (norbornadiene anion A_2 resonance) and 30 (norbornadiene anion B_2 resonance). If not stated otherwise, in the case of the dinitrogen anion $^2\Pi_g$ resonance the number of subspace vectors included was 49 (strict and standard EA-ADC(3)) or 37 (EA-ADC(2)).

If not explicitly specified otherwise, trajectories were computed for real potential strengths η, and resonance parameters were extracted from the corrected trajectories according to Eq. (2.85) at the minimum of the respective logarithmic velocity (2.88).

Finally, Dyson orbital plots were generated using version 1.9.4a27 of the VMD software,[205] employing input data obtained by linear combination of Dyson orbitals computed for EA-ADC(2)/TZ eigenstates of the respective non-CAP-augmented EA-ADC Hamiltonians as outlined in Section II.3.4. Isosurfaces were drawn at function values of 0.0175 (cyclohexadiene anion A_u and B_{2g} resonances), 0.02 (norbornadiene anion A_2 resonance) and 0.0175 (norbornadiene anion B_2 resonance).

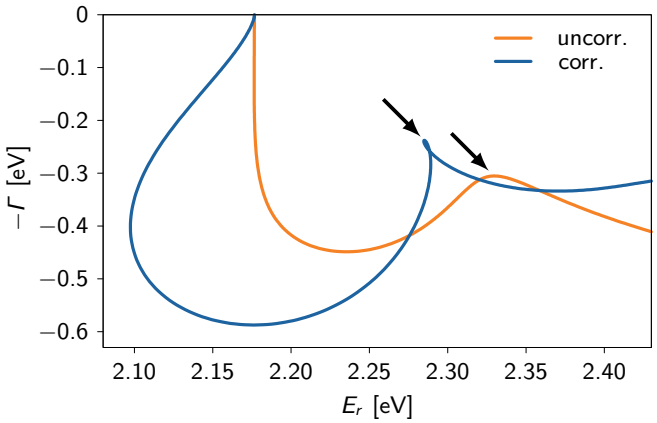

Figure VIII.1. Corrected (blue) and uncorrected (orange) complex energy trajectories for the $^2\Pi_g$ resonance of the dinitrogen anion computed using the standard EA-ADC(3) scheme. The resonance positions are marked with arrows.

VIII.2. A First Test: $^2\Pi_g$ Resonance of the Dinitrogen Anion

As a first test of CAP-EA-ADC, the new method was applied for the calculation of the position and width of the $^2\Pi_g$ resonance of the dinitrogen anion N_2^-, which has been subject of extensive studies in the past decades. A compilation of resonance positions and widths computed using a variety of theoretical approaches can be found in Ref. [153].

The most accurate theoretical value so far was obtained using a Feshbach projection formalism based on experimental data.[221] In the respective study, a resonance position of $E_r = 2.32\,\text{eV}$ and a width of $\Gamma = 0.41\,\text{eV}$ was found, and these values have been used as a reference since then.

The corrected and uncorrected trajectories computed using standard CAP-EA-ADC(3) are depicted in Figure VIII.1. At the minimum of the logarithmic velocity, a resonance position of $E_r = 2.33\,\text{eV}$ and a decay width of $\Gamma = 0.31\,\text{eV}$ were obtained from the uncorrected trajectory. Using the corrected trajectory, similar resonance parameters were found, the resonance energy and width being $E_r = 2.28\,\text{eV}$ and $\Gamma = 0.24\,\text{eV}$, respectively.

In this case, the results extracted from the uncorrected trajectory show thus smaller deviations from the reference values, and this observation is particularly pronounced for the resonance width. For the resonance position, however, both treatments yield excellent values, the deviation of the corrected value from the reference being as small as 0.05 eV. The decay widths, on the other hand, lie well within the usual range of variation, as shows a comparison with values obtained using different theoretical approaches. As an example,

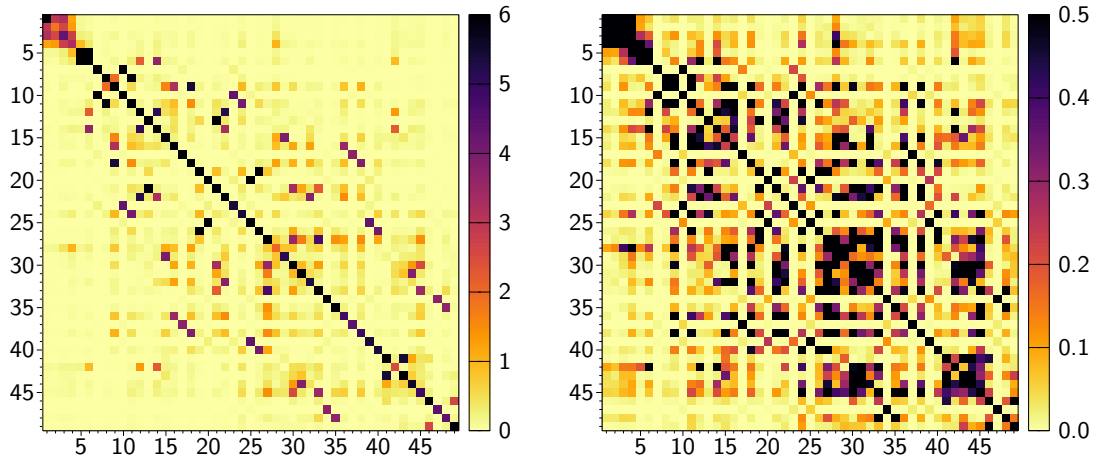

Figure VIII.2. Representation of a smoothed Voronoi potential ($r_{\mathrm{cut}} = 3.5\, r_{\mathrm{Bohr}}, \eta = 1$) in the subspace of the 49 lowest converged standard EA-ADC(3) states of the dinitrogen molecule, ordered by their respective energies. Different cutoff values have been used for the representation, such that all matrix elements with absolute values larger than the cutoff value are displayed in black. Left panel: states with bright diagonal elements are compact and thus likely to represent resonance states; the $^2\Pi_g$ resonance is best approximated by the second-lowest state. Right panel: Dark off-diagonal elements represent reasonable couplings; the second-lowest state couples virtually only within the subspace of the few lowest states.

one can consider a corresponding CAP-EOM-EA-CCSD study for comparison, in which the same trend has been observed for the decay width.[153] Employing the same basis set as in the present study, the uncorrected and corrected treatments yielded decay widths of $\Gamma = 0.364\,\mathrm{eV}$ and $\Gamma = 0.286\,\mathrm{eV}$, respectively.

VIII.2.1. Choice of the Subspace

After this first encouraging result, the problem of the choice of the subspace of EA-ADC states used for the representation of the CAP was addressed. In this respect, it is helpful to recall that an exact description of a resonance state and its complex Siegert energy is achieved in the limit of vanishing potential strengths, $\eta \to 0^+$,[125] provided that a complete basis set is employed. Hence, an electronic structure calculation employing a truncated basis set of reasonable spatial extension can be expected to yield an approximate description of a resonance state too, even the potential strength is zero. Compared to diffuse continuum-like states, the interaction of resonance states with the CAP should be considerably smaller due to their bound nature.

This behavior can be observed in Figure VIII.2, in which the representation of a smoothed Voronoi potential with an onset parameter of $r_{\mathrm{cut}} = 3.5\, r_{\mathrm{Bohr}}$ within the subspace of the 49 lowest standard EA-ADC(3) states of the dinitrogen molecule is visualized.

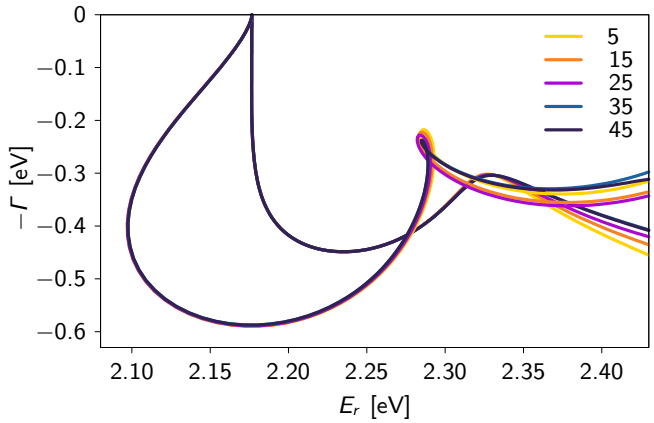

Figure VIII.3. Corrected and uncorrected resonance energy trajectories of the dinitrogen anion $^2\Pi_g$ resonance. Different numbers of (standard) EA-ADC(3) states were considered for the CAP subspace representation.

Focusing on the left panel, the diagonal values give a metric how strong the direct interaction of a particular state with the potential is. Within this subspace, the state with the weakest interaction (brightest diagonal element) is the second-lowest one, and indeed this state approximates the $^2\Pi_g$ resonance of N_2^-.

One can now estimate which states will have the strongest effect on the resonance upon addition of the CAP by considering the direct couplings, i.e., the off-diagonal elements belonging to the second-lowest state. Inspection of these elements in the left panel of Figure VIII.2 shows that strong direct couplings only exist among the four lowest states. There is actually also a physical reasoning behind this finding: Only continuum states which are energetically accessible, i.e., those close in energy to the resonance state, may substantially contribute as decay channels. In this specific case, there are only four additional states within the range of $E_r \pm 5\,\mathrm{eV}$.

However, some additional states may be involved by means of indirect or weaker direct coupling. The right panel of Figure VIII.2 displays the same representation of the potential with a different color scheme favoring small matrix elements. From this it is evident that also states 5 and 28 might have reasonable contributions to the resonance.

In order to investigate the effect of the subspace choice further, trajectories were computed for different numbers of EA-ADC eigenstates. Since the $^2\Pi_g$ resonance is located close to the lower boundary of the spectrum, continuous subspaces at the low end of the spectrum were chosen. Figure VIII.3 displays the corrected and uncorrected trajectories computed using different EA-ADC eigenstate subspace sizes.

For small potential strengths, resulting in computed widths Γ close to zero, barely any

difference can be observed between the trajectories computed using different subspace sizes. The variations get more pronounced for stronger potentials, i.e., at the right edge of the plot displayed in Figure VIII.3. In this system, larger deviations are seen just beyond the stabilization point. The resonance parameters extracted from the corrected and uncorrected trajectories are summarized in Table VIII.1.

Table VIII.1. Resonance parameters of the N_2^- $^2\Pi_g$ resonance extracted from the uncorrected and corrected trajectories for different numbers of standard EA-ADC(3) vectors considered for the CAP subspace projection.

subspace size	Uncorrected			Corrected		
	E_r [eV]	Γ [eV]	η_{opt}	E_r [eV]	Γ [eV]	η_{opt}
5	2.325	0.303	0.0276	2.286	0.218	0.0563
15	2.326	0.304	0.0275	2.285	0.223	0.0533
25	2.326	0.305	0.0273	2.284	0.229	0.0529
35	2.327	0.306	0.0272	2.285	0.239	0.0504
45	2.327	0.306	0.0272	2.285	0.238	0.0531
49	2.327	0.306	0.0272	2.285	0.238	0.0516

As already implied by Figure VIII.3, nearly no differences are observed between the smallest and largest subspace considered in case of the uncorrected treatment. For the corrected treatment, slightly larger changes towards larger decay widths are observed when increasing the subspace size used for the CAP representation. The resonance position, on the other hand, is still nearly unaffected.

The results presented in this section give thus strong support for the applicability of the subspace projection approach. The choice of the subspace, however, has to be considered carefully for each system and resonance state. As a rule of thumb, an energy criterion may be used to decide which EA-ADC states to consider for the CAP subspace projection: in the investigated case of the $^2\Pi_g$ resonance of the dinitrogen anion, a subspace composed of all states within the range of $E_r \pm 5\,\mathrm{eV}$ is sufficient to achieve satisfactory results.

VIII.2.2. The Effect of Different EA-ADC Approximation Schemes

So far only the standard EA-ADC(3) scheme has been considered. In this section, a brief comparison of the performance of different EA-ADC schemes is given.

Figure VIII.4 displays the corrected (dashed) and uncorrected (solid) trajectories computed using standard and strict EA-ADC(3) as well as EA-ADC(2). The resonance parameters extracted from the respective trajectories are summarized in Table VIII.2.

In comparison with standard EA-ADC(3), the strict EA-ADC(3) scheme yields width values closer to the reference value of $\Gamma = 0.41\,\mathrm{eV}$.[221] At the same time, larger errors of 0.10 eV and 0.15 eV are found for the corrected and uncorrected resonance positions,

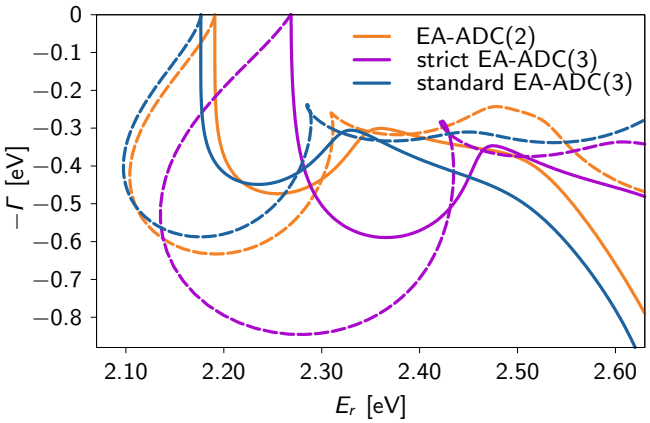

Figure VIII.4. Corrected (dashed) and uncorrected (solid) resonance energy trajectories of the dinitrogen anion $^2\Pi_g$ resonance computed using different EA-ADC schemes.

Table VIII.2. Resonance parameters of the N_2^- $^2\Pi_g$ resonance extracted from the uncorrected and corrected trajectories computed using different EA-ADC schemes.

EA-ADC scheme	Uncorrected			Corrected		
	E_r [eV]	Γ [eV]	η_{opt}	E_r [eV]	Γ [eV]	η_{opt}
EA-ADC(2)	2.354	0.302	0.0283	2.310	0.260	0.0494
strict EA-ADC(3)	2.471	0.348	0.0276	2.421	0.279	0.0533
standard EA-ADC(3)	2.327	0.306	0.0272	2.285	0.238	0.0516

respectively. Most notably, the level of accuracy found for EA-ADC(2) is comparable to that of standard EA-ADC(3). Especially the resonance position obtained from the corrected trajectory is in excellent agreement with the reference value of $E_r = 2.32\,\text{eV}$, showing an error of only 0.01 eV.

VIII.2.3. Extension to Complex Potential Strengths

Within the subspace-projected CAP approach, it is straightforward to extend the methodology to complex potential strengths $\eta = |\eta|\,(\cos\vartheta + i\sin\vartheta)$, since only minor modifications of the η-trajectory generating code are required. Here, an approach similar to that introduced in the context of CAP-XMCQDPT2[130] has been followed and is presented in this section.

As discussed in Section II.3.1, the logarithmic velocity of the complex energy of a resonance state with respect to the potential strength parameter can be considered a metric for the quality of the approximation (cf. Eq. (2.84)). Figure VIII.5 displays a plot of this quantity for a section of the two-dimensional $\{|\eta|, \vartheta\}$ parameter space.

Therein, minima correspond to the best approximations of the complex energy $E(\eta)$

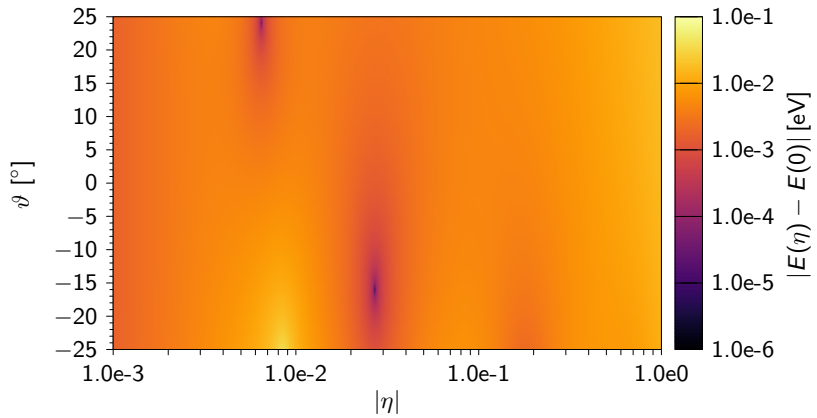

Figure VIII.5. Logarithmic velocity of the uncorrected trajectory $|E(\eta) - E(0)|$ (cf. Eq. (2.84)) evaluated for complex potential strengths $\eta = |\eta|\,(\cos\vartheta + i\sin\vartheta)$.

with respect to the exact Siegert energy $E(0)$. The global minimum in this section of the parameter space is located at $(|\eta|_{\text{opt}}\,, \vartheta_{\text{opt}}) = (0.0270, -16.0\,^\circ)$, for which the resonance parameters are $E_r = 2.328\,\text{eV}$ and $\Gamma = 0.317\,\text{eV}$. Compared to the case of purely real potential strengths discussed above, a small improvement in the resonance width is observed, while the resonance position is virtually unchanged.

One also easily notices that the stabilization point computed for different angles $\vartheta \lesssim 5\,^\circ$ is found at very similar potential strengths $|\eta|$, reflected in a nearly perfectly vertical "valley" in Figure VIII.5 at $|\eta| \approx 0.027$.

Combining these findings, additional accuracy may be gained by going to complex potential strengths. However, the treatment using real potential strengths (and thus, a purely imaginary CAP) yields similarly accurate results, and this methodology will consequently be used throughout the remaining part of this chapter.

VIII.3. π^* Resonances in Unsaturated Hydrocarbons

Temporary anion π^* resonances have been commonly observed in many unsaturated organic molecules.[102, 104] Because knowledge about different aspects of the electronic structure of π-conjugated molecules can be gained from related studies, a lot of experimental as well as theoretical work has been devoted to this topic.

VIII.3.1. Ethylene

The prototype of this molecular class is ethylene, for which a π^* shape resonance of B_{2g} symmetry has been experimentally identified.[102, 222] In these studies, the resonance

energy was determined as $E_r = 1.78\,\text{eV}$ by electron transmission spectroscopy (ETS)[102] and later as $E_r \approx 1.8\,\text{eV}$ in elastic electron scattering (ES) experiments.[222] In the latter work, this resonance state was found to have a width of $\Gamma = 0.7\,\text{eV}$.

A compilation of the various available theoretical resonance parameters is given in Ref. [153]. Most notably, CAP-EOM-EA-CCSD calculations yielded a resonance energy of $E_r = 2.091\,\text{eV}$ using the corrected trajectory, while the corresponding decay width was stated as $\Gamma = 0.430\,\text{eV}$.[153]

Table VIII.3. Resonance parameters of the ethylene $^2B_{2g}$ resonance as extracted from the corrected trajectory computed using different EA-ADC schemes and employing double-zeta (DZ) and triple-zeta (TZ) basis sets as specified in Section VIII.1.

EA-ADC scheme	DZ			TZ		
	E_r [eV]	Γ [eV]	η_{opt}	E_r [eV]	Γ [eV]	η_{opt}
EA-ADC(2)	2.029	0.435	0.0424	1.802	0.353	0.0294
strict EA-ADC(3)	2.155	0.537	0.0435	2.048	0.547	0.0297
standard EA-ADC(3)	2.098	0.492	0.0435	1.971	0.478	0.0298

Table VIII.3 summarizes the results obtained using CAP-EA-ADC. As it has already been observed for the $^2\Pi_g$ resonance of the dinitrogen anion, EA-ADC(2) performs extraordinarily well with respect to the resonance position. The value obtained using the triple-zeta basis set is perfectly in line with the experimental value of $E_r = 1.80\,\text{eV}$. The resonance width, on the other hand, seems to be better reproduced by the EA-ADC(3) treatment, where the differences between strict and standard EA-ADC(3) are generally not as pronounced as in the case of N_2^-.

VIII.3.2. Dienes: 1,4-Cyclohexadiene and Norbornadiene

In the past decades, there has been a long-standing discussion among physical organic and theoretical chemists, if the interaction of different π-type orbitals in cyclic diene molecules may lead to a "reversal" of the energetic ordering of the molecular orbitals constructed from them. In this context, the concept of *through-space* and *through-bond* interactions was introduced.[220]

In systems where a mostly independent treatment of the electronic π-system is possible, i.e., in which no additional orbitals of appropriate symmetry exist, molecular orbitals can simply be constructed by linear combination of all available ethylenic π orbitals, in which case the interaction is called *through-space*, causing a *natural* ordering of the π-type molecular orbitals. This situation is given for the norbornadiene molecule, where two unoccupied π^* molecular orbitals can be constructed from the two ethylenic π^* orbitals. The symmetric "+"-combination π_+^*, i.e., the combination minimizing the number of nodal

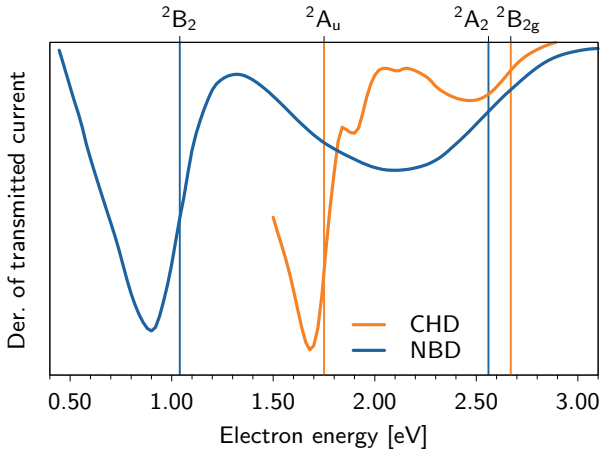

Figure VIII.6. Electron transmission spectra recorded for norbornadiene (NBD, blue) and 1,4-cyclohexadiene (CHD, orange). Experimentally determined resonance energies are indicated by vertical lines. Data digitized from Ref. [223].

planes, should consequently have a lower orbital energy than the antisymmetric "−"-combination π^*_-.

By contrast, in the case of 1,4-cyclohexadiene, additional orbitals of compatible symmetry can be constructed by linear combination of the four C-H σ orbitals located at the methylene moieties. In particular, an interaction with the π^*_+ orbital can lead to an upshift of the latter such that its orbital energy becomes larger than that of the π^*_- molecular orbital.

Direct experimental observation of molecular orbitals is, however, not possible because they are not physical observables but rather a mathematical concept. As has been discussed in Section II.1.6, Dyson orbitals connected to electron-detachment and attachment processes are mostly determined by a single occupied and unoccupied molecular orbital, respectively, if the considered process is dominated by a single one-electron transition. Similarly, orbital energies can be recovered as electron-attachment or detachment energies.

In case of unoccupied π^* molecular orbitals of norbornadiene and 1,4-cyclohexadiene, the electron-attached states to be investigated are actually resonance states, which were experimentally identified by electron transmission spectroscopy,[223] and eventually assigned using, e.g., high-energy electron impact measurements,[224] also supported by comparative ETS studies of 1,4-dioxane and similar molecular systems.[225] The recorded electron transmission spectra of both diene molecules are displayed in Figure VIII.6.

According to these studies, the $^2B_{2g}$ resonance in 1,4-cyclohexadiene (π^*_+ combination) is indeed found at a higher energy of $E_r = 2.67\,\text{eV}$ than the ^2A_u state (π^*_- combination)

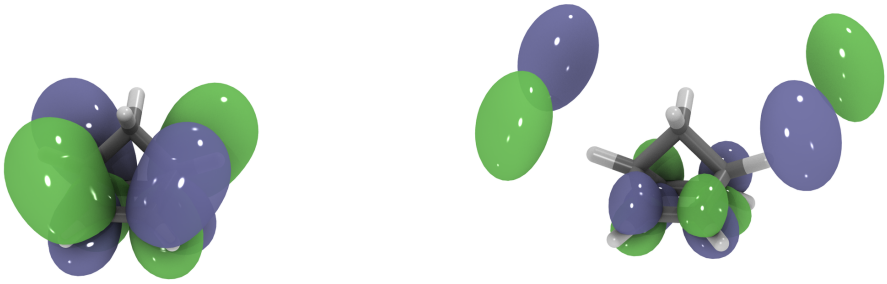

Figure VIII.7. Real (left) and imaginary (right) parts of the Dyson orbital connected to the $^2A_2$ shape resonance in norbornadiene computed at the EA-ADC(2)/TZ level of theory.

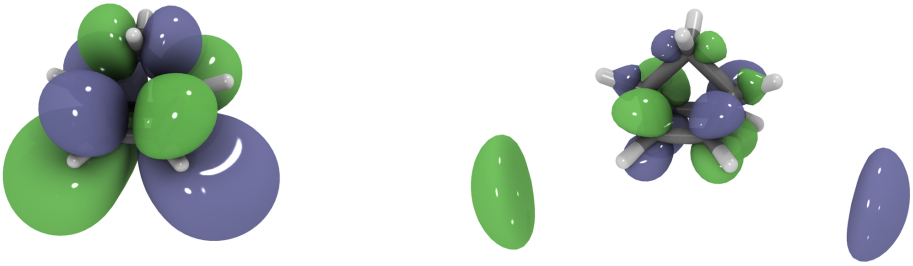

Figure VIII.8. Real (left) and imaginary (right) parts of the Dyson orbital connected to the $^2B_2$ shape resonance in norbornadiene computed at the EA-ADC(2)/TZ level of theory.

with a resonance energy of $E_r = 1.75\,\text{eV}$. On the contrary, in norbornadiene the normal ordering is preserved, meaning that the $^2B_2$ resonance (π^*_+ combination) is observed at a lower energy of $E_r = 1.04\,\text{eV}$ than the $^2A_2$ resonance (π^*_- combination), for which the resonance energy was determined as $E_r = 2.56\,\text{eV}$. However, the lack of vibrational resolution in the electron transmission spectra forbids the determination of resonance widths for all considered resonance states.

On the theoretical side, a number of studies have been conducted, most notably using the stabilization technique,[226, 227] confirming the reversal of the energetic ordering of the π^* orbitals in 1,4-cyclohexadiene. Here, the π^* resonance states are studied using CAP-EA-ADC.

The real and imaginary parts of the Dyson orbitals of the $^2A_2$ and $^2B_2$ resonance states of norbornadiene as calculated on the CAP-EA-ADC(2)/TZ level of theory are displayed in Figures VIII.7 and VIII.8, respectively. Indeed, in the case of the π^*_+ combination ($^2B_2$, Figure VIII.8), there is also a through-bond contribution arising from orbitals not located at the double bonds but at the bridging methylene moiety. However, at the bottom side of the molecule, a direct through-space interaction not mediated by additional bonds is possible, reflected in the absence of a vertical nodal plane parallel to the double bonds. The resonance positions and decay widths computed for norbornadiene are summarized

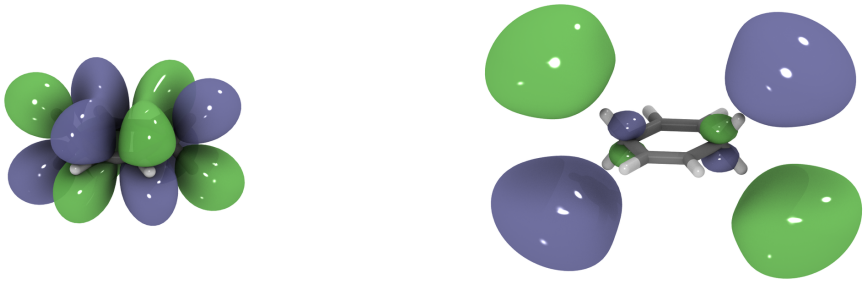

Figure VIII.9. Real (left) and imaginary (right) parts of the Dyson orbital connected to the $^2B_{2g}$ shape resonance in 1,4-cyclohexadiene computed at the EA-ADC(2)/TZ level of theory.

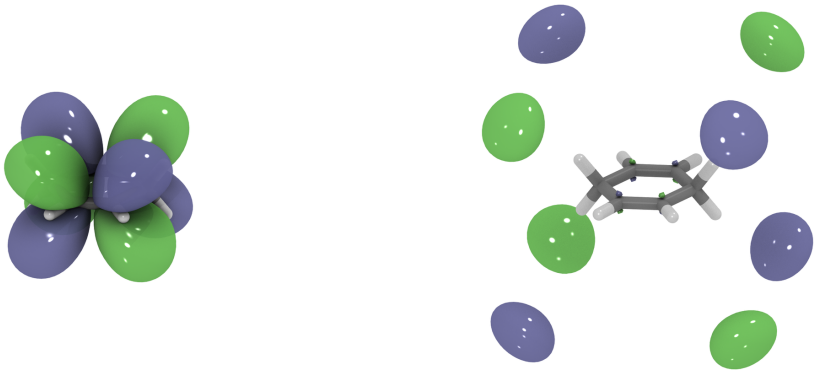

Figure VIII.10. Real (left) and imaginary (right) parts of the Dyson orbital connected to the ^2A_u shape resonance in 1,4-cyclohexadiene computed at the EA-ADC(2)/TZ level of theory.

in Table VIII.4.

The computed resonance parameters indicate that the π^* resonance states of the norbornadiene anion indeed follow a natural energetic ordering: The resonance position of the π^*_+ ($^2B_2$) state predicted by CAP-EA-ADC(2)/TZ is $E_r = 0.955\,\text{eV}$, being only approximately 0.08 eV lower than the experimental value of $E_r = 1.04\,\text{eV}$.[223] The energy

Table VIII.4. Resonance parameters of the $^2B_2$ and $^2A_2$ anionic shape resonances of norbornadiene as extracted from the corrected trajectories computed using different EA-ADC schemes and employing double-zeta (DZ) and triple-zeta (TZ) basis sets as specified in Section VIII.1. The experimentally determined resonance positions are $E_r(^2B_2) = 1.04\,\text{eV}$ and $E_r(^2A_2) = 2.56\,\text{eV}$.[223]

State	EA-ADC scheme	DZ			TZ		
		E_r [eV]	Γ [eV]	η_{opt}	E_r [eV]	Γ [eV]	η_{opt}
$^2B_2$	EA-ADC(2)	1.185	0.216	0.0243	0.955	0.189	0.0066
	strict EA-ADC(3)	1.577	0.379	0.0152	1.564	0.410	0.0108
	standard EA-ADC(3)	1.563	0.362	0.0151	1.495	0.351	0.0106
$^2A_2$	EA-ADC(2)	2.822	0.738	0.0186	2.591	0.670	0.0074
	strict EA-ADC(3)	3.647	1.192	0.108	3.322	1.067	0.0385
	standard EA-ADC(3)	3.626	1.186	0.106	3.270	0.974	0.0401

Table VIII.5. Resonance parameters of the $^2B_{2g}$ and ^2A_u anionic shape resonances of 1,4-cyclohexadiene as extracted from the corrected trajectories computed using different EA-ADC schemes and employing double-zeta (DZ) and triple-zeta (TZ) basis sets as specified in Section VIII.1. The experimentally determined resonance positions are $E_r(^2B_{2g}) = 2.67\,\text{eV}$ and $E_r(^2A_u) = 1.75\,\text{eV}$.[223]

State	EA-ADC scheme	DZ			TZ		
		E_r [eV]	Γ [eV]	η_{opt}	E_r [eV]	Γ [eV]	η_{opt}
$^2B_{2g}$	EA-ADC(2)	2.922	0.096	0.0196	2.651	0.078	0.0137
	strict EA-ADC(3)	3.253	0.162	0.0199	3.185	0.228	0.0162
	standard EA-ADC(3)	3.203	0.148	0.0200	3.090	0.175	0.0151
^2A_u	EA-ADC(2)	1.974	0.178	0.0124	1.735	0.127	0.0086
	strict EA-ADC(3)	2.359	0.233	0.0480	2.289	0.240	0.0336
	standard EA-ADC(3)	2.311	0.215	0.0477	2.203	0.205	0.0335

computed for the π^*_- ($^2A_2$) state, on the other hand, is $E_r = 2.591\,\text{eV}$ (experimental value: $E_r = 2.56\,\text{eV}$), and thus considerably higher than that of the π^*_+ state. Concerning the resonance widths, the CAP-EA-ADC calculations yield higher values for the $^2A_2$ state than for the $^2B_2$ state. Although no definite experimental data is available in this case, this trend is consistent with the shape of the recorded electron transmission spectrum,[223] where a broader peak is observed for the higher-lying spectral feature (see Figure VIII.6).

Turning to 1,4-cyclohexadiene, a different situation is found, which is consistent with experimental findings. The real and imaginary parts of the Dyson orbitals of the $^2B_{2g}$ and ^2A_u resonance states of 1,4-cyclohexadiene as calculated at the CAP-EA-ADC(2)/TZ level of theory are displayed in Figures VIII.9 and VIII.10, respectively.

Here, the π^*_+ ($^2B_{2g}$) state is strongly affected by through-bond interactions, and additional nodal planes appear due to interactions with π-shaped contributions at the methylene moieties. By contrast, the antisymmetric π^*_- combination (^2A_u) is mainly determined by the two ethylenic π^* orbitals. The computed resonance positions and decay widths are summarized in Table VIII.5.

At the CAP-EA-ADC(2)/TZ level, a resonance energy of $E_r = 2.651\,\text{eV}$ is found for the $^2B_{2g}$ (π^*_+) state, being in perfect agreement with the experimentally determined value of 2.67 eV.[223] Thus it lies higher in energy than the ^2A_u (π^*_-) state, for which the corresponding CAP-EA-ADC(2)/TZ calculation yields $E_r = 1.735\,\text{eV}$. Again, the computed value matches the experimental one, which has been given as 1.75 eV.[223] As in the case of norbornadiene, vibrational bands were not resolved in the ETS experiment, and a direct comparison with computed data is thus not possible. However, the recorded spectrum reveals considerably narrower bands than seen in the norbornadiene spectrum, as is visible from Figure VIII.6. The same trend is also observed for the calculated CAP-EA-ADC widths.

Chapter IX

Conclusions and Future Prospects

In this thesis I have presented the implementation and pilot applications of a number of propagator methods. The implementation of various ADC approaches has been extended by a number of different features, considerably broadening the spectrum of possible applications in studies of electronically stable molecules. The new aspects presented in this work include the combination of an improved fourth-order static self-energy scheme, the so-called $\Sigma(4+)$ scheme, with PP-ADC(3) as well as one-particle density matrix-based analyses of electron-attached and electron-detached states in the framework of EA-ADC(3) and IP-ADC(3).

In addition, the ADC methodology has been combined with two different approaches for the description of electronic resonances, which are metastable electronic states prone to electronic decay. The first one is constituted by the Fano-Stieltjes-ADC methodology, which has been combined with the third-order PP-ADC(3) scheme for the first time. Particularly well-suited for the description of low-lying anion π^* shape resonances is the second of the two considered methodologies, which is the combination of the CAP and ADC methods. The novel CAP-PP-ADC as well as CAP-EA-ADC approaches have been implemented using a subspace projection approach.

The first systematic benchmark study of the IP-ADC(3)/ISR(2) method with respect to high-level CI results for the calculation of vertical IPs and dipole moments has been presented in Chapter IV. In this study of 44 $1h$-type transitions in closed- and open-shell molecules, two third-order IP-ADC schemes differing by the employed static self-energy treatment have been evaluated. For the standard IP-ADC(3)/ISR(2) scheme in which the improved fourth-order static self-energy and the corresponding ground state density computed according to the $\Sigma(4+)$ procedure are employed throughout, a mean absolute error of calculated IPs in the range of $\overline{|\Delta|} \approx 0.2\,\text{eV}$ is found, accompanied by a maximum deviation of $|\Delta|_{\text{max}} \approx 0.6\,\text{eV}$. The strict IP-ADC(3)/ISR(2) scheme, employing the second-

order ground state density and the corresponding third-order static self-energy, performs slightly worse, the corresponding error measures in this case being $\overline{|\Delta|} \approx 0.3\,\mathrm{eV}$ and $|\Delta|_{\mathrm{max}} \approx 0.9\,\mathrm{eV}$. For the computed dipole moments, a similar trend has been found, the relative mean absolute errors of the standard and strict IP-ADC(3)/ISR(2) schemes being $\overline{|\Delta|} = 19\,\%$ and $\overline{|\Delta|} = 36\,\%$, respectively. Also, the observed maximum deviation from the FCI reference is considerably larger for the strict scheme ($|\Delta|_{\mathrm{max}} = 310\,\%$) than for the standard scheme ($|\Delta|_{\mathrm{max}} = 167\,\%$) and thus renders the latter scheme more trustworthy.

Another interesting aspect which has been discussed in the context of the application of the IP-ADC/ISR methodology to open-shell reference states arises from the fact that the description of different ionization classes, i.e., $1h$-type and $2h1p$-type transitions, is correct to different orders of perturbation theory. As a consequence, special care has to be taken when interpreting the results obtained for electron-detachment processes in molecules with doublet ground states. In this case, singlet and triplet states can be formed in the respective processes, which may not be described in a satisfactory manner by a single $1h$-configuration. As a consequence, the corresponding transition properties and, in particular, the associated IPs as computed using IP-ADC(3) are only correct to first order of perturbation theory.

On the other hand, the open-shell methodology can also be applied to the lowest triplet states of molecules with singlet ground states. In this case, another set of final states is accessible by means of $1h$-transitions, and even particular $3h2p$-type transitions with respect to the singlet ground state can be treated by IP-ADC(3), although only in first order of perturbation theory, which are otherwise first considered at the IP-ADC(4) level.

The usefulness of density matrix-based analyses in the context of electron-detachment processes has been discussed in Chapter V at the example of the photoelectron spectrum of the galvinoxyl free radical. Especially the interpretation of $2h1p$-satellite states is considerably simplified using these techniques, whereas the inspection of Dyson orbitals is usually sufficient if $1h$-type transitions are concerned.

The effective transition amplitudes, which are needed for the computation of the relative spectroscopic intensities of electron-detachment transitions, were further exploited for the computation of the third-order ground state density and, in a self-consistent procedure, an improved third-order density containing also higher-order contributions, from which an improved fourth-order static self-energy can be computed by means of the so-called $\Sigma(4+)$ procedure. The latter quantity can be employed in different ADC(3) schemes, and for IP-ADC, this approach had previously been shown to be superior to the strict third-order IP-ADC(3) scheme.

In Chapter VI, the effect of the $\Sigma(4+)$ static self-energy on the accuracy of PP-ADC(3)

was investigated in an extended benchmark study covering a total of 275 electronically excited states. Therein, virtually the same accuracy as for the strict PP-ADC(3) scheme was found, and no clear recommendation can be given based on these results. In this respect, the implementation of more complete infinite partial summation schemes for the static self-energy, as available through the Σ(DEM) approximation, should be considered.

Turning to the description of unstable electronic states or, more precisely, electronic resonances, the PP-ADC methods as implemented in Q-Chem were combined with the Fano-Stieltjes-ADC methodology. For this purpose, the block-Lanczos iterative matrix diagonalization algorithm as well as a new ADC variant allowing for arbitrary intermediate state subspace projections were integrated in Q-Chem. In Chapter VII, the applicability of the novel implementation for medium-sized organic molecules was demonstrated using the example of a Feshbach resonance in the naphthalene molecule.

As a second method for the description of electronic resonances, the CAP methodology was combined with PP-ADC and EA-ADC up to third order of perturbation theory. For this purpose, a subspace projection approach was pursued, which is superior to other CAP approaches in the sense that it allows for the computation of decay widths at the expense of a single electronic structure calculation. Methodological aspects of the subspace-projected CAP-EA-ADC approach were studied in Chapter VIII at the example of the well-investigated $^2\Pi_g$ shape resonance of the dinitrogen anion, for which a very good agreement with theoretical best estimates and experimental values for the decay width and resonance position was found.

As a pilot application of the new CAP-EA-ADC methodology, the π^* shape resonances in unsaturated organic compounds were investigated. In particular, the two lowest resonance states in 1,4-cyclohexadiene and norbornadiene were considered, which have been extensively studied in the past due to their role as model systems for the interaction of non-conjugated ethylenic π orbitals. As an interesting result of this study it was found that the resonance positions computed on the CAP-EA-ADC(2) level of theory were in excellent agreement with experimental values obtained by electron transmission spectroscopy. The third-order EA-ADC schemes yielded less accurate, but still satisfactory results.

In the future, further assessment of the accuracy of the two implemented methodologies, i.e., Fano-Stieltjes-ADC and CAP-ADC, should be conducted. In particular, the limits of the two methodologies should be investigated in comparative studies. In addition, the availability of the unrestricted variant of Fano-Stieltjes-PP-ADC enables the application to open-shell systems, and respective studies of π^* shape resonances in organic molecules are thus now also possible. In addition, it is straightforward to extend the subspace-projected CAP methodology also to IP-ADC, and this option should be pursued in the future.

Bibliography

[1] L. S. Cederbaum, W. Domcke, J. Schirmer, W. von Niessen, "Correlation Effects in the Ionization of Molecules: Breakdown of the Molecular Orbital Picture", *Adv. Chem. Phys.* **1986**, *65*, 115–159.

[2] S. Hüfner, *Photoelectron Spectroscopy - Principles and Applications*, Springer, Berlin, **2003**.

[3] A. Stolow, A. E. Bragg, D. M. Neumark, "Femtosecond Time-Resolved Photoelectron Spectroscopy", *Chemical Reviews* **2004**, *104*, 1719–1758.

[4] G. Wu, P. Hockett, A. Stolow, "Time-resolved photoelectron spectroscopy: from wavepackets to observables", *Phys. Chem. Chem. Phys.* **2011**, *13*, 18447–18467.

[5] B. W. D'Andrade, S. Datta, S. R. Forrest, P. Djurovich, E. Polikarpov, M. E. Thompson, "Relationship between the ionization and oxidation potentials of molecular organic semiconductors", *Org. Electron.* **2005**, *6*, 11–20.

[6] *Electronic Processes in Organic Electronics: Bridging Nanostructure, Electronic States and Device Properties*, 1st ed., (Eds.: H. Ishii, K. Kudo, T. Nakayama, N. Ueno), Springer Japan, Tokyo, **2015**.

[7] T. Koopmans, "Über die Zuordnung von Wellenfunktionen und Eigenwerten zu den Einzelnen Elektronen Eines Atoms", *Physica* **1934**, *1*, 104–113.

[8] J. F. Janak, "Proof that $\frac{\partial E}{\partial n_i} = \epsilon$ in density-functional theory", *Phys. Rev. B* **1978**, *18*, 7165–7168.

[9] C. Møller, M. S. Plesset, "Note on an approximation treatment for many-electron systems", *Phys. Rev.* **1934**, *46*, 618–622.

[10] R. J. Bartlett, "Coupled-cluster approach to molecular structure and spectra: a step toward predictive quantum chemistry", *J. Phys. Chem.* **1989**, *93*, 1697–1708.

[11] A. L. Fetter, J. D. Walecka, *Quantum Theory of Many-Particle Systems*, McGraw-Hill Book Company, New York, **2003**.

[12] A. A. Abrikosov, L. P. Gorkov, I. E. Dzyaloshinski, R. A. Silverman, *Methods of Quantum Field Theory in Statistical Physics*, Dover Publications, **2012**.

[13] J. Schirmer, *Many-body methods for atoms, molecules and clusters*, 1st ed., Springer International Publishing, **2018**.

[14] H. H. Corzo, J. V. Ortiz in *Löwdin Volume*, (Eds.: J. R. Sabin, E. J. Brändas), Adv. Quantum Chem. Academic Press, **2017**, Chapter 13, pp. 267–298.

[15] J. V. Ortiz, "Electron propagator theory: an approach to prediction and interpretation in quantum chemistry", *WIREs Comput. Mol. Sci.* **2013**, *3*, 123–142.

[16] J. Linderberg, Y. Öhrn, *Propagators in Quantum Chemistry*, 2nd ed., John Wiley & Sons, Inc., Hoboken, New Jersey, **2004**.

[17] P. Jørgensen, J. Simons, *Second Quantization-Based Methods in Quantum Chemistry*, 1st ed., Academic Press, Inc., London, **1981**.

[18] L. S. Cederbaum, W. Domcke, "Theoretical Aspects of Ionization Potentials and Photoelectron Spectroscopy: A Green's Function Approach", *Adv. Chem. Phys.* **1977**, *36*, 205–344.

[19] Y. Öhrn, G. Born, "Molecular Electron Propagator Theory and Calculations", *Adv. Quantum Chem.* **1981**, *13*, (Ed.: P.-O. Löwdin), 1–88.

[20] M. F. Herman, K. F. Freed, D. L. Yeager, "Analysis and Evaluation of Ionization Potentials, Electron Affinities, and Excitation Energies by the Equations of Motion—Green's Function Method", *Adv. Chem. Phys.* **1981**, *48*, 1–69.

[21] W. von Niessen, J. Schirmer, L. S. Cederbaum, "Computational methods for the one-particle Green's function", *Comp. Phys. Rep.* **1984**, *1*, 57–125.

[22] J. V. Ortiz in *Computational Chemistry: Reviews of Current Trends*, (Ed.: J. Leszczynski), World Scientific, Singapore, **1997**, Chapter 1, pp. 1–61.

[23] R. Santra, L. S. Cederbaum, "Non-Hermitian electronic theory and applications to clusters", *Phys. Rep.* **2002**, *368*, 1–117.

[24] O. Dolgounitcheva, V. Zakrzewski, J. V. Ortiz in *Fundamental World of Quantum Chemistry*, (Eds.: E. J. Brändas, E. S. Kryachko), A Tribute to the Memory of Per-Olov Löwdin, Kluwer, Dordrecht, **2003**, pp. 525–555.

[25] M. Pernpointner, A. I. Kuleff, L. S. Cederbaum in *Modeling of Molecular Properties*, John Wiley & Sons, Ltd, **2011**, Chapter 5, pp. 65–75.

[26] V. G. Zakrzewski, O. Dolgounitcheva, A. V. Zakjevskii, J. V. Ortiz, "Ab initio Electron Propagator Calculations on Electron Detachment Energies of Fullerenes, Macrocyclic Molecules, and Nucleotide Fragments", *Adv. Quantum Chem.* **2011**, *62*, (Eds.: J. R. Sabin, E. Brändas), 105–136.

[27] D. Danovich, "Green's function methods for calculating ionization potentials, electron affinities, and excitation energies", *WIREs Comput. Mol. Sci.* **2011**, *1*, 377–387.

[28] V. Averbukh, L. S. Cederbaum, P. V. Demekhin, S. Scheit, P. Kolorenč, Y.-C. Chiang, K. Gokhberg, S. Kopelke, N. V. Kryzhevoi, A. I. Kuleff, N. Sisourat, S. D. Stoychev in *Dynamical Processes In Atomic And Molecular Physics*, (Eds.: G. Ogurtsov, D. Dowek), Bentham Science, Sharjah, **2012**, pp. 29–56.

[29] M. Díaz-Tinoco, H. H. Corzo, J. V. Ortiz, "Electron Propagator Methods for Vertical Electron Detachment Energies of Anions: Benchmarks and Case Studies", *J. Chem. Theory Comput.* **2018**, *14*, 5881–5895.

[30] J. Schirmer, L. S. Cederbaum, O. Walter, "New approach to the one-particle Green's function for finite Fermi systems", *Phys. Rev. A* **1983**, *28*, 1237–1259.

[31] J. Schirmer, A. B. Trofimov, G. Stelter, "A non-Dyson third-order approximation scheme for the electron propagator", *J. Chem. Phys.* **1998**, *109*, 4734–4744.

[32] J. Schirmer, "Beyond the random-phase approximation: A new approximation scheme for the polarization propagator", *Phys. Rev. A* **1982**, *26*, 2395–2416.

[33] J. Schirmer, A. Barth, "Higher-order approximations for the particle-particle propagator", *Z. Phys. A* **1984**, *317*, 267–279.

[34] A. Tarantelli, L. S. Cederbaum, "Particle-particle propagator in the algebraic diagrammatic construction scheme at third order", *Phys. Rev. A* **1989**, *39*, 1656–1664.

[35] A. Tarantelli, L. S. Cederbaum, "Approximation scheme for the three-particle propagator", *Phys. Rev. A* **1992**, *46*, 81–94.

[36] A. B. Trofimov, G. Stelter, J. Schirmer, "A consistent third-order propagator method for electronic excitation", *J. Chem. Phys.* **1999**, *111*, 9982–9999.

[37] F. Mertins, J. Schirmer, "Algebraic propagator approaches and intermediate-state representations. I. The biorthogonal and unitary coupled-cluster methods", *Phys. Rev. A* **1996**, *53*, 2140–2152.

[38] F. Mertins, J. Schirmer, A. Tarantelli, "Algebraic propagator approaches and intermediate-state representations. II. The equation-of-motion methods for N, $N \pm 1$, and $N \pm 2$ electrons", *Phys. Rev. A* **1996**, *53*, 2153–2168.

[39] A. B. Trofimov, G. Stelter, J. Schirmer, "Electron excitation energies using a consistent third-order propagator approach: Comparison with full configuration interaction and coupled cluster results", *J. Chem. Phys.* **2002**, *117*, 6402–6410.

[40] A. Dreuw, M. Wormit, "The algebraic diagrammatic construction scheme for the polarization propagator for the calculation of excited states", *WIREs Comput. Mol. Sci.* **2015**, *5*, 82–95.

[41] J. Schirmer, F. Mertins, "Size consistency of an algebraic propagator appraoch", *Int. J. Quantum Chem.* **1996**, *58*, 329–339.

[42] J. Schirmer, G. Angonoa, "On Green's function calculations of the static self-energy part, the ground state energy and expectation values", *J. Chem. Phys.* **1989**, *91*, 1754–1761.

[43] H.-G. Weikert, H.-D. Meyer, L. S. Cederbaum, F. Tarantelli, "Block Lanczos and many-body theory: Application to the one-particle Green's function", *J. Chem. Phys.* **1996**, *104*, 7122–7138.

[44] V. G. Zakrzewski, O. Dolgounitcheva, J. V. Ortiz, "Improved algorithms for renormalized electron propagator calculations", *Int. J. Quantum Chem.* **1999**, *75*, 607–614.

[45] M. K. Scheller, H. G. Weikert, L. S. Cederbaum, F. Tarantelli, "Correlation phenomena in the ionization of CN dimers", *J. Electron Spectrosc. Relat. Phenom.* **1990**, *51*, 75–89.

[46] H.-G. Weikert, L. S. Cederbaum, "On the satellite structure accompanying the ionization of benzene", *Chem. Phys. Lett.* **1995**, *237*, 1–6.

[47] P. Baltzer, L. Karlsson, B. Wannberg, G. Öhrwall, D. M. P. Holland, M. A. MacDonald, M. A. Hayes, W. von Niessen, "An experimental and theoretical study of the valence shell photoelectron spectrum of the benzene molecule", *Chem. Phys.* **1997**, *224*, 95–119.

[48] M. S. Deleuze, A. B. Trofimov, L. S. Cederbaum, "Valence one-electron and shake-up ionization bands of polycyclic aromatic hydrocarbons. I. Benzene, naphthalene, anthracene, naphthacene, and pentacene", *J. Chem. Phys.* **2001**, *115*, 5859–5882.

[49] M. S. Deleuze, "Valence one-electron and shake-up ionization bands of polycyclic aromatic hydrocarbons. II. Azulene, phenanthrene, pyrene, chrysene, triphenylene, and perylene", *J. Chem. Phys.* **2002**, *116*, 7012–7026.

[50] A. W. Potts, D. M. P. Holland, A. B. Trofimov, J. Schirmer, L. Karlsson, K. Siegbahn, "An experimental and theoretical study of the valence shell photoelectron spectra of purine and pyrimidine molecules", *J. Phys. B: At. Mol. Opt. Phys.* **2003**, *36*, 3129–3143.

[51] M. S. Deleuze, "Valence One-Electron and Shake-Up Ionization Bands of Polycyclic Aromatic Hydrocarbons. III. Coronene, 1.2,6.7-Dibenzopyrene, 1.12-Benzoperylene, Anthanthrene", *J. Phys. Chem. A* **2004**, *108*, 9244–9259.

[52] S. Knippenberg, M. S. Deleuze, T. J. Cleij, J.-P. François, L. S. Cederbaum, J. H. D. Eland, "The Band 12 Issue in the Electron Momentum Spectra of Norbornane: A Comparison with Additional Green's Function Calculations and Ultraviolet Photoemission Measurements", *J. Phys. Chem. A* **2005**, *109*, 4267–4273.

[53] A. B. Trofimov, J. Schirmer, V. B. Kobychev, A. W. Potts, D. M. P. Holland, L. Karlsson, "Photoelectron spectra of the nucleobases cytosine, thymine and adenine", *J. Phys. B: At. Mol. Opt. Phys.* **2005**, *39*, 305–329.

[54] M. S. Deleuze, "Valence one-electron and shake-up ionisation bands of polycyclic aromatic hydrocarbons. IV. The dibenzanthracene species", *Chem. Phys.* **2006**, *329*, 22–38.

[55] I. L. Zaytseva, A. B. Trofimov, J. Schirmer, O. Plekan, V. Feyer, R. Richter, M. Coreno, K. C. Prince, "Theoretical and Experimental Study of Valence-Shell Ionization Spectra of Guanine", *J. Phys. Chem. A* **2009**, *113*, 15142–15149.

[56] S. Knippenberg, M. S. Deleuze, "Correlation effects in the valence ionization spectra of large conjugated molecules: p-Benzoquinone, anthracenequinone and pentacenequinone", *J. Electron Spectrosc. Relat. Phenom.* **2010**, *178-179*, 61–79.

[57] F. Morini, S. H. R. Shojaei, M. S. Deleuze, "Momentum space analysis of the electronic structure of biphenyl", *J. Phys. B: At. Mol. Opt. Phys.* **2014**, *47*, 225102.

[58] A. B. Trofimov, D. M. P. Holland, I. Powis, R. C. Menzies, A. W. Potts, L. Karlsson, E. V. Gromov, I. L. Badsyuk, J. Schirmer, "Ionization of pyridine: Interplay of orbital relaxation and electron correlation", *J. Chem. Phys.* **2017**, *146*, 244307.

[59] O. Goscinski, B. Lukman, "Moment-conserving decoupling of green functions via pade approximants", *Chem. Phys. Lett.* **1970**, *7*, 573–576.

[60] B. T. Pickup, O. Goscinski, "Direct calculation of ionization energies", *Mol. Phys.* **1973**, *26*, 1013–1035.

[61] P. Jørgensen, "Molecular and Atomic Applications of Time-Dependent Hartree-Fock Theory", *Annu. Rev. Phys. Chem.* **1975**, *26*, 359–380.

[62] D. J. Rowe, "Equations-of-Motion Method and the Extended Shell Model", *Rev. Mod. Phys.* **1968**, *40*, 153–166.

[63] C. W. McCurdy, T. N. Rescigno, D. L. Yeager, V. McKoy in *Methods of Electronic Structure Theory*, (Ed.: H. F. Schaefer III), Springer Science+Business Media, New York, **1977**, Chapter 9, pp. 339–386.

[64] J. V. Ortiz, "A nondiagonal, renormalized extension of partial third-order quasiparticle theory: Comparisons for closed-shell ionization energies", *J. Chem. Phys.* **1998**, *108*, 1008–1014.

[65] L. S. Cederbaum, "One-body Green's function for atoms and molecules: theory and application", *J. Phys. B: At. Mol. Phys.* **1975**, *8*, 290–303.

[66] V. G. Zakrzewski, W. von Niessen, "Vectorizable algorithm for green function and many-body perturbation methods", *J. Comp. Chem.* **1993**, *14*, 13–18.

[67] V. G. Zakrzewski, J. V. Ortiz, "Semidirect algorithms for third-order electron propagator calculations", *Int. J. Quantum Chem.* **1995**, *53*, 583–590.

[68] J. V. Ortiz, "Partial third-order quasiparticle theory: Comparisons for closed-shell ionization energies and an application to the Borazine photoelectron spectrum", *J. Chem. Phys.* **1996**, *104*, 7599–7605.

[69] A. M. Ferreira, G. Seabra, O. Dolgounitcheva, V. G. Zakrzewski, J. V. Ortiz in *Quantum-Mechanical Prediction of Thermochemical Data*, (Ed.: J. Cioslowski), Kluwer Academic Publishers, Dordrecht, **2001**, pp. 131–160.

[70] J. V. Ortiz, "An efficient, renormalized self-energy for calculating the electron binding energies of closed-shell molecules and anions", *Int. J. Quantum Chem.* **2005**, *105*, 803–808.

[71] H. H. Corzo, A. Galano, O. Dolgounitcheva, V. G. Zakrzewski, J. V. Ortiz, "NR2 and P3+: Accurate, Efficient Electron-Propagator Methods for Calculating Valence, Vertical Ionization Energies of Closed-Shell Molecules", *J. Phys. Chem. A* **2015**, *119*, 8813–8821.

[72] O. Dolgounitcheva, M. Díaz-Tinoco, V. G. Zakrzewski, R. M. Richard, N. Marom, C. D. Sherrill, J. V. Ortiz, "Accurate Ionization Potentials and Electron Affinities of Acceptor Molecules IV: Electron-Propagator Methods", *J. Chem. Theory Comput.* **2016**, *12*, 627–637.

[73] O. Dolgounitcheva, M. Díaz-Tinoco, V. G. Zakrzewski, R. M. Richard, N. Marom, C. D. Sherrill, J. V. Ortiz, "Correction to Accurate Ionization Potentials and Electron Affinities of Acceptor Molecules IV: Electron-Propagator Methods", *J. Chem. Theory Comput.* **2017**, *13*, 389–391.

[74] A. B. Trofimov, J. Schirmer, "Molecular ionization energies and ground- and ionic-state properties using a non-Dyson electron propagator approach", *J. Chem. Phys.* **2005**, *123*, 144115.

[75] Y. Shao, Z. Gan, E. Epifanovsky, A. T. B. Gilbert, M. Wormit, J. Kussmann, A. W. Lange, A. Behn, J. Deng, X. Feng, D. Ghosh, M. Goldey, P. R. Horn, L. D. Jacobson, I. Kaliman, R. Z. Khaliullin, T. Kuś, A. Landau, J. Liu, E. I. Proynov, Y. M. Rhee, R. M. Richard, M. A. Rohrdanz, R. P. Steele, E. J. Sundstrom, H. L. Woodcock, P. M. Zimmerman, D. Zuev, B. Albrecht, E. Alguire, B. Austin, G. J. O. Beran, Y. A. Bernard, E. Berquist, K. Brandhorst, K. B. Bravaya, S. T. Brown, D. Casanova, C.-M. Chang, Y. Chen, S. H. Chien, K. D. Closser, D. L. Crittenden, M. Diedenhofen, R. A. DiStasio, H. Do, A. D. Dutoi, R. G. Edgar, S. Fatehi, L. Fusti-Molnar, A. Ghysels, A. Golubeva-Zadorozhnaya, J. Gomes, M. W. D. Hanson-Heine, P. H. P. Harbach, A. W. Hauser, E. G. Hohenstein, Z. C. Holden, T.-C. Jagau, H. Ji, B. Kaduk, K. Khistyaev, J. Kim, J. Kim, R. A. King, P. Klunzinger, D. Kosenkov, T. Kowalczyk, C. M. Krauter, K. U. Lao, A. D. Laurent, K. V. Lawler, S. V. Levchenko, C. Y. Lin, F. Liu, E. Livshits, R. C. Lochan, A. Luenser, P. Manohar, S. F. Manzer, S.-P. Mao, N. Mardirossian, A. V. Marenich, S. A. Maurer, N. J. Mayhall, E. Neuscamman, C. M. Oana, R. Olivares-Amaya, D. P. O'Neill, J. A. Parkhill, T. M. Perrine, R. Peverati, A. Prociuk, D. R. Rehn, E. Rosta, N. J. Russ, S. M. Sharada, S. Sharma, D. W. Small, A. Sodt, T. Stein, D. Stück, Y.-C. Su, A. J. W. Thom, T. Tsuchimochi, V. Vanovschi, L. Vogt, O. Vydrov, T. Wang, M. A. Watson, J. Wenzel, A. White, C. F. Williams, J. Yang, S. Yeganeh, S. R. Yost, Z.-Q. You, I. Y. Zhang, X. Zhang, Y. Zhao, B. R. Brooks, G. K. L. Chan, D. M. Chipman, C. J. Cramer, W. A. Goddard, M. S. Gordon, W. J. Hehre, A. Klamt, H. F. Schaefer, M. W. Schmidt, C. D. Sherrill, D. G. Truhlar, A. Warshel, X. Xu, A. Aspuru-Guzik, R. Baer, A. T. Bell, N. A. Besley, J.-D. Chai, A. Dreuw, B. D. Dunietz, T. R. Furlani, S. R. Gwaltney, C.-P. Hsu, Y. Jung, J. Kong, D. S. Lambrecht, W. Liang, C. Ochsenfeld, V. A. Rassolov, L. V. Slipchenko, J. E. Subotnik, T. Van Voorhis, J. M. Herbert, A. I. Krylov, P. M. W. Gill, M. Head-Gordon, "Advances in molecular quantum chemistry contained in the Q-Chem 4 program package", *Mol. Phys.* **2015**, *113*, 184–215.

[76] M. Schneider, "Weiterentwicklung und Implementierung quantenchemischer Methoden zur direkten Berechnung von Ionisationspotentialen und Elektronenaffinitäten", *PhD thesis*, Universität Heidelberg, **2015**.

[77] M. Schneider, D. Y. Soshnikov, D. M. P. Holland, I. Powis, E. Antonsson, M. Patanen, C. Nicolas, C. Miron, M. Wormit, A. Dreuw, A. B. Trofimov, "A fresh look at the photoelectron spectrum of bromobenzene: A third-order non-Dyson electron propagator study", *J. Chem. Phys.* **2015**, *143*, 144103.

[78] J. Schirmer, "Closed-form intermediate representations of many-body propagators and resolvent matrices", *Phys. Rev. A* **1991**, *43*, 4647–4659.

[79] J. Schirmer, F. Mertins, "Review of biorthogonal coupled cluster representations for electronic excitation", *Theor. Chem. Acc.* **2010**, *125*, 145–172.

[80] H. Sekino, R. J. Bartlett, "A linear response, coupled-cluster theory for excitation energy", *Int. J. Quantum Chem.* **1984**, *26*, 255–265.

[81] J. Geertsen, M. Rittby, R. J. Bartlett, "The equation-of-motion coupled-cluster method: Excitation energies of Be and CO", *Chem. Phys. Lett.* **1989**, *164*, 57–62.

[82] J. F. Stanton, R. J. Bartlett, "The equation of motion coupled-cluster method. A systematic biorthogonal approach to molecular excitation energies, transition probabilities, and excited state properties", *J. Chem. Phys.* **1993**, *98*, 7029–7039.

[83] D. C. Comeau, R. J. Bartlett, "The equation-of-motion coupled-cluster method. Applications to open- and closed-shell reference states", *Chem. Phys. Lett.* **1993**, *207*, 414–423.

[84] A. I. Krylov, "Equation-of-Motion Coupled-Cluster Methods for Open-Shell and Electronically Excited Species: The Hitchhiker's Guide to Fock Space", *Annu. Rev. Phys. Chem.* **2008**, *59*, 433–462.

[85] R. J. Bartlett, "Coupled-cluster theory and its equation-of-motion extensions", *WIREs Comput. Mol. Sci.* **2012**, *2*, 126–138.

[86] M. Nooijen, J. G. Snijders, "Coupled cluster approach to the single-particle Green's function", *Int. J. Quantum Chem.* **1992**, *44*, 55–83.

[87] J. F. Stanton, J. Gauss, "Analytic energy derivatives for ionized states described by the equation-of-motion coupled cluster method", *J. Chem. Phys.* **1994**, *101*, 8938–8944.

[88] M. Musiał, S. A. Kucharski, R. J. Bartlett, "Equation-of-motion coupled cluster method with full inclusion of the connected triple excitations for ionized states: IP-EOM-CCSDT", *J. Chem. Phys.* **2003**, *118*, 1128–1136.

[89] A. C. Paul, "Intermediate State Representation Within the Algebraic Diagrammatic Construction for Ionized States", *Master's thesis*, Universität Heidelberg, **2018**.

[90] N. Vaval, L. S. Cederbaum, "Ab initio lifetimes in the interatomic Coulombic decay of neon clusters computed with propagators", *J. Chem. Phys.* **2007**, *126*, 164110.

[91] H. Hennig, J. Breidbach, L. S. Cederbaum, "Charge transfer driven by electron correlation: A non-Dyson propagator approach", *J. Chem. Phys.* **2005**, *122*, 134104.

[92] H. Hennig, J. Breidbach, L. S. Cederbaum, "Erratum: "Charge transfer driven by electron correlation: A non-Dyson propagator approach" [J. Chem. Phys. 122, 134104 (2005)]", *J. Chem. Phys.* **2005**, *122*, 249901.

[93] A. I. Kuleff, J. Breidbach, L. S. Cederbaum, "Multielectron wave-packet propagation: General theory and application", *J. Chem. Phys.* **2005**, *123*, 044111.

[94] J. Breidbach, L. S. Cederbaum, "Migration of holes: Numerical algorithms and implementation", *J. Chem. Phys.* **2007**, *126*, 034101.

[95] S. Lünnemann, A. I. Kuleff, L. S. Cederbaum, "Charge migration following ionization in systems with chromophore-donor and amine-acceptor sites", *J. Chem. Phys.* **2008**, *129*, 104305.

[96] A. I. Kuleff, S. Lünnemann, L. S. Cederbaum, "Ultrafast Charge Migration Following Valence Ionization of 4-Methylphenol: Jumping over the Aromatic Ring", *J. Phys. Chem. A* **2010**, *114*, 8676–8679.

[97] A. I. Kuleff, S. Lünnemann, L. S. Cederbaum, "Ultrafast reorganization of the hole charge created upon outer-valence ionization of porphyrins", *Chem. Phys.* **2012**, *399*, 245–251.

[98] A. I. Kuleff, L. S. Cederbaum, "Ultrafast correlation-driven electron dynamics", *J. Phys. B: At. Mol. Opt. Phys.* **2014**, *47*, 124002.

[99] T.-C. Jagau, K. B. Bravaya, A. I. Krylov, "Extending Quantum Chemistry of Bound States to Electronic Resonances", *Annu. Rev. Phys. Chem.* **2017**, *68*, 525–553.

[100] A. J. F. Siegert, "On the Derivation of the Dispersion Formula for Nuclear Reactions", *Phys. Rev.* **1939**, *56*, 750–752.

[101] J. M. Herbert in *Reviews in Computational Chemistry Volume 28*, John Wiley & Sons, Ltd, **2015**, Chapter 8, pp. 391–517.

[102] K. D. Jordan, P. D. Burrow, "Studies of the temporary anion states of unsaturated hydrocarbons by electron transmission spectroscopy", *Acc. Chem. Res* **1978**, *11*, 341–348.

[103] V. Balaji, L. Ng, K. D. Jordan, M. N. Paddon-Row, H. K. Patney, "Study of long-range π,π^* interactions in rigid molecules by electron transmission spectroscopy", *J. Am. Chem. Soc.* **1987**, *109*, 6957–6969.

[104] K. D. Jordan, P. D. Burrow, "Temporary anion states of polyatomic hydrocarbons", *Chemical Reviews* **1987**, *87*, 557–588.

[105] M. Allan, L. Andric, "σ^* resonances in electron impact-induced vibrational excitation of *n*-propane, cyclopropane, ethylene oxide, cyclopentane, and cyclohexane", *J. Chem. Phys.* **1996**, *105*, 3559–3568.

[106] L. Meitner, "Über die Entstehung der β-Strahl-Spektren radioaktiver Substanzen", *Z. Phys.* **1922**, *9*, 131–144.

[107] P. V. Auger, "Sur les rayons β^- secondaires produits dans un gaz par des rayons X", *C. R. A. S.* **1923**, *177*, 169–171.

[108] L. S. Cederbaum, J. Zobeley, F. Tarantelli, "Giant Intermolecular Decay and Fragmentation of Clusters", *Phys. Rev. Lett.* **1997**, *79*, 4778–4781.

[109] S. Marburger, O. Kugeler, U. Hergenhahn, T. Möller, "Experimental Evidence for Interatomic Coulombic Decay in Ne Clusters", *Phys. Rev. Lett.* **2003**, *90*, 203401.

[110] J. Zobeley, R. Santra, L. S. Cederbaum, "Electronic decay in weakly bound heteroclusters: Energy transfer versus electron transfer", *J. Chem. Phys.* **2001**, *115*, 5076–5088.

[111] M. Förstel, M. Mucke, T. Arion, A. M. Bradshaw, U. Hergenhahn, "Autoionization Mediated by Electron Transfer", *Phys. Rev. Lett.* **2011**, *106*, 033402.

[112] B. G. Armen, H. Aksela, T. Åberg, S. Aksela, "The resonant Auger effect", *J. Phys. B* **2000**, *33*, R49–R92.

[113] K. Gokhberg, V. Averbukh, L. S. Cederbaum, "Interatomic decay of inner-valence-excited states in clusters", *J. Chem. Phys.* **2006**, *124*, 144315.

[114] K. Gokhberg, A. B. Trofimov, T. Sommerfeld, L. S. Cederbaum, "Ionization of metal atoms following valence-excitation of neighbouring molecules", *Europhys. Lett.* **2005**, *72*, 228.

[115] F. Trinter, J. B. Williams, M. Weller, M. Waitz, M. Pitzer, J. Voigtsberger, C. Schober, G. Kastirke, C. Müller, C. Goihl, P. Burzynski, F. Wiegandt, R. Wallauer, A. Kalinin, L. P. H. Schmidt, M. S. Schöffler, Y.-C. Chiang, K. Gokhberg, T. Jahnke, R. Dörner, "Vibrationally Resolved Decay Width of Interatomic Coulombic Decay in HeNe", *Phys. Rev. Lett.* **2013**, *111*, 233004.

[116] K. Gokhberg, P. Kolorenč, A. I. Kuleff, L. S. Cederbaum, "Site- and energy-selective slow-electron production through intermolecular Coulombic decay", *Nature* **2014**, *505*, 661–663.

[117] U. Hergenhahn, "Production of low kinetic energy electrons and energetic ion pairs by Intermolecular Coulombic Decay", *Int. J. Radiat. Biol.* **2012**, *88*, 871–883.

[118] X. Luo, Y. Zheng, L. Sanche, "DNA strand breaks and crosslinks induced by transient anions in the range 2-20 eV", *J. Chem. Phys.* **2014**, *140*, 155101.

[119] V. Stumpf, K. Gokhberg, L. S. Cederbaum, "The role of metal ions in X-ray-induced photochemistry", *Nature Chem.* **2016**, *8*, 237–241.

[120] S. Faraji, L. Wirz, A. Dreuw, "Quantum Chemical Study of the Enzymatic Repair of T(6-4)C/C(6-4)T UV-Photolesions by DNA Photolyases", *ChemPhysChem* **2013**, *14*, 2817–2824.

[121] P. H. P. Harbach, M. Schneider, S. Faraji, A. Dreuw, "Intermolecular Coulombic Decay in Biology: The Initial Electron Detachment from $FADH^-$ in DNA Photolyases", *J. Phys. Chem. Lett.* **2013**, *4*, 943–949.

[122] S. Faraji, A. Dreuw, "Physicochemical Mechanism of Light-Driven DNA Repair by (6-4) Photolyases", *Annu. Rev. Phys. Chem.* **2014**, *65*, 275–292.

[123] G. Wentzel, "Über strahlungslose Quantensprünge", *Z. Phys.* **1927**, *43*, 524–530.

[124] S. Kopelke, K. Gokhberg, V. Averbukh, F. Tarantelli, L. S. Cederbaum, "Ab initio interatomic decay widths of excited states by applying Stieltjes imaging to Lanczos pseudospectra", *J. Chem. Phys.* **2011**, *134*, 094107.

[125] U. V. Riss, H.-D. Meyer, "Calculation of resonance energies and widths using the complex absorbing potential method", *J. Phys. B* **1993**, *26*, 4503.

[126] R. Santra, L. S. Cederbaum, "Complex absorbing potentials in the framework of electron propagator theory. I. General formalism", *J. Chem. Phys.* **2002**, *117*, 5511–5521.

[127] S. Feuerbacher, T. Sommerfeld, R. Santra, L. S. Cederbaum, "Complex absorbing potentials in the framework of electron propagator theory. II. Application to temporary anions", *J. Chem. Phys.* **2003**, *118*, 6188–6199.

[128] T.-C. Jagau, A. I. Krylov, "Complex Absorbing Potential Equation-of-Motion Coupled-Cluster Method Yields Smooth and Internally Consistent Potential Energy Surfaces and Lifetimes for Molecular Resonances", *J. Phys. Chem. Lett.* **2014**, *5*, 3078–3085.

[129] T.-C. Jagau, D. Zuev, K. B. Bravaya, E. Epifanovsky, A. I. Krylov, "A Fresh Look at Resonances and Complex Absorbing Potentials: Density Matrix-Based Approach", *J. Phys. Chem. Lett.* **2014**, *5*, 310–315.

[130] A. A. Kunitsa, A. A. Granovsky, K. B. Bravaya, "CAP-XMCQDPT2 method for molecular electronic resonances", *J. Chem. Phys.* **2017**, *146*, 184107.

[131] M. Ehara, T. Sommerfeld, "CAP/SAC-CI method for calculating resonance states of metastable anions", *Chem. Phys. Lett.* **2012**, *537*, 107–112.

[132] H. Feshbach, "Unified theory of nuclear reactions", *Ann. Phys. (N. Y.)* **1958**, *5*, 357–390.

[133] H. Feshbach, "A unified theory of nuclear reactions. II", *Ann. Phys. (N. Y.)* **1962**, *19*, 287–313.

[134] U. Fano, "Effects of Configuration Interaction on Intensities and Phase Shifts", *Phys. Rev.* **1961**, *128*, 1866–1878.

[135] A. U. Hazi, "A purely L^2 method for calculating resonance widths", *J. Phys. B* **1978**, *11*, L259–L264.

[136] G. Howat, T. Åberg, O. Goscinski, "Relaxation and final-state channel mixing in the Auger effect", *J. Phys. B* **1978**, *11*, 1575–1588.

[137] G. Howat, "The effects of orbital relaxation and interchannel interaction on magnesium K Auger transition rates", *J. Phys. B* **1978**, *11*, 1589–1595.

[138] T. Åberg, G. Howat in *Handbuch der Physik*, *Vol. 31*, (Ed.: W. Mehldorn), Springer, Berlin, **1982**, pp. 469–619.

[139] V. Averbukh, L. S. Cederbaum, "Ab initio calculation of interatomic decay rates by a combination of the Fano ansatz, Green's-function methods, and the Stieltjes imaging technique", *J. Chem. Phys.* **2005**, *123*, 204107.

[140] K. Gokhberg, V. Averbukh, L. S. Cederbaum, "Decay rates of inner-valence excitations in noble gas atoms", *J. Chem. Phys.* **2007**, *126*, 154107.

[141] S. Kopelke, K. Gokhberg, L. S. Cederbaum, F. Tarantelli, V. Averbukh, "Autoionization widths by Stieltjes imaging applied to Lanczos pseudospectra", *J. Chem. Phys.* **2011**, *134*, 024106.

[142] K. Gokhberg, V. Vysotskiy, L. S. Cederbaum, L. Storchi, F. Tarantelli, V. Averbukh, "Molecular photoionization cross sections by Stieltjes–Chebyshev moment theory applied to Lanczos pseudospectra", *J. Chem. Phys.* **2009**, *130*, 064104.

[143] P. W. Langhoff, "Stieltjes imaging of atomic and molecular photoabsorption profiles", *Chem. Phys. Lett.* **1973**, *22*, 60–64.

[144] J. Schirmer, A. Thiel, "An intermediate state representation approach to K-shell ionization in molecules. I. Theory", *J. Chem. Phys.* **2001**, *115*, 10621–10635.

[145] R. G. Parr, W. Yang, *Density Functional Theory of Atoms and Molecules*, Oxford University Press, New York, **1989**.

[146] F. Plasser, M. Wormit, A. Dreuw, "New tools for the systematic analysis and visualization of electronic excitations. I. Formalism", *J. Chem. Phys.* **2014**, *141*, 024106.

[147] E. R. Davidson, "The iterative calculation of a few of the lowest eigenvalues and corresponding eigenvectors of large real-symmetric matrices", *J. Comp. Phys.* **1975**, *17*, 87–94.

[148] H.-D. Meyer, S. Pal, "A band-Lanczos method for computing matrix elements of a resolvent", *J. Chem. Phys.* **1989**, *91*, 6195–6204.

[149] F. Müller-Plathe, G. H. F. Diercksen in *Electronic Structure of Atoms, Molecules and Solids*, (Eds.: S. Canuto, J. D'Albuquerque e Castro, F. J. Paixão), World Scientific, Singapore, **1990**, pp. 1–29.

[150] P. W. Langhoff, C. T. Corcoran, J. S. Sims, F. Weinhold, R. M. Glover, "Moment-theory investigations of photoabsorption and dispersion profiles in atoms and ions", *Phys. Rev. A* **1976**, *14*, 1042–1056.

[151] B. L. Whitten, A. U. Hazi, "Autoionization widths of doubly excited states for highly ionized systems: An application of the Stieltjes moment theory", *Phys. Rev. A* **1986**, *33*, 1039–1044.

[152] R. Santra, L. S. Cederbaum, H.-D. Meyer, "Electronic decay of molecular clusters: non-stationary states computed by standard quantum chemistry methods", *Chem. Phys. Lett.* **1999**, *303*, 413–419.

[153] D. Zuev, T.-C. Jagau, K. B. Bravaya, E. Epifanovsky, Y. Shao, E. Sundstrom, M. Head-Gordon, A. I. Krylov, "Complex absorbing potentials within EOM-CC family of methods: Theory, implementation, and benchmarks", *J. Chem. Phys.* **2014**, *141*, 024102.

[154] A. A. Kunitsa, K. B. Bravaya, "First-Principles Calculations of the Energy and Width of the 2Au Shape Resonance in p-Benzoquinone: A Gateway State for Electron Transfer", *J. Phys. Chem. Lett.* **2015**, *6*, 1053–1058.

[155] T. Sommerfeld, M. Ehara, "Complex Absorbing Potentials with Voronoi Isosurfaces Wrapping Perfectly around Molecules", *J. Chem. Theory Comput.* **2015**, *11*, 4627–4633.

[156] T.-C. Jagau, A. I. Krylov, "Characterizing metastable states beyond energies and lifetimes: Dyson orbitals and transition dipole moments", *J. Chem. Phys.* **2016**, *144*, 054113.

[157] M. Wormit, D. R. Rehn, P. H. P. Harbach, J. Wenzel, C. M. Krauter, E. Epifanovsky, A. Dreuw, "Investigating excited electronic states using the algebraic diagrammatic construction (ADC) approach of the polarisation propagator", *Mol. Phys.* **2014**, *112*, 774–784.

[158] E. Epifanovsky, M. Wormit, T. Kuś, A. Landau, D. Zuev, K. Khistyaev, P. Manohar, I. Kaliman, A. Dreuw, A. I. Krylov, "New implementation of high-level correlated methods using a general block tensor library for high-performance electronic structure calculations", *J. Comput. Chem.* **2013**, *34*, 2293–2309.

[159] P. Pulay, "Convergence acceleration of iterative sequences. The case of SCF iteration", *Chem. Phys. Lett.* **1980**, *73*, 393–398.

[160] J. Wenzel, M. Wormit, A. Dreuw, "Calculating core-level excitations and X-ray absorption spectra of medium-sized closed-shell molecules with the algebraic-diagrammatic construction scheme for the polarization propagator", *J. Comp. Chem.* **2014**, *35*, 1900–1915.

[161] B. N. Parlett, *The Symmetric Eigenvalue Problem*, 1st ed., Prentice-Hall, Englewood Cliffs, NJ, USA, **1980**.

[162] Å. Björk, *Numerical Methods in Matrix Computations*, 1st ed., Springer, Heidelberg, **2015**.

[163] E. Fasshauer, stieltjes, **2013**, `https://gitlab.com/stieltjes/stieltjes/` (visited on 02/20/2020).

[164] Boost C++ libraries, version 1.62.0, **2016**, `http://www.boost.org/` (visited on 02/20/2020).

[165] H. Bowdler, R. S. Martin, C. Reinsch, J. H. Wilkinson, "The QR and QL algorithms for symmetric matrices", *Num. Math.* **1968**, *11*, 293–306.

[166] J. M. Hyman, "Accurate Monotonicity Preserving Cubic Interpolation", *SIAM J. Sci. Stat. Comput.* **1983**, *4*, 645–654.

[167] R. L. Dougherty, A. Edelman, J. M. Hyman, "Nonnegativity-, Monotonicity-, or Convexity-Preserving Cubic and Quintic Hermite Interpolation", *Math. Comp.* **1989**, *52*, 471–494.

[168] F. N. Fritsch, R. E. Carlson, "Monotone Piecewise Cubic Interpolation", *SIAM J. Numer. Anal.* **1980**, *17*, 238–246.

[169] T. E. Oliphant, *A guide to NumPy*, USA: Trelgol Publishing, **2006**.

[170] P. Virtanen, R. Gommers, T. E. Oliphant, M. Haberland, T. Reddy, D. Cournapeau, E. Burovski, P. Peterson, W. Weckesser, J. Bright, S. J. van der Walt, M. Brett, J. Wilson, K. Jarrod Millman, N. Mayorov, A. R. J. Nelson, E. Jones, R. Kern, E. Larson, C. J. Carey, I. Polat, Y. Feng, E. W. Moore, J. VanderPlas, D. Laxalde, J. Perktold, R. Cimrman, I. Henriksen, E. A. Quintero, C. R. Harris, A. M. Archibald, A. H. Ribeiro, F. Pedregosa, P. van Mulbregt, Scipy 1.0 Contributors, "SciPy 1.0: Fundamental Algorithms for Scientific Computing in Python", *Nature Methods* **2020**.

[171] J. Ivanic, K. Ruedenberg, "Identification of deadwood in configuration spaces through general direct configuration interaction", *Theor. Chem. Acc.* **2001**, *106*, 339–351.

[172] J. Ivanic, "Direct configuration interaction and multiconfigurational self-consistent-field method for multiple active spaces with variable occupations. I. Method", *J. Chem. Phys.* **2003**, *119*, 9364–9376.

[173] M. W. Schmidt, K. K. Baldridge, J. A. Boatz, S. T. Elbert, M. S. Gordon, J. H. Jensen, S. Koseki, N. Matsunaga, K. A. Nguyen, S. Su, T. L. Windus, M. Dupuis, J. A. Montgomery Jr, "General atomic and molecular electronic structure system", *J. Comp. Chem.* **1993**, *14*, 1347–1363.

[174] M. S. Gordon, M. W. Schmidt in *Theory and Applications of Computational Chemistry*, (Eds.: C. E. Dykstra, G. Frenking, K. S. Kim, G. E. Scuseria), Elsevier, Amsterdam, **2005**, Chapter 41, pp. 1167–1189.

[175] I. Morino, K. Kawaguchi, "Fourier Transform Far-Infrared Spectroscopy of the NH_2, NHD, and ND_2 Radicals", *J. Mol. Spectrosc.* **1997**, *182*, 428–438.

[176] K. P. Huber, G. Herzberg, *Molecular Spectra and Molecular Structure. IV. Constants of Diatomic Molecules*, *Vol. 716*, Van Nostrand Reinhold Company, New York, **1979**.

[177] G. Herzberg, *Molecular spectra and molecular structure. Vol. 3: Electronic spectra and electronic structure of polyatomic molecules*, Van Nostrand, Reinhold, New York, **1966**.

[178] A. G. Császár, G. Czakó, T. Furtenbacher, J. Tennyson, V. Szalay, S. V. Shirin, N. F. Zobov, O. L. Polyansky, "On equilibrium structures of the water molecule", *J. Chem. Phys.* **2005**, *122*, 214305.

[179] T. H. Dunning, "Gaussian basis sets for use in correlated molecular calculations. I. The atoms boron through neon and hydrogen", *J. Chem. Phys.* **1989**, *90*, 1007–1023.

[180] R. A. Kendall, T. H. Dunning, R. J. Harrison, "Electron affinities of the first-row atoms revisited. Systematic basis sets and wave functions", *J. Chem. Phys.* **1992**, *96*, 6796–6806.

[181] R. Ditchfield, W. J. Hehre, J. A. Pople, "Self-Consistent Molecular-Orbital Methods. IX. An Extended Gaussian-Type Basis for Molecular-Orbital Studies of Organic Molecules", *J. Chem. Phys.* **1971**, *54*, 724–728.

[182] W. J. Hehre, R. Ditchfield, J. A. Pople, "Self-Consistent Molecular Orbital Methods. XII. Further Extensions of Gaussian—Type Basis Sets for Use in Molecular Orbital Studies of Organic Molecules", *J. Chem. Phys.* **1972**, *56*, 2257–2261.

[183] P. C. Hariharan, J. A. Pople, "The influence of polarization functions on molecular orbital hydrogenation energies", *Theor. Chim. Acta* **1973**, *28*, 213–222.

[184] T. Clark, J. Chandrasekhar, G. W. Spitznagel, P. V. R. Schleyer, "Efficient diffuse function-augmented basis sets for anion calculations. III. The 3-21+G basis set for first-row elements, Li–F", *J. Comp. Chem.* **1983**, *4*, 294–301.

[185] B. P. Prascher, D. E. Woon, K. A. Peterson, T. H. Dunning, A. K. Wilson, "Gaussian basis sets for use in correlated molecular calculations. VII. Valence, core-valence, and scalar relativistic basis sets for Li, Be, Na, and Mg", *Theor. Chem. Acc.* **2011**, *128*, 69–82.

[186] D. Feller, "The role of databases in support of computational chemistry calculations", *J. Comp. Chem.* **1996**, *17*, 1571–1586.

[187] K. L. Schuchardt, B. T. Didier, T. Elsethagen, L. Sun, V. Gurumoorthi, J. Chase, J. Li, T. L. Windus, "Basis Set Exchange: A Community Database for Computational Sciences", *J. Chem. Inf. Model.* **2007**, *47*, 1045–1052.

[188] J. C. Rienstra-Kiracofe, G. S. Tschumper, H. F. Schaefer, S. Nandi, G. B. Ellison, "Atomic and Molecular Electron Affinities: Photoelectron Experiments and Theoretical Computations", *Chem. Rev.* **2002**, *102*, 231–282.

[189] J. T. Snodgrass, J. V. Coe, C. B. Freidhoff, K. M. McHugh, S. T. Arnold, K. H. Bowen, "Negative Ion Photoelectron Spectroscopy of $NH_2^-(NH_3)_1$ and $NH_2^-(NH_3)_2$: Gas Phase Basicities of Partially Solvated Anions", *J. Phys. Chem.* **1995**, *99*, 9675–9680.

[190] J. M. Brown, S. W. Chalkley, F. D. Wayne, "Determination of the dipole moment of the amino radical by optical Stark spectroscopy with a tunable dye laser", *Mol. Phys.* **1979**, *38*, 1521–1537.

[191] F. X. Powell, D. R. Lide, "Improved Measurement of the Electric-Dipole Moment of the Hydroxyl Radical", *J. Chem. Phys.* **1965**, *42*, 4201–4202.

[192] R. Thomson, F. W. Dalby, "Experimental determination of the dipole moments of the $X(^2\Sigma^+)$ and $B(^2\Sigma^+)$ states of the CN molecule", *Can. J. Phys.* **1968**, *46*, 2815–2819.

[193] J. A. Hodgeson, E. E. Sibert, R. F. Curl, "Dipole Moment of Nitrogen Dioxide", *J. Phys. Chem.* **1963**, *67*, 2833–2835.

[194] L. Wharton, L. P. Gold, W. Klemperer, "Dipole Moment of Lithium Hydride", *J. Chem. Phys.* **1960**, *33*, 1255–1255.

[195] D. K. Coles, W. E. Good, J. K. Bragg, A. H. Sharbaugh, "The Stark Effect of the Ammonia Inversion Spectrum", *Phys. Rev.* **1951**, *82*, 877–878.

[196] R. Weiss, "Stark Effect and Hyperfine Structure of Hydrogen Fluoride", *Phys. Rev.* **1963**, *131*, 659–665.

[197] B. N. Bhattacharya, W. Gordy, "Observation of π Stark Components in Microwave Spectroscopy: Precision Measurements on HCN", *Phys. Rev.* **1960**, *119*, 144–149.

[198] D. M. P. Holland, A. W. Potts, A. B. Trofimov, J. Breidbach, J. Schirmer, R. Feifel, T. Richter, K. Godehusen, M. Martins, A. Tutay, M. Yalcinkaya, M. Al-Hada, S. Eriksson, L. Karlsson, "An experimental and theoretical study of the valence shell photoelectron spectrum of tetrafluoromethane", *Chem. Phys.* **2005**, *308*, 43–57.

[199] J. Schirmer, A. B. Trofimov, "Intermediate state representation approach to physical properties of electronically excited molecules", *J. Chem. Phys.* **2004**, *120*, 11449–11464.

[200] G. Herzberg, *The spectra and structures of simple free radicals: an introduction to molecular spectroscopy*, Dover Publications, Mineola, N.Y., **2003**.

[201] I. Shibata, K. Nakamura, A. Baba, H. Matsuda, "Remarkable difference of chemoselectivity in the reduction of α-bromo ketones with dibutyltin dihydride system", *Tetrahedron Lett.* **1990**, *31*, 6381–6384.

[202] C. Thom, P. Kocieński, K. Jarowicki, "A Practical Synthesis of (*R*)-(+)-Cyclohex-3-enecarboxylic Acid via an Asymmetric Diels-Alder Reaction", *Synthesis* **1993**, *1993*, 475–477.

[203] M. F. Lappert, P. W. Lednor, "Free Radicals in Organometallic Chemistry", *Adv. Organomet. Chem.* **1976**, *14*, (Eds.: F. G. A. Stone, R. West), 345–399.

[204] I. Ljubić, A. Kivimäki, M. Coreno, S. Kazazić, I. Novak, "Characterisation of the electronic structure of galvinoxyl free radical by variable energy UPS, XPS and NEXAFS spectroscopy", *Phys. Chem. Chem. Phys.* **2018**, *20*, 2480–2491.

[205] W. Humphrey, A. Dalke, K. Schulten, "VMD – Visual Molecular Dynamics", *J. Molec. Graphics* **1996**, *14*, 33–38.

[206] H. Koch, O. Christiansen, P. Jørgensen, J. Olsen, "Excitation energies of BH, CH_2 and Ne in full configuration interaction and the hierarchy CCS, CC2, CCSD and CC3 of coupled cluster models", *Chem. Phys. Lett.* **1995**, *244*, 75–82.

[207] O. Christiansen, H. Koch, P. Jørgensen, J. Olsen, "Excitation energies of H_2O, N_2 and C_2 in full configuration interaction and coupled cluster theory", *Chem. Phys. Lett.* **1996**, *256*, 185–194.

[208] H. Larsen, K. Hald, J. Olsen, P. Jørgensen, "Triplet excitation energies in full configuration interaction and coupled-cluster theory", *J. Chem. Phys.* **2001**, *115*, 3015–3020.

[209] M. Schreiber, M. R. Silva-Junior, S. P. A. Sauer, W. Thiel, "Benchmarks for electronically excited states: CASPT2, CC2, CCSD, and CC3", *J. Chem. Phys.* **2008**, *128*, 134110.

[210] A. Schäfer, C. Huber, R. Ahlrichs, "Fully optimized contracted Gaussian basis sets of triple zeta valence quality for atoms Li to Kr", *J. Chem. Phys.* **1994**, *100*, 5829–5835.

[211] P. H. P. Harbach, M. Wormit, A. Dreuw, "The third-order algebraic diagrammatic construction method (ADC(3)) for the polarization propagator for closed-shell molecules: Efficient implementation and benchmarking", *J. Chem. Phys.* **2014**, *141*, 064113.

[212] P.-F. Loos, A. Scemama, A. Blondel, Y. Garniron, M. Caffarel, D. Jacquemin, "A Mountaineering Strategy to Excited States: Highly Accurate Reference Energies and Benchmarks", *J. Chem. Theory Comput.* **2018**, *14*, 4360–4379.

[213] D. E. Woon, T. H. Dunning, "Gaussian basis sets for use in correlated molecular calculations. V. Core-valence basis sets for boron through neon", *J. Chem. Phys.* **1995**, *103*, 4572–4585.

[214] K. Kaufmann, W. Baumeister, M. Jungen, "Universal Gaussian basis sets for an optimum representation of Rydberg and continuum wavefunctions", *J. Phys. B* **1989**, *22*, 2223.

[215] K. Codling, R. P. Madden, D. L. Ederer, "Resonances in the Photo-Ionization Continuum of Ne I (20-150 eV)", *Phys. Rev.* **1967**, *155*, 26–37.

[216] K. Schulz, M. Domke, R. Püttner, A. Gutiérrez, G. Kaindl, G. Miecznik, C. H. Greene, "High-resolution experimental and theoretical study of singly and doubly excited resonances in ground-state photoionization of neon", *Phys. Rev. A* **1996**, *54*, 3095–3112.

[217] A. J. Yencha, R. I. Hall, L. Avaldi, G. Dawber, A. G. McConkey, M. A. MacDonald, G. C. King, "Threshold photoelectron spectroscopy of benzene up to 26.5 eV", *Can. J. Chem.* **2004**, *82*, 1061–1066.

[218] E. Ruehl, S. D. Price, S. Leach, "Single and double photoionization processes in naphthalene between 8 and 35 eV", *J. Phys. Chem.* **1989**, *93*, 6312–6321.

[219] R. Hoffmann, E. Heilbronner, R. Gleiter, "Interaction of nonconjugated double bonds", *J. Am. Chem. Soc.* **1970**, *92*, 706–707.

[220] R. Hoffmann, "Interaction of orbitals through space and through bonds", *Acc. Chem. Res* **1971**, *4*, 1–9.

[221] M. Berman, H. Estrada, L. S. Cederbaum, W. Domcke, "Nuclear dynamics in resonant electron-molecule scattering beyond the local approximation: The 2.3-eV shape resonance in N_2", *Phys. Rev. A* **1983**, *28*, 1363–1381.

[222] R. Panajotovic, M. Kitajima, H. Tanaka, M. Jelisavcic, J. Lower, L. Campbell, M. J. Brunger, S. J. Buckman, "Electron collisions with ethylene", *J. Phys. B: At. Mol. Opt. Phys.* **2003**, *36*, 1615–1626.

[223] K. D. Jordan, J. A. Michejda, P. D. Burrow, "A study of the negative ion states of selected cyclodienes by electron transmission spectroscopy", *Chem. Phys. Lett.* **1976**, *42*, 227–231.

[224] R. McDiarmid, J. P. Doering, "Electron impact investigation of the electronic transitions of 1,4-cyclohexadiene and 1,5-cyclo-octadiene", *J. Chem. Phys.* **1981**, *75*, 2687–2692.

[225] A. Modelli, D. Jones, S. Rossini, G. Distefano, "Characterization of the temporary π anion states of 1,4-cyclohexadiene, γ-pyran, 1,4-dioxin and γ-pyrone by electron transmission spectroscopy", *Chem. Phys. Lett.* **1986**, *123*, 375–378.

[226] M. F. Falcetta, K. D. Jordan, "Stabilization calculations on the π^* anion states of 1,4-cyclohexadiene: confirmation of the π^{-*} below π^{+*} orbital ordering", *J. Am. Chem. Soc.* **1991**, *113*, 2903–2909.

[227] C.-Y. Juang, J. S.-Y. Chao, "Splitting Energies of π^* Anion States of 1,4-Cyclohexadiene via the Exponent Stabilization Method", *J. Phys. Chem.* **1994**, *98*, 13506–13512.

Publication List

1. a) M. Schelwies, A. L. Dempwolff, F. Rominger, G. Helmchen, "Gold-Catalyzed Intermolecular Addition of Carbonyl Compounds to 1,6-Enynes", *Angewandte Chemie International Edition* **2007**, *46*, 5598–5601. b) M. Schelwies, A. L. Dempwolff, F. Rominger, G. Helmchen, "Gold-katalysierte intermolekulare Addition von Carbonylverbindungen an 1,6-Enine", *Angewandte Chemie* **2007**, *119*, 5694–5697.

2. M. Schelwies, R. Moser, A. L. Dempwolff, F. Rominger, G. Helmchen, "Gold-Catalyzed Intermolecular Addition of Carbonyl Compounds to 1,6-Enynes: Reactivity, Scope, and Mechanistic Aspects", *Chemistry – A European Journal* **2009**, *15*, 10888–10900.

3. A. L. Dempwolff, M. Schneider, M. Hodecker, A. Dreuw, "Efficient Implementation of the Non-Dyson Third-Order Algebraic Diagrammatic Construction Approximation for the Electron Propagator for Closed- and Open-Shell Molecules", *The Journal of Chemical Physics* **2019**, *150*, 064108.

4. M. Hodecker, A. L. Dempwolff, D. R. Rehn, A. Dreuw, "Algebraic-Diagrammatic Construction Scheme for the Polarization Propagator Including Ground-State Coupled-Cluster Amplitudes. I. Excitation Energies", *The Journal of Chemical Physics* **2019**, *150*, 174104.

5. A. L. Dempwolff, A. C. Paul, A. M. Belogolova, A. B. Trofimov, A. Dreuw, "Intermediate State Representation Approach to Physical Properties of Molecular Electron-Detached States: I. Theory and Implementation", *The Journal of Chemical Physics* **2020**, *152*, 024113.

6. A. L. Dempwolff, A. C. Paul, A. M. Belogolova, A. B. Trofimov, A. Dreuw, "Intermediate State Representation Approach to Physical Properties of Molecular Electron-Detached States: II. Benchmarking", *The Journal of Chemical Physics* **2020**, *152*, 024125.

7. N. H. List, A. L. Dempwolff, A. Dreuw, P. Norman, T. J. Martínez, "Probing Competing Relaxation Pathways in Malonaldehyde with Transient X-ray Absorption Spectroscopy", *Chemical Science*, in revision.

Appendix A

Benchmark Results for PP-ADC(3) Schemes

A.1. Thiel Benchmark Set

Table A.1. Benchmark results for singlet states from the Thiel benchmark set.

Compound	State	TBE[a]	CC3[a]	ADC(2)	ADC(3(3))	ADC(3(4))	ADC(3(4+))
Ethylene							
	$1\ ^1B_{1u}$	7.80	8.37	8.36	8.14	8.19	8.17
Butadiene							
	$1\ ^1B_u$	6.18	6.58	6.43	6.36	6.37	6.37
	$2\ ^1A_g$	6.55	6.77	7.68	5.77	5.77	5.77
Hexatriene							
	$1\ ^1B_u$	5.10	5.58	5.35	5.35	5.35	5.35
	$2\ ^1A_g$	5.09	5.72	6.72	4.53	4.52	4.52
Octatetraene							
	$1\ ^1B_u$	4.47	4.97	4.66	4.70	4.69	4.69
	$2\ ^1A_g$	4.66	4.94	5.93	3.74	3.73	3.73
Cyclopropene							
	$1\ ^1B_1$	6.76	6.90	6.97	6.75	6.77	6.76
	$1\ ^1B_2$	7.06	7.10	7.14	6.91	6.92	6.91
Cyclopentadiene							
	$1\ ^1B_2$	5.55	5.73	5.66	5.52	5.55	5.54
	$2\ ^1A_1$	6.31	6.61	7.08	5.81	5.81	5.81
	$3\ ^1A_1$		6.69	8.85	8.58	8.61	8.60
Norbornadiene							
	$1\ ^1A_2$	5.34	5.64	5.57	5.48	5.52	5.51
	$1\ ^1B_2$	6.11	6.49	6.39	6.45	6.47	6.47
	$2\ ^1B_2$		7.64	7.63	7.54	7.58	7.57
	$2\ ^1A_2$		7.71	7.67	7.63	7.66	7.65
Benzene							
	$1\ ^1B_{2u}$	5.08	5.07	5.27	4.99	5.01	5.00
	$1\ ^1B_{1u}$	6.54	6.68	6.64	6.47	6.49	6.49
	$1\ ^1E_{1u}$	7.13	7.45	7.43	7.35	7.39	7.38
	$2\ ^1E_{2g}$	8.41	8.43	9.06	8.58	8.60	8.59

Table A.1. (continued)

Compound	State	TBE[a]	CC3[a]	ADC(2)	ADC(3(3))	ADC(3(4))	ADC(3(4+))
Naphthalene							
	$1\ ^1B_{3u}$	4.24	4.27	4.45	4.14	4.15	4.14
	$1\ ^1B_{2u}$	4.77	5.03	4.93	4.90	4.91	4.91
	$2\ ^1A_g$	5.90	5.98	6.22	5.54	5.55	5.55
	$1\ ^1B_{1g}$	6.00	6.07	6.23	6.06	6.07	6.07
	$2\ ^1B_{3u}$	6.07	6.33	6.23	6.26	6.28	6.28
	$2\ ^1B_{2u}$	6.33	6.57	6.55	6.47	6.49	6.49
	$2\ ^1B_{1g}$	6.48	6.79	6.80	6.63	6.66	6.65
	$3\ ^1A_g$	6.71	6.90	7.38	6.41	6.42	6.42
Furan							
	$1\ ^1B_2$	6.32	6.60	6.76	6.39	6.54	6.49
	$2\ ^1A_1$	6.57	6.62	6.85	6.48	6.48	6.48
	$3\ ^1A_1$	8.13	8.53	8.73	8.23	8.14	8.18
Pyrrole							
	$2\ ^1A_1$	6.37	6.40	6.60	6.38	6.39	6.38
	$1\ ^1B_2$	6.57	6.71	6.89	6.53	6.60	6.58
	$3\ ^1A_1$	7.91	8.17	8.43	7.92	7.94	7.93
Imidazole							
	$2\ ^1A'$	6.19	6.58	6.73	6.49	6.53	6.52
	$1\ ^1A''$	6.81	6.82	6.74	6.46	6.64	6.59
	$3\ ^1A'$	6.93	7.10	7.26	6.98	7.00	6.99
	$2\ ^1A''$		7.93	7.80	7.72	7.83	7.79
	$4\ ^1A'$		8.45	8.60	8.67	8.72	8.72
Pyridine							
	$1\ ^1B_1$	4.59	5.05	5.10	5.05	4.96	4.98
	$1\ ^1B_2$	4.85	5.15	5.32	5.06	5.08	5.07
	$2\ ^1A_2$	5.11	5.50	5.37	5.80	5.71	5.78
	$2\ ^1A_1$	6.26	6.85	6.83	6.58	6.60	6.59
	$3\ ^1A_1$	7.18	7.70	7.70	7.59	7.61	7.61
	$2\ ^1B_2$	7.27	7.59	7.59	7.46	7.49	7.49
	$4\ ^1A_1$		8.68	7.99	8.73	8.75	8.75
	$3\ ^1B_2$		8.77	8.84	9.59	9.64	9.66
Pyrazine							
	$1\ ^1B_{3u}$	4.95	4.24	4.29	4.21	4.20	4.20
	$1\ ^1B_{2u}$	4.64	5.02	5.16	4.88	4.92	4.90
	$1\ ^1A_u$	4.81	5.05	4.97	5.28	5.25	5.26
	$1\ ^1B_{2g}$	5.56	5.74	5.93	5.65	5.62	5.63
	$1\ ^1B_{1u}$	6.58	7.07	7.06	6.85	6.88	6.87
	$1\ ^1B_{1g}$	6.60	6.75	6.70	7.18	7.12	7.14
	$2\ ^1B_{2u}$	7.60	8.05	8.06	8.02	8.02	8.03
	$2\ ^1B_{1u}$	7.72	8.06	8.11	7.95	7.96	7.96
	$1\ ^1B_{3g}$		8.77	9.39	8.75	8.75	8.75
	$2\ ^1A_g$		8.69	8.11	8.59	8.64	8.63
Pyrimidine							
	$1\ ^1B_1$	4.55	4.50	4.45	4.57	4.47	4.50
	$1\ ^1A_2$	4.91	4.93	4.80	5.10	5.02	5.07
	$1\ ^1B_2$	5.44	5.36	5.49	5.30	5.30	5.30
	$2\ ^1A_1$	6.95	7.06	7.03	6.66	6.67	6.64
	$2\ ^1B_2$		8.01	7.89	7.90	7.89	7.90
	$3\ ^1A_1$		7.74	7.70	7.53	7.54	7.55
Pyridazine							
	$1\ ^1B_1$	3.78	3.92	3.91	3.92	3.89	3.91

Table A.1. (continued)

Compound	State	TBE[a]	CC3[a]	ADC(2)	ADC(3(3))	ADC(3(4))	ADC(3(4+))
	$1\ ^1A_2$	4.32	4.49	4.41	4.68	4.64	4.66
	$2\ ^1A_1$	5.18	5.22	5.37	5.10	5.11	5.11
	$2\ ^1A_2$	5.77	5.74	5.83	5.70	5.67	5.68
	$2\ ^1B_1$		6.41	6.40	6.64	6.60	6.61
	$1\ ^1B_2$		6.93	6.97	6.73	6.75	6.74
	$2\ ^1B_2$		7.55	7.33	7.43	7.47	7.47
	$3\ ^1A_1$		7.82	7.89	7.64	7.67	7.67
Triazine							
	$1\ ^1A_1''$	4.60	4.78	4.62	5.03	4.96	5.05
	$1\ ^1A_2''$	4.66	4.76	4.73	4.79	4.69	4.69
	$1\ ^1E''$	4.71	4.81	4.70	4.95	4.85	4.90
	$1\ ^1A_2'$	5.79	5.76	5.76	5.71	5.67	5.68
	$1\ ^1A_1'$		7.41	7.34	6.86	6.81	6.78
	$2\ ^1E''$		7.80	7.96	8.05	7.95	7.99
	$1\ ^1E'$		8.04	7.92	7.86	7.85	7.87
	$2\ ^1E'$		9.44	8.64	9.31	9.34	9.40
Tetrazine							
	$1\ ^1B_{3u}$	2.24	2.53	2.52	2.48	2.47	2.48
	$1\ ^1A_u$	3.48	3.79	3.72	3.96	4.00	3.99
	$1\ ^1B_{1g}$	5.73	5.97	5.13	5.00	4.98	4.99
	$1\ ^1B_{2u}$	4.91	5.12	5.20	4.98	4.97	4.97
	$1\ ^1B_{2g}$	5.18	5.34	5.57	4.95	4.94	4.94
	$2\ ^1A_u$	5.47	5.46	5.54	5.39	5.37	5.38
	$1\ ^1B_{3g}$	5.79		7.84	6.48	6.48	6.48
	$2\ ^1B_{2g}$		6.23	6.34	6.56	6.57	6.57
	$2\ ^1B_{1g}$		6.87	6.93	7.13	7.16	7.14
	$2\ ^1B_{3u}$		6.67	6.73	6.82	6.83	6.83
	$3\ ^1B_{1g}$		7.08	7.71	6.57	6.58	6.58
	$1\ ^1B_{1u}$		7.45	7.54	7.18	7.18	7.18
	$2\ ^1B_{1u}$		7.79	7.76	7.66	7.69	7.69
	$2\ ^1B_{3g}$		8.47	8.85	8.25	8.27	8.27
	$2\ ^1B_{2u}$		8.51	8.59	8.48	8.51	8.50
Formaldehyde							
	$1\ ^1A_2$	3.88	3.95	3.91	3.85	3.51	3.66
	$1\ ^1B_1$	9.10	9.18	9.17	9.10	8.78	8.93
	$2\ ^1A_1$	9.30	10.45	9.37	9.09	8.87	9.00
Acetone							
	$1\ ^1A_2$	4.40	4.40	4.30	4.38	3.94	4.15
	$1\ ^1B_1$	9.10	9.17	9.12	9.14	8.80	8.97
	$2\ ^1A_1$	9.40	9.65	9.44	9.96	9.74	9.90
Benzoquinone							
	$1\ ^1B_{1g}$	2.78	2.75	2.67	2.83	2.43	2.66
	$1\ ^1A_u$	2.80	2.85	2.75	2.98	2.49	2.75
	$1\ ^1B_{3g}$	4.25	4.59	4.80	4.29	4.57	4.45
	$1\ ^1B_{1u}$	5.29	5.62	5.41	5.43	5.20	5.33
	$1\ ^1B_{3u}$	5.60	5.82	5.62	5.33	5.25	5.30
	$2\ ^1B_{3g}$	6.98	7.27	7.24	6.94	6.66	6.79
Formamide							
	$1\ ^1A''$	5.63	5.65	5.46	5.69	5.16	5.40
	$2\ ^1A'$	7.44	8.27	7.13	7.48	7.22	7.36
	$3\ ^1A'$		10.93	7.82	8.83	8.48	8.68
Acetamide							

Table A.1. (continued)

Compound	State	TBE[a]	CC3[a]	ADC(2)	ADC(3(3))	ADC(3(4))	ADC(3(4+))
	$1\ ^1A''$	5.80	5.69	5.48	5.78	5.22	5.48
	$2\ ^1A'$	7.27	7.67	6.77	7.59	7.31	7.46
	$3\ ^1A'$		10.50	7.47	8.09	7.76	7.95
Propanamide							
	$1\ ^1A''$	5.72	5.72	5.49	5.81	5.25	5.50
	$2\ ^1A'$	7.20	7.62	6.77	7.58	7.29	7.43
	$3\ ^1A'$		10.06	7.39	8.09	7.76	7.96
Cytosine							
	$2\ ^1A'$	4.66		4.60	4.83	4.56	4.67
	$1\ ^1A''$	4.87		4.81	5.41	5.19	5.26
	$2\ ^1A''$	5.26		5.24	6.16	5.51	5.78
	$3\ ^1A'$	5.62		5.56	5.76	5.58	5.63
Thymine							
	$1\ ^1A''$	4.82		4.67	5.23	4.55	4.87
	$2\ ^1A'$	5.20		5.30	5.36	5.25	5.30
	$2\ ^1A''$	6.10		6.09	6.52	6.03	6.37
	$3\ ^1A'$	6.27		6.29	6.57	6.24	6.37
	$4\ ^1A'$	6.53		6.72	6.80	6.72	6.76
Uracil							
	$1\ ^1A''$	4.80		4.64	5.19	4.51	4.83
	$2\ ^1A'$	5.35		5.41	5.44	5.31	5.37
	$2\ ^1A''$	6.10		6.01	6.68	5.96	6.30
	$3\ ^1A'$	6.26		6.26	6.53	6.22	6.34
	$3\ ^1A''$	6.56		6.96	6.71	6.90	6.82
	$4\ ^1A'$	6.70		6.89	6.94	6.85	6.89
Adenine							
	$1\ ^1A''$	5.12		5.19	5.56	5.43	5.48
	$2\ ^1A'$	5.25		5.20	5.19	5.12	5.13
	$3\ ^1A'$	5.25		5.33	5.30	5.26	5.26
	$2\ ^1A''$	5.75		5.84	6.12	5.99	6.04

[a] Ref. [209].

Table A.2. Benchmark results for triplet states from the Thiel benchmark set.

Compound	State	TBE[a]	CC3[a]	ADC(2)	ADC(3(3))	ADC(3(4))	ADC(3(4+))
Ethylene							
	$1\ ^3B_{1u}$	4.50	4.48	4.52	4.23	4.29	4.27
Butadiene							
	$1\ ^3B_u$	3.20	3.32	3.40	3.03	3.06	3.05
	$1\ ^3A_g$	5.08	5.17	5.23	4.89	4.94	4.93
Hexatriene							
	$1\ ^3B_u$	2.40	2.69	2.79	2.38	2.40	2.39
	$1\ ^3A_g$	4.38	4.15	4.38	4.00	4.03	4.02
Octatetraene							
	$1\ ^3B_u$	2.20	2.30	2.41	1.97	1.99	1.98
	$1\ ^3A_g$	3.55	3.67	3.74	3.34	3.36	3.35
Cyclopropene							
	$1\ ^3B_2$	4.34	4.34	4.43	4.08	4.11	4.10
	$1\ ^3B_1$	6.62	6.62	6.66	6.45	6.48	6.47
Cyclopentadiene							

Table A.2. (continued)

Compound	State	TBE[a]	CC3[a]	ADC(2)	ADC(3(3))	ADC(3(4))	ADC(3(4+))
	$1\ ^3B_2$	3.25	3.25	3.35	2.97	3.00	2.99
	$1\ ^3A_1$	5.09	5.09	5.19	4.83	4.86	4.85
Norbornadiene							
	$1\ ^3A_2$	3.72	3.72	3.74	3.46	3.49	3.48
	$1\ ^3B_2$	4.16	4.16	4.24	3.91	3.94	3.92
Benzene							
	$1\ ^3B_{1u}$	4.15	4.12	4.30	3.88	3.89	3.88
	$1\ ^3E_{1u}$	4.86	4.90	5.13	4.62	4.63	4.62
	$1\ ^3B_{2u}$	5.88	6.04	6.05	5.73	5.74	5.74
	$1\ ^3E_{2g}$	7.51	7.49	7.90	7.66	7.81	7.77
Naphthalene							
	$1\ ^3B_{2u}$	3.11	3.11	3.26	2.85	2.85	2.84
	$1\ ^3B_{3u}$	4.18	4.18	4.36	3.90	3.90	3.90
	$1\ ^3B_{1g}$	4.47	4.47	4.63	4.21	4.21	4.20
	$2\ ^3B_{2u}$	4.64	4.64	4.86	4.37	4.37	4.36
	$2\ ^3B_{3u}$	5.08	5.11	5.08	4.82	4.82	4.82
	$1\ ^3A_g$	5.74	5.52	5.74	5.24	5.25	5.24
	$2\ ^3B_{1g}$	6.48	6.48	6.45	6.27	6.27	6.27
	$2\ ^3A_g$	6.47	6.47	6.82	6.16	6.17	6.17
	$3\ ^3B_{1g}$	6.76	6.76	7.24	6.49	6.51	6.51
	$3\ ^3A_g$	6.79	6.79	6.94	6.59	6.60	6.59
Furan							
	$1\ ^3B_2$	4.17	4.17	4.35	3.84	3.93	3.88
	$1\ ^3A_1$	5.48	5.48	5.59	5.22	5.23	5.24
Pyrrole							
	$1\ ^3B_2$	4.48	4.48	4.66	4.21	4.25	4.23
	$1\ ^3A_1$	5.51	5.51	5.67	5.26	5.28	5.28
Imidazole							
	$1\ ^1A'$	4.69	4.69	4.86	4.40	4.42	4.40
	$2\ ^1A'$	5.79	5.79	5.98	5.52	5.54	5.55
	$1\ ^1A''$	6.37	6.37	6.38	6.26	6.18	6.20
	$3\ ^1A'$	6.55	6.55	6.71	6.29	6.26	6.25
	$4\ ^1A'$		7.42	7.60	7.20	7.16	7.15
	$2\ ^1A''$		7.51	7.61	7.50	7.60	7.57
Pyridine							
	$1\ ^3A_1$	4.06	4.25	4.45	3.98	3.97	3.95
	$1\ ^3B_1$	4.25	4.50	4.52	4.43	4.34	4.35
	$1\ ^3B_2$	4.64	4.86	5.06	4.55	4.56	4.54
	$2\ ^3A_1$	4.91	5.05	5.30	4.74	4.74	4.74
	$1\ ^3A_2$	5.28	5.46	5.34	5.72	5.64	5.70
	$2\ ^3B_2$	6.08	6.40	6.47	6.08	6.08	6.08
	$3\ ^3B_2$		7.83	8.38	7.40	7.40	7.40
	$3\ ^3A_1$		7.66	8.17	7.23	7.23	7.22
Tetrazine							
	$1\ ^3B_{3u}$	1.89	1.89	1.89	1.75	1.74	1.74
	$1\ ^3A_u$	3.52	3.52	3.47	3.58	3.61	3.60
	$1\ ^3B_{1g}$	4.21	4.21	4.29	4.03	4.00	4.01
	$1\ ^3B_{1u}$	4.33	4.33	4.60	3.92	3.89	3.88
	$1\ ^3B_{2u}$	4.54	4.54	4.79	4.05	4.02	4.02
	$1\ ^3B_{2g}$	4.93	4.93	5.04	4.70	4.68	4.68
	$2\ ^3A_u$	5.03	5.03	5.08	4.98	4.96	4.97
	$2\ ^3B_{1u}$	5.38	5.38	5.64	5.00	4.99	4.98

Table A.2. (continued)

Compound	State	TBE[a]	CC3[a]	ADC(2)	ADC(3(3))	ADC(3(4))	ADC(3(4+))
	$2\ ^3B_{2g}$		6.04	6.09	6.12	6.12	6.12
	$2\ ^3B_{1g}$		6.60	6.75	6.95	6.97	6.96
	$2\ ^3B_{3u}$		6.53	6.54	6.64	6.65	6.65
	$2\ ^3B_{2u}$		7.36	7.59	6.95	6.96	6.95
Formaldehyde							
	$1\ ^3A_2$	3.50	3.55	3.41	3.43	3.11	3.24
	$1\ ^3A_1$	5.87	5.83	5.96	5.46	5.26	5.29
Acetone							
	$1\ ^3A_2$	4.05	4.05	3.88	4.00	3.58	3.76
	$1\ ^3A_1$	6.03	6.03	6.12	5.71	5.39	5.47
Benzoquinone							
	$1\ ^3B_{1g}$	2.51	2.51	2.35	2.57	2.16	2.37
	$1\ ^3A_u$	2.62	2.62	2.44	2.72	2.22	2.47
	$1\ ^3B_{1u}$	2.96	2.96	3.07	2.63	2.47	2.52
	$1\ ^3B_{3g}$	3.41	3.41	3.52	3.05	3.25	3.18
Formamide							
	$1\ ^3A''$	5.36	5.36	5.13	5.36	4.85	5.07
	$1\ ^3A'$	5.74	5.74	5.81	5.51	5.22	5.29
Acetamide							
	$1\ ^3A''$	5.42	5.42	5.16	5.46	4.92	5.15
	$1\ ^3A'$	5.88	5.88	5.92	5.70	5.35	5.45
Propanamide							
	$1\ ^3A''$	5.45	5.45	5.18	5.49	4.95	5.18
	$1\ ^3A'$	5.90	5.90	5.92	5.72	5.37	5.47

[a] Ref. [209].

A.2. Jacquemin Benchmark Set

Table A.3. Benchmark results for singlet states from the Jacquemin benchmark set.

Compound	State	TBE[a]	CC3[a]	ADC(2)[a]	ADC(3(3))	ADC(3(4))	ADC(3(4+))
Acetaldehyde							
	$1\ ^1A''$	4.31	4.31	4.23	4.28	3.92	4.09
Acetylene							
	$1\ ^1\Sigma_u^-$	7.10	7.09	7.24	6.72	6.78	6.76
	$1\ ^1\Delta_u$	7.44	7.42	7.57	7.06	7.12	7.10
	$1\ ^1A_u$[F]	3.64	3.64	3.78	2.85	2.85	2.83
	$1\ ^1A_2$[F]	3.85	3.84	3.99	3.08	3.10	3.08
Ammonia							
	$1\ ^1A_2$	6.59	6.57	6.42	6.63	6.74	6.68
	$1\ ^1E$	8.16	8.15	7.88	8.21	8.32	8.26
	$1\ ^1A_1$	9.33	9.32	9.06	9.38	9.49	9.43
	$2\ ^1A_2$	9.96	9.95	9.69	10.01	10.12	10.06
Carbon monoxide							
	$1\ ^1\Pi$	8.49	8.49	8.68	8.23	8.45	8.39
	$1\ ^1\Sigma^-$	9.92	9.99	10.01	9.72	9.18	9.41
	$1\ ^1\Delta$	10.06	10.12	10.30	9.82	9.27	9.51
	$2\ ^1\Sigma^+$	10.95	10.94	11.33	10.80	11.25	11.10

Table A.3. (continued)

Compound	State	TBE[a]	CC3[a]	ADC(2)[a]	ADC(3(3))	ADC(3(4))	ADC(3(4+))
	$3\ ^1\Sigma^+$	11.52	11.49	11.84	11.34	11.78	11.62
	$2\ ^1\Pi$	11.72	11.69	12.04	11.56	11.96	11.83
Cyclopropene							
	$1\ ^1B_1$	6.68	6.68	6.75	6.55	6.58	6.57
	$1\ ^1B_2$	6.79	6.73	6.77	6.56	6.58	6.57
Diazomethane							
	$1\ ^1A_2$	3.14	3.07	3.34	2.74	2.69	2.69
	$1\ ^1B_1$	5.54	5.45	5.64	5.24	5.43	5.33
	$2\ ^1A_1$	5.90	5.84	5.97	5.48	5.51	5.48
	$1\ ^1A''$[F]	0.71	0.68	0.81	0.24	0.17	0.16
Dinitrogen							
	$1\ ^1\Pi_g$	9.34	9.34	9.47	9.16	9.22	9.21
	$1\ ^1\Sigma_u^-$	9.88	9.88	10.25	9.32	9.33	9.32
	$1\ ^1\Delta_u$	10.29	10.29	10.79	9.74	9.75	9.74
	$2\ ^1\Sigma_g^+$	12.98	13.01	13.01	12.97	13.01	13.01
	$1\ ^1\Pi_u$	13.03	13.22	13.34	13.02	13.32	13.25
	$2\ ^1\Sigma_u^-$	13.09	13.12	13.08	12.97	13.01	13.01
	$2\ ^1\Pi_u$	13.46	13.49	13.95	13.40	13.70	13.63
Ethylene							
	$1\ ^1B_{3u}$	7.39	7.35	7.35	7.17	7.32	7.27
	$1\ ^1B_{1u}$	7.93	7.91	7.92	7.69	7.76	7.73
	$1\ ^1B_{1g}$	8.08	8.03	8.00	7.84	7.98	7.94
Formaldehyde							
	$1\ ^1A_2$	3.98	3.97	3.92	3.90	3.59	3.73
	$1\ ^1B_2$	7.23	7.18	6.51	7.62	7.35	7.52
	$2\ ^1B_2$	8.13	8.07	7.54	8.45	8.21	8.37
	$2\ ^1A_1$	8.23	8.18	7.48	8.61	8.34	8.51
	$2\ ^1A_2$	8.67	8.64	8.00	9.02	8.76	8.93
	$1\ ^1B_1$	9.22	9.19	9.16	9.16	8.85	8.99
	$3\ ^1A_1$	9.43	9.48	9.47	9.05	8.84	8.95
	$1\ ^1A''$[F]	2.80	2.84	2.71	2.77	2.22	2.48
Formamide							
	$1\ ^1A''$	5.65	5.66	5.44	5.74	5.25	5.46
	$2\ ^1A'$	6.77	6.74	6.27	7.20	6.91	7.06
	$3\ ^1A'$	7.38	7.40	6.84	7.80	7.49	7.64
	$4\ ^1A'$	7.63	7.62	7.32	8.13	7.76	7.96
HCl							
	$1\ ^1\Pi$	7.84	7.84	7.95	7.79	7.77	7.78
H_2S							
	$1\ ^1A_2$	6.18	6.19	6.35	6.04	6.04	6.04
	$1\ ^1B_1$	6.24	6.24	6.31	6.17	6.16	6.16
Ketene							
	$1\ ^1A_2$	3.86	3.88	4.11	3.66	3.64	3.67
	$1\ ^1B_1$	6.01	5.96	6.04	5.88	6.08	6.03
	$2\ ^1A_2$	7.18	7.16	7.20	7.07	7.31	7.24
Methanimine							
	$1\ ^1A''$	5.23	5.20	5.28	5.04	5.00	5.01
Nitrosomethane							
	$1\ ^1A''$	1.96	1.96	1.87	1.72	1.52	1.63
	$2\ ^1A'$	6.40	6.31	5.87	6.49	6.56	6.58
	$1\ ^1A''$[F]	1.67	1.69	1.55	1.40	1.18	1.31
Streptocyanine-C1							

Table A.3. (continued)

Compound	State	TBE[a]	CC3[a]	ADC(2)[a]	ADC(3(3))	ADC(3(4))	ADC(3(4+))
	$1\ ^1B_2$	7.13	7.13	7.00	7.16	7.05	7.08
Thioformaldehyde							
	$1\ ^1A_2$	2.22	2.23	2.21	2.05	1.83	1.91
	$1\ ^1B_2$	5.96	5.91	5.78	5.96	5.83	5.92
	$2\ ^1A_1$	6.38	6.48	5.56	5.98	5.93	5.96
	$1\ ^1A_2$[F]	1.95	1.97	1.92	1.80	1.47	1.60
Water							
	$1\ ^1B_1$	7.62	7.65	7.19	7.84	7.76	7.78
	$1\ ^1A_2$	9.41	9.40	8.85	9.63	9.55	9.57
	$2\ ^1A_1$	9.99	10.00	9.53	10.22	10.14	10.15

[a] Ref. [212].

Table A.4. Benchmark results for triplet states from the Jacquemin benchmark set.

Compound	State	TBE[a]	CC3[a]	ADC(2)[a]	ADC(3(3))	ADC(3(4))	ADC(3(4+))
Acetaldehyde							
	$3\ ^1A''$	3.97	3.95	3.82	3.89	3.54	3.69
Acetylene							
	$1\ ^3\Sigma_u^+$	5.53	5.50	5.74	5.24	5.28	5.26
	$1\ ^3\Delta_u$	6.40	6.40	6.57	6.06	6.11	6.09
	$1\ ^3\Sigma_u^-$	7.08	7.07	7.27	6.71	6.77	6.75
Ammonia							
	$1\ ^3A_2$	6.31	6.29	6.17	6.31	6.42	6.36
Carbon monoxide							
	$1\ ^3\Pi$	6.28	6.30	6.45	5.96	6.21	6.12
	$1\ ^3\Sigma^+$	8.45	8.45	8.53	8.21	7.73	7.93
	$1\ ^3\Delta$	9.27	9.30	9.33	9.02	8.51	8.73
	$1\ ^3\Sigma^-$	9.80	9.82	10.00	9.52	9.00	9.22
	$2\ ^3\Sigma^+$	10.47	10.45	10.85	10.30	10.71	10.57
Cyclopropene							
	$1\ ^3B_2$	4.38	4.34	4.45	4.08	4.11	4.09
	$1\ ^3B_1$	6.45	6.40	6.45	6.25	6.28	6.27
Diazomethane							
	$1\ ^3A_2$	2.79	2.83	3.00	2.44	2.40	2.41
	$1\ ^3A_1$	4.05	4.03	4.19	3.64	3.56	3.54
	$1\ ^3B_1$	5.35	5.31	5.52	5.09	5.28	5.19
	$2\ ^3A_1$	6.82	6.80	7.08	6.35	6.33	6.28
Dinitrogen							
	$1\ ^3\Sigma_u^+$	7.70	7.68	8.14	7.24	7.22	7.21
	$1\ ^3\Pi_g$	8.01	8.04	8.20	7.76	7.81	7.80
	$1\ ^3\Delta_u$	8.87	8.87	9.25	8.36	8.34	8.34
	$1\ ^3\Sigma_u^-$	9.66	9.68	10.23	9.15	9.15	9.14
Ethylene							
	$1\ ^3B_{1u}$	4.54	4.53	4.59	4.28	4.33	4.31
	$1\ ^3B_{3u}$	7.23	7.24	7.25	7.06	7.20	7.16
	$1\ ^3B_{1g}$	7.98	7.98	7.96	7.80	7.91	7.88
Formaldehyde							
	$1\ ^3A_2$	3.58	3.57	3.45	3.47	3.18	3.30
	$1\ ^3A_1$	6.06	6.05	6.19	5.70	5.51	5.54
	$1\ ^3B_2$	7.06	7.03	6.40	7.45	7.19	7.35

Table A.4. (continued)

Compound	State	TBE[a]	CC3[a]	ADC(2)[a]	ADC(3(3))	ADC(3(4))	ADC(3(4+))
	$2\ ^3B_2$	7.94	7.92	7.42	8.24	8.01	8.16
	$2\ ^3A_1$	8.10	8.08	7.40	8.47	8.21	8.37
	$1\ ^3B_1$	8.42	8.41	8.38	8.31	8.02	8.14
Formamide							
	$1\ ^3A''$	5.38	5.38	5.14	5.41	4.94	5.14
	$1\ ^3A'$	5.81	5.82	5.88	5.62	5.36	5.43
H_2S							
	$1\ ^3A_2$	5.81	5.82	5.90	5.67	5.68	5.68
	$1\ ^3B_1$	5.88	5.88	5.95	5.81	5.80	5.80
Ketene							
	$1\ ^3A_2$	3.77	3.78	3.92	3.56	3.53	3.56
	$1\ ^3A_1$	5.61	5.61	5.66	5.38	5.35	5.37
	$1\ ^3B_1$	5.79	5.76	5.87	5.68	5.87	5.83
	$2\ ^3A_2$	7.12	7.12	7.17	7.03	7.26	7.20
Methanimine							
	$1\ ^3A''$	4.65	4.61	4.60	4.43	4.39	4.40
Nitrosomethane							
	$1\ ^3A''$	1.16	1.14	1.02	0.84	0.69	0.77
	$1\ ^3A'$	5.60	5.51	5.74	5.04	4.83	4.88
Streptocyanine-C1							
	$1\ ^3B_2$	5.47	5.48	5.54	5.32	5.20	5.20
Thioformaldehyde							
	$1\ ^3A_2$	1.94	1.94	1.84	1.77	1.56	1.62
	$1\ ^3A_1$	3.43	3.38	3.44	3.06	3.03	3.02
	$1\ ^3B_2$	5.72	5.72	5.60	5.75	5.63	5.71
Water							
	$1\ ^3B_1$	7.25	7.28	6.87	7.42	7.35	7.36
	$1\ ^3A_2$	9.24	9.26	8.74	9.43	9.36	9.37
	$1\ ^3A_1$	9.54	9.56	9.16	9.70	9.63	9.64

[a] Ref. [212].

Danksagung

An dieser Stelle gebührt mein Dank zuallererst Prof. Dr. Andreas Dreuw, der mir die Möglichkeit gegeben hat meine Doktorarbeit in seiner Arbeitsgruppe anzufertigen. Die spannende Themenstellung einerseits und die Freiheit bei der Ausgestaltung der Arbeit andererseits haben dazu beigetragen, dass die vergangenen Jahre für mich eine ganz besondere Zeit waren, in der ich mich in vielerlei Hinsicht weiterentwickeln konnte. Auch in persönlicher Hinsicht möchte ich mich bei Andreas bedanken, der für mich in dieser Zeit mehr als nur der Doktorvater war und mir in jeder Situation Rückhalt gegeben und den Rücken freigehalten hat.

Bei Dr. Markus Pernpointner möchte ich mich dafür bedanken, dass er mir durch seine unübertroffenen Vorlesungen und seine zugewandte Art einen einfachen Einstieg in die theoretische Chemie ermöglicht und mich auch darüber hinaus im Studium unterstützt hat. Ebenso gilt mein Dank Prof. Dr. Günter Helmchen für die Unterstützung während des Studiums.

Für das Korrekturlesen dieser Arbeit danke ich ganz herzlich Max Scheurer, Lukas Wirz und Dirk Rehn. Zum Gelingen dieser Arbeit haben außerdem durch viele hilfreiche Diskussionen und Handreichungen Prof. Dr. Alexander Trofimov, Prof. Dr. Thomas Sommerfeld, Dr. Kirill Gokhberg und nicht zuletzt Prof. Dr. Jochen Schirmer beigetragen. Ihnen gilt mein ganz besonderer Dank. Dr. Kirill Gokhberg danke ich zudem für die Begutachtung dieser Arbeit.

Ich möchte mich weiterhin bei der gesamten Arbeitsgruppe Dreuw für die angenehme Atmosphäre und die vielen erhellenden Gespräche bedanken. Meinen Büromitbewohnern Marvin, Tim und Manu, sowie allen derzeitigen (Dirk, Max, Sebi, Ben, Rogo, Marvin, Manu, Reena, Maximilien, Jie, Mikael und Thomas) und ehemaligen Gruppenmitgliedern (Daniel, Max K., Daria, Stefan, Katie, Jan, Duygu, Mary, Chong, Tobi und Michael) gilt mein Dank für die große Unterstützung, die ich in den letzten Jahren erfahren habe. Desweiteren danke ich ganz besonders Manfred für die großartige IT-Administration, die er für die gesamte Gruppe leistet, die besonnene Art, wenn einmal etwas besonders schief gegangen ist, und die vielen Kaffee-Sprechstunden.

Ich bedanke mich herzlich bei Dr. Matthias Schneider und Alexander Paul, deren Arbeit

an IP-ADC und EA-ADC ich weiterführen durfte, sowie bei den ForschunkspraktikantInnen und MasterstudentInnen, die auf dem Gebiet der Propagator-Methoden mitgewirkt haben. Sina Ziegler, Andy Fink, Tobias Saxl und Goh Fang Ting haben mir während der letzten Jahre durch ihre Mitarbeit wichtige Impulse gegeben und damit zum Gelingen dieser Arbeit beigetragen.

Für die Minimierung des verwaltungstechnischen Aufwands danke ich Ellen Vogel. Desweiteren gilt mein Dank der Heidelberg Graduate School of Mathematical and Computational Methods for the Sciences (HGS MathComp) für die Finanzierung von Reisen zu Konferenzen und Winterschulen, sowie für die administrative Betreuung derselben Sarah Steinbach und Ria Hillenbrand-Lynott.

Ich möchte mich weiterhin bei allen Freunden bedanken, die auf die eine oder andere Weise am Gelingen dieser Arbeit beteiligt waren. Besonders erwähnen möchte ich an dieser Stelle Demi, Michel und Annette sowie Familie Exner. Auch meiner Familie möchte ich für die Unterstützung danken.

Zuguterletzt gilt mein aufrichtiger Dank Laura, die mir stets Rückhalt gegeben und mir häufig geholfen hat, schwierige Situationen hinter mir zu lassen. Ohne ihre Unterstützung in jedweder Hinsicht wäre diese Arbeit nicht möglich gewesen.

Eidesstattliche Versicherung gemäß § 8 der Promotionsordnung für die Naturwissenschaftlich-Mathematische Gesamtfakultät der Universität Heidelberg

1. Bei der eingereichten Dissertation zu dem Thema
   Development and Implementation of High-Level Propagator Methods for the Description of Electronically Stable and Unstable States
   handelt es sich um meine eigenständig erbrachte Leistung.

2. Ich habe nur die angegebenen Quellen und Hilfsmittel benutzt und mich keiner unzulässigen Hilfe Dritter bedient. Insbesondere habe ich wörtlich oder sinngemäß aus anderen Werken übernommene Inhalte als solche kenntlich gemacht.

3. Die Arbeit oder Teile davon habe ich bislang nicht an einer Hochschule des In- oder Auslands als Bestandteil einer Prüfungs- oder Qualifikationsleistung vorgelegt.

4. Die Richtigkeit der vorstehenden Erklärungen bestätige ich.

5. Die Bedeutung der eidesstattlichen Versicherung und die strafrechtlichen Folgen einer unrichtigen oder unvollständigen eidesstattlichen Versicherung sind mir bekannt.

Ich versichere an Eides statt, dass ich nach bestem Wissen die reine Wahrheit erklärt und nichts verschwiegen habe.

_____ _____

Ort und Datum Unterschrift